MICROMACHINED ULTRASONIC SILICON HORN ACTUATORS FOR BIOMEDICAL APPLICATIONS: SURGICAL TOOLS, CARDIAC ELECTROPHYSIOLOGICAL RECORDINGS, TESTICULAR TUBULE-SIZE DETECTION AND FLUID VISCOSITY MEASUREMENT

A Dissertation

Presented to the Faculty of the Graduate School

of Cornell University

in Partial Fulfillment of the Requirements for the Degree of

Doctor of Philosophy

by

Ramkumar Abhishek

May 2010

MICROMACHINED ULTRASONIC SILICON HORN ACTUATORS FOR BIOMEDICAL APPLICATIONS: SURGICAL TOOLS, CARDIAC ELECTROPHYSIOLOGICAL RECORDINGS, TESTICULAR TUBULE-SIZE DETECTION AND FLUID VISCOSITY MEASUREMENT

Ramkumar Abhishek, Ph.D.

Cornell University 2010

This thesis presents the continuing research effort towards the use of ultrasonic silicon-based microelectromechanical systems (MEMS) systems for biomedical applications. Microfabricated silicon-horn based surgical microprobes are developed to reduce penetration force into biological tissues by actuating the surgical tool at its ultrasonic resonance. Silicon serves as an ideal platform for integration of a variety of microfabricated sensors on the surgical tools to monitor tissue activity. In this thesis, two sensors are integrated on the microprobes namely platinum electrodes and piezoresistive polysilicon strain gauge sensors. The use of these microprobes in biomedical applications is explored including ultrasonically actuated microprobes with platinum electrodes for cardiac signal recording and stimulation, and ultrasonically actuated microprobes with strain sensors for a testicular tubule-size assay and fluid viscosity measurement.

The first part of the thesis presents silicon microprobes integrated with horn-PZT actuator for reduction in penetration force in cardiac left ventricular tissue. Platinum electrodes integrated on the microprobes measure the action potentials along the ventricular wall. This device can potentially help provide a 3D map of the electrophysiological activity (wave propagation) in the heart, which may lead to the understanding of cardiac arrhythmias, as well as the prevention and

cure of the disease. Also, by ultrasonically stimulating the tissue invasively using the horn with microprobes, the ability to stimulate cardiac tissue and initiate electrophysiological activity in the tissue is demonstrated.

The second part of the thesis presents ultrasonic silicon microprobes integrated with strain gauges to monitor the reaction force when inserted into tissue, and its potential for *in vitro* microscale tissue characterization is demonstrated. A testicular tubule-size assay is demonstrated by monitoring the strain signal output recorded during insertion of the microprobe in rat testis tissue to estimate the average diameter of the seminiferous tubules. This information is important for the surgeon to distinguish between tubules with (larger diameter) and without (smaller diameter) fertile sperm during microdissection-TESE (testicular sperm extraction) surgery, thus enabling a microprobe-based assay for sperm viability. This technique is effectively a new biomedical imaging technique that can be used to image physical characteristics of tissue non-invasively. This can prove to be an invaluable tool during surgery for intelligent tissue biopsy by identifying specific regions of the tissue that exhibit detectable physical characteristics (stiffness, temperature, etc.).

The final part of the thesis presents a silicon horn-based ultrasonic microprobes for fluid viscosity measurement with integrated capacitance-based microprobe immersion depth sensors. The longitudinal and flexural vibrations induced in the microprobes due to the PZT-based ultrasonic actuation of the silicon horn structure is precisely monitored by means of the strain gauge, and its damping when the microprobes are immersed in fluid is used to estimate the fluid viscosity. The high sensitivity demonstrated by the viscosity sensor allows for measurement in small sample volumes ($\approx 5\ \mu$l).

BIOGRAPHICAL SKETCH

Ramkumar Abhishek was born in New Delhi, India and brought up in Hyderabad, India. He graduated with a Bachelors degree in Electrical Engineering from the Indian Institute of Technology-Bombay (IITB), India in 2004. He began his Ph.D. study soon after under the guidance of Dr. Amit Lal in the field of Microelectromechanical systems with applications in medicine and bioengineering. During the last few years of his Ph.D. study at Cornell University, he came to appreciate the importance and excitements in entrepreneurship in engineering and technology. In the future, he hopes to use the skills and experience he gained from his Ph.D. in developing revolutionary technologies for practical applications in the biomedical industry.

This work is dedicated to my loving parents, Ramkumar Seshadri and Anuradha Ramkumar and my beloved brother, Avinash Ramkumar for all their support, guidance and encouragement. This work is also dedicated to my late grandfather Vaidyanath Seshadri who encouraged me to always be curious, open-minded and to never give up.

ACKNOWLEDGEMENTS

I would first like to thank Prof. Amit Lal for his guidance and direction throughout my Ph.D. I have him to thank for instilling the knowledge and confidence in me to approach any problem with an open mind, aim high and expect more out of myself. I will always admire and be inspired by his exceptional enthusiasm, far-sighted thinking and his ability to motivate his students to do more than their best. I would also like to thank Prof. Robert F. Gilmour Jr., Prof. Manfred Lindau and Prof. Sunil Bhave for their advice and encouragement throughout my Ph.D. Special thanks go to Prof. Robert F. Gilmour Jr. and his laboratory in the Department of Biomedical Sciences, for their support and numerous helpful discussions they have offered as part of our collaboration. I would also like to thank the Urology surgeons and professors at the Weill Cornell Medical College in New York city, Dr. Peter N. Schlegel and Dr. Darius A. Paduch, for their time and patience to help us establish a fruitful collaboration - I sincerely hope that this work fosters collaboration on future projects with the Weill Cornell Medical College!

I would like to thank the staff members of Cornell Nanoscale Science and Technology Facility (CNF) and Nanobiotechnology Center (NBTC) for their suggestions to fabricate the devices needed to perform my research. I would also like to thank Dr. Diane Creasy for being open to discussion to me without introduction and her prompt responses regarding histological and morphological analysis of testicular tissue. I am indebted to Patricia Fisher and the staff of the immunopathology and histology laboratories at the Veterinary school for being patient with me and helping me out at odd hours in the day and night.

I cannot thank Xi Chen enough for teaching and helping me get started with my research and fabrication in CNF. I have learnt a lot from her and, will always

be thankful to her for being patient with me and allowing me to fabricate her devices for crucial experiments at the end of her Ph.D. And my thanks go to all the previous and present group members of the *Sonic*MEMS laboratory I have worked with. I am very fortunate to be a part of this talented group and will always cherish the many fun times we had at the laboratory. I would like to especially thank Norimasa Yoshimizu, Serhan Ardanuc, Shankar Radhakrishnan, Kursad Araz and Rajesh Duggirala for the many 'quick' discussion sessions about my research which at times lasted for hours. I would like to thank all my friends in Ithaca for making my experience at Cornell a memorable one. Special thanks goes to Clarissa Lui for her support and encouragement, and being patient with me throughout my Ph.D.

Finally, I would like to thank my parents and brother for their support and being openminded with me, and always encouraging me to do my best. I would like to especially thank my father for teaching me to be objective in my thinking, his never-say-die attitude and his dedication to excellence - I owe a large part of my success to him.

TABLE OF CONTENTS

LIST OF FIGURES

LIST OF TABLES

CHAPTER 1

INTRODUCTION

This thesis presents the ongoing research on Ultrasonic MEMS devices and its applications in biomedical engineering. The work presented here is focused on biomedical applications of ultrasonic silicon-horn actuators namely ultrasonic surgical tools, ultrasonic microprobes for cardiac electrophysiological recordings and ultrasonic microprobes with integrated strain gauges for testicular tubule-size detection and fluid viscosity measurement. This chapter introduces the field of power ultrasonics and the crucial role played by micromachined silicon transducers in potentially revolutionizing this industry.

1.1 Silicon-based power ultrasonics

Ultrasound is traditionally defined as vibrations in a medium at frequencies above 20 kHz. Based on the widespread applications of ultrasound in many fields, it is broadly categorized based on the vibration amplitude into two categories namely, low-intensity and high-intensity ultrasound. Low-intensity ultrasound is used for applications where the effect is minimal in order not to change the physical properties of the subject under test, such as medical ultrasound-based imaging and non-destructive testing. High-intensity ultrasound ($\geq$ 1 W/cm^2) applications require the change in physical or chemical properties of the subject under test through a variety of ultrasond-based effects. High-intensity ultrasound is used for drilling and cutting ceramics, welding plastics, and sonochemical processing. It is also used in surgical procedures such as lithotripsy, where unwanted tissue is broken up using high-intensity ultrasound via cavitation and direct cutting.

In order to optimize the design of a power ultrasonic tool the parameter of importance is vibration amplitude for a given actuation voltage. High vibration amplitudes result in large inertial contact forces, which are necessary for mechanical manipulation of materials in applications such as cutting and machining. This in turn results in high local acoustic intensity which is required for producing non-linear effects such as acoustic cavitation. The inertial force exerted by an ultrasound transducer is defined as the product of its intertial mass, angular frequency of actuation and the amplitude of vibrational particle velocity. The corresponding relationship for intensity can be defined as the product of the characteristic acoustic impedance ($Z = \rho c$) of the medium/material and the square of the vibrational velocity amplitude. Practically speaking, the vibrational particle velocity of an ultrasonic transducer is limited by the yield strength and the velocity of sound in the material. The maximum attainable particle velocity is proportional to the product $S_m c$, where S_m denotes the maximum strain that can be sustained by the material without plastic failure and c is the velocity of sound in the material [6]. The traditional choice for power ultrasonic transducers is high-strength titanium alloy ($S_m c = 41$ m/s). The ultrasonic handpiece used in phacoemulsification surgery (Langevin transducer) is made out of this alloy, with the cutting tip reaching longitudinal vibration amplitudes of ≈ 100 μm_{pp} at frequencies in the range of 40-60 kHz. Single crystal silicon is capable of reaching vibration amplitudes almost 10 times that of the titanium transducers, owing to its high $S_m c$ product of 335 m/s. This is one of the compelling arguments for the advantages silicon offers in the power ultrasonics industry when it was first proposed more than a decade ago [1, 7].

1.2 Ultrasonic horn transducers

For design optimization of ultrasonic transducers, along with selecting a material with a high particle velocity limit it is necessary to have an appropriate interface for electro-mechanical actuation using piezoelectric lead zirconate titanate (PZT) transducers. Since PZT ceramics have low $S_m c$ values (≈ 0.93 m/s), the vibration amplitudes generated by electro-mechanical transduction are too low to be directly used at the actuation stage. The solution is to use an appropriate velocity transforming waveguide (ultrasonic horn) made of a material with a high particle velocity limit (high $S_m c$), that is capable of magnifying the vibration amplitude produced by the electro-mechancal transduction (using PZT) to much higher levels. Ultrasonic horn transducers are resonators with tapered cross-sections optimized to concentrate mechanical energy at the tip of the transducer with a small cross-sectional area, therefore achieving high vibration amplitudes [8].

When a differential element from a rod with a variable cross section is considered, under the assumptions of uniform stress distribution, material homogeneity and negligible lateral inertia, the equation of motion is given by [9]:

$$-\sigma A + (\sigma + \frac{\partial \sigma}{\partial x} dx)(A + \frac{dA}{dx} dx) = \frac{1}{2}\rho \left\{ A + (A + \frac{dA}{dx} dx) \right\} dx \frac{\partial^2 u}{\partial t^2} \tag{1.1}$$

where σ is the stress acting on the cross section of the element, $A(x)$ is the variable cross section as a function of the distance along the axis of the rod x, ρ is the density, and $u(x)$ is the displacement along the x-direction. Ignoring the second-order partial differential terms, Eq. 1.1 can be reduced to

$$\frac{1}{A}\frac{\partial}{\partial x}(\sigma A) = \rho \frac{\partial^2 u}{\partial t^2} \tag{1.2}$$

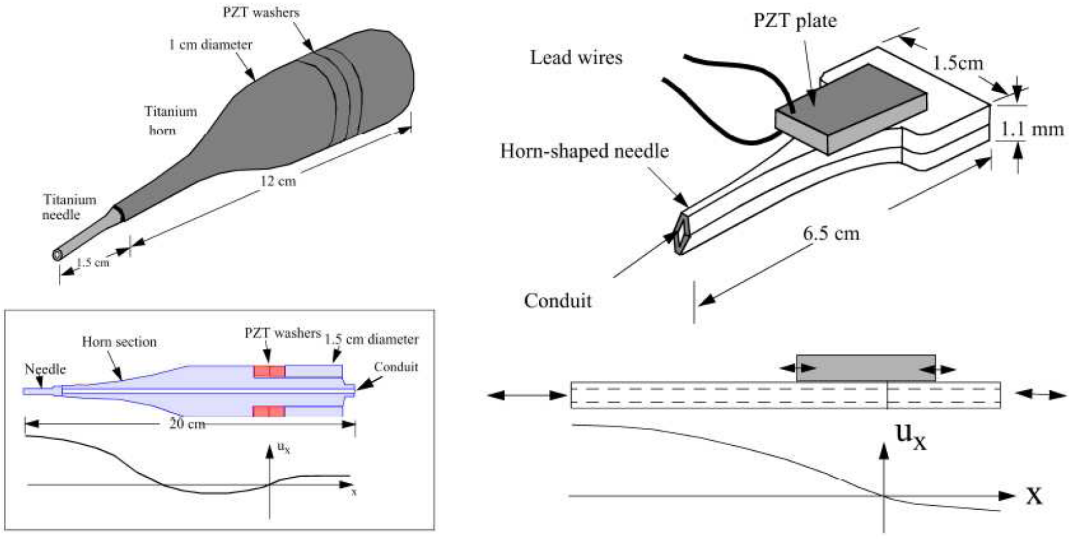

Figure 1.1: Schematics for coupling PZT transducers to Langevin-bolted titanium-alloy and silicon acoustic horn transducers to achieve high particle velocity. Adapted from [1].

Substituting stress with $\sigma = E\frac{\partial u}{\partial x}$, results in:

$$\frac{\partial}{\partial x}(EA\frac{\partial u}{\partial x}) = \rho A\frac{\partial^2 u}{\partial t^2} \tag{1.3}$$

Assuming uniform E and ρ,

$$\frac{1}{A}\frac{\partial}{\partial x}(A\frac{\partial u}{\partial x}) = \frac{1}{c_0^2}\frac{\partial^2 u}{\partial t^2} \tag{1.4}$$

or

$$\frac{\partial^2 u}{\partial x^2} + (\frac{\partial u}{\partial x})\frac{\partial}{\partial x}(lnA(x)) = \frac{1}{c_0^2}\frac{\partial^2 u}{\partial t^2} \tag{1.5}$$

where $c_0 = \sqrt{E/\rho}$ is the speed of sound, and E is the Young's modulus of the rod. Equation 1.5 is the Webster horn equation, used often in the field of acoustics. Ultrasonic horns with varying cross-sectional profiles have been investigated in the past [10, 11]. The displacement profile of the horns of different shapes can be obtained analytically or numerically calculated [9]. The particle velocity is

amplified at the tip of the smaller cross section of the horn when compared to the velocity at the end with the larger cross section. This amplification in particle velocity is dependent on the horn profile and the ratio of areas of the larger and smaller cross sections at the ends of the horn [9]. Figure 1.1 shows the Langevin-bolted transducer and the silicon horn with PZT transduction for high particle velocity at the tips. The use of silicon-based MEMS in the field of ultrasonics has opened new avenues and provided innovative solutions for various applications. Silicon-horn based transducers have been emerging as a popular transducer because of their superior material properties and their capability for integration of microfabrication technology. The silicon-horn transducers driven by bulk PZT plates in their longitudinal mode have been shown to produce high vibration amplitudes comparable to the traditional titanium-alloy transducers with lower thermal dissipation. Silicon horns with integrated sensors have been developed for strain measurement in applications such as phacoemulsification microsurgery [9].

1.3 Summary of contributions

Based on the previous work mentioned above, the current thesis focuses on the following three biomedical applications contributing further to the field of silicon-horn based ultrasonic surgical tools.

1. Silicon horn-based ultrasonic microprobes with platinum electrodes were used to record canine cardiac action potentials along the thickness of the canine left ventricular wall in order to better understand the mechanisms involved in cardiac arrhythmias. The ultrasonic actuation of the silicon horn is used

to reduce the penetration force of the microprobes with the electrodes along its length into the cardiac tissue. A new area of research was investigated with a vision of creating an implantable pacemaker by demonstrating the microprobes' ultrasound-based purely mechanical stimulation capability with minimal tissue damage, as an alternative to the high-power electrical shock currently used. Preliminary experiments were performed as a proof-of-concept for ultrasound-based stimulation of cardiac myocardium.

2. Silicon-based ultrasonic microprobes with integrated piezoresistive strain gauge sensors was used to develop a minimally invasive approach for determing the seminiferous tubule size inside the testis, as part of TEsticular Sperm Extraction (TESE) surgery for In-Vitro Fertilization (IVF). Experiments were performed in multiple rat testes and statistically significant microprobe metrology was performed to determine the diameter of the seminiferous tubules. This result can be generalized to determine inhomogeneous properties of tissue, or soft materials in general.

3. Strain gauge sensors on the ultrasonic microprobes were used to monitor the high-frequency vibration in the microprobes and the damping of this vibration when the microprobes are immersed in a fluid is used for estimating its viscosity. Pt-electrode based capacitive immersion-depth sensors are also integrated on the microprobes in order to precisely estimate the damping. Proof-of-concept experiments were performed in ethylene glycol solutions demonstrating its high sensitivity to fluid viscosity and its potential use in measuring blood-coagulation time is explored.

CHAPTER 2

ULTRASONICALLY ACTUATED SILICON MICROPROBES FOR CARDIAC MAP RECORDING

This chapter describes the work on ultrasonically actuated silicon thin microprobes that successfully penetrated canine cardiac tissue *in vitro*, and recorded the electrophysiological signals from multiple sites simultaneously within the heart wall. The penetration force - maximum force encountered by the probe during penetration - is found to be reduced with increasing ultrasonic driving voltage, on both excised canine right ventricular muscle and chicken breast muscle [9]. With ultrasonic actuation, the silicon microprobes are inserted into isolated perfused canine heart tissue without breakage or significant buckling under 10 V_{pp} actuating voltage. A model for ultrasound-based tissue penetration force reduction using vibrating microprobes is presented in this work, quantifying decrease in force as a function of PZT drive voltage and velocity of insertion of microprobes into tissue. Impedance characterization of planar platinum electrode on the microprobes for measuring action potentials revealed that the cardiac monophasic action potential (MAP) morphology can be maintained if the input impedance of the amplifier is higher than 10 GΩ. Recordings were obtained from isolated and perfused canine left ventricle tissue during pacing by means of electrical stimulation, following the induction of ventricular tachycardia, and during the transition from ventricular tachycardia to ventricular fibrillation. Local conduction velocity of cardiac action potentials $\approx$ 0.5 m/s was observed from the multichannel recordings from the canine right ventricular wall under epicardial pacing. We also present a hypothesis for mechanical stimulation of cardiac tissue, through the vibration of microprobes as a result of the ultrasonic longitudinal actuation of the horn. The application of the ultrasonically inserted microprobes in cardiac electrophysiology can provide

information for reconstruction of electrical wave propagation within the heart, which is important for understanding the mechanisms of cardiac arrhythmias.

2.1 Introduction

For a heart to function properly the contraction of cardiac muscle cells needs to be well coordinated to result in the dual pumping activity of the atria and the ventricles. Contraction (excitation) of cardiac muscle is triggered by depolarization of the cell membrane. In the heart, the initial excitation starts from the depolarization arising from a group of pacemaker cells, the sinoatrial (SA) node, located in the right atrium. The action potential then spreads from SA node through conduction system fibers to the ventricles and spreads within myocardium from cell to cell through gap junctions. This spreading of action potential wavefront from SA node throughout the whole heart follows specific pathways. When this specific propagation pattern of cardiac action potential is disrupted, cardiac arrhythmias often develop so that the heart is not able to pump blood effectively, and in more serious cases not able to pump blood at all, which could lead to fatal outcomes. The electrophysiological basis for cardiac myocyte excitation-contraction mechanism is discussed, followed by an introduction to ventricular fibrillation, the origin of which is the main motivation of this work.

Cardiacmyocyte action potential

The biophysical processes taking place when an action potential occurs are complex, involving the interplay of many unique ion channels and ion exchangers

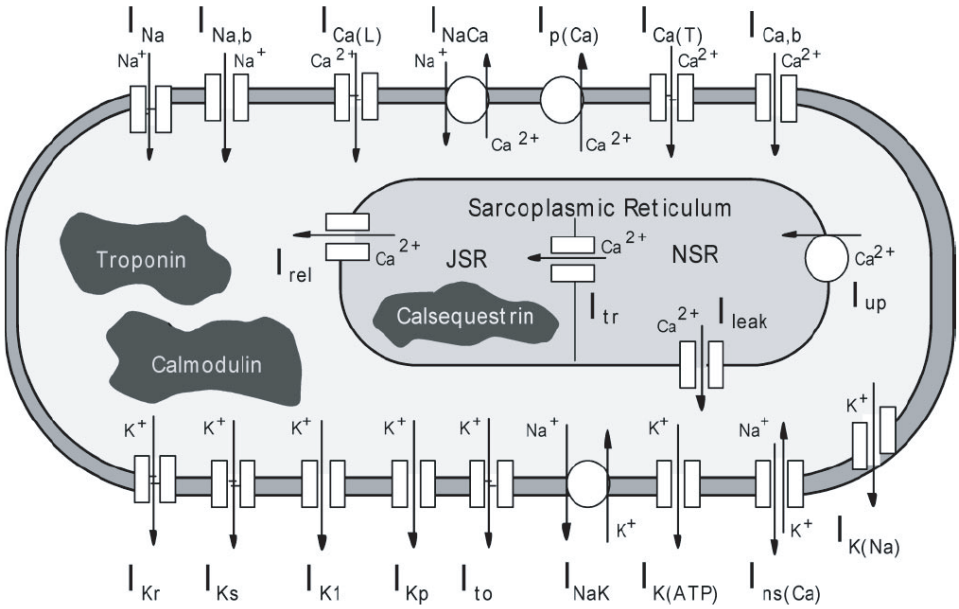

Figure 2.1: Schematic of the ventricular cardiac myocyte showing the many electrophysiological components that contribute to the action potential [2]. See Table 1.1 for descriptions of the variables and terms used.

(see Figure 2.1). In general, an action potential is largely the result of voltage-gated ion-channel conductances that cause a depolarization and repolarization of the plasma membrane. The resting potential across the membrane is maintained by large transmembrane protein-based pumps that moves ions against their electrochemical gradient in and out of the cell. Driving this pumping action is energy that is stored in the phosphate bonds of adenosine triphosphate (ATP). The event itself is triggered when the membrane is depolarized to a threshold value causing voltage-gated ion channels to open. Ions flow down their electrochemical gradient across the cell membrane, further depolarizing the membrane. Depolarization causes other ion channels to open, causing a current flow in the opposite direction that repolarizes the membrane. Finally, exchange pumps generate a current that returns the membrane to its resting potential.

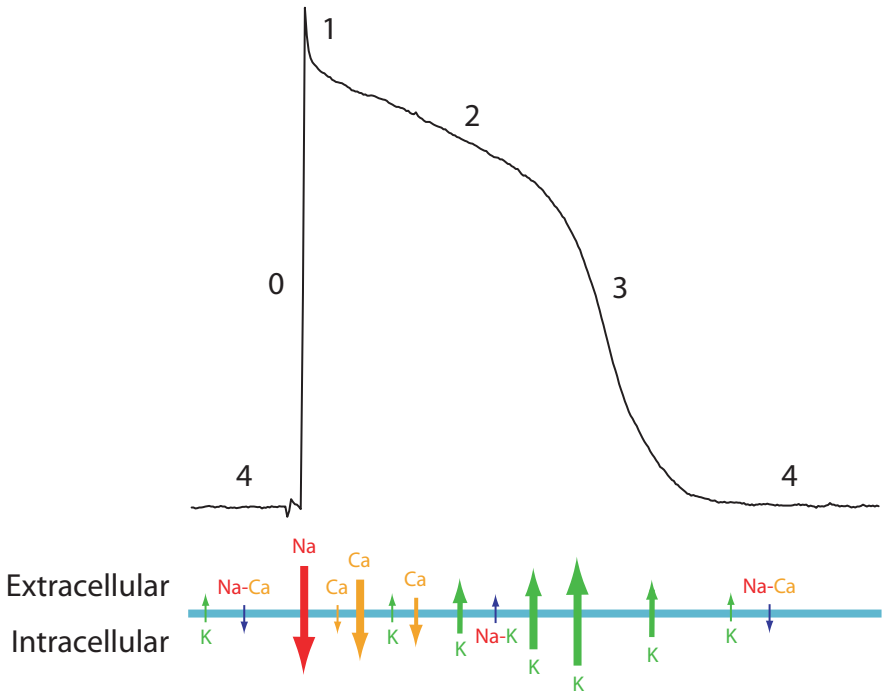

Figure 2.2: Phases of the normal ventricular action potential (intracellular recording). The transmembrane ion currents are in the bottom of the figure.

The cardiomyocyte action potential is initiated when the membrane potential, V_m, reaches a threshold, triggering the opening of sodium ion channels and a rapid depolarization of the membrane potential (phase 0, Figure 2.2). Within 1 ms, the inward flowing I_{Na} reaches its maximum and inactivates (phase 1, Figure 2.2, and Figure 2.3). Membrane depolarization opens the calcium ion channels when V_m reaches $\approx$ -40 mV, initiating the inward L-type Ca^{2+} current, $I_{Ca(L)}$. In departure from the general explanation given above, $I_{Ca(L)}$ provides a depolarizing current against the repolarizing currents, that supports a plateau phase of the action potential (phase 2, Figure 2.2). During the plateau phase, the two repolarizing potassium currents, I_{Kr} and I_{Ks}, slowly increase. Throughout this process, the sodium/calcium exchanger pumps ions across the membrane at a stoichiometry of 3 Na^+ to 1 Ca^{2+}. Initially, the exchanger serves to extrude Na^+ from the cell, although toward the end of the event it changes directions and pumps Ca^{2+} ions out of the cell, providing an inward current additionally prolonging the plateau phase. Eventually, the membrane potential causes the Ca^{2+} channels to close and an inward rectifying K^+ ion current, I_{K1}. Finally, the two repolarizing potassium currents (delayed rectifiers), I_{Kr} and I_{Ks}, gradually increase during the plateau, shifting the currents in the outward direction to repolarize the membrane towards its resting potential [2, 12].

It is the transient increase of cytosolic Ca^{2+} ions, a result of the action potential, that triggers muscle contraction. This is termed excitation-contraction coupling. When the membrane is depolarized, voltage-sensitive proteins open the L-type Ca^{2+} channels located in membranous folds of the cell membrane (called transverse tubules or T-tubules) allowing Ca^{2+} ions to flow into the cytoplasm. An increase in cytosolic Ca^{2+} ions opens more Ca^{2+} release channels, thereby amplifying the response. The flooding of Ca^{2+} ions into the cytosol causes

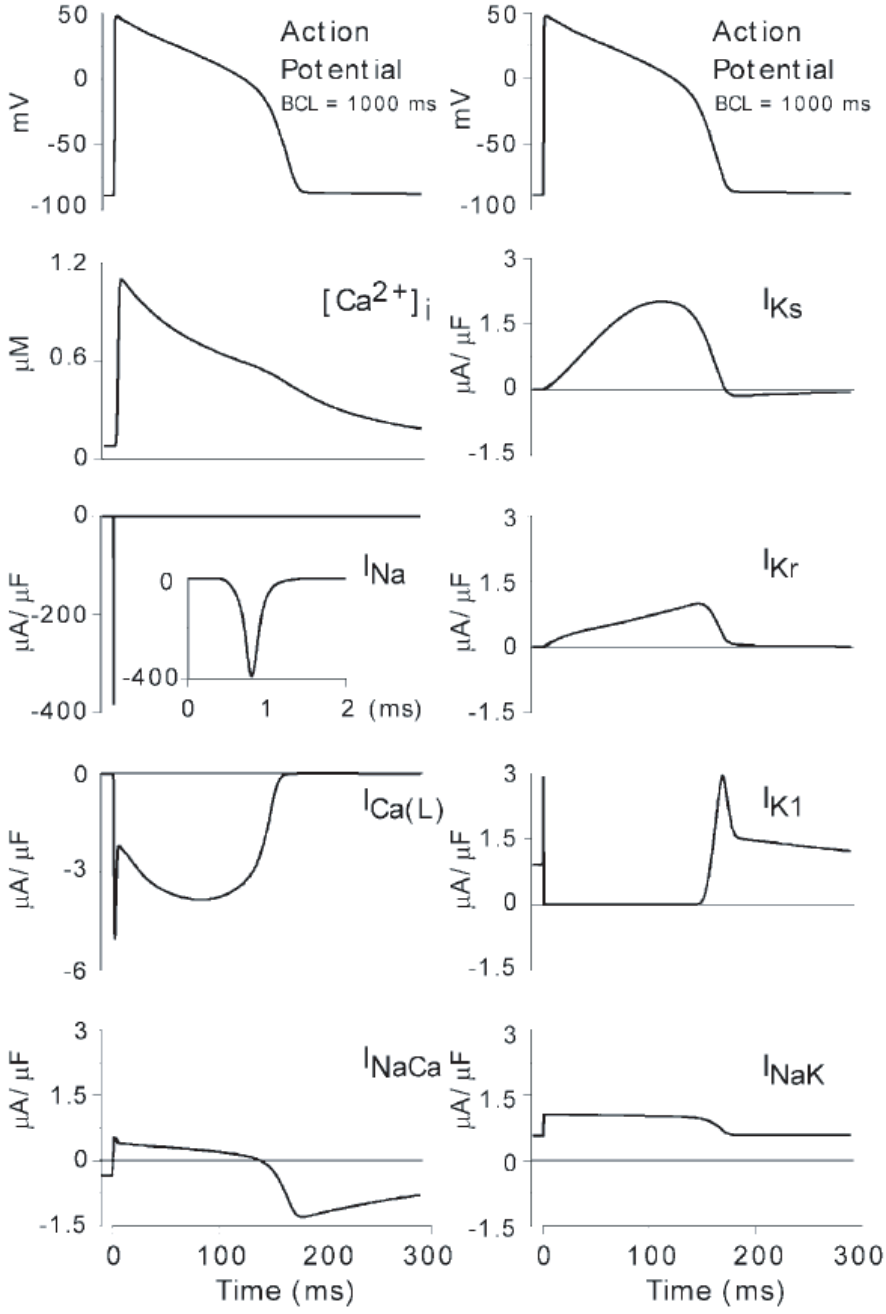

Figure 2.3: Major ionic currents ocurring during the cardiac action potential. Refer to Table 2.1 for a description of the currents cited. $[Ca^{2+}]_i$ is the concentration of free calcium in the myoplasm [2].

Table 2.1: Description of variables used in Figures 2.1, 2.2 and 2.3

Variable	Description
I_{Na}	fast sodium current
$I_{Ca(L)}$	calcium current through L-type calcium channels
$I_{Ca(T)}$	calcium current through T-type calcium channels
I_{Kr}	rapid delayed rectifier potassium current
I_{Ks}	slow delayed rectifier potassium current
I_{to}	transient potassium outward current
I_{K1}	inward rectifier potassium current
$I_{K(ATP)}$	ATP-sensitive potassium current
I_{Kp}	plateau potassium current
$I_{K(Na)}$	sodium-activated potassium current
$I_{ns(Ca)}$	nonspecific calcium-background current
I_{NaK}	sodium-potassium pump current
I_{NaCa}	sodium-calcium exchange current
$I_{P(Ca)}$	sarcolemmal calcium pump
I_{up}	calcium uptake from myoplasm (contractile part of muscle cell) to the network sarcoplasmic reticulum (NSR)
I_{rel}	calcium release from junctional sarcoplasmic reticulum (JSR)
I_{leak}	calcium leakage from NSR to the myoplasm
I_{tr}	calcium translocation from NSR to JSR
Calmodulin	calcium buffer in myoplasm
Troponin	calcium buffer in myoplasm
Calsequestrin	calcium buffer in the JSR

myofibrils to contract. Myofibrils are composed of repeating units of thin and thick proteinaceous filaments. The base unit of a myofibril is a contractible sarcomere. A sarcomere comprises of thin filaments, made up of the actin protein, that are arranged in a hexagonal lattice. In the center of the lattice are the thick filaments, which are made of the protein myosin-II. Tiny cross-bridges, called myosin-II heads, extend from the myosin filaments, intermittantly making contact with adjacent actin filaments. During contraction, these myosin-II heads cause the actin and myosin-II filaments to slide relative to one another, converting ATP to adenosine diphosphate (ADP) in the process [12, 13].

Motivation

Sudden cardiac death - likely to be caused by ventricular fibrillation (VF) - is the leading cause of mortality in the industrialized world [14]. The mechanism of VF remains unclear, but it has been widely accepted that electrophysiological potential structures with characteristic spatial and temporal order - named 'rotors' in the cardiology community - underlie ventricular fibrillation. The two-dimensional form of rotors has been reported as rotating spiral waves observed on both epicardial and endocardial surfaces of mammalian hearts, during *in vitro* experiments where the reentrant spiral waves led to tachycardia [15, 16, 17] and fibrillation [18, 19, 20, 21]. The two-dimensional mapping of electrical activation on the heart have been performed with either potential sensitive dye imaging [16, 17, 19, 20, 21] or plaque type electrode arrays [15, 16] to measure the electrical activity of the surface cells. However, the heart is a three dimensional structure and experiments revealed that quite often, surface spiral waves are not seen or only seen transiently during fibrillation, indicating that the rotors could be masked by the three-dimensional

nature of the heart wall [21]. On the other hand, truly two-dimensional cardiac tissue samples, i.e., thin slices of epicardium were found to be able to sustain rotors indefinitely but would not develop more complex electrical patterns and fibrillate [22]. The transition from reentrant waves to fibrillation may be inherently three-dimensional and it is, therefore, necessary to obtain three dimensional mapping data to accurately study electrical wave propagation within the tissue.

Due to the size limitations of the traditional metal wire and glass micropipette electrodes used in cardiac electrophysiology studies, there have been relatively few experimental observations of three-dimensional reentrant waves (or scroll waves) compared with the two-dimensional case. One remarkable and representative example is [23] where the authors assembled forty 21-gauge needles into five columns and eight rows with 5 mm space between each needle. Each needle had three bipolar electrode pairs inserted to appropriate depths, 2 mm apart to record potentials across the heart wall. The array of needles was inserted into the myocardium of canine right ventricles and persistence of a rotor generating scroll waves spanning the 7 mm thickness of the right ventricle was observed. The authors reported interstitial hemorrhage throughout much of the endocardium caused by the intrusion of the needle arrays, and commented that the 5 mm inter-electrode distance may be inadequate to map the interaction between Purkinje fibers and ventricular myocytes, which may be important in the maintenance of reentry after the onset of VF.

Silicon based microprobes have been reported for three-dimensional electrical activity recording in neural tissues [24, 25, 26, 27]. They provide high spatial resolution, reduced tissue damage, and easy integration with microelectronics. These probes therefore become a potential candidate for recording cardiac signals

from within the myocardium. Their typical thicknesses range from 8 - 30 μm for diffused boron etch stop and 5 - 90 μm for RIE (reactive ion etching) fabricated microprobes, with typical lengths ranging from 1.5 - 3 mm [28, 29]. Previous studies have demonstrated that these probes are strong enough for recording and stimulation in neural tissues [30].

Recording electrical potentials using silicon microprobes within the ventricular wall of the heart poses new challenges. Although the three meninges (dura, anachrod and pia) surrounding the brain or spinal cord have higher tensile strength than the cardiac muscle tissue [31], the underlying neural tissues are much softer than the cardiac muscle comprising most of the heart walls. Therefore, the microprobes will encounter a large force during insertion in cardiac tissues. In addition, to reach across the thickness of the ventricular wall the microprobes need to be longer than the typical length of the neural probes (e.g., 5 - 10 mm for canine ventricle). The thickness of the microprobe needs to increase significantly for higher buckling-load and mechanical strength. Thicker probes provide greater rigidity, but will cause more damage to the tissue being investigated and may affect their electrophysiological activity. In this chapter, we demonstrate that ultrasonic actuation of the microprobe reduces penetration force and allows the use of thinner microprobes on cardiac tissues.

Microfabricated silicon ultrasonic surgical tools have been reported before, which, by actuating the surgical tools at their ultrasonic resonance [32, 33, 34], can reduce the penetration force in biological samples. In this work, we integrate an ultrasonic horn actuator with the microprobes that are also able to reduce the penetration force significantly by ultrasonic actuation. The vibration modes of the microprobes are flexural modes excited by longitudinal periodic actuation of

the silicon horn. The results indicate that the possible mechanism of ultrasound induced penetration force reduction is the high frequency stress in the tissue resulting from the vibration of the microprobe. This additional stress helps the tissue to reach its yield strength and fracture, reducing the DC force required for penetrating the tissue. For electrical potential recording, the microprobes have Pt/Cr electrode arrays along the length of the probes. Multichannel recordings were obtained from isolated and perfused canine heart. The electrophysiological signals from cardiac cells under both normal and fibrillating conditions were recorded and can be easily distinguished. The time delay between different channels indicated propagation of electrical activities within the heart.

2.2 Device fabrication and assembly

Silicon ultrasonic horns were fabricated by bulk micromachining from silicon wafers as shown in Figure 2.4 [9]. First a 6000 ^{0}A LPCVD (low-pressure chemical vapour deposition) silicon nitride was deposited on 4-inch <100> silicon wafers to act as electrical insulation and wet KOH-etch mask layer. A 3000 ^{0}A Pt and 300 ^{0}A Cr layer was evaporated and patterned to form the electrode arrays, interconnects, and bonding pads. A 1 μm PECVD (plasma-enhanced chemical vapour deposition) silicon nitride insulation layer was deposited on top of the metal layer. A second layer of Pt/Cr was evaporated and patterned to form a ground layer covering all the metal traces, except at the recording sites and the bonding pads, to reduce cross-talk between channels. A 1 μm PECVD silicon nitride passivation layer was deposited and openings were etched for the electrode recording sites and bonding pads. A DRIE etch on the front side of the wafer was done to define the shape and depth of the two microprobes at the tip of the ultrasonic horn. Finally, backside-

only KOH etching releases the silicon horn from the wafer, with the thin-beam microprobes at the high-velocity end (the smaller tip) of the horn.

The width of the microprobes is 200 μm and the thickness is 140 μm. The tip of microprobe is triangular with 45 degrees tip angle. There are five 40 μm $\times$ 40 μm Pt/Cr electrodes on each of the two microprobes, forming a 2 by 5 electrode array. The inter-electrode distance is 2 mm along the 10 mm microprobes. The microprobes are of much smaller dimensions, so they act as a small mass load and do not significantly affect the primary longitudinal resonance mode of the ultrasonic horn. The microprobes can be independently viewed as clamped-free cantilevers with the clamped end excited at ultrasonic frequency in the longitudinal direction. To reduce the excitation force in bending mode, another silicon horn with the same shape and dimension, but without the two microprobes is bonded to the horn with microprobes to achieve symmetry in the thickness direction. The bonding between the two horns is achieved by silk printing with epoxy (Epoxy Technology, 360T).

Next, two piezoelectric PZT-4 plates (EBL-1, Staveley Sensors Inc.) with matching resonance with the silicon ultrasonic horn are bonded to both sides of the horn at the half-wavelength displacement node. The horn is then clamped to a custom made PC board, also at the location of the displacement node. The Pt/Cr pads on the probe are wire-bonded to the PC board and then connected to an external circuit through a ribbon cable. Figure 2.5 is a photo of the assembled device. The inset in Figure 2.5 is a close up view of the two microprobes showing the tip profile and the Pt/Cr electrode for electrical potential recording.

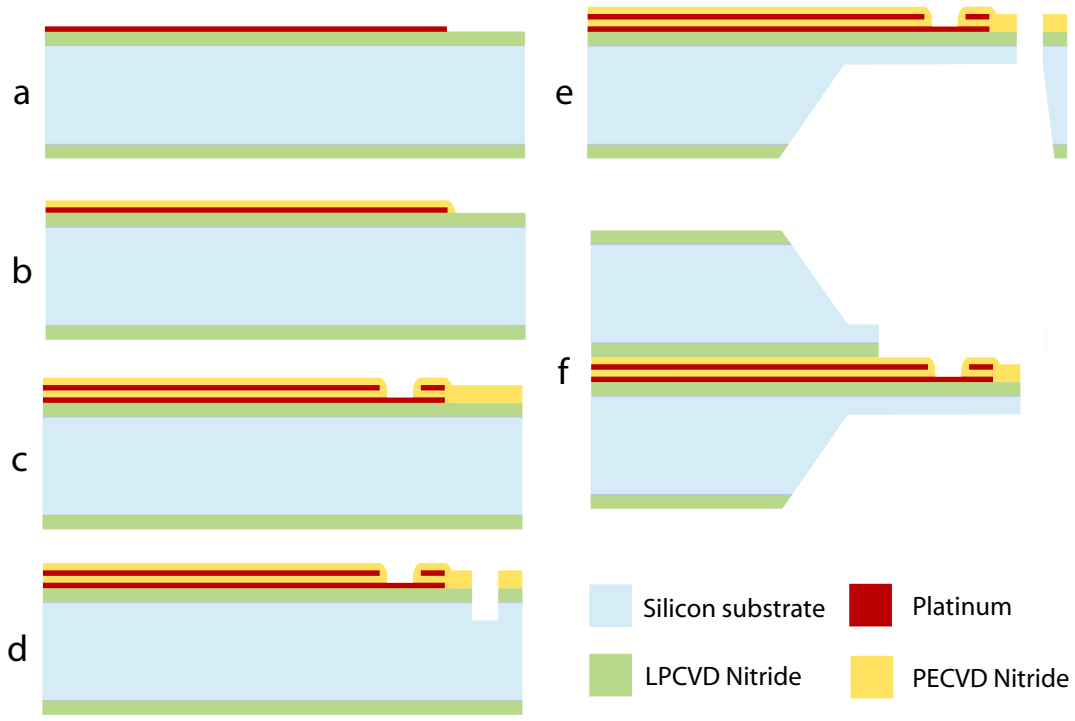

Figure 2.4: Process flow for fabricating the silicon ultrasonic microprobe. a: Evaporation and patterning of Pt/Cr metallization on 100 mm wafer with LPCVD low stress silicon nitride layer; b: Deposition and patterning of PECVD silicon nitride insulation layer; c: Evaporation and patterning of Pt/Cr for ground layer, deposition of PECVD silicon nitride passivation layer and etching of electrode openings; d: Front side DRIE with PR mask for desired probe tip thickness; e: Backside-only KOH etching to release the device; f: Second silicon horn without tips is bonded to the first horn device for symmetrical drive.

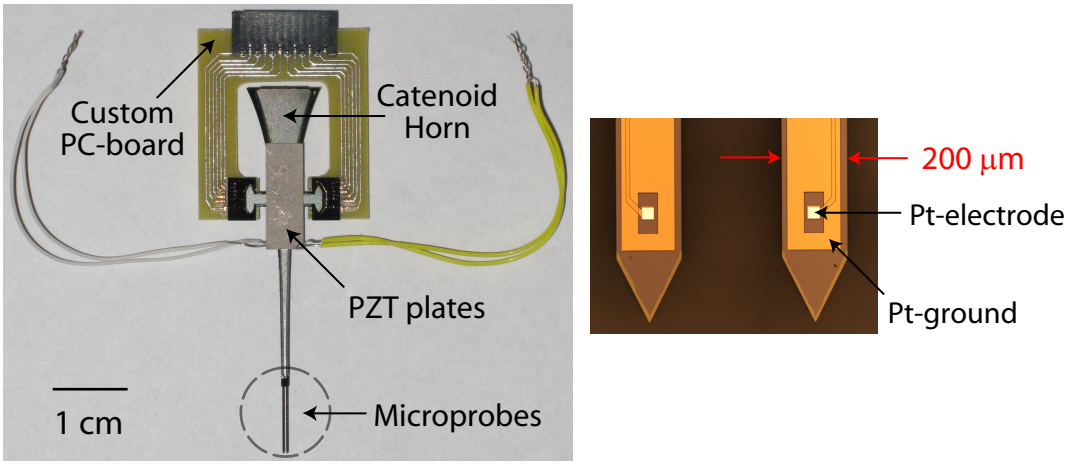

Figure 2.5: Optical photograph of the assembled ultrasonic microprobe (left) and a close-up view of the microprobes' tips and electrode recording sites with ground layer, only the electrode closest to the tip is shown (right).

2.3 Ultrasound based tissue penetration force reduction

There are two types of ultrasonic tissue cutting modalities: the focused ultrasound mode, and the direct or impact mode. The actuator developed in this work was designed for direct contact surgery. Hence, most of this section concerns direct cutting.

Focused ultrasound: In this mode of cutting, an ultrasonic field focused on the unwanted tissue is induced into the body. Most water-containing tissues absorb high frequency ultrasound (1-20 MHz) [35], becoming heated to destructively high temperatures. The ultrasonic waves and high temperature also generate microbubbles which implode causing cavitation, that can play a large role in tissue destruction. This form of tissue cutting is performed by an array of transducers placed outside the body, with their focus inside the body. This modality has been effectively used for gall-stone and cancer removal surgeries [36].

Impact mode: In this mode of surgery, the ultrasonic transducer is placed in direct contact with the tissue to be cut. The transducer surface impacts the tissue transferring kinetic energy. The impact energy results in break-up of the tissue. Usually the tool impacting is a needle attached to an ultrasonic transducer.

The main advantage of ultrasonic impact mode of cutting is that the direct force applied by the doctor is considerably reduced. Part of the cutting force is shared by the vibrating tool, thus reducing the amount of direct force required. If one tries to slowly cut a free object with a steady force, the force is distributed quickly to the center of mass of the object and causes it to move. However, if the force is applied in the form of an impulse, and the mass of the body is large, the inertial forces oppose steady motion causing the object to stay in place. Instead, the impact energy is absorbed by the surface, where tissue destruction takes place. This effect is often called inertia stiffening of a soft material. It has been been discovered that this principle is used by leaf-eating ants [37] that vibrate their blades at 300 Hz to cut the leaves. The same principle is also used in a vibratome to cut very thin slices of tissue for biological tissue histology.

From the mechanical point of view, a heart muscle in the resting state is an inhomogeneous, anisotropic, and incompressible material. Its properties change with temperature and other environmental conditions [38]. In our case, since the insertion of the ultrasonic microprobes is perpendicular to the direction of arrangement of the striated muscle tissue, the penetration force required (i.e. stiffness) for needle insertion is quite high. The ultrasound modality of the horn helps couple additional AC force to the microprobes, thus helping the microprobes penetrate cardiac tissue with less force applied by the user.

2.3.1 Advantages of using silicon transducers

The current technology that is used for ultrasound based surgery (impact mode) employs titanium-based ultrasonic resonators that operate at 40-60 kHz with 20-30 watts output power. Many material properties such as the output power density, maximum tip velocity, acoustic loss and thermal conductivity are superior for silicon compared to titanium (see Chapter 1). These properties ensure that silicon based transducers can be much smaller, produce more power, and do it safely without transducer heating and failure. Listed below are some more advantages that are specific to ultrasonic surgery.

Sharper edges for cutting: Anisotropically etched silicon tips are very sharp, reducing the force needed to make a cut in the tissue. The radius of curvature of a titanium needle ($\approx$ 2-5 μm) is an order of magnitude higher than the silicon tips.

Increased particle velocity: The maximum tip velocity a titanium handpiece (a common term for the ultrasonic surgical held by hand) can generate is limited by two material properties - the maximum achievable particle velocity in a material and the internal acoustic loss. The maximum tip velocity that an ultrasonic resonator can sustain is proportional to $S_m c$, where S_m is the maximum strain and c is the speed of sound in the material. Titanium alloys have a $S_m c$ value of 45 m/s. With the typical peak stroke of 50 μm at 40 kHz, the titanium handpieces can generate tip velocities of 13 m/s (velocity = $2\pi \times$frequency$\times$excursion), about 1/3 of their maximum value. This is a necessary and sufficient safety margin to operate the titanium handpieces. The value of $S_m c$ for silicon is 335 m/s, a value eight times that of titanium. This means that silicon can be driven to much higher tip velocities than titanium before failure. Displacements of 100 μm_{pp} at a frequency of 72 kHz, resulting in the tip velocity of 23 m/s have already been achieved. This

is almost twice the velocity that titanium surgical handpieces generate.

Reduced heat generation: Another major problem with titanium handpieces is heating due to friction between the needle and the tissue. The heat can destroy the surrounding tissues. Hence, constant fluid flow is needed to remove heat near the cutting tip. Silicon's order-of-magnitude higher thermal conductivity will help in heat removal from the cutting area, and minimize tissue damage in case the liquid coolant supply is inadvertently stopped.

High actuation voltages and failure due to arcing: Very high actuation voltages ($\approx 1200\ V_{pp}$), are needed to sustain the necessary displacements for surgery. This is because in order to maintain a high electromechanical coupling, the PZT plates are thick and hence large voltages are needed to generate a sufficient electric field. Also from the equivalent circuit of the PZT [1] it can be observed that a large portion of the drive voltage is divided across the series resistor. Furthermore, the handpiece is autoclaved after every surgical procedures, permitting steam to get trapped around the PZT plates. Eventually, buildup of moisture and the large drive voltages cause arcing and failure of the device.

In contrast, the silicon device's electromechanical coupling can be controlled by its length. The silicon device uses thinner PZT plates that require lower voltages to produce the same electric fields. With the silicon device, the arcing will be eliminated by keeping the drive voltage lower than the arcing threshold.

2.3.2 Finite element analysis of ultrasonic microprobes

As described in Chapter 1, silicon ultrasonic horns are ultrasonic actuators with a tapered cross-section to achieve high magnification of mechanical displacement at

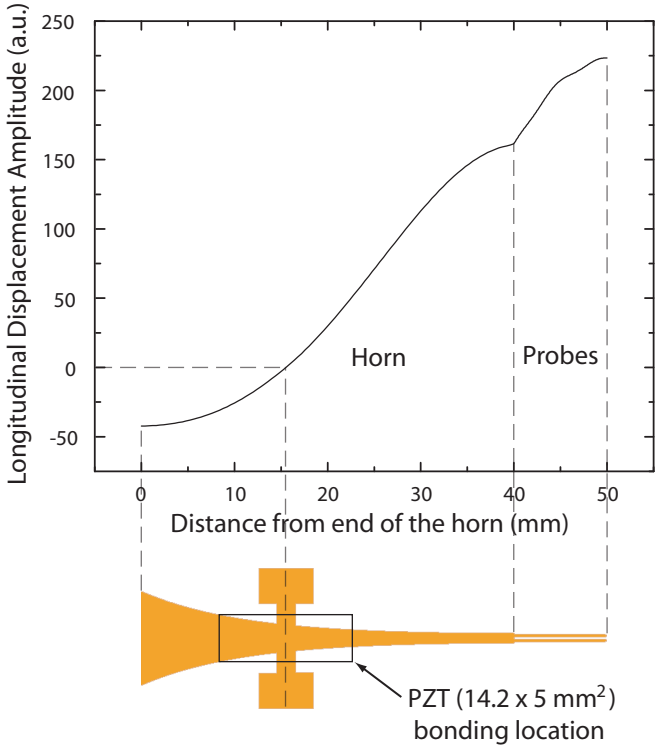

Figure 2.6: FEM-calculated longitudinal displacement amplitude along the central axis of the silicon horn and the microprobes, at $\lambda/2$ resonance, normalized against the amplitude at the end of the horn. The displacement magnification of the tip of the microprobes w.r.t the end of the horn is 5.3. The irregular motion of the microprobes can be attributed to their thickness being a third of that of the horn.

the tip of smaller cross-sectional area. In this work, silicon ultrasonic horns with 4 cm length, 10 mm to 1 mm end-to-tip width ratio were fabricated out of 500 μm thick silicon wafers. The profile of the cross-sectional area variation was catenoidal. The cross sectional area profile was described by Eq. 2.1, where $A(x)$ is the area as a function of x coordinate, L is the length of the horn, A_0 is the cross-sectional area at the larger end and A_1 is the cross-sectional area at the smaller end of the horn. The microprobes were 10 mm in length, 200 μm in width and 140 μm thick.

$$A(x) = A_1 cosh^2[\alpha(L - x)] \tag{2.1}$$

$$\alpha = \frac{acosh\sqrt{\frac{A_0}{A_1}}}{L} \tag{2.2}$$

Because of the non-regular structure, to obtain analytical solutions for Webster horn equation is difficult, even numerically solving the second order nonlinear differential equation would be a daunting task. Therefore Finite Element Analysis (FEM) was used for modeling the silicon horn with the microprobes with the commercial FEM program ANSYS^{TM}. The solid model used in the simulation in order to define the 2 silicon horn sandwich structure along with the microprobes was SOLID95, which is a 3D 8-node solid element wih 20 degrees of freedom. Modal analysis (Block-Lanczos method) of the structure was performed to estimate its half-wavelength ($\lambda/2$) longitudinal resonant frequency (110.646 kHz). The ANSYS code is listed in Appendix A. Figure 2.6 is the calculated relative longitudinal displacement amplitude along the central axis of the silicon horn at resonance, with the ears of the device clamped (as is the case in the realistic scenario, Fig. 2.5). The amplitude at the tip of the microprobes is magnified compared to that at the end of the horn. The calculated displacement magnification is 5.3. The longitudinal displacement node indicates the location of the PZT (14.2 x 5 mm^2) bonding to the silicon horn.

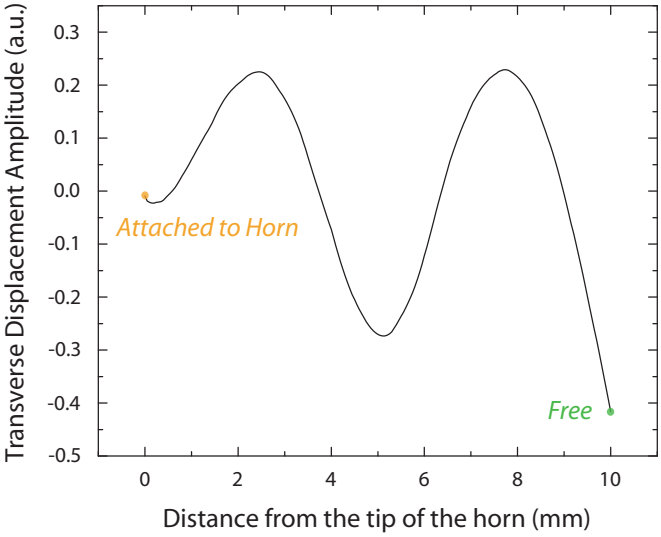

Figure 2.7: FEM-calculated transverse (width-direction) displacement amplitude along the central axis of the microprobes at $\lambda/2$ resonance of the horn normalized against the amplitude at the clamped end of the microprobe.

Flexural modes	*Frequency (kHz)*
1st	*3.00*
2nd	*18.85*
3rd	*52.92*
4th	*104.19*

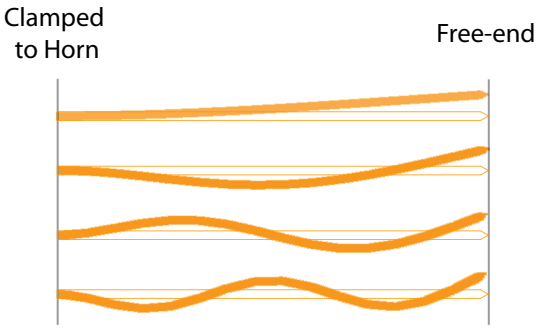

Figure 2.8: First four width-direction flexural modes of the microprobe with horn-side end clamped and the tip free to move, predicted by ANSYS^{TM} simulation. The predicted mode shape of the microprobe is also depicted.

Figure 2.7 is the calculated relative transverse (width-direction) displacement amplitude along the central axis of the microprobes at the end of the silicon horn. The two microprobes can be modeled as clamped-free cantilevers with their clamped ends at the tip of the silicon ultrasonic horn. The clamped ends are under sinusoidal excitation in the longitudinal direction. The major mode excited in the clamped-free cantilever microprobes can be estimated to be the flexural mode (in the width direction) close to the driving ultrasonic frequency, which is the 4^{th} (n = 3) flexural mode in this case. Figure 2.8 lists the first four width-direction flexural modes of the microprobe predicted by ANSYS^{TM} simulation assuming the horn-side of the microprobe to be clamped and the tip to be free. The mode shape is expected to agree with the calculated 4^{th} flexural mode of a clamped-free silicon beam of the same dimensions, since the frequency is close to the PZT drive frequency (110.646 kHz).

The excitation of bending motion in the microprobe by longitudinal sinusoidal actuation at its clamped end is a nonlinear process. In previous work, the vibration of the microprobe was not observed to be a single frequency vibration, although the most prominent frequency component was the one corresponding to the driving frequency of the horn. Other harmonic components have been observed by recording the vibration velocity at the tip of the microprobe as a function of time [9].

2.3.3 Model for impact ultrasonic cutting

A successful model of ultrasonic cutting of soft tissues by an ultrasonic chisel has been presented by Nabibebkov and Plyushchenkov [39, 40]. Their fundamental assumption was that the force required to penetrate tissue is a constant threshold.

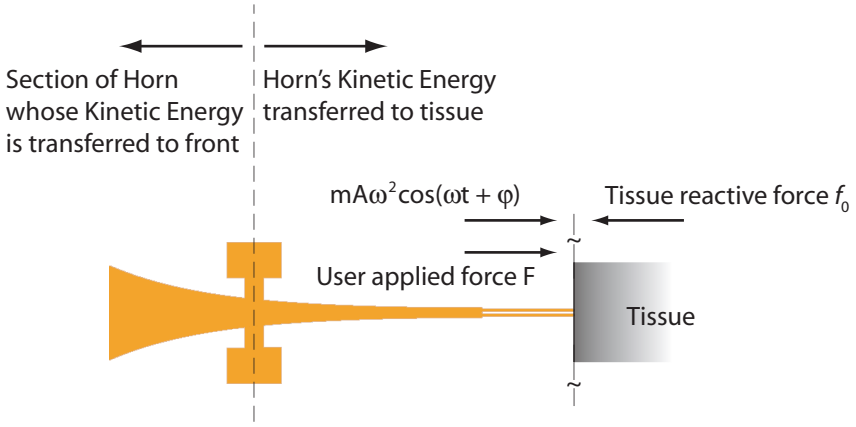

Figure 2.9: Force diagram at tissue-microprobes interface depicting the user applied force F, ultrasound-based force ($\mathrm{mA}\omega^2\cos(\omega t + \varphi)$) and the tissue reaction force f_0.

Frictional forces in fluid and tissue are assumed negligible. Furthermore, effects of cavitation and microstreaming are not considered. The goal of Nabibebkov and Plyushchenkov was to determine the cutting velocity, or the rate at which an ultrasonic chisel can progress through a tissue. The user applies a steady force, F, to the complete surgical unit containing the transducer, which also acts against the tissue being cut. The force F, and the force generated by the vibrating transducer acts against the reaction force of the tissue (Figure 2.9). Summing up the forces, the differential equation of motion for the surgical unit is:

$$M\ddot{x} = F - mA\omega^2 sin(\omega t + \varphi) - f_0 \tag{2.3}$$

The first term is the intertial force of the entire mass of the surgical unit. The force F is applied by the user and f_0 is the constant force of reaction of the tissue. The third term is the force generated by the section of the transducer that is cutting the tissue. It is the product of the acceleration $\omega^2 A$ (ω = radian frequency, A = transducer tip displacement amplitude) and an effective mass m. In the case of a resonator (silicon horn) half-wavelength long, m will be the effective mass of

the section (see Figure 2.9) from the cutting tip to the first displacement node (the front $\lambda/4$ section), such that

$$mv_{Tip}^2 = \int_{Node}^{Tip} \rho A(x)(v(x))^2 dx \tag{2.4}$$

where A(x) is the cross-sectional area, v(x) is the longitudinal velocity along the transducer and $v_{Tip} = A\omega$ is the transducer tip velocity. During each cutting cycle, there will be an active cutting phase and an inactive cutting phase, where the tip is thrusting toward uncut tissue and withdrawing from cut tissue. For a particular range of constant forces $0 < F < f_0$ applied by the user, there exists a *stationary* cutting mode wherein the movement of the instrument in the tissue over some time occurs with a constant, stabilized velocity. Assuming the tissue reaction force $f_0 \ll mA\omega^2$, the use of high-frequency ultrasound and low-amplitude ultrasonic waves and, neglecting the friction and the first and second order terms of reaction force of tissue, Eq. 2.3 can be solved to determine the cutting velocity V (defining $\xi = F/f_0$):

$$V = v_{Tip}\frac{m}{M}\frac{sin^2\pi\xi}{\pi\sqrt{\left(1-\xi+\frac{sin2\pi\xi}{2\pi}\right)+\frac{sin^4\pi\xi}{\pi^2}}} \tag{2.5}$$

$$\xi = \frac{1}{\pi}ArcSin\sqrt{\left(\frac{\sqrt{\pi^2+4\left[\left(\frac{v_{Tip}}{V}\right)^2-1\right]\left[\pi^2(1-\xi)+\frac{\pi}{2}\right]}-\pi}{2\left[\left(\frac{v_{Tip}}{V}\right)^2-1\right]}\right)} \tag{2.6}$$

When inserting the microprobes attached to the silicon horn into tissue, there are three kinds of forces applied on the tissue by the microprobes. First, the DC force in longitudinal direction applied by the inserting mechanism; second, the back and forth (AC) longitudinal motion generated directly by the longitudinal resonance of the ultrasonic horn; lastly, the transverse force at ultrasonic frequency

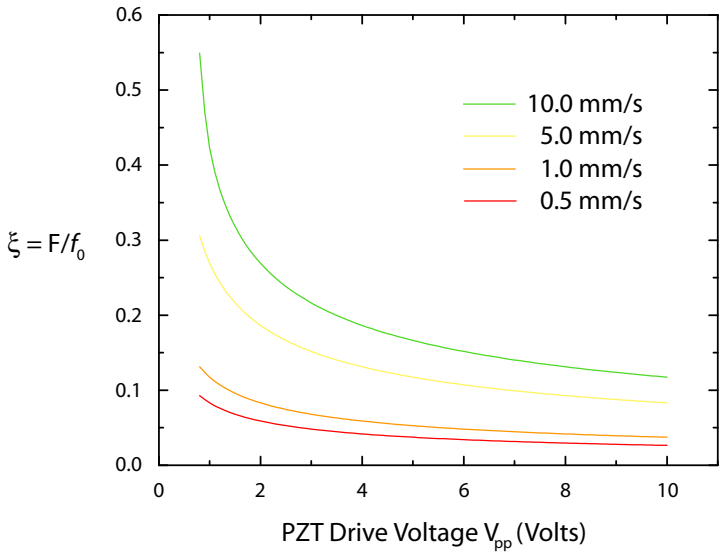

Figure 2.10: The estimated decrease in ξ i.e. the user applied force F for a constant tissue reaction force f_0 with increasing PZT drive actuation voltage V_{pp}, at insertion velocities of 0.5, 1, 5 and 10 mm/s.

by exciting flexural modes of the microprobes. It has been reported previously [41] that for a constant velocity of insertion of the microprobes into the tissue, the DC force (applied by user, F) required to penetrate biological tissue (left ventricle) is reduced as the PZTs are driven at higher voltages. By neglecting the transverse force due to the flexural modes of the microprobes, from Eq. 2.5 we can say that assuming a constant insertion velocity of the microprobes, the force F applied by the user increases instantaneously at contact with the tissue and settles at a constant value before penetrating the tissue ($0 < \tau \ll T_{break}$). The value of ξ was numerically solved for a given value of v_{Tip} using Eq. 2.6 (Mathematica^{TM}). By solving the Webster's horn equation of motion [1] for a silicon horn of length 4 mm with 10:1 end-to-tip ratio and a resonance frequency $\approx$ 110 kHz, the ratio of the effective mass $\frac{m}{M}$ was estimated to be 9.45%. The horn tip displacement A was taken to be 0.37 μm/V_{pp} [9].

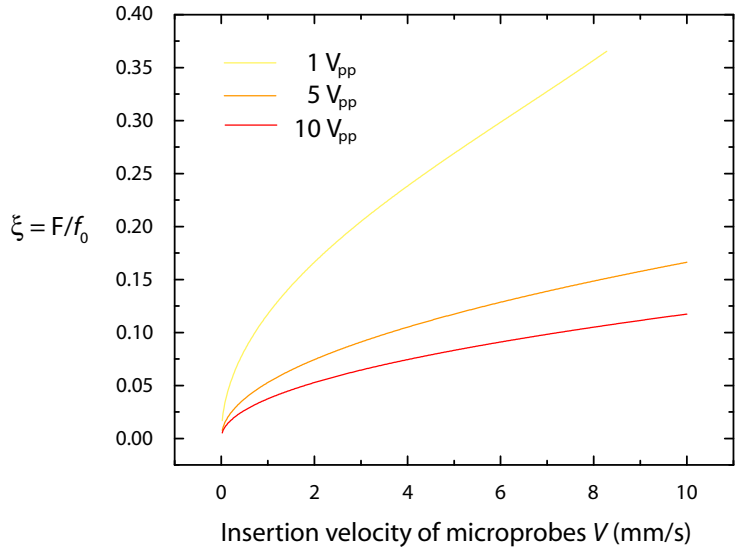

Figure 2.11: The estimated increase in ξ i.e. the user applied force F for a constant tissue reaction force f_0 with increasing insertion velocity of microprobes V, at PZT drive actuation voltages of 1, 5 and 10 V_{pp}.

Figure 2.10 shows the estimated decrease in the user applied force F, at different insertion velocities, with increasing values of PZT drive voltage V_{pp}, since f_0 corresponds to the constant force required by user to puncture a given tissue without ultrasound. Figure 2.11 shows the estimated increase in ξ with increasing values of insertion velocities at a PZT drive voltages of 1, 5 and 10 V_{pp}. From the Eq. 2.6 we can say that by optimizing the insertion velocity V and the tip displacement velocity v_{Tip}, one can ideally minimize the force required by the user F. In order to assume *stationary* cutting mode for the case of the silicon ultrasonic microprobes inserted at constant insertion velocities, the elasticity of the tissue is ignored (no buckling). The above model is valid of insertion velocities $V \ll v_{Tip}$. Since v_{Tip} is known to increase with PZT drive voltage, at higher drive voltages the working range w.r.t insertion velocities is larger. One of the goals for future work is to develop a model which takes into account the transverse force due to the flexural vibration of the microprobes.

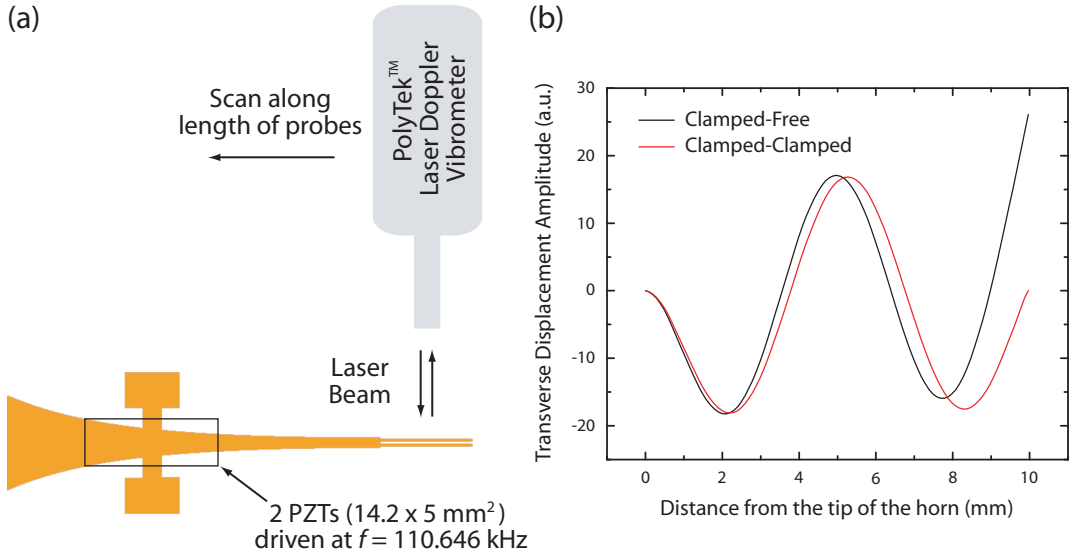

Figure 2.12: Experimental setup for measuring microprobe flexural (width-direction) vibration amplitude at the tip of the ultrasonic horn with the microprobes. The FEM calculated vibration amplitude in the clamped-free and the clamped-clamped conditions are also shown.

In order to validate the model for ultrasonic tissue-penetration, force reduction experiments need to be performed and the motion of the microprobes during insertion needs to be monitored. During insertion into cardiac tissue, the microprobe tip might be clamped against the tissue surface and the free-tip boundary condition no longer applies. Transverse displacement measurements need to be carried out with the tip of the microprobe compressed (at a constant DC force) against the surface of a silicone sheet to simulate the new boundary condition. The expected transverse displacement of the clamped-clamped beam condition during tissue penetration estimated by FEM analysis is shown in Figure 2.12. By fixing the silicone sheet to a 3-axis strain gauge, the force applied by the microprobes due to the (AC) longitudinal motion generated by the horn resonance and the the transverse force at ultrasonic frequency due to the flexural modes of the microprobes can be measured. By recording the AC longitudinal force (Eq. 2.3) generated at varying PZT drive voltage we can estimate the tip displacement

amplitude A in the loaded condition as a function of the PZT drive voltage. The effective mass m is calculated using Eq. 2.4.

The penetration force required to penetrate chicken breast and canine left-ventricle with no ultrasound, equal to the reaction force of the tissue f_0, can be determined by moving the microprobes at a constant insertion velocity V towards the tissue placed on a strain gauge measuring the constant DC force. The above experiment should be performed at varying PZT drive voltages (1-15 V_{pp}) for a constant insertion velocity V and is expected to match the estimated values of $\xi = F/f_0$ in Figure 2.10. Also, experiments need to be performed at varying insertion velocities for a constant PZT drive voltage and compared to the analytically estimated values of ξ in Figure 2.11. The range of insertion velocities used will be such that $V \ll v_{Tip}$ for a given PZT drive voltage.

2.4 Effect of microelectrode impedance on cardiac MAP recordings

Metal-based electrodes as a transducer for measuring bioelectric signals such as action potentials (cardiac and neural), Electromyograms (EMG) etc., and stimulation of excitable tissues (neuron, muscle etc.) have been widely used since the early 1800s [42]. In the physiologic environment, the bioelectric signals are carried in the electrolytic media in the form of ionic currents. The purpose of the metal-based electrodes is to transduce these signals to and from electronic signals. Thus the electrical characteristics (impedance) of the electrode-electrolyte interface are of atmost importance during electrophysiological studies. Experimental results have shown that the impedance of the interface has both reactive and resistive

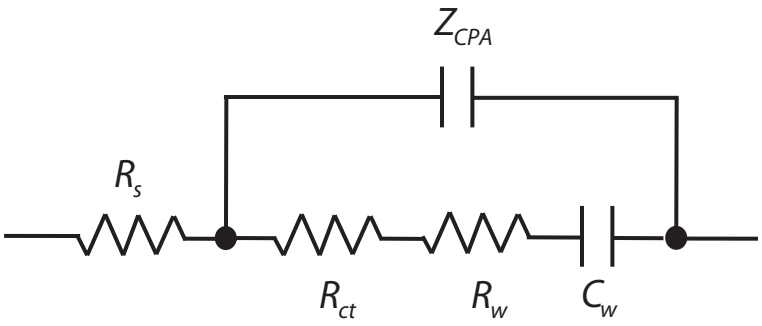

Figure 2.13: Equivalent circuit model of the electrode-electrolyte interface.

components which vary with frequency and current density. In this section, the theoretical origins of the different components of the electrode-electrolyte interface are discussed. An equivalent circuit model is used to characterize the platinum-electrolyte interface, used to measure cardiac MAP in the ultrasonic silicon microprobes, and the equivalent circuit parameters are estimated by fitting the model to experimentally measured interface impedance. The effect of the equivalent circuit parameters on cardiac MAP signal morphology is discussed. Also the effect of electrical parasitic elements (R,L,C) from the conduction traces on the device are also considered.

2.4.1 Theoretical model of the electrode-electrolyte interface

Figure 2.13 shows the equivalent circuit model considered which is comprised of a constant phase angle impedance Z_{CPA} that represents the interfacial capacitance. The capacitance is further shunted by the charge transfer resistance R_{ct}, Warburg capacitance C_w and Warburg resistance R_w, together in series with the spreading

resistance R_s [43, 44, 45].

A. Interface Capacitance

A metal when introduced into an ionic solution undergoes chemical reactions at the interface and builds up a space charge layer. These reactions being thermodynamically favourable proceed spontaneously, and result in the dissolution of metal (oxidation) in solution to form metal ions, leaving behind free electrons which repel each other and accumulate at the interface. The excess electrons on the surface of the electrode and the metal ions dissolve in the solution for a space charge layer, as shown in Figure 2.14. The electric potential developed by the space charge layer in turn lowers the barrier for the reverse electrochemical reaction (reduction of metal ions). This process eventually reaches an equilibrium when a sufficient charge separation is achieved, wherein the forward and reverse reaction rates are equal, resulting in a zero net current across the interface. In terms of an electrical circuit element, this space charge layer represents a capacitance.

The constant phase angle impedance Z_{CPA} models the capacitive characteristics of the electrode-electrolyte interface. A theoretical derivation of the interface capacitance C_I (i.e. $Z_{CPA} = \mathrm{j}\omega C_I$) is given by the Gouy-Chapman-Stern model (GCS) [46]. The interface capacitance is taken to be the series combination of the double-layer (Helmholtz) capacitance C_H and the diffuse layer (Gouy-Chapman) capacitance C_G -

$$\frac{1}{C_I} = \frac{1}{C_H} + \frac{1}{C_G} \tag{2.7}$$

The Helmholtz capacitance C_H assumes that the charges in the solution are concentrated in a plane (the outer Helmholtz plane, OHP) parallel to the metal

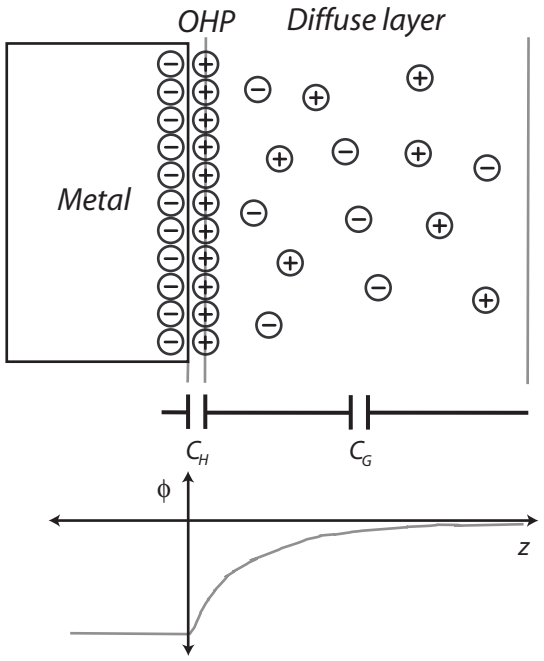

Figure 2.14: Formation of Outer Helmholtz Plane (OHP) and Diffuse layer (metal-electrolyte interaction), and their contribution to interfactial capacitance.

surface, and the capacitance can be described as that of a parallel plate capacitor - Helmholtz-Perin model:

$$C_H = \frac{\epsilon_o \epsilon_r A}{d_{OHP}} \tag{2.8}$$

where ϵ_o is the dielectric permittivity of free space ($\epsilon_o = 8.854 \times 10^{-12} F/m$), ϵ_r is the relative dielectric permittivity of the medium between the plates of the capacitor, A is the surface area and d_{OHP} is the distance between the outer Helmholtz plane and the metal surface. In aqueous solutions, the medium between the outer Helmholtz plane and the metal surface is a layer of oriented water molecules with relative dielectric permitivity of ≈ 6 [47].

The actual space charge region extends from the interface into the solution, with charge density decreasing from a maximum value at the interface to its bulk concentration in the solution. As the potential applied to the electrode is increased, the ions tend to closely pack near the metal surface reducing the thickness of the space charge region, therefore increasing the interfacial capacitance. The potential dependant capacitance of the diffuse charge region described by the Guoy-Chapman model, C_G, is given by -

$$C_G = \frac{\epsilon_o \epsilon_r cosh(\frac{z\varphi_o}{2V_t})}{L_D} \tag{2.9}$$

where $V_t = \frac{kT}{q}$ is the thermal voltage ($\approx$ 26 mV at 25^{o}C), z is the charge of the ions in question and φ_o is the applied electrode potential. The Debye length, LD, is given by -

$$L_D = \frac{\epsilon_o \epsilon_r V_t}{2n^o z^2 q} \tag{2.10}$$

where n^o is the bulk number concentration of the ion and q is the charge of the electron ($1.602 \times 10^{-19} C$). For physiological saline (0.9% w/v NaCl) at 25^{o}C, ϵ_r

≈ 78.54 and $L_D = 7.8 \times 10^{-10} m$. Therefore the interfacial capacitance C_I is given by -

$$\frac{1}{C_I} = \frac{d_{OHP}}{\epsilon_o \epsilon_r A} + \frac{L_D}{\epsilon_o \epsilon_r cosh(\frac{z\varphi_o}{2V_t})} \tag{2.11}$$

Adding the Helmholtz and the Guoy-Chapman capacitances in series satisfactorily describes the behaviour of the interface capacitance at DC. The Guoy-Chapman capacitance dominates at lower applied electrode potentials, and as the potential is increased the Guoy-Chapman capacitance increases and the total capacitance approaches the Helmholtz capacitance. For physiological saline solutions, the total interface capacitance increases from $0.099 F/m^2$ at zero applied potential to about $0.11 F/m^2$ for potentials of 0.2 V and above [47]. This corresponds to approximately 158-176 pF for the 35 μm $\times$ 35 μm platinum electrode surface used in the ultrasonic silicon microprobes.

B. Charge Transfer Resistance (R_{ct})

The DC current path across the electrode-electrolyte interface is represented by a non-linear resistive element in parallel with the interfacial capacitance (Figure 2.13). This resistive element takes into account several mechanisms - charge transfer processes at the electrode, chemical reactions, diffusion of reactants to and from the electrode surface and crystallization processes. During electrophysiological recordings using metal electrodes, crystallization processes and chemical reactions should not occur at the electrode and hence can be ignored. The resistive element is mainly due to charge transfer through the electrode double layer which is necessary for any steady-state current flow. The movement of charge into or out of an electrode requires a shift in potential from its equilibrium value called the *overpotential* η.

In the state of equilibrium, the current due to the oxidation and reduction reactions are equal in magnitude since the reactions takes place at an equal rate. The absolute value of this current for a given surface area, referred to as the *exchange current density,* J_o [47], is given by -

$$J_o = F k_c c_A e^{\frac{-\beta \Delta \varphi_o}{V_t}} \tag{2.12}$$

where $V_t = \frac{kT}{q}$ is the thermal voltage ($\approx$ 26 mV at 25^{o}C), k_c is the reduction reaction rate constant, c_A is the concentration of electron-acceptor ions A in solution plane of the interface, β is the symmetry factor and $\Delta\varphi_o$ is the equilibrium potential. The value of J_o is a property of the electrode material and the reactions taking place. In the presence of a non-zero overpotential (η), the additional current through the electrode will be determined by the magnitude of J_o. The value of the overpotential can be realated to the current density by the Butler-Volmer equation [46], *exchange current density,* J_o [47], is given by -

$$J = J_o \left[e^{\frac{(1-\beta) z \eta}{V_t}} - e^{\frac{-\beta z \eta}{V_t}} \right] \tag{2.13}$$

where z is the charge of the ion in question. The charge transfer resistance R_{ct} can be derived from the above equation:

$$R_{ct} = \left(\frac{V_t}{J_o z} \right) \frac{1}{cosh\left(\frac{z\eta}{2V_t} \right)} \tag{2.14}$$

$$R_{ct} \approx \frac{V_t}{J_o z} \qquad \forall \ \frac{z\eta}{2V_t} \ll 1 \tag{2.15}$$

$$R_{ct} \approx \frac{2V_t}{J_o z} e^{\frac{-z\eta}{2V_t}} \quad \forall \ \frac{z\eta}{2V_t} \gg 1 \tag{2.16}$$

R_{ct} is linear with η for low field and exponentially decaying at large η. Therefore R_{ct} can be electrically modelled as a pair of semiconductor diodes connected in reverse parallel.

C. Warburg capacitance (C_w) and resistance (R_w)

Warburg proposed the dependance of the spatial concentration gradient near the electrode-electrolyte interface on the frequency of a sinusoidal forcing function - $|Z_D| = \frac{k}{\sqrt{f}}$, where k is a constant determined by the electrochemistry and mobilities of the reactant species involved and f is the frequency in hertz. The Warburg impedance is often expressed as a series combination of a resistance (R_w) and a capacitance (C_w) -

$$Z_w = R_w + \frac{1}{j2\pi C_w}, \qquad R_w = \frac{1}{j2\pi C_w} \tag{2.17}$$

Therefore Z_w has a constant phase of -45^o. Experimental studies and models in the literature [42] have shown that the resistance and reactance both vary as $\frac{1}{f_m}$, with m varying between 0.15 and 0.86 for different metals and at different temperatures.

D. Spreading resistance (R_s)

The final element to be considered in the theoretical model of the electrode-electrolyte interface is the net resistance encountered by the current spreading out from an electrode into a conductive solution, referred to as *Spreading resistance* (R_s). The magnitude of the resistance is determined by the *geometric* surface area of the electrode and is expressed as -

$$R_s = \int_{x=0}^{x=\infty} dR_s \tag{2.18}$$

where x is the distance normal to the surface. For a planar rectangular

electrode, it can be shown that the spreading resistance amounts to -

$$R_s = \frac{\rho ln(\frac{4l}{w})}{\pi l} \tag{2.19}$$

where l and w are the length and width of the rectangular surface, ρ is the resistivity of the solution (72 $\Omega \cdot cm$ for physiological saline). For the 35 μm $\times$ 35 μm platinum electrode surface used in the ultrasonic silicon microprobes, the spreading resistance $R_s \approx 9.08$ kΩ.

2.4.2 Parasitic impedance in ultrasonic silicon microprobes

The on-chip metal traces leading to the electrode recording sites from the bonding pads and amplifying circuits lead to stray resistance, capacitances and inductances that affect the signal in the equivalent circuit of the microprobe. As shown in Figure 2.15, the parasitic capacitances are between the electrode metal trace and the substrate (C_s), between adjacent electrode metal traces (C_{TC}), electrode metal trace and the ground metal trace (C_G), and ground metal trace and the electrolyte solution (C_y). In the case of the silicon microprobes, the capacitance between the ground metal trace and the electrolyte solution (C_y) is neglected because the electrolyte solution is grounded. The parasitic resistance arises from the finite resistivity of the electrode metal trace. These parasitics can be modeled as distributed resistances and capacitances in a transmission line, or approximated as lumped R-C combination circuit elements [48, 49]. The lumped parasitic resistance can be estimated as follows -

$$R_p = \frac{\rho L}{Wt} \tag{2.20}$$

where ρ is the resistivity of the metal material, W, L and t are the width,

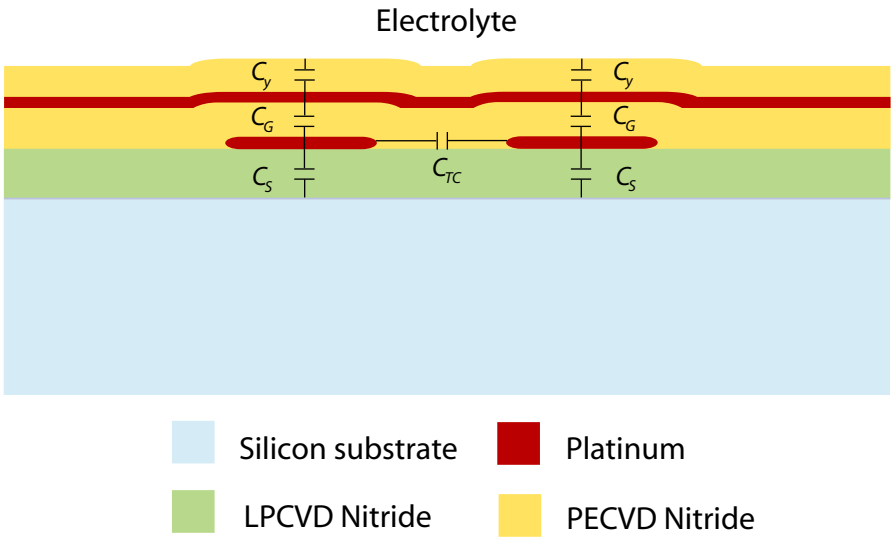

Figure 2.15: Cross-section of two adjacent electrode metal traces running below the ground metal trace on the ultrasonic microprobes, depicting the possible sources of parasitics.

length and thickness of the metal traces respectively. For the ultrasonic silicon microprobes, with Platinum interconnecting metal traces 10 μm wide, 0.25 μm thick and 4 cm long and resistivity of $\rho_{Pt} = 10.6 \times 10^{-6}\Omega \cdot cm$, the parasitic resistance amounts to $R_p \approx 1.7$ kΩ.

The lumped values of the parasitic capacitances, taking sidewall contributions and field effects into account, can be estimated as -

$$C_s = 1.15\epsilon_o\epsilon_s\frac{LW}{d_s} + 2.8\epsilon_o\epsilon_s L(\frac{t}{d_s})^{0.222} \tag{2.21}$$

$$C_s = 1.15\epsilon_o\epsilon_G\frac{LW}{d_G} + 2.8\epsilon_o\epsilon_G L(\frac{t}{d_G})^{0.222} \tag{2.22}$$

where ϵ_s and ϵ_G are the relative permittivity of the insulation layer between the electrode metal trace and the substrate and the electrode metal trace and the ground metal trace, and d_s and d_G are the thicknesses of the two insulation

layers respectively. For the silicon nitride insulations used in the ultrasonic silicon microprobes, $\epsilon_s = \epsilon_G = 7.5$ and $d_s = d_G = 1\mu$m. Using equations 2.21 and 2.22, the parasitic capacitances can be estimated to be $C_s = C_G = 36$ pF.

Assuming that each electrode metal trace only interacts with its nearest two neighbors, the coupling capacitance (C_C) through a single ground layer can be expressed as [49]:

$$C_C = 2\epsilon_o\epsilon_G L \left[0.03(\frac{W}{d_G}) + 0.83(\frac{t}{d_G}) - 0.07(\frac{t}{d_G})^{0.222}\right] (\frac{s}{d_G})^{-1.34} \tag{2.23}$$

where variable s is the spacing between the electrode metal traces and d_G is the thickness of the insulation layer on the electrode metal traces. For the ultrasonic silicon microprobes, the spacing between adjacent metal traces s equals 15 μm. The coupling capacitance C_C for the microprobes can be calculated to be 0.065 pF. Since there exists two ground layers in the silicon microprobes i.e. silicon substrate and ground metal trace with silicon nitride insulation, the total coupling capacitance $C_{TC} = 2C_C = 0.13$ pF. Therefore, the total lumped parasitic capacitance can be estimated as $C_p = C_s + C_G + C_{TC} \approx 72.13$ pF. Inductances resulting from current loops between the electrode metal traces can be estimated from analytical formulae [50] -

$$L = 3ln(\frac{s+w}{w+t}\pi) - ln2 + I \tag{2.24}$$

$$I = 0.75tanh(\frac{2\delta\pi}{w+t}) \tag{2.25}$$

$$\delta = \frac{1}{\sqrt{\pi\sigma f\mu}} \tag{2.26}$$

where s is the spacing between the signal trace and the nearest ground, w is the width of the trace and t is the thickness of the trace, I is the frequency-dependant internal inductance, δ is the skin depth of the material, f is the frequency of signal

and, σ and μ are the conductivity and permeability of the material. The unit of the inductance in equation 2.24 is 10^{-1} nH/mm. For platinum metal traces used in the silicon microprobes, $s \approx 1$ μm, w = 10 μm, t = 0.25 μm, $\sigma = 9.66 \times 10^6/\Omega \cdot m$ and $\mu = 1.26 \times 10^{-6} N/A^2$. The parasitic inductance can be estimated to be 0.30×10^{-6} H/m. For 4 cm traces running along the length of the silicon microprobe, the total inductance amounts to 11.8 nH. The frequency range of the signal being from 0-5 kHz, the inductive impedance reaches a maximum of 59 $\mu\Omega$, therefore the effect of this inductance can be neglected.

2.4.3 Equivalent circuit of silicon microprobes

Figure 2.16 shows the equivalent circuit model for the ultrasonic silicon microprobes, including on-chip parasitics. Among the various components of the theoretical model of the electrode-electrolyte impedance, the constant phase angle impedance (Z_{CPA}, i.e. interface capacitance C_I) and the charge transfer resistance (R_{ct}) are the most important according to the electrode material and design. The Warburg impedance (R_w and C_w) due to diffusion of the chemical reactants in solution is not included in this model because for the materials (platinum electrode) and frequency range of interest, the Warburg impedance does not significantly contribute to the overall impedance. Estimation of components of the theoretical model is difficult because they depend on actual current densities applied on the electrode and the actual electrochemical reaction rate on the surface. In the case of noble metals such as gold and platinum, the exchange reactions may be dominated by those of impurities rather than those of the metals and need to be experimentally determined. In practice, simplifed models with serial or parallel R-C circuit are often used to characterize the interface impedance of the electrode

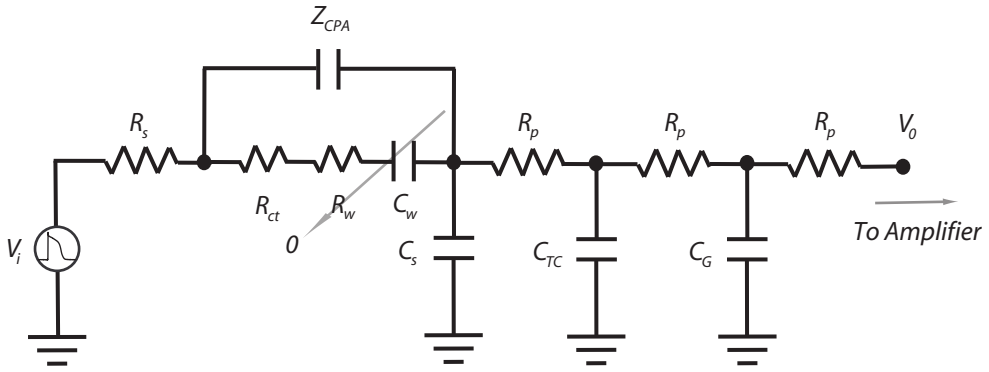

Figure 2.16: Equivalent circuit model for the ultrasonic microprobes including on-chip parasitics.

[44, 51]. Another simplification is to treat the parasitic resistance and capacitance as lumped components. The parasitic resistance due to the metal traces can be ignored because it is usually orders of magnitude lower than the interfacial impedance and the input impedance of the amplifier. Hence the equivalent circuit consists of the interfacial impedance, the parasitic capacitance (C_p) and the input impedance of the amplifier (R_L). The characterization of the above parameters by experimental methods is discussed in the following section.

2.4.4 Experimental measurement of electrode-electrolyte interface impedance

A. Experimental methods

The standard three-electrode system is used [46], consisting of the electrode system of interest referred to as the Working Electrode (WE), coupled with an electrode of known potential that approaches ideal non-polarizability known as

the Reference Electrode (RE) and a Counter Electrode (CE) to apply the ac perturbation signal (overpotential η) between the working electrode and itself (Figure 2.17). Measurements are performed with respect to the open-circuit potential (OCP), the potential naturally occuring between the working and reference electrodes. A commercially available Gamry^{TM} FAS2 potentiostat system with frequency response analysis software is used to perform Electrochemical Impedance Spectroscopy (EIS) measurements. The internal circuitry in the potentiostat allows for a high impedance interface between the WE and RE to measure the OCP and to apply ac perturbation signal (overpotential η) between CE and WE for impedance measurements. The perturbation potential of the ac signal (w.r.t the OCP) is set to 1 mV and the scan range was 10 mHz to 300 kHz. A chloridized Ag/AgCl electrode immersed 1 cm in the electrolyte (0.015" diameter, CATno. 531500, A-M Systems, Carlsborg, WA) is the reference electrode (RE), the counter electrode (CE) is a platinum sheet with 4.5 cm^2 exposed to electrolyte (0.125 mm thick, CAT no. PT000250/52, GoodFellow, Huntingdon, England) and the working electrode (WE) is the device under test (DUT), which in this case is the silicon ultrasonic microprobe. The electrolyte used for the measurments is 0.9% w/v NaCl solution (physiological saline).

The CE is chosen to be of a large area compared to the WE to ensure that the impedance due to the CE-electrolyte interface is much lower than the WE-electrolyte interface. The OCP is allowed to settle to a constant value, for 10 minutes before EIS measurements are performed. Since the OCP is a function of the interface, the OCP is used as a quality control to ensure that the initial conditions are the same from measurement to measurement. The amplitude of the ac perturbation signal (overpotential η) needs to be kept at a low level, in order to ensure the low-field approximation is satisfied for determining the value

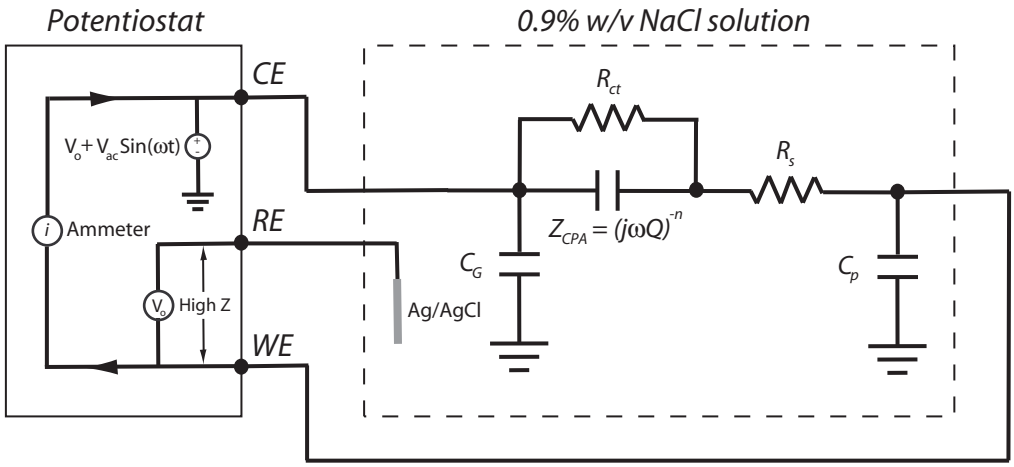

Figure 2.17: Equivalent circuit of electrode-electrolyte interface and connections to potentiostat for EIS measurements.

of the charge transfer resistance (R_{ct}). In the literature [42], work suggests that for platinum in physiological saline, the interface impedance did not vary much for current densities below 1 mA/cm^2. When the ac signal amplitude is set at 1 mV, the maximum current for the silicon microprobes, close to the highest frequency of interest (5 kHz) is measured to be $\approx$ 12 nA or 0.98 mA/cm^2. Therefore the ac signal is set at 1 mV for all experiments to ensure a constant value of R_{ct}.

B. Interface impedance measurements

The equivalent circuit for EIS measurements of the silicon microprobe, using the potentiostat is shown in Figure 2.17. It is similar to the equivalent circuit in Figure 2.16 with the addition of a parasitic capacitance C_y, which exists between the electrolyte and the ground metal trace. The constant phase angle impedance Z_{CPA} can be defined by using an empirical relation [52] -

$$Z_{CPA} = \frac{1}{(j\omega Q)^n} \tag{2.27}$$

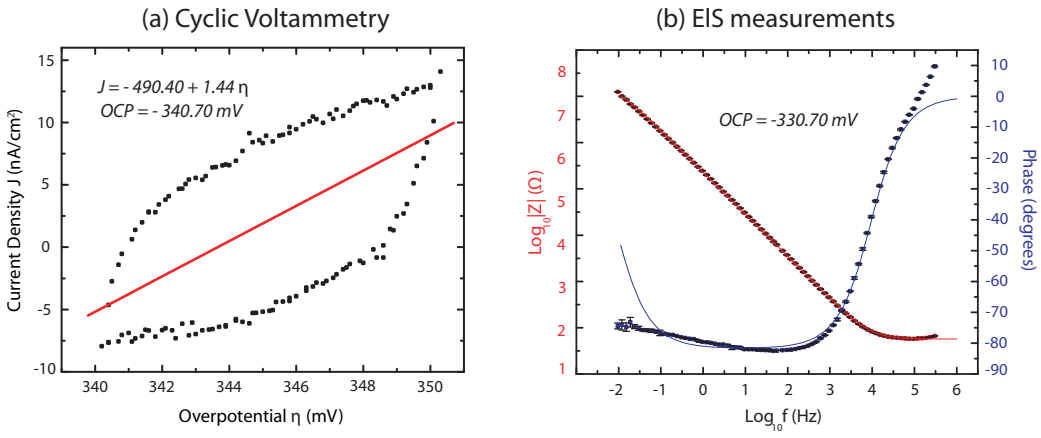

(c) Table of parameters of equivalent circuit

	n	R_{ct} (MΩ)	R_s (Ω)	$1/Q^n$ (MΩ.s)
Empirical	*0.91*	*18.25*	*56.84*	*1.22*
Theoretical	*1.00*	*17.77*	-	*1.95*

Figure 2.18: (a) Cyclic voltammetry measurements of Platinum wire (0.039 cm^2) to determine value of R_{ct}, (b) EIS measurements (modulus and phase) and the corresponding fit based on the empirical model and (c) Table of parameters showing the empirical and theoretically predicted values of the parameters of the equivalent circuit.

where Q is a measure of the magnitude of Z_{CPA}, n is a constant ($0 \leq$ n ≤ 1) representing inhomogeneities in the surface and $\omega = 2\pi f$. The values of n and Q are estimated by fitting the model to impedance measurements at varied frequencies. In order to determine the charge transfer resistance (R_{ct}), the equilibrium exchange current density (J_o) of the WE needs to be measured. Cyclic voltammetry experiments are done by perturbing the ac voltage (overpotential) on the WE by $\eta = 5$ mV w.r.t OCP at 0.5 mV/s scan rate and at 0.15 mV steps, and measuring the current at the CE. By using the low-field approximation of Butler-Volmer, the value of J_o and R_{ct} can be calculated from the I vs. η curve -

$$J = \frac{J_o F \eta}{RT} \tag{2.28}$$

$$R_{ct} = \frac{RT}{J_o F} \tag{2.29}$$

Impedance measurements were first performed on a Platinum wire immersed 1 cm in the electrolyte (0.005" diameter, CAT no. 767000, A-M Systems, Carlsborg, WA) to check the validity of the empirical model. Figure 2.18a shows the plot of current (I, in nA) vs. overpotential (η, in mV) from the cyclic voltammetry experiments performed using the Platinum wire as the WE. The equilibrium exchange current density J_o and the charge transfer resistance R_{ct} are calculated to be $1.44 \pm 0.03 \times 10^{-8} A/cm^2$ and 17.72 $M\Omega$ respectively, with an OCP of 345.7 mV. From the cyclic voltammetry measurements it is observed that as the value of OCP drops, the magnitude of Rct increases. Decrease in OCP by $\approx$ 20 mV exhibited an increase in the value of Rct by $\approx$ 5 MΩ. Figure 2.18b shows EIS measurements i.e. the modulus of impedance and phase, of Platinum wire (Area exposed = 0.039 cm^2, OCP = 330.7 ± 1.5 mV) and the corresponding fit to the empirical model. The table in Figure 2.18c gives a summary of the averaged, empirical fit-based and predicted theoretical values of the parameters of the equivalent circuit (Q, n, R_{ct},

R_s). The Mathematica^{TM} code used to extract the equivalent circuit paremeters is listed in Appendix B. The parameters Q and n are predicted by calculating the impedance of the interface capacitance using $Z_{CI} = (j\omega C_I)^{-1}$, and at an angular frequency of 1 s^{-1} i.e. $|Z_{CI}(\omega = 1)| = Q^{-n}$. The value of R_s is theoretically estimated using equation 2.19 and the value of R_{ct} from the cyclic voltammetry measurements. The variation in R_{ct} was seen to be as high as 110%, which can be attributed to its sensitivity to initial electrode-electrolyte interface conditions [51], and also because it is extrapolated from low frequency data which leads to increased uncertainty. The phase measured at low frequencies (0.01 to 1 Hz) in the EIS measurements is known to be very sensitive to any variation in R_{ct} (the modulus of impedance shows no variation) [51]. Along with the steady drop in OCP, as is expected with any metal immersed in a solution, the value of R_{ct} increases, which results in the value of phase to decrease at low frequencies. This drop in phase to a lower more negative value at low frequencies is seen in Figure 2.18b (the data deviates from the fit in this region). The phase plot suggests the model to be mostly capacitive (0.1 to 1000 Hz) in the region of interest. The deviation of the data from the model at high frequencies (above 7 kHz) is due to the presence of parasitics in the system, which are not accounted for in the model.

Figure 2.19a shows the results from the cyclic voltammetry experiments performed using the lower-most electrode at the tip of the Silicon microprobe. The equilibrium exchange current density J_o and the charge transfer resistance R_{ct} are calculated to be $38.99 \pm 2.06 \times 10^{-8} A/cm^2$ and 5.38 $G\Omega$ respectively, with an OCP of 201.7 mV. The modulus of impedance and phase of the electrode (Area exposed = $1.23 \times 10^{-5} cm^2$, OCP = 142.6 ± 12.2 mV) and the corresponding fit to the model is shown in Figure 2.19b, and the emperical fit-based and predicted

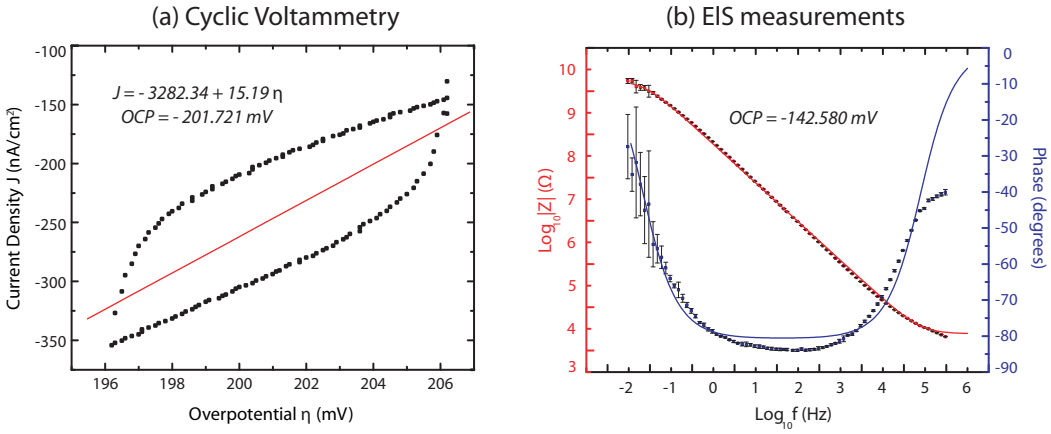

(c) Table of parameters of equivalent circuit

	n	R_{ct} (GΩ)	R_s (kΩ)	$1/Q^n$ (GΩ.s)
Empirical	*0.90*	*5.79*	*7.76*	*0.97*
Theoretical	*1.00*	*5.38*	*9.08*	*6.23*

Figure 2.19: (a) Cyclic voltammetry measurements of silicon microprobe to determine value of R_{ct}, (b) EIS measurements (modulus and phase) and the corresponding fit based on the empirical model and (c) Table of parameters showing the empirical and theoretically predicted values of the parameters of the equivalent circuit.

values of the parameters of the equivalent circuit are shown in Figure 2.19c. The Mathematica^{TM} code used to extract the equivalent circuit parements is listed in Appendix B. The values of the parameters R_{ct} and R_s are seen to be orders of magnitude higher than those correponding to the platinum wire due to the reduced area of electrode, but scaling of the parameters with respect to area is not always possible [53]. The surface of the evaporated platinum electrode being prone to contamination leads to variation in the interfacial conditions, which results in drift in the magnitude of R_{ct}. This explains the large error bars in the phase data at low frequencies. The poor fit of the model to the phase data can be attributed to the presence of parasitics in the microprobe and the potentiostat experimental arrangement, which are not accounted for in the model. A model taking into account the parasitics of the system needs to be developed to better fit the data.

2.4.5 Transfer function of silicon microprobe

A. Bode plots

When measuring cardiac action potentials using the silicon microprobes, the signal from the electrode after passing through the length of probe is fed into the negative terminal of a LT1113 JFET opamp from Linear Technologies^{TM}. Figure 2.20 shows the schematic of the equivalent circuit of the microprobe with the opamp and the environment around the electrode inside the heart tissue. The input impedance of the opamp, in parallel with the parasitic capacitance, needs to be included in the transfer function that the action potential signal experiences. The nominal value of the input resistance is $R_L = 100\ G\Omega$ (at low frequencies) and input capacitance is $C_L = 27$ pF.

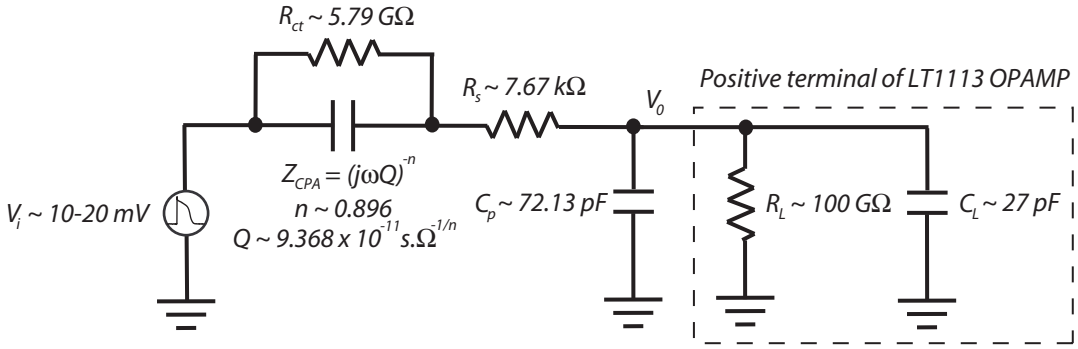

Figure 2.20: Schematic of equivalent circuit of the microprobe when measuring cMAP from heart tissue.

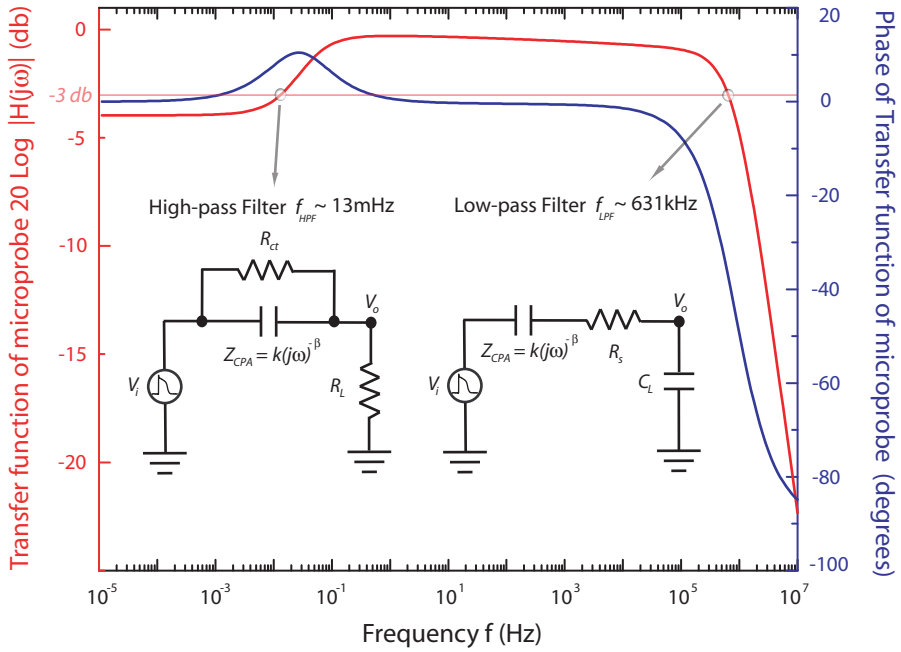

Figure 2.21: Bode plots of the magnitude and phase of the transfer function ($|H(j\omega)|$) of the microprobe for $R_L = 10\ G\Omega$. Equivalent circuit at low- and high- frequency regimes are depicted.

Figure 2.21 shows the bode plots of the magnitude and phase of the transfer function ($H(j\omega)$) of the microprobe. This shows that the transfer function has a low pass cut-off at the high frequency end at $\approx$ 631 kHz, which is good enough for recording cardiac action potentials. The equivalent circuit of the system at high frequencies (as shown in Figure 2.21) shows the output voltage being sampled at the input capacitance of the opamp C_L (since $C_L \ll C_p$). The cut-off frequency is determined by the spreading resistance R_s and C_L (since $R_s \gg (j\omega Q)^{-n}$ at high frequencies) - $f_{LPF} \approx (2\pi R_s C_L)^{-1}$. The phase also exhibits a roll-off from 0 to $-\pi/2$, with an inflection point at $-\pi/4$ indicating the presence of a pole at the cut-off frequency. At the lower end of the frequency range, the magnitude of the transfer function rolls-off and settles down at a constant negative value. The equivalent circuit of the system at low frequencies (as shown in Figure 2.21) shows the output voltage being sampled at the input resistance of the opamp R_L (since $R_L \ll |\frac{1}{j\omega C_L}|$). The cut-off frequency is determined by the charge transfer resistance R_{ct} and the input resistance of the opamp R_L, and the constant phase angle impedance (Z_{CPA}) - $f_{HPF} \approx (2\pi(R_{ct}//R_L)Q^n)^{-\frac{1}{n}}$. The system also has a zero at $\approx (Q^{-n}R_{ct})$, which results in the magnitude of the transfer function settling down at a constant value. Since $R_{ct} \ll (j\omega Q)^{-n}$ at low frequencies, this constant value corresponds to a voltage divider circuit with R_L and R_{ct} ($|Z| = \frac{R_L}{R_L+R_{ct}}$). The cut-off frequency in our case (using LT1113 opamp) can be estimated to be 0.73 mHz. But the modulus of the transfer function exhibits little reduction in magnitude at frequencies lower than the theoretically predicted f_{HPF}, which implies that the strength of the pole at f_{LPF} is low and hence its effect on the action potential signal is low. If the saturation value at low frequencies is higher than the -3 db point in the Bode plot (i.e. $\frac{R_L}{R_L+R_{ct}} \gg \frac{1}{\sqrt{2}}$), we can conclude that the effect of the pole on the data will be minimal. From this we can say that when choosing

the opamp, the figure of merit on the input impedance is $R_L \gg 2.4R_{ct}$. In the case of the silicon microprobes, this condition is satisfied - $R_L = 100$ G$\Omega \approx 20 \times R_{ct}$.

From the transfer function characteristics at the high frequency regime, we can note that the cut-off frequency can be increased by reducing the spreading resistance R_s, for a given input capacitance of the opamp (C_L). At the low frequency regime, we can conclude that the value of R_L should be ideally chosen to be much higher compared to the R_{ct}. This allows the cut-off frequency to be dependant only on R_{ct} and Q^n, which can be adjusted by designing a suitable electrode.

B. Effect on cardiac MAP signal morphology

The cardiac monophasic action potential (cMAP) signal is known to have frequencies as low as 1-10 mHz. In the above system, the choice in system parameters (R_L in particular) can lead to attenuation of magnitude in the transfer function around 1-10 mHz. Figure 2.22 shows the Bode plot of the modulus of the transfer function ($|H(j\omega)|$) at the low frequency regime, for varying values of R_L = 1, 2, 10, 25 and 100 $G\Omega$. For the values of $R_L = 1, 2, 10\ G\Omega$, $|H(j\omega)|$ falls below the -3db value and have high-pass filter cut-off values of $f_{HPF} = 153, 82, 30$ mHz respectively. The cardiac MAP data obtained from intracellular microelectrode recordings, filtered for the above 3 values of f_{HPF} (4-pole Butterworth filter using MATLAB, shown in Figure 2.22) shows the effect of the filter cut-off frequency on the signal morphology. As f_{HPF} increases the filtered cMAP signal exhibits a dip in the baseline value and shows a hint of bi-phasic nature, deviating from the original monophasic signal morphology. The $|H(j\omega)|$ for $R_L = 25$ and 100 $G\Omega$ settles down at a value greater than -3 db and hence show now significant change

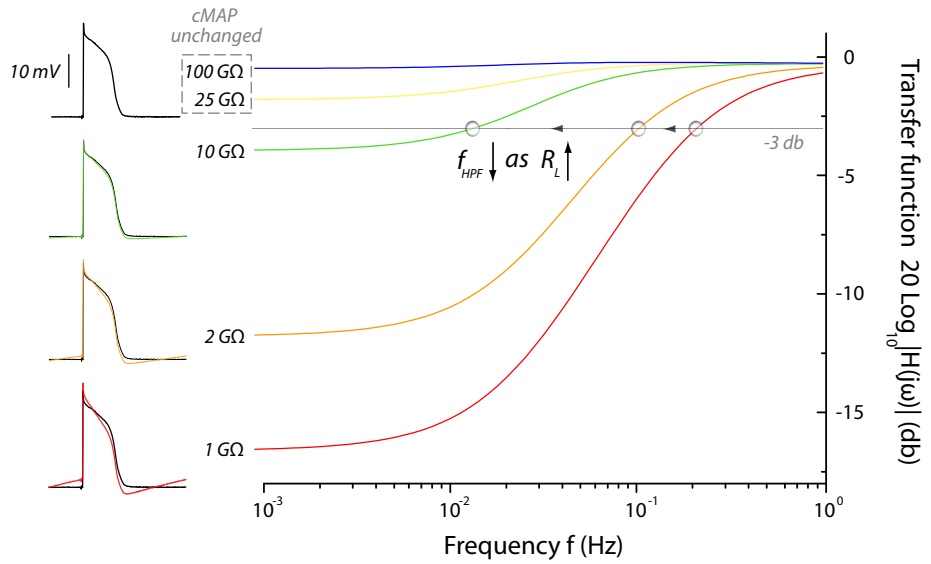

Figure 2.22: Bode plot of the modulus of the transfer function ($|H(j\omega)|$) in the low frequency regime for R_L = 1, 2, 10, 25 and 100 $G\Omega$ with filtered cMAP signals.

in the signal morphology.

Figure 2.23 shows the circuit of the high input impedance amplifier, DC offset elimination and 60 Hz notch filtering. The low noise, precision, JFET input opamps LT1113 are used. Figure 2.24 shows the frequency response ($\frac{V_o}{V_i}$) of the circuit at low frequencies. The cut-off frequency of the high-pass filter is $f_{HPF} \approx$ 225 mHz, which arises because of the presence of the passive RC high-pass filter to eliminate the drift from the system. This drift arises from the lack of local ground in the tissue during measurements and can be eliminated in the future, hence eliminating the need for a high-pass filter.

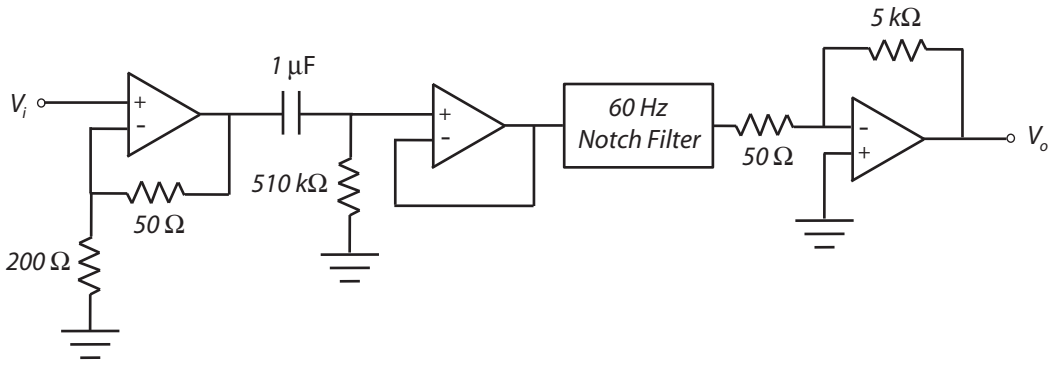

Figure 2.23: Circuit schematics of the amplifier for the microelectrode.

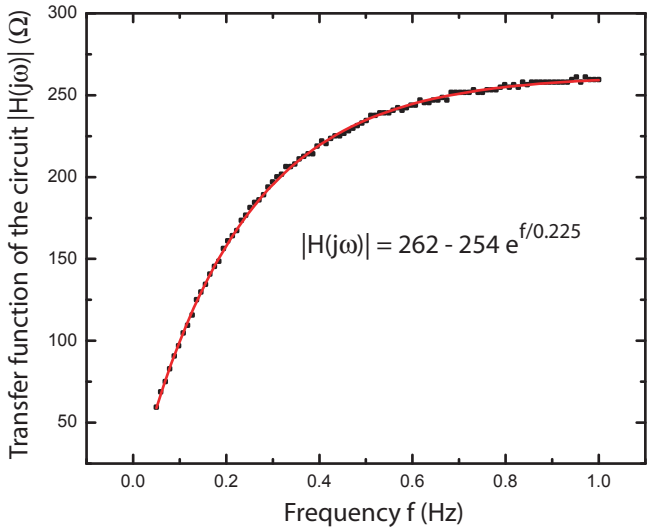

Figure 2.24: Frequency response of the transfer function of the circuit at low frequencies; cut-off frequency of high-pass filter $f_{HPF} \approx 225$ mHz.

2.5 *In vitro* cardiac MAP recording from canine heart

Electrical recordings were obtained from isolated perfused sections of canine left and right ventricles. The hearts were excised from deeply anesthetized dogs and the region of the heart supplied by the left anterior descending coronary artery or the right coronary artery was isolated. The coronary artery was cannulated and perfused with oxygenated Tyrode solution maintained at 37.5^{o}C. The preparations were allowed to beat spontaneously or were paced at a constant cycle length using a bipolar stimulating electrode placed on the epicardial surface. Detailed description of the experimental procedure is given in [54].

The ultrasonic horn with microprobes is actuated at the $\lambda/2$ longitudinal resonance frequency of the horn and the microprobes were inserted using a manual positioning stage. A driving signal of 5-10 V_{pp} is used to ensure insertion of the microprobes without significant buckling. Microprobes, 10 mm in length and 140 μm in thickness, were successfully inserted into the ventricular wall. The ultrasonic actuation was turned off once the microprobes were fully inserted to reduce RF coupling noise from the PZT electrodes. The signals from multiple recording sites on the microprobe were amplified in unipolar configuration and recorded at a 1 kHz sampling rate with a National Instrument DAQ system ($DAQCard^{TM}$-6024E for PCMCIA).

Figure 2.25 is a multichannel recording from the isolated perfused canine left ventricle, paced at a 700 ms cycle length by the surface stimulator. In this recording the action potentials have a MAP-like shape - the action potentials have peaks of only one polarity relative to the resting potentials - with subtle morphology difference and time delays between different electrodes, indicating the action potentials were propagated from the same stimulating source. The surface

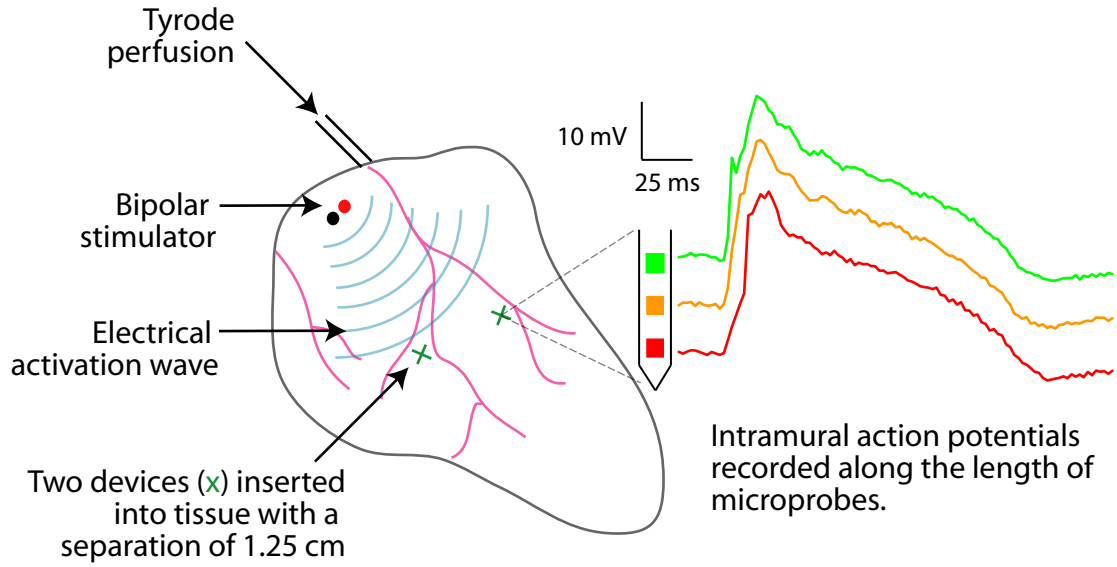

Figure 2.25: Left: Sketch of the canine left ventricular tissue setup paced using a bipolar electrode, with microprobes inserted into the tissue. Right: Multi-channel recordings from isolated perfused canine left ventricle, showing monophasic action potentials (MAP), as recorded through 10 mm long microprobes. The activation time difference between each pad ($\Delta\tau_a$) is 4 ms. The DC level of each channel is adjusted for viewing convenience.

stimulating electrode was located a few centimeters away from the microprobe, therefore the shape and direction of the wavefront is indeterminate in this case due to the inhomogeneity of the heart. If the surface stimulating electrode was placed very close to the inserting location of the microprobe, or if the bottom most microelectrode was used as the stimulating electrode, the conduction speed across the heart wall can be estimated from the inter-electrode distance and time delays between channels.

The activation time is identified as the moment of the maximum negative time derivative of the intrinsic deflection in the cardiac signals [55]. Taking the activation time in the uppermost channel (closest to the epicardial stimulator in

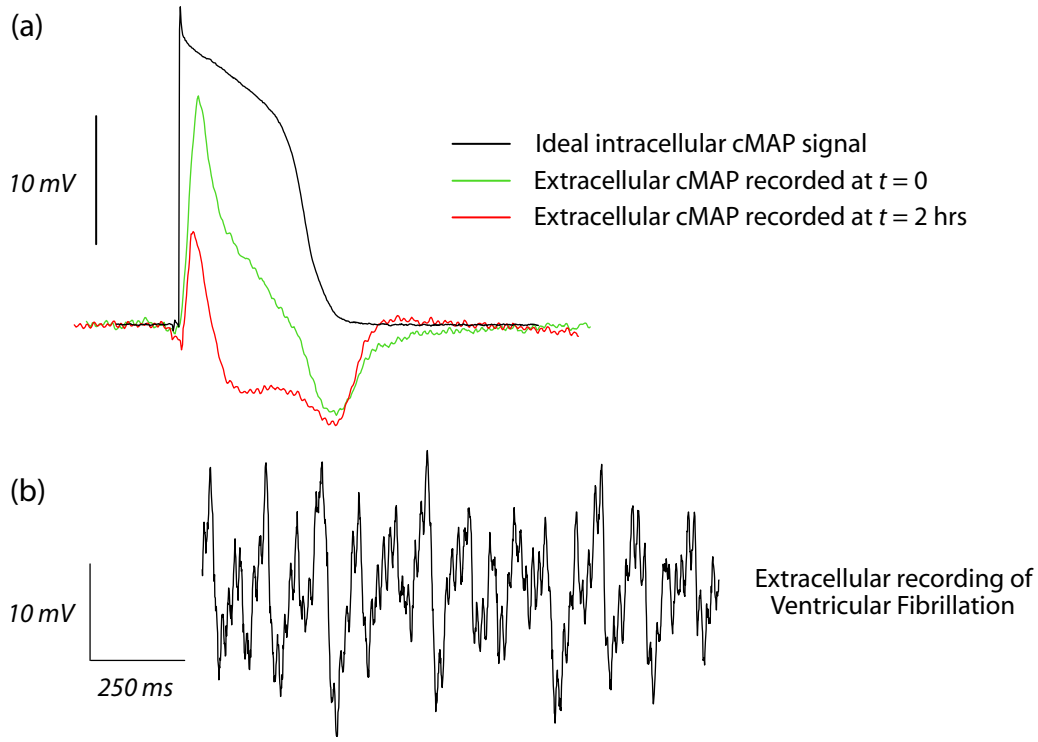

Figure 2.26: (a) Morphology of extracellular cardiac MAP recorded using microprobes, from canine left ventricle paced at 500 ms, at $t = 0$ and $t = 2$ hours compared to that of the ideal intracellular cardiac MAP signal from microelectrode recordings. (b) Extracellular recording of ventricular fibrillation using microprobes.

this experiment) as baseline, the activation time delay progressively increases as the location of the electrodes moves downward, indicating the spread of activation from the epicardial pacing site across the thickness of the ventricular wall. The mean time delay between the third and fourth, and the fourth and fifth channel from the epicardial surface is $\Delta\tau_a \approx 4$ ms. The conduction velocity can be estimated to be ≈ 0.5 m/s, which is typical for ventricular myocardium [56].

The cardiac MAP signal morphology was observed to change with length of time of the microprobes inserted into the tissue. The amplitude of the Na^+ spike in the extracellular cMAP signal is seen to be $\approx$ 18 mV as opposed to the intracellular microelectrode cMAP signal of $\approx$ 25 mV (Figure 2.26a). The

amplitude of the signal peak is observed to drop with time, reducing to ≈ 7 mV in 2 hours. Also the sharpness of the MAP peak is seen to deteriorate, with an increase in Na^+ peak rise-time from 2 ms in the ideal signal to ≈ 20 ms. The signal is seen to have peaks of both polarities relative to the resting potential. In Figure 2.26a the recorded cMAP is seen to have a partial bipolar nature at $t = 0$ because of the circuitry having a high-pass filter cut-off of ≈ 0.225 Hz. At $t = 2$ hours the signal morphology is seen to be highly bipolar. This change in signal morphology is likely to be caused by the electrochemical changes (with time) taking place on the surface of the electrode, as opposed to physiological reasons. As demonstrated in the previous section, the shape of the cardiac MAP signal depends on the low- and high- pass cut-off frequency of the system. The bipolar nature of the signal can be explained by the increase in the high-pass cut-off frequency ($f_{HPF} \approx (2\pi(R_{ct}//R_L)Q^n)^{-\frac{1}{n}}$), which can be attributed to a decrease in interfacial capacitance (Q^n). Similarly, the sharpness of the peak can be explained by a decrease in the low-pass cut-off frequency ($f_{LPF} \approx (2\pi R_s C_L)^{-1}$), which can be a result of an increase in the spreading resistance (R_s) because of the presence of cardiac tissue all around the platinum electrodes. Impedance measurement of the electrode-electrolyte interface needs to be performed with the ultrasonic microprobes inside the cardiac tissue to validate the above hypothesis and characterize the change in the interface impedance parameters with time.

Cardiac arrhythmias were also recorded by the ultrasonic microprobes by pacing the heart sample at progressively shorter cycle lengths until fibrillation was seen. Prior to VF, the electrical activity in each of the different channels was regular and coordinated. When externally paced at higher than normal heart rate, ventricular tachycardia was observed exhibiting period-doubling bifurcations with alternans (alternating high-low-high action potential durations) and eventually

leading to ventricular fibrillation [57] (Figure 2.26b). After fibrillation has set in, higher frequency components (compared to the pacing frequency) and multiple peaks are developed in the frequency spectrum. The difference in frequency characteristics could be used as detection method to distinguish ventricular fibrillation from tachycardias.

MAP recordings visualize local cardiac repolarization, allowing accurate measurement of important parameters such as action potential duration (APD) and effective refractory period (ERP). Alternatively, computational models of the generation of extracellular action potentials from intracellular activities of the cell can be established similar to the models established for neurons [58]. It is then possible to reverse engineer the problem and obtain important parameters of the intracellular signal from extracellular recordings.

2.6 Ultrasonic actuation-based direct mechanical stimulation of cardiac tissue

Implantable cardioverter-defibrillators (ICDs) are the recommended therapy for many patients who are at risk for sudden death from ventricular arrhythmias [59]. ICDs constantly monitor and correct the heart rate by electrically pacing and can deliver therapies by way of electrical shock ($\approx$ 3.5 kW, 2 kV, 2 A, 10 ms [60]) when ventricular fibrillation is manifested with characteristics of rotating spiral waves of electrical activity. One of the disadvantages of ICDs is that the electrical shocks required to terminate VF, are reported to be painful and distressing to the patient and can cause post-traumatic stress syndrome [61]. Although the ICDs are an excellent means to monitor and control heart rhythm, there is need for a less

intensive and patient-friendly method to terminate ventricular arrhythmias.

In this section, we present a hypothesis for mechanical stimulation of cardiac tissue by means of the ultrasonic longitudinal actuation of the horn. The motivation behind this hypothesis is to develop an implantable purely-mechanical pacemaker device in order to replace the commercially available cardiac ICDs which utilize electric shocks to restore regular cardiac rhythm to the heart. This will eliminate existing problems with ICDs such as tissue damage, shock based tissue refractoriness, etc. The mechanoelectric feedback mechanism in cardiac myocytes, mechanical stimulation of cardiac tissue/cells and the literature showing premature ventricular contractions due to exposure to focused ultrasound beam is reviewed. A biophysical hypothesis for localized mechanical activation of cardiac myocytes in the canine left ventricle using microprobes is presented and experiments performed to support the hypothesis are outlined.

2.6.1 Cardiac mechanoelectric feedback (MEF)

MEF is a constituent part of the heart's intrinsic electromechanical regulatory loop. It provides the information pathway from the mechanical environment of cardiac cells to their electrophysiological activity (Figure 2.27). Recently the underlying (sub-) cellular mechanisms of cardiac MEF have started to be elucidated, which include (a) stretch activation of sarcolemmal ion channels [62], and (b) the electrophysiological effects of mechanical modulation of cellular Ca^{2+} handling [63]. Since the time-constants for Ca^{2+} signalling are in the milli-second time scale, the transient high-frequency mechanical perturbation due to the microprobes will have little to no affect on the Ca^{2+} handling [3]. The discussion in this section will be focused on the stretch-activated ion channels, the activation of which can lead to

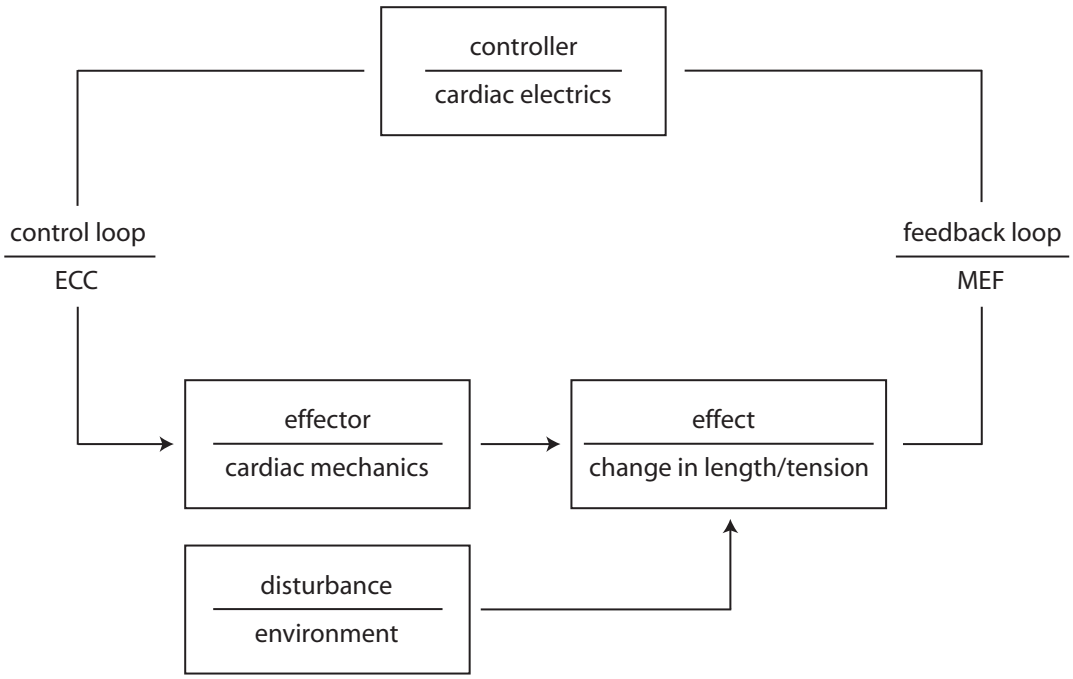

Figure 2.27: Scheme of cardiac electromechanical regulatory interactions. Regulation is based on the integration of control and feedback processes. Cardiac electrical activity controls cardiac mechanics via excitation-contraction coupling (ECC). Changes in tissue length and/or tension affect electrophysiological properties via MEF [3].

depolarization of the cell.

A. Stretch-activated channels (SAC)

Mechanically operated ion channels may either be activated or inactivated by stretch. So far, only stretch-activated channels (SACs) have been identified in cardiac cells [64, 65]. SACs respond to stretch by an increase in open probability (rather than an increase in channel conductance), although it is not clear yet how the macroscopic stimulus (stretch) is sensed by the microscopic structure (ion channel) [66]. Studies have been performed in order to examine the effects at the cellular level - voltage clamped cells are carefully stretched axially and the mechanosensitive current properties such as I-V relationship and its dependence on sarcomere length (i.e. extent of stretch) are deteremined [65, 67]. Effects of constant, transient and cyclic loading of the cell are also examined. The mechanosensitive current is observed to be inward in direction with a constant reversal potential $E_{rev} \approx$ -20 mV independent of cell deformation, thus aiding in depolarizing the cell [65, 68]. Experimental studies have shown that by stretching the cardiac tissue the cell membrane of the myocytes can be depolarized to cross the threshold of eliciting action potentials, hence stimulating the cardiac tissue. Efforts are currently being directed towards quantifying the increase in mechanosensitive current with increases in sarcomere length, in order to form a physiological current-sarcomere length relationship to be included in the standard cardiac MAP generation models. The precise effects of SAC activation on cardiac MAP morphology are still under investigation. There appears to be consensus about the predominantly depolarizing effect of diastolic stretch [69]. Systolic stretch, however, may have a variety of effects on the action potential, including shortening [70], prolongation [67], and crossover of repolarization [71]. The

above effects describe the change in action potential morphology in an electrically stimulated cardiac myocyte preparation due to mechanical perturbation of the cells.

Several researchers have invetigated the electrophysiological effect of volume increases in intact mammalian hearts. Lerman et al. [72] and Calkins et al. [73] found that monophasic action potential durations and refractory periods shortened after an increase in ventricular volume. Franz et al. [74] concluded from their findings that membrane depolarization in the intact heart is caused by both gradual and rapid ventricular stretch, but premature ventricular excitations are more easily elicited by rapid stretch. Stacy et al. [4] in their study concluded that as diastolic stretch in the isolated heart increases, stretch-induced depolarizations become larger and reach threshold potential more often (Figure 2.28).

B. Mathematical model

Combined studies of cardiomyocyte electrophysiology, contractility and Ca^{2+} handling during mechanical perturbations are extremely difficult [70], so most reports are based on consecutive investigation of parameters. Also, given the central role Ca^{2+} plays in cardiac electromechanical activity, it is exceedingly difficult to establish chains of causally linked events from mechanical effects on cardiomyocyte Ca^{2+} handling to changes in electrophysiology. These experimental difficulties emphasize the role that mathematical modeling may play in unraveling the contribution of this mechanism to cardiac MEF.

$$I_{SAC} = G_{SAC} \frac{V - E_{SAC}}{1 + e^{-\alpha(L - L_x)}} \tag{2.30}$$

Stretch-activated ion currents have been approximated in mathematical

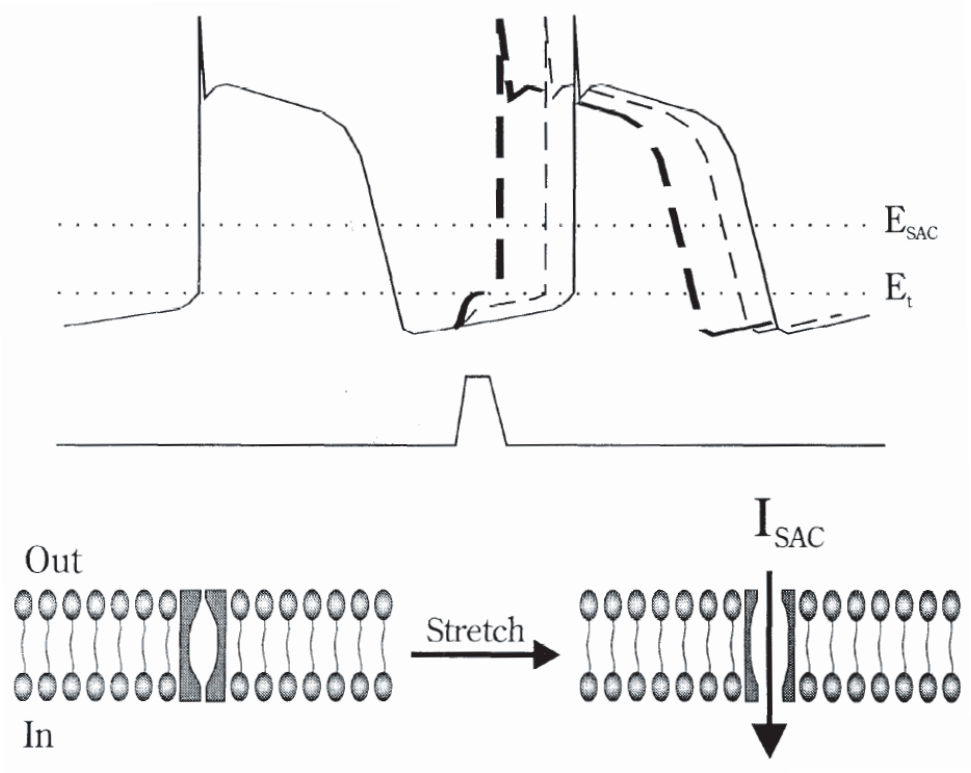

Figure 2.28: Diagrammatic representation of the stretch-activated channel (SAC) hypothesis. Top: theoretical action potentials (solid trace) of cardiac Purkinje fibres from an isovolumetrically beating ventricle; transmembrane potential after transient diastolic stretch is imposed, yielding transient depolarizations that elicit an immediate (thick dashed curve) or delayed (thin dashed curve) action potential. Dotted horizontal lines indicate equilibrium potential of stretch-activated channel (E_{SAC}) and threshold potential (E_t), respectively. Middle: trace shows timing of volume increase. Bottom: portion of cell membrane containing a SAC before (left) and after (right) stretch is applied. An inward current flows through the SAC (I_{SAC}) when channel changes from closed to open configuration with stretch [4].

models by simulation of constant current injection, by introduction of ohmic conductances with an appropriate reversal potential [75], or by a step-increase in the values assigned to sodium and potassium background conductances to simulate mechanical activation of cation-selective SACs [76]. Detailed models of SACs that allow computation of stretch effects in a dynamic setting tend to be based on expressions similar to Eq. 2.30, where the stretch-activated current I_{SAC} is calculated as the product of the stretch-activated conductance G_{SAC} (equal to the product of channel conductance and density) and the voltage difference between actual membrane potential, V, and SAC reversal potential, E_{SAC} (driving force for charge movement), divided by the term $1+e^{-\alpha(L-L_x)}$, the inverse of which gives the probability of SACs to open (here, α is a scaling factor, L is the actual sarcomere length, and L_x is the reference length). SACs, modeled according to Eq. 2.30, may either represent a solely 'electrogenic' mechanism where only charge transportation rates are considered [77, 78], or be linked to the calculation of intracellular ionic concentrations [79]. The ion SAC models currently used assume a contribution to 'bulk' ionic concentrations, and it is not surprising, under these conditions, that the effects of transient stretch (like in our case) on cellular electrophysiology show little dependence on whether or not 'electrogenic' or 'ionic' models are used [80]. Rice et al. in their study incorporated idealized models of mechano-sensitive channels into biophysically detailed single cell and one-dimensional cardiac cable models and determined the threshold value of conductance G_{SAC} (i.e. stretch) required to elicit premature ventricular excitations. The absence of sufficient information on acute stretch effects on ionic currents *in situ* [67], cell coupling or impulse conduction, lends these studies to be, at best, first approximations.

2.6.2 Direct mechanical stimulation of cardiac myocytes

In order to record electrophysiological cardiac MAP signals elicited by myocytes in an isolated and perfused preparation of cardiac tissue (say left ventricle), the cardiac tissue is electrically stimulated using a dual-wire electrode by supplying short bursts (2 ms) of current at regular intervals with period close to the normal heart rate. The electrical stimulus, above a threshold current density, activates the myocytes to elicit cardiac MAP and the signal propogates through the tissue producing contractions. Electrical stimulation of cardiac tissue takes advantage of depolarization of myocyte cell membrane which leads to contraction of tissue. In cardiac pacemakers, the electrical stimulus is used as a means to reset the cardiac rhythm *in vivo* when cardiac disorders manifest themselves as irregular rhythms such as ventricular fibrillation. Although the electrical stimulus has proven to be an effective means of activating cardiac myocytes, prolonged localized exposure to electrical stimulus in pacemakers may lead to permanent cardiac muscle damage [81].

Cardiac tissue composed of myocytes, connective tissue and endothelium can be modelled as a viscoelastic solid continuously undergoing cyclic contractions. Cyclic mechanical loading as a consequence of propagating electrophysiological changes in a three-dimensional volume of cardiac myocytes is their main function, thus serving an integral part in the function of the heart. When a mechanical stretch stimulus is applied to an isolated and perfused cardiac tissue, the presence of stretch-activated channels allows the myocytes' cell membrane to reach a depolarized state. This depolarized state can excede the threshold to elicit an action potential response and this signal can propagate in the tissue leading to contraction of myocytes [82]. Moreover, a mechanical stimulus to cardiac tissue, as opposed to an electrical one,

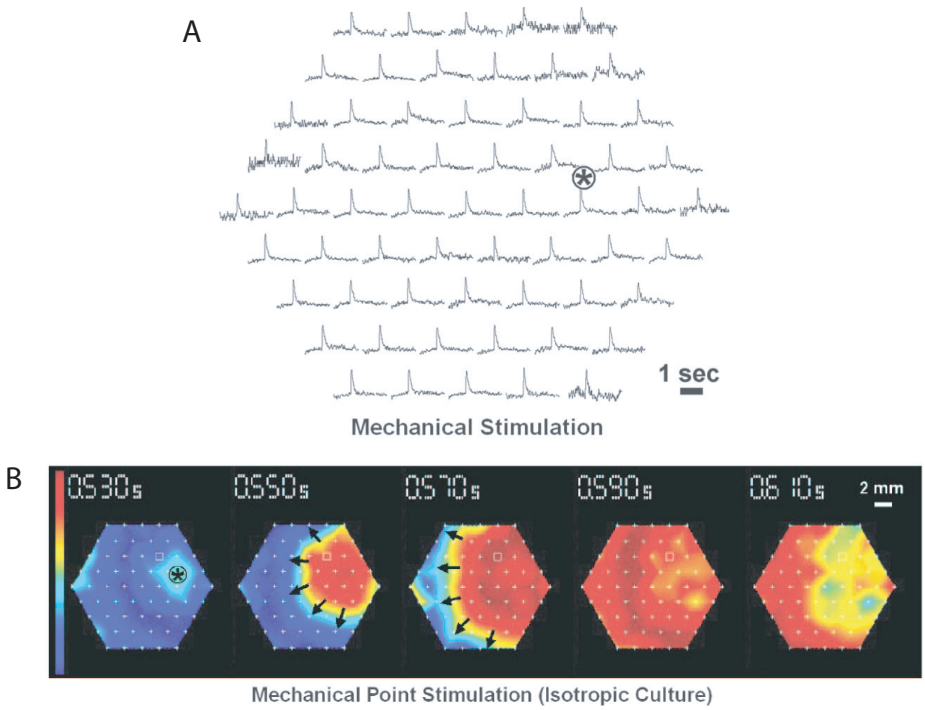

Figure 2.29: Mechanically induced action potential propogation, by means of a fluid jet, in an isotropic monolayer of cultured cardiac myocytes. *A*: optical action potentials shown at 61 recording sites for mechanical stimulation. *, location of 0.4-mm-diameter nozzle for fluid jet (0.5 m/s, 10 ms). *B*: propagation maps. Optical signals are normalized per site to the action potential amplitude. Color bar at left indicates resting potential (in blue) and peak of action potential (in red). Mechanical stimulation resulted in wavefronts that spread radially from the stimulating nozzle [5].

can serve as a more familar mode of excitation for the tissue. Once it is known in which ways a mechanical stimulus mimics an electrical one, it may be possible to envision or even design situations in which a mechanical perturbation can induce self-sustained electrical activity.

Fasciano II et al. [82] conducted an experimental study in which they mechanically stimulated an isolated frog ventricular tissue by stretching a sheet of tissue and estimated the threshold stretch required for stimulation. Their results showed that faster stretch pulses activate tissue more easily, increased

levels of baseline stretch make mechanical stimulation easier and that the width of the stretch pulse does not change the mechanical threshold. Recently, it has been shown that compression and shear elicit different mechanosensitive responses in membrane ion currents when applied to single cardiomyocytes in the absence of cellular length changes [83]. In order to quantify the whole cell mechanosensitive cardiac currents arising due to compression and shear based mechanical stimulation, Bett et al. [84] conducted a study in which current recordings were taken from acutely isolated voltage-clamped adult rat ventricular myocytes, undergoing direct deformation of the membrane with a glass pipette acting as a mechanical probe. The mechanosensitive current was reported to always begin with a large inward spike of current, which suggests a structural failure of a protecting element, and once elicited the characteristics of the mechanosensitive current was highly reproducible as a response to sinusoidal mechanical stimulation. The cells were reported to begin spontaneously contracting in the region where the probe and the cell had been in contact. The cells were mechanically stimulated in the x-y and z- direction, and were shown to exhibit inward mechanosensitive current in both cases. In order to understand the contribution of pressure and shear stresses on cardiac myocytes to mechanoelectric feedback, Kong et al. [5] applied mechanical stimuli in the form of localized fluid jet pulses to neonatal rat ventricular cells cultured as confluent monolayers. Cells were stained with voltage-sensitive dye RH237 and multi-site optical mapping was used to record the spread of electrical activity in isotropic and anisotropic monolayers. The localized pressure and shear stresses generated at the point of impingement was seen to trigger excitation and initiate a propagating circular wavefront that spreads radially from the site of stimulus (Figure 2.29).

From the experimental literature on mechanical response of cardiac myocytes

cited above, we can conclude that periodic force applied normal or tangential to the direction of orientation of sarcomeres in cardiac myocytes, can result in depolarization of the cell membrane due to the mechanosensitive current. By applying the cyclic direct-mechanical stimulation for long enough the cell membrane can be depolarized above the threshold for eliciting an action potential and, the threshold for eliciting an action potential can be lowered at high resting tensions in myocytes. Also localized pressure or stress based stimulus on cardiac myocytes can result in triggering excitation and propogation in cardiac tissue.

2.6.3 Ultrasound-based mechanical stimulation of cardiac myocytes

A. Background

Both mechanical impacts as well as high-intensity ultrasound are known to produce cardiac depolarization in small animals. Stretching of the myocardium by sudden impacts to the chest (commotio cordis) can evode cardiac bioelectric events sufficient to interrupt heart rhythms [85]. Ultrasonic energy applied to the body produces mostly tissue vibration rather than large stretch displacements characteristic of impact but reportedly still produces bioelectric effects. Early experiments with the effects of ultrasound energy on the heart rhythm date back to 1929 when Harvey [86] applied pulses of 100 kHz ultrasound to the amphibian heart and observed pacing at the pulse frequency. In a study conducted by Zakharov et al. [87], on the action of ultrasound on strength of contraction and action potential of the papillary muscle of the rat heart, the effect of ultrasound was observed to be non-thermal and transient in nature - despite continued irradiation

the force of contraction decreased after reaching a peak value (sometimes reaching a maximum several times). The effect of ultrasound was observed to be accompanied by membrane depolarization and by marked lengthening of the plateau phase of the action potential. In more recent years, Dalecki et al. [88, 89, 90] investigated effects of pulsed ultrasound energy that produced premature ventricular contractions and pacing on frog and guinea pig hearts. Studies have shown that the bioeffects of ultrasound are caused by bubble collapse during acoustic cavitation, which releases energy that temporarily increases the internalization of exogenous molecules by living cells [91, 92]. Schlicher et al. demonstrated repairable micron-scale disruptions in the cell membrane with lifetimes of $\approx$ 1 minute, via induced cavitation by non-invasive focused ultrasound as a method for drug delivery [93]. Although focused ultrasound has been demonstrated to be able to stimulate/pace cardiac tissue [94, 87], one of the major problems is the high ultrasonic power required (externally applied) to achieve the desired effect and localization of the stimulation effect in tissue.

Ultrasound pulses, generated by a transducer face directed towards the epicardium, produce two distinct forms of mechanical events on tissue; an oscillatory wave pressure and acoustic radiation pressure. The oscillatory wave pressure is 1.9 atm/W at 1 MHz sound frequency [95] however the tissue displacement is miniscule, only 18 nm at this power and frequency. The tissue displacement decreases with frequency and by the square root of intensity. Acoustic radiation pressure is a non-linear second order effect of the propagating wave intensity [96, 97]. It creates a unidirectional force (F) that pushes matter away from the source of sound intensity and is given by $F = (I_{abs} + 2I_{scat})\alpha/c$, where ultrasound absorbed by the tissue is I_{abs} and that scattered is I_{scat}, and c is the speed of sound in the tissue and α is the attenuation coefficient. Thus, the radiation

force increases on tissue in proportion to tissue attenuation coefficient which is in turn a function of ultrasound frequency. Attenuation coefficients in muscle are on the order of 1.5-2 db/cm-MHz [95]. Direct determination of radiation pressure from ultrasound intensity is complicated by tissue frequency dependence, composition, and sound reflection. In biological tissue, ultrasound radiation pressure can be estimated to be in the range of 0.1 - 1 % of the instantaneous sound pressure [96, 97]. At high power levels similar to those used in this work there is an additional pressure contribution arising from non-linear propagation effects within the medium [97]. The physical mechanisms whereby ultrasound produces bioelectric activation are unclear. Dalecki et al. looked at the possibility of ultrasound heating as a reason for cardiac activation at 1.2-MHz frequencies and concluded that heat alone was not the mechanism [90]. A hypothesis is that high-intensity ultrasound pulses produce radiation pressure effects and that this is the cause of bioelectric activation [94]. Radiation pressures produce a transient push and displacement of tissue. If the radiation pressure was for example 1% of a 3 MPa wave pressure, this would create a 30 KPa (slightly less than 1/3 atmosphere) transient pressure on the heart. This pressure has a fast 56 μs rise time and might be like to an impact but created by a carrier wave.

B. An invasive approach

The silicon horn with the microprobes bonded to 2 PZTs when actuated at the $\lambda/2$ longitudinal resonance frequency of the silicon horn, has been reported previously [9] to reduce the DC force of penetration of microprobes (moving at constant velocity) into canine cardiac left ventricle tissue. Once inserted into the tissue, the microprobe creates a local fracture in the highly organized cardiac myocyte arrangement in the ventricular tissue. This break in continuity in the muscle

tissue leads to a localized high-stress region, in other words the resting tension in the myocytes is higher than normal. As described earlier mechanical perturbation of this high-stress region may lead to premature ventricular excitation. Finite element analysis of the free-vibration of microprobes (see section 2.3.2), when the silicon horn is actuated at its $\lambda/2$ resonance frequency, shows that both flexural and longitudinal motion of microprobes is expected. The localized mechanical perturbation of cardiac ventricular tissue by means of the vibrating microprobes could manifest two stimulation modalities namely, direct mechanical stimulation (flexural vibration) and ultrasonic radiation pressure based stimulation (longitudinal and flexural vibration):

Direct mechanical stimulation: The flexural vibration of the microprobes will be damped once inserted into the tissue. The myocytes surrounding the microprobes along its length, will experience direct sinusoidal compression in the direction of orientation of the sarcomeres due to the flexural vibration of the microprobes. This sinusoidal pressure on the myocytes can lead to premature ventricular excitations [82]. In the idealistic scenario, the antinodes of the dominant flexural mode (4^{th} mode, in our case) will act as point sources of ultrasonic mechanical pressure. From the shape of the 4^{th} flexural mode (Figure 2.8), we can conclude that there will be 2 antinode point sources of mechanical pressure in-phase and 1 antinode out-of-phase. The point sources of mechanical pressure can be assumed to be isotropic in the directions perpendicular to the length of the microprobes.

Ultrasonic radiation pressure-based stimulation: The longitudinal vibration of the microprobes in the tissue will result in ultrasonic radiation pressure to be generated at the tip of the microprobes (Figure 2.6). Assuming piston like motion of the tip of the microprobe, with effective piston mass to be 9.45% of the entire

mass of horn and microprobes, and tissue-damped tip displacement being 10% of undamped displacement 0.37 μm/V_{pp} (see section 2.3.3), the radiation pressure can be estimated to be $\approx$ 3 KPa at 5 V_{pp}. The tip of the microprobes can be assumed to be an isotropic source of radiation pressure propogating along the longitudinal axis of the probes. Similarly, the flexural vibration is also expected to provide radiation pressure along with direct mechanical pressure. The antinodes of flexural vibration will act as point sources of radiation pressure leading to cavitation in the tissue. Since the amplitude of flexural vibration is expected to be an order of magnitude lower than the longitudinal vibration, the magnitude of radiation pressure due to flexural vibration is expected to be low.

Towe et al. [94] demonstrated cardiac pacing in the porcine model using periodic pulses of intense ultrasound energy at physiologic rhythm. The presence of vibration microprobes inside the tissue can allow for invasive ultrasonic perturbation in order to control heart rhythm. Multiple sites of insertion of microprobes in the tissue can allow for monitoring and more controlled ultrasonic actuation providing feedback for maintianing heart rhythm. Thus the advantages of our technique over using focused ultrasound pulses are - direct mechanical stimulation of myocytes is possible, ultrasonic radiation generated by microprobes allows for localized stimulation control and radiating the entire organ with ultrasound can be avoided.

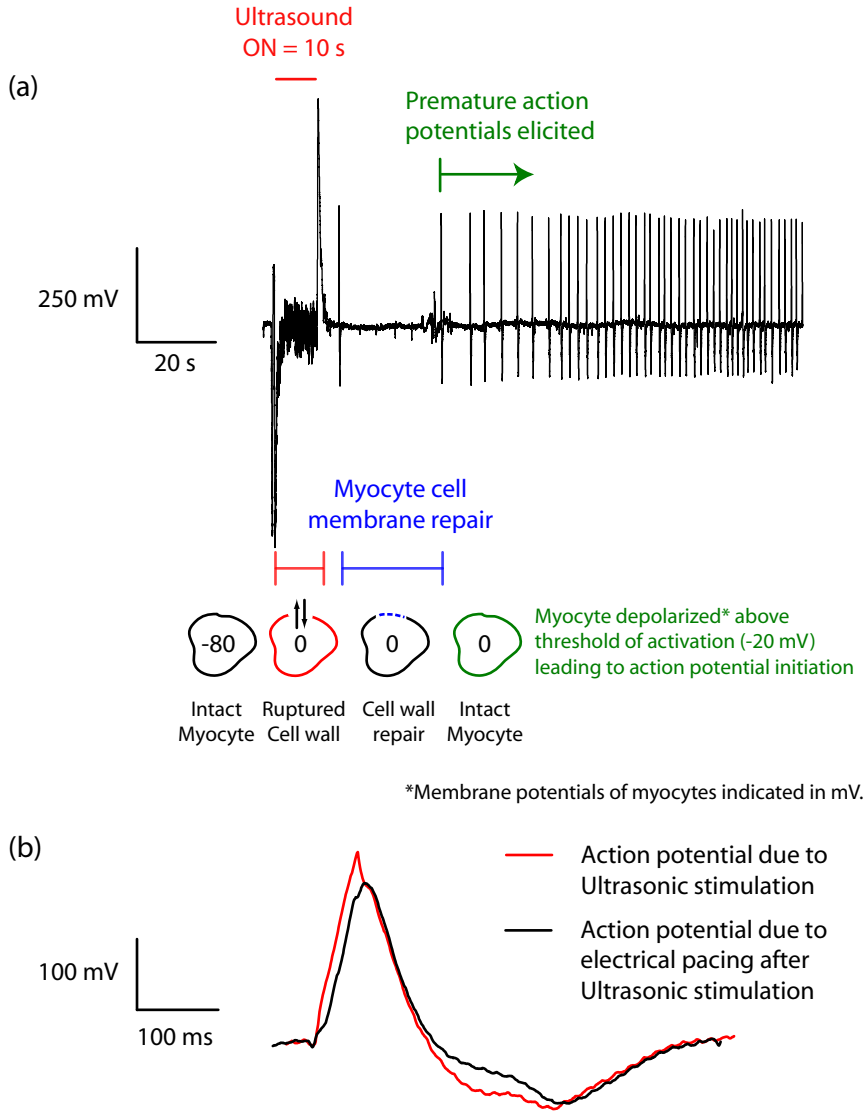

Figure 2.30: Response to microprobe-based ultrasonic stimulation of canine LV tissue, recorded at the stimulation site by Pt electrodes on the microprobes. Measured action potentials ampified by a factor of 100. (a) Top: Reversible myocyte cell membrane rupture due to $\approx$ 10 s stimulation, leading to premature action potentials elicited after membrane repair ($\approx$ 30 s). Bottom: Sketch of myocyte and its corresponding membrane potential at different stages of the experiment; (b) Comparison of morphology of action potentials elicited due to ultrasonic stimulation and due to electrical pacing after stimulation.

2.6.4 Experiments

A. Proof-of-concept

Two devices actuated at the $\lambda/2$ longitudinal resonance frequency of the horn and the microprobes (driving voltage = 10 V_{pp}), were inserted into an isolated and perfused (oxygenated tyrode solution at 37^o C) canine left-ventricular preparation using a manual positioning stage (Fig. 2.5). The cardiac preparation was paced at a constant cycle length using a bipolar electrical stimulation electrode placed on the epicardial surface. Pre-stimulus (ultrasound) conditioning was performed by recording action potentials at the electrodes on the two devices inserted in the tissue. After conditioning the devices to measure action potentials, the bipolar stimulator was removed and one of the devices was ultrasonically actuated for a period of 10 seconds. Signals were recorded from the two devices separated by a distance of $\approx$ 1.25 cm for a period of $\approx$ 10 minutes. When the ultrasonic stimulation was applied to one of the devices, negative potential spikes at the tissue perfusion rate were observed at the electrodes on both the devices for a period of $\approx$ 30 seconds. Our hypothesis is that by invasively applying ultrasound energy, the cells membranes in the tissue are reversibly wounded by ultrasound-based pressure driven cavitation (Fig. 2.30a, Bottom). As a result of the induced cell membrane permeability, the tissue conductivity is increased and tissue perfusion is sensed at the electrodes. At the end of the cell membrane repair period the cells are depolarized to 0 mV, thus leading to premature ventricular action potentials to be observed (Fig. 2.30a, Top). No time delay was observed in the initiation of action potentials recorded at the two devices separated by a distance of $\approx$ 1.25 cm indicating the possibility of the effect of ultrasonic stimulation to be global. After a period of 10 minutes, post-stimulus conditioning revealed that

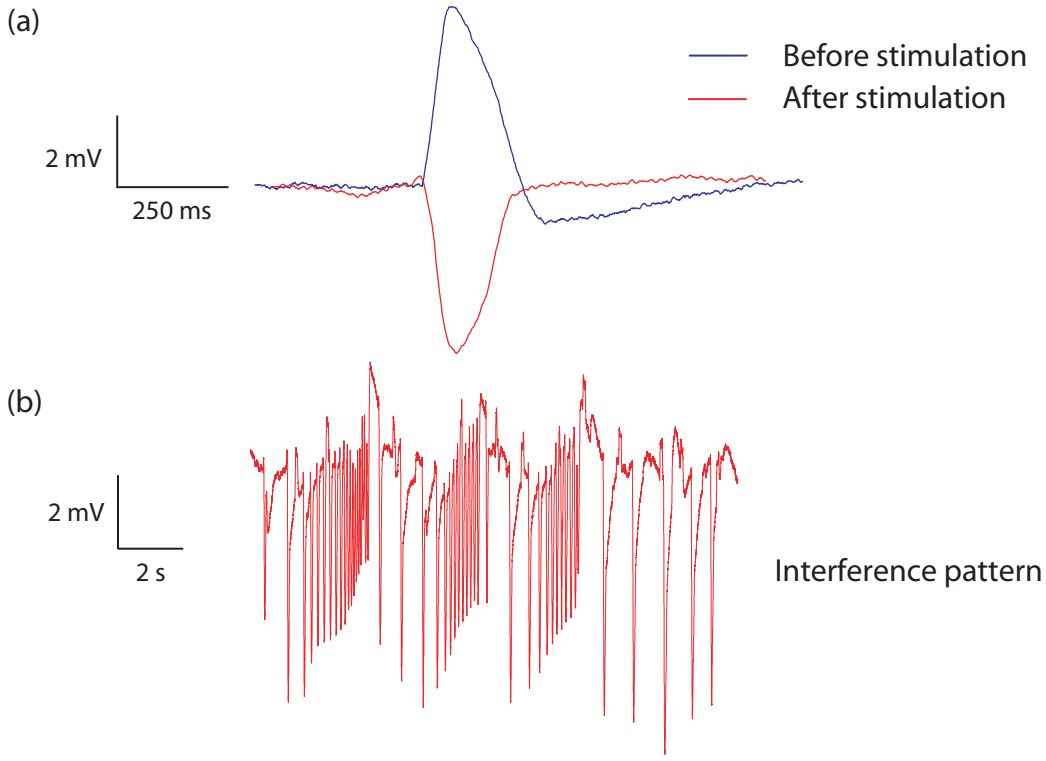

Figure 2.31: Response to microprobe-based ultrasonic stimulation ($\approx$ 5 s) of canine LV tissue also under continuous electrical pacing at T = 500 ms by a bipolar electrode. (a) Action potential morphology before (monophasic) and after (biphasic) stimulation and (b) Interference pattern of action potentials recorded at the stimulation site, evident from action potentials occurring at decreasing time-intervals between 2 excitations, as a result of interference of ultrasonic stimulation and the electrical pacing wavefront.

the electrophysiological properties of the tissue after stimulation were normal suggesting minimal tissue damage due to ultrasound (Fig. 2.30b).

In order to understand the effect of invasive ultrasonic stimulation on a beating heart, a second experiment was performed where ultrasonic stimulation was applied to LV tissue under continuous electrical pacing (T = 500 ms). Interference pattern of action potentials were recorded at the devices inserted in the tissue indicating an interfering effect of the ultrasonic stimulation and the electrical pacing wavefront (Fig. 2.31). After the interference activity stopped, action potentials were recorded

occurring at ≈ 2 seconds time-intervals. Also the action potentials recorded after seemed to be biphasic in nature suggesting a structural change that may have taken place at the site of mechanical stimulation. This shows that by means of ultrasonic stimulation an independent effect, overriding the electrical pacing, can be established on a beating heart tissue.

B. Optical mapping using voltage-sensitive dye

In order to understand the big picture of ultrasound-based mechanical stimulation of cardiac tissue, it is important to understand the propogation of action potentials starting from an intiation location depending on the type of stimulation viz. electrical, ultrasound or spontaneous. A canine left-ventricular preparation was isolated and perfused with low-Ca^{2+} oxygenated tyrode solution at 37^o C for minimal motion artifact. A voltage-sensitive dye (VSD) RH237 was delivered into the tissue via the perfused tyrode solution and allowed to perfuse through the tissue for ≈ 2 hours. Pre-stimulus (ultrasound) conditioning was done by pacing the cardiac preparation at a constant cycle length of T = 500 ms with impulse duration of Δt = 2 ms using a bipolar electrical stimulation electrode placed on the epicardial surface. A high-speed camera was used to digitally capture the optical response of the VSD at a frame rate of 500 Hz with a field-of-view of 5 x 5 cm^2. Figure 2.32 shows the frames captured during an electrical stimulation event depicting the propogation of the stimulation wavefront, and a grayscale image indicating the position of initiation of the wavefront (blue circle) and the recorded monophasic action potentials (red circle) indicating the activation following the electrical stimulation cycle length.

The device actuated at the $\lambda/2$ longitudinal resonance frequency ($\approx$ 110 KHz)

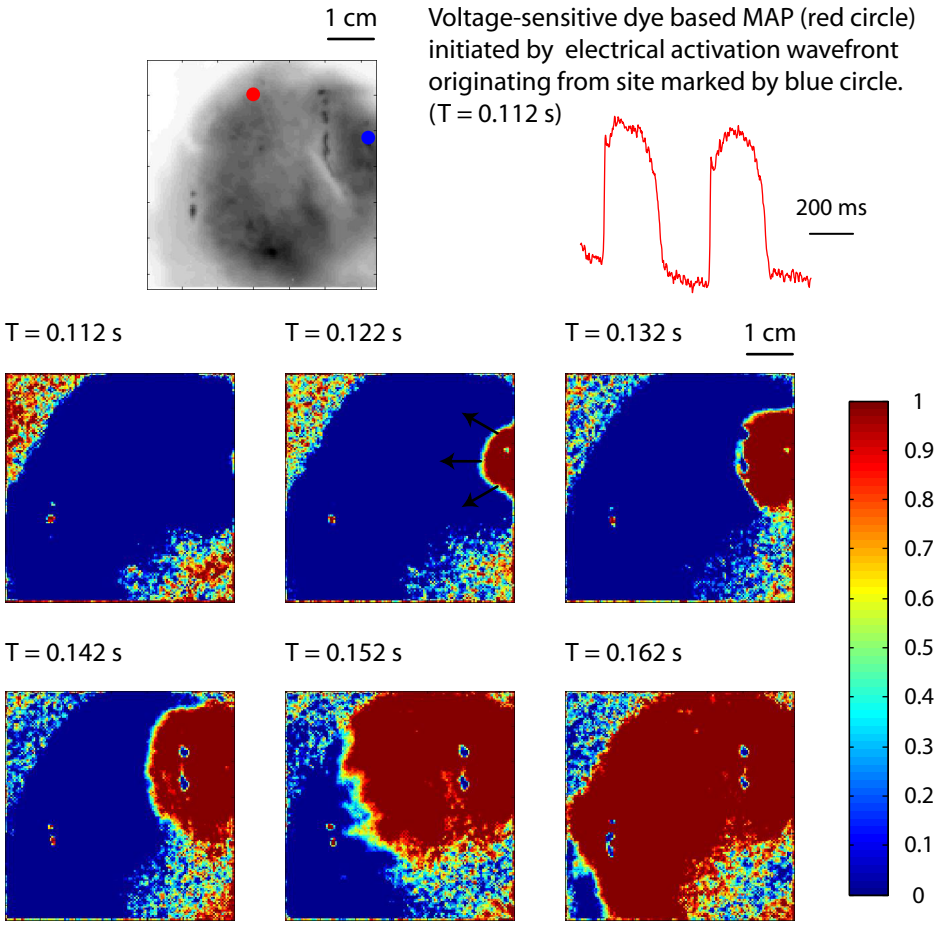

Figure 2.32: Voltage-sensitve dye based response to electrical stimulation (T = 500ms and impulse duration Δt = 2ms) of canine left-ventricular tissue using a bipolar electrode. Top: Grayscale image showing the location of stimulation electrode (blue circle) and monophasic action potentials recorded at location indicated by the red circle; Bottom: Frames depicting the optical response of the VSD indicating the spread of the stimulation wavefront in the tissue preparation.

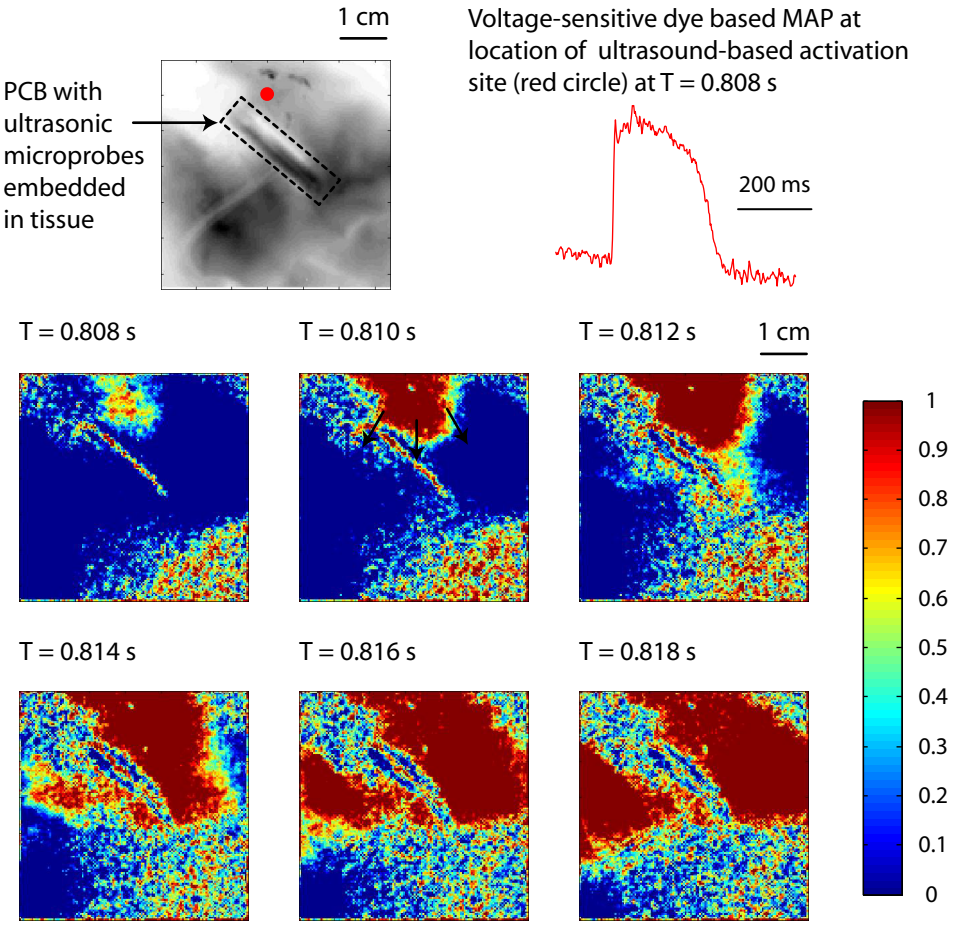

Figure 2.33: Voltage-sensitve dye based response to pulsed-ultrasound stimulation (T = 500ms and impulse duration Δt = 20ms) of canine left-ventricular tissue using ultrasonic microprobes. Top: Grayscale image showing the location of PCB with microprobes embedded in tissue and monophasic action potential recorded at location of initiation of activation wavefront indicated by the red circle; Bottom: Frames depicting the optical response of the VSD indicating the spread of the stimulation wavefront initiating close to the microprobes in the tissue preparation.

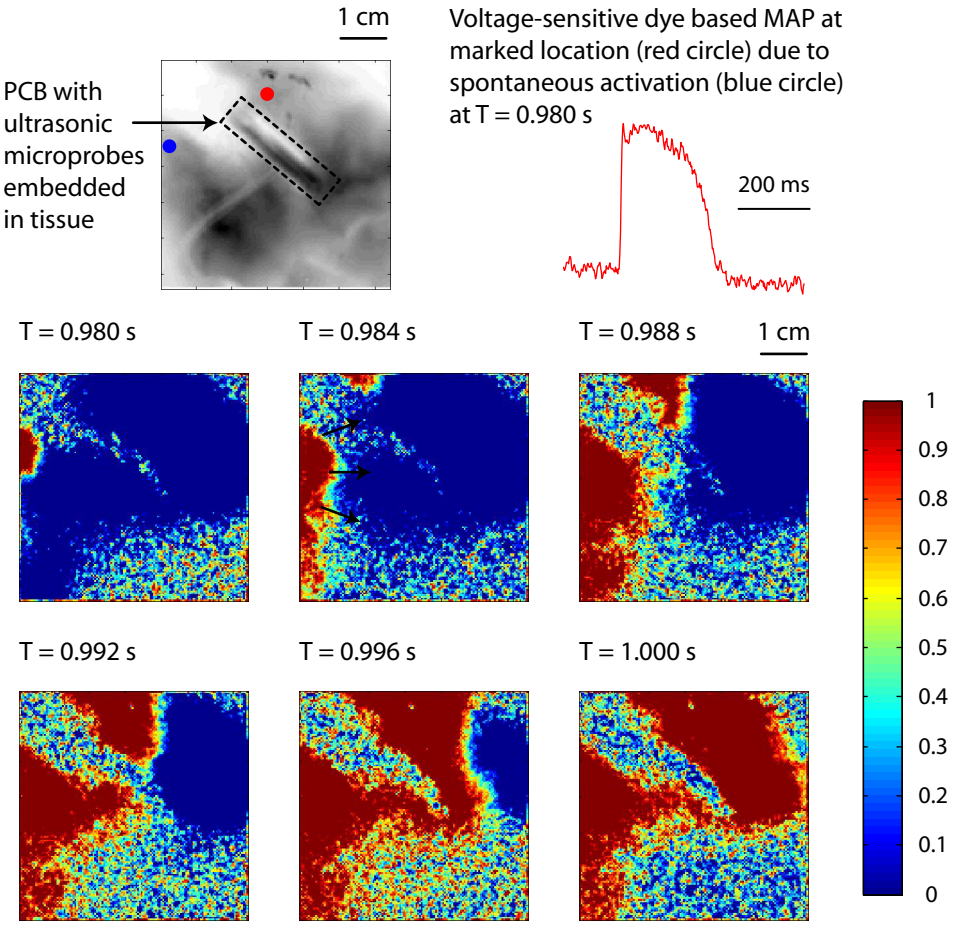

Figure 2.34: Voltage-sensitve dye based response to spontaneous activations arising from the edge of the canine left-ventricular tissue during pulsed-ultrasound stimulation (T = 500ms and impulse duration Δt = 20ms). Top: Grayscale image showing the location of origin of activation (blue circle) and monophasic action potential recorded at location indicated by the red circle; Bottom: Frames depicting the optical response of the VSD indicating the spread of the stimulation wavefront from the activation site in the tissue preparation.

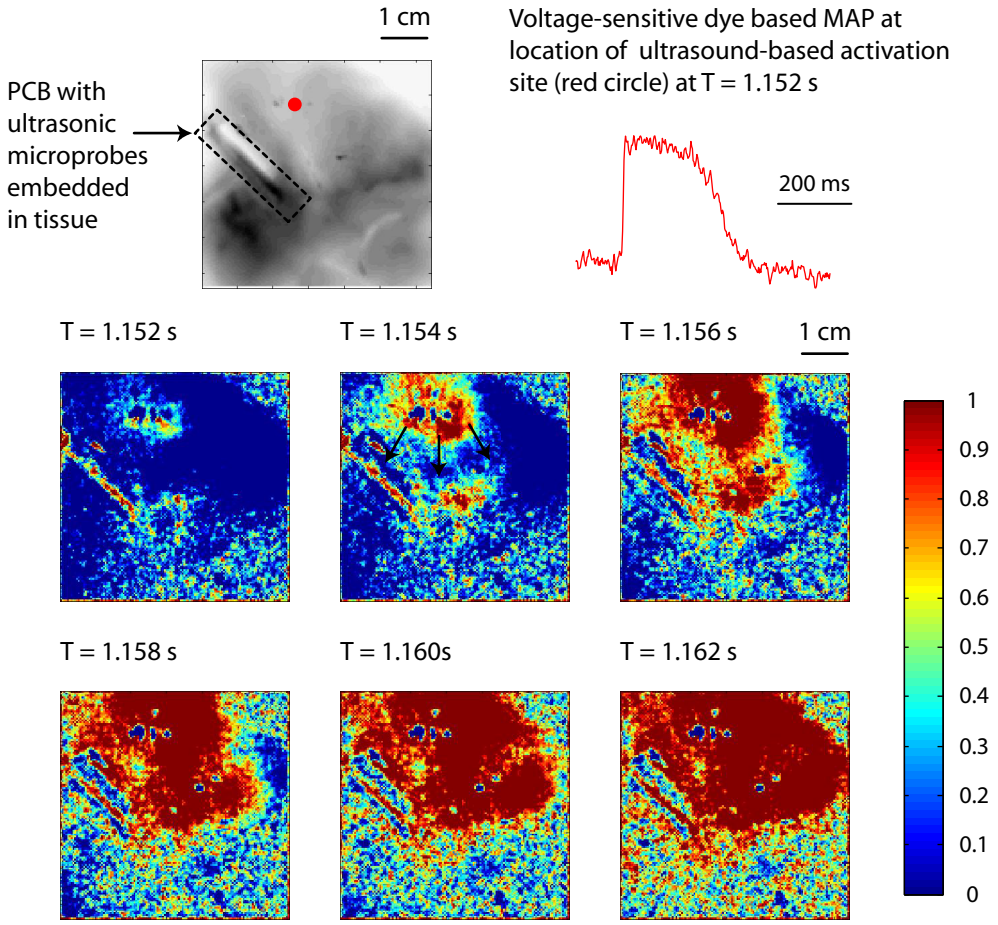

Figure 2.35: Voltage-sensitve dye based response to pulsed-ultrasound stimulation (T = 500ms and impulse duration Δt = 20ms) of canine left-ventricular tissue using ultrasonic microprobes inserted at a different location 3.35 mm below the previous location (Fig. 2.33). Top: Grayscale image showing the location of PCB with microprobes embedded in tissue and monophasic action potential recorded at location of initiation of activation wavefront indicated by the red circle; Bottom: Frames depicting the optical response of the VSD indicating the spread of the stimulation wavefront initiating close to the microprobes in the tissue preparation.

of the horn and the microprobes, is inserted into the tissue using a manual positioning stage (Fig. 2.25). The cardiac preparation is stimulated using pulsed ultrasound at a cycle length of 500 ms and a stimulus width of 20 ms. Cardiac stimulation wavefronts were observed, originating from a fixed location close to the probes, with a cycle length of 1.84±0.02 ms. Figure 2.33 shows the frames captured indicating stimulation wavefronts generated from a location (red circle) close to the probes. Also, the profile of the PCB with the ultrasonic microprobes embedded in the tissue can be seen in the grayscale image, and the monophasic action potential evoked at the activation site (red circle) is shown. The rate of occurence of evoked activations generated was not observed to follow that of the ultrasound pacing, but the location of initiation of the wavefront was observed to be close to the microprobes. Also, during the experiment spontaneous activations were also observed arising from the edge of the cardiac tissue preparation at no observable frequency of occurence (Fig. 2.34). The pulsed-ultrasound stimulation was repeated by re-inserting the microprobes at a different location which was 3.35 mm below (y-direction) the initial location. The point of initiation of the stimulation wavefront is observed (see Figure 2.35) to move down in the y-direction by the same amount as that of the microprobes (3.35 mm), indicating the possibility of the initiation location being inherently related to the ultrasound stimulation. One possibe explanation for this phenomenon is that the ultrasound maybe triggering the Purkinje fiber system in the left-ventricular tissue at a constant distance away from the microprobes. Since the Purkinje fiber system is well mapped in the left ventricle, the location of activation observed can be correlated to the position on the Purkinje fiber system to have an accurate estimate of the location of origin of activation. From the above experimental results, we can infer that by means of ultrasonic stimulation, an electrophysiological response

similar to that of electrically pacing heart tissue can be elicited with minimal tissue damage. Also, the Pt-electrodes in the microprobes can provide means for a three-dimensional approach to monitor cardiac failure and control heart rate by electrical pacing.

2.7 Conclusions and future work

In this chapter, we have demonstrated the use of ultasonically actuated silicon thin microprobes for penetrating isolated and perfused canine cardiac left ventricle tissue in vitro, and recording action potentials from multiple sites simultaneously within the heart wall. The ultrasonic modality of the devices allows for reduced force required for penetrating cardiac tissue. Platinum electrodes on the microprobes are characterized and capacitively sense the action potential voltage signal, in the extracellular environment around the cells close to the electrodes. Ultrasonic stimulation of canine LV tissue by the horn actuator via microprobes embedded in the tissue, are shown to evoke premature ventricular action potentials which are recorded at the Pt-electrodes along the microprobes. We hypothesize reversible injury of myocyte cell-membrane by acoustic cavitation to be the mechanism for depolarization of cells in the tissue. This method of stimulation and recording of action potentials from cardiac tissue can prove to be an invaluable tool in ICDs by monitoring activity and restoring heart rhythm.

Device and experiment design improvements need to be made in order to ensure better performance of the device with respect to its 3 main aspects namely, cardiac MAP recording, ultrasound based penetration force reduction and ultrasound-based stimulation of cardiac tissue.

Cardiac MAP recording

- *Motion artifact removal:* A package needs to be designed in order to carry the microprobes inserted in the tissue along with the motion of the heart. This will help us de-couple the motion artifact from the signal recorded, thus paving the path for a multi-sensor wireless array monitoring cardiac activity.
- *Multi-electrode array:* There is a need for a new design to be developed for fabricating a multiple probe-based multi-electrode array (MEA). The MEA will help in generating a map of the action potential propogation in a 3D volume of heart wall tissue and opens possibility of monitoring spiral wave activity during ventricular fibrillation.
- *On-chip low-frequency electronics:* By incorporating low-frequency electronics on-chip, the metal line parasitics can be by-passed before amplification of the signal recorded, thus allowing for a higher signal-to-noise ratio.
- *Parasitics:* Characterization of parasitics and verification of the estimated parasitic model parameters (see section 2.4.2) needs to be done. This includes measuring crosstalk between different electrode metal traces and capacitive signal pick-up by passive electrodes from an active electrode. The parasitics can then be included in modelling the transfer characteristics of the probe to better fit the data recorded. Also, grounding of tyrode bath and having a local ground in the tissue can avoid signal drift and shot noise.
- *Electrode material:* The favourable electrical and biocompatibility characteristics, and increased effective electrode area of thin films such as of TiN, PEDOT, TiN-Carbon nanotubes (CNT) [98, 99, 100] etc., make them a possible candidate for coating the platinum electrode. The advantages of using TiN are increase in signal-to-noise ratio [100] and lowering of high-pass

filter cut-off of the system preserving cardiac MAP signal morphology (see section 2.4.5).

- *In vitro electrode impedance measurement:* Platinum electrode impedance measurement in the isolated and perfused ventricular tissue preparation can help monitor the electrode-electrolyte interface as a function of time. Thus the variation in model parameters such as n, R_{ct}, Q and R_s (see section 2.4.4) can be monitored as a function of time.

Ultrasound-based penetration force reduction

- *Analytical model:* Transverse vibration of microprobes needs to be included in the analytical model for force reduction 2.3, in order to understand the contribution of longitudinal and flexural vibration towards reduction in penetration force.
- *Tissue histology:* Histology of canine ventricle tissue needs to be done, after insertion of microprobes with and without ultrasound, in order to estimate the tissue damage with application of ultrasound.

Ultrasound-based stimulation of cardiac tissue

- *Stimulation experiments:* In order to validate the ultrasonic mechanical stimulation hypothesis presented in this work, a new device needs to be designed and experiments need to be performed to further validate the stimulation hypothesis. The microprobes need to be designed to incorporate two sets of polysilicon resistors which can serve as local temperature sensors and strain gauges. The temperature sensor will serve to isolate the

effect of local temperature increase from the effect of ultrasonic pressure-drive cavitation-based action potential generation. The strain gauge will help determine the ultrasonic strain experienced by the microprobes under tissue damping and, estimate the longitudinal/flexural displacement of the microprobes inside the tissue.

- *Analysis of mechanical stimulation site:*
  - Histology of the cardiac tissue around the microprobes, where the tissue has been ultrasonically actuated needs to be done to quantify the mechanical and ultrasonic pressure-based radiation damage to the tissue.
  - From the preliminary findings it can be observed that the electrical response of the cardiac myocytes around the microprobes undergoes change after ultrasound-based stimulation, possibly due to some damage to the cardiac myocytes. In order to characterize this effect the activity of the tissue surrounding the microprobes can be estimated, by electrically stimulating the tissue using a biphasic electrode and recording potentials from the stimulation site using the Pt-electrodes on the microprobes.

CHAPTER 3

SILICON ULTRASONIC SURGICAL MICROPROBES WITH INTEGRATED PIEZORESISTIVE STRAIN GAUGE SENSOR

3.1 Introduction

Silicon-based power ultrasonic transducers were introduced by Lal [1], suggesting silicon's high output power density, larger stroke velocity, lower internal loss and heat generation as compared with transducers made with traditional metal materials. Theoretically, silicon-based ultrasonic actuators can produce output power about 35 times that from titanium alloys, stroke velocity about 8 times higher, and heat generation at least 10 times lower than titanium alloys. In experiments, a maximum ultrasonic velocity of 14.2 m/s was obtained with catenoidal silicon horns at 150 V_{pp} drive and 64.5 KHz longitudinal resonance, and silicon ultrasonic actuators have been used to cut cataracts in-vitro successfully. Other interesting phenomena related with high intensity ultrasound were also reported with silicon devices, such as atomization and acoustic streaming [1]. During the past decade, silicon power ultrasonics have seen developments in the fields of microsurgery [101], material characterization [102], ultrasonic nebulizer [103], etc. Advantages in integrating microscale sensors using MEMS technology has also been explored [34].

Minimally invasive medical procedures such as percutaneous liver biopsy and endoscopic surgery reduce tissue damage and patient discomfort but also pose great challenges to the surgeon due to reduced direct sensory feedback. Research efforts to improve the success rate of these procedures have been focused on experimental characterization and numerical modelling of the tissue-

surgical tool interaction [104, 105]. Force measurement during the tissue-tool interaction is important for building a realistic model based on which haptic interface and robotic assistance can be developed to help the surgeons regain tactile information during surgery. Furthermore, ability to distinguish tissue stiffness at microscale will allow for more accurate feedback and precise control of robotic minimally-invasive systems. MEMS (Micro-Electro-Mechanical-Systems) devices are expected to play an increasingly important role in this field, e.g., measurement of mechanical properties of tiny tissue samples have been performed by a Lithographie, Galvanoformung, and Abformung (LIGA)-fabricated microgripper [106]. Thin-beam silicon microprobes [24, 25, 26, 27, 28] provide high spatial resolution, reduced tissue damage, and easy integration with microelectronics. Silicon microprobes for tissue characterization in robotic surgery are especially favorable due to the potential of integrating a variety of sensors for monitoring different parameters such as insertion/cutting force, tissue viscosity and temperature etc.

In this chapter, a silicon horn-based actuator with microprobes integrated with piezoresistive strain gauges is presented. The device fabrication and mechanical characterization is discussed in detail. Its application as a force sensor in microdissection testicular sperm extraction surgery is demonstrated. Finally, by sensing the ultrasonic strain developed on the microprobes due to the longitudinal resonance of the horn, its application as a fluid viscosity sensor is demonstrated.

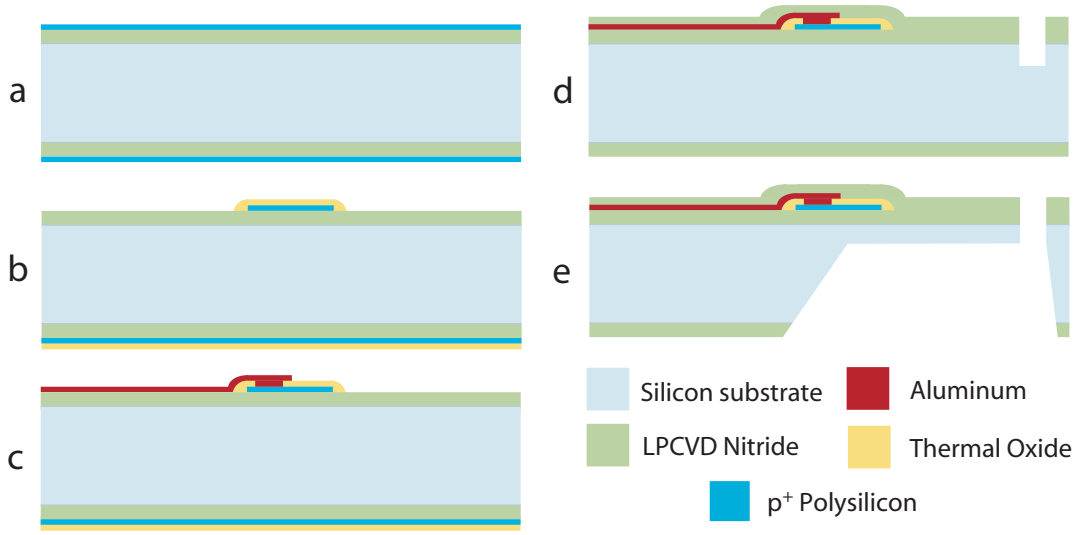

Figure 3.1: Process flow for fabricating the silicon ultrasonic microprobe. **a:** LPCVD deposition of polysilicon and boron implantation on 100 mm p-type silicon wafer with LPCVD nitride layer. **b:** Pattern and oxidize polysilicon. **c:** Pattern oxidized polysilicon to open contact holes and sputter deposition of Al+1%Si. **d:** Deposit PECVD low-stress nitride passivation layer and pattern to open metal pads for wirebonding. Pattern nitride passivation defining the probe tips and DRIE for desired probe thickness. **e:** Backside-only KOH etching to release the device.

3.2 Device fabrication and characterization

3.2.1 Fabrication

The design and fabrication of the microprobe is similar to the ultrasonic microprobes disccused in section 2.2. The catenoid horn is 4 cm long with shank-to-tip area ratio 10:1 and a longitudinal $\lambda/2$ resonance at $\approx$ 110 kHz, with two silicon microprobes 5 mm long, 100 μm wide and 140 μm thick projecting outwards at the tip of the horn. A further modification to the silicon microprobe, is the addition of a set of four polysilicon resistors forming a Wheatstone bridge arrangement for each of the two tips.

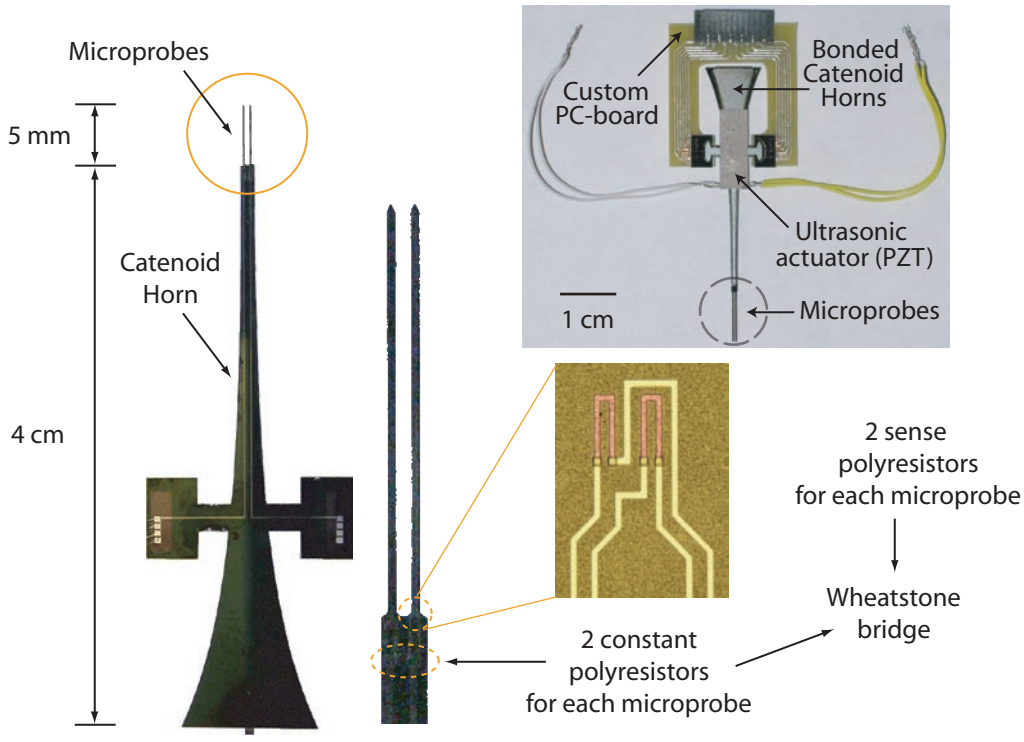

Figure 3.2: Optical photograph of the fabricated and PCB-assembled device. The two microprobes, with polysilicon resistors forming a Wheatstone bridge, integrated at the horn-probe interface of the silicon ultrasonic catenoid horn are 5 mm long, 100 μm wide, and 140 μm thick, and 0.5 mm apart.

Figure 3.1 shows the entire process flow of fabrication. The substrate used is a 100 mm-diameter p-type silicon wafer. Low-pressure CVD (LPCVD) silicon nitride is deposited on the wafer to serve as an etch mask for KOH. 9000 ^{0}A of undoped LPCVD polysilicon is deposited and implanted with Boron ($2\times10^{15}/cm^2$ at 100 keV) by Core Systems, Inc. The polysilicon is patterned into U-shaped resistors (Figure 3.2). Then, a 3000 ^{0}A wet oxide is grown on the polysilicon as an insulation layer. The oxide is patterned for contact openings to the metal aluminum layer. Aluminum with 1% silicon was sputter-deposited on the wafer, and metal lines are patterned such that four polyresistors form a Wheatstone bridge strain gauge on each of the two microprobes at the tip of the horn. Plasma-enhanced CVD (PECVD) nitride is deposited on the wafer as a passivation layer, and it is patterned to open metal pads for wire bonding. The LPCVD nitride on the backside of the wafer is patterned to allow backside-only KOH etching. The front side LPCVD and PECVD nitride is then patterned to define the microprobes, and timed deep reactive ion etching (DRIE) is done for desired probe thickness. Back-side-only KOH etching using a single-sided etch holder (Single 4, AMMT, Inc.) is done to release the device from the wafer. The device is then adhesively bonded using an insulative epoxy (EPO-TEK 360-T, cured at 120^{0}C on a hot plate) to another silicon horn having the same catenoid shape but with no microprobes. Two PZT plates are bonded on the top and bottom at the longitudinal node of the silicon compound horn using a high-strength and fast-setting cyanoacrylate adhesive (3M Pronto Instant adhesive CA40). The polarization directions of the two PZT plates face opposite to each other to cancel moments generated and add longitudinal forces. The PZT-silicon actuator is then adhesively mounted onto a printed circuit board (PCB) using 3M CA40 fast-setting adhesive, and the contact metal pads on the actuator are wire-bonded to the PCB contacts.

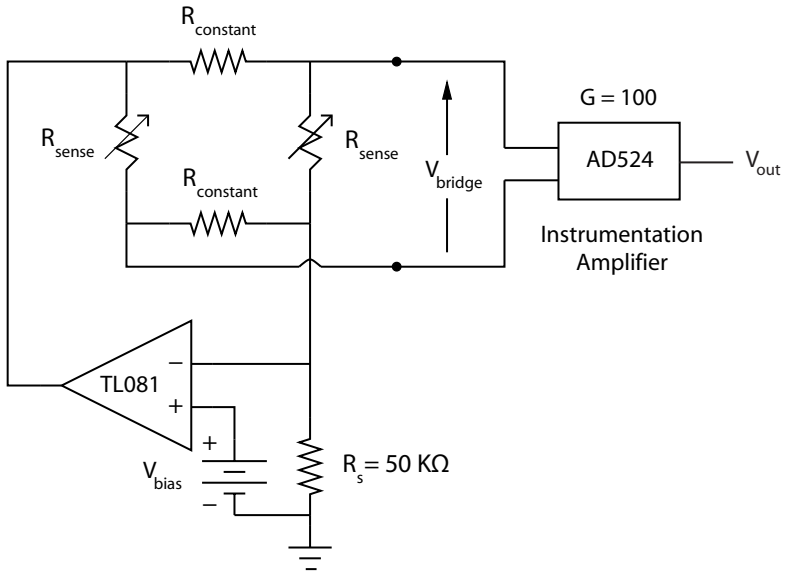

Figure 3.3: Wheatstone bridge formed by the polysilicon resistors on the microprobe, connected in a constant-current configuration with the current supplied by an operational amplifier (TL081). The bridge output voltage (V_{bridge}) is amplified by a factor of 100 using an instrumentation amplifier (AD524).

The polysilicon strain gauges ($\approx$ 10 kΩ), the resistance of which changes with the strain experienced by them, are positioned on both the microprobes - two reference polysilicon resistors positioned on the bulk silicon part of the horn so their resistance remains nearly constant with respect to strain on the microprobe, and the other two piezoresistive polysilicon resistors are positioned on the microprobe near its clamped edge where the strain is expected to be high (Figure 3.2). The polysilicon resistors on the microprobe forming a Wheatstone bridge are connected in a constant current configuration, with the current supplied by an operational amplifier (Figure 3.3). The bias voltage (V_{bias}) is set at 4V and the circuit is driven at $V_s = \pm$8V. The Wheatstone bridge output voltage is amplified by a factor of 100 using an instrumentation amplifier (AD524, Analog Devices, Inc.). Depending on the application, the circuit is modified in order to achieve the appropriate strain sensitivity (discussed in detail in later sections).

3.2.2 Mechanical characterization

The microprobe assembly was clamped to a micromanipulator (MP-285, Sutter Instruments, Inc.), and placed across a force gauge sensitive up to 1 mN (DFGS series digital force gauge, Chatillon, Inc.), which is clamped to a stage such that the microprobes are perpendicular to the surface of the force gauge. The force calibration tests were carried out below this threshold load for elastic buckling, so that the microprobes can be assumed to be under uniform compressive load. The assumption in this testing was that the force experienced by each microprobes is identical, i.e., the force recorded by the force gauge is twice the force experienced by a single microprobe. The microprobes were pressed against the force gauge at steps of 20 mN from 0 to 300 mN, and the Wheatstone bridge voltage was recorded. The variation of the bridge voltage with the force applied is fit to a 2^{nd} degree polynomial (Figure 3.4). The 2^{nd} degree variation is because of imperfect alignment of the probe perpendicular to the force gauge. From this longitudinal force characterization curve, it is clear that the polysilicon resistors are sensitive to minute changes in strain experienced by the microprobe, with a sensitivity of -0.41 V/N after electronic amplification by a factor of 100. Finite-element analysis (using ANSYS) of the microprobes was performed to estimate the strain induced on the polysilicon resistors due to forces experienced at the tip of the microprobes. Longitudinal and transverse gauge factors of 28 and -8 were used to estimate the resistance change corresponding to the expected longitudinal and transverse strains [107]. The longitudinal force sensitivity was estimated to be -0.43 V/N, which is close to the experimentally measured value.

The force sensitivity of the polyresistors to bending of the microprobes is characterized by positioning the microprobes with their longitudinal axes

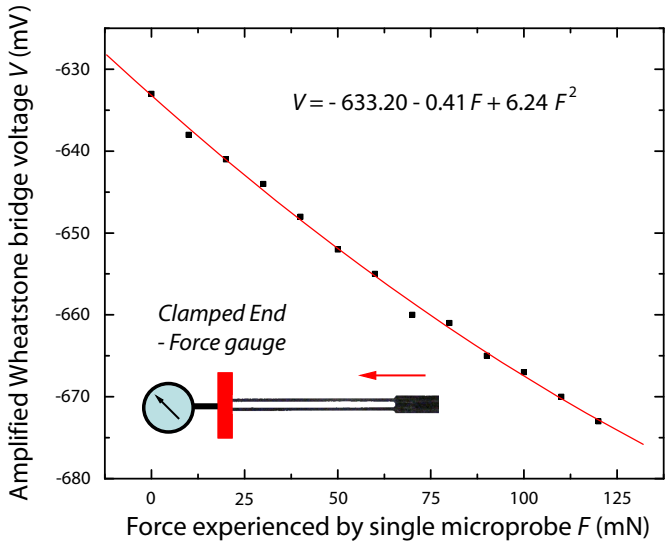

Figure 3.4: Force sensitivity characterization of the polysilicon resistors on the microprobe in the axial direction. The microprobes are axially compressed against the strain gauge and the Wheatstone bridge voltage is recorded after electronic amplification of 100.

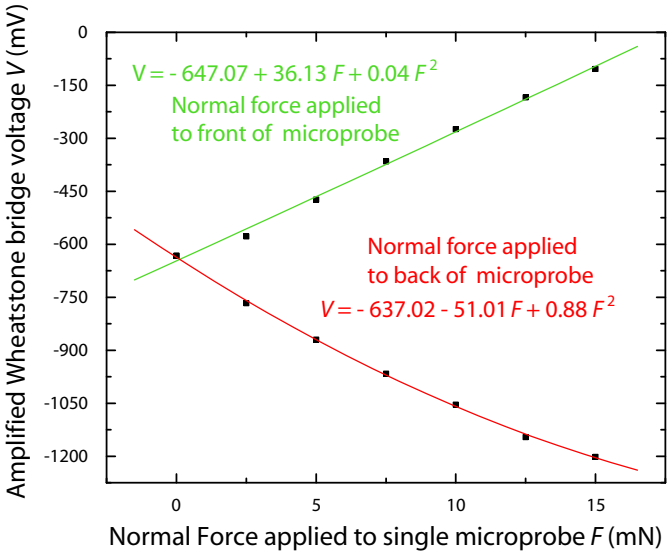

Figure 3.5: Force sensitivity characterization of the polysilicon resistors on the microprobe in the thickness direction normal to the plane of the microprobes: tensile strain (*green*) and compressive strain (*red*).

perpendicular to that of the strain guage. The polyresistors experience tensile strain when the force is applied to the front of the microprobes (on the side of the polyresistors) and compressive strain when the force is applied to the back of the microprobes. The assumption in this testing is that the force experienced by each microprobe is identical i.e. the force recorded by the force gauge is twice the force experienced by a single microprobe. The microprobes were pressed against the force gauge at steps of 5 mN from 0 to 30 mN, and the Wheatstone bridge voltage was recorded. The variation of the bridge voltage with the force applied is fit to a 2^{nd} degree polynomial (Figure 3.5). The 2^{nd} degree variation is because of imperfect alignment of the probe parallel to the force gauge surface. From this characterization curve it is clear that the polysilicon resistors are sensitive to minute changes in bending-based strain experienced by the microprobe, with a sensitivity of 51.01 V/N for transverse compressive strain and 36.13 V/N for transverse tensile strain after electronic amplification by a factor of 100.

3.3 Ultrasonic microprobe based testicular tubule-size assay

3.3.1 Introduction

Testicular failure affects approximately 1% of the male population and 10% of men who seek fertility evaluation. Men with testicular failure (non-obstructive azoospermia) show signs of severely impaired to non-existent sperm production [108, 109]. Until recently, it was assumed that men with non-obstructive azoospermia were untreatable, and the only options offered to these couples to

have children were the use of donor spermatozoa or adoption. Several clinically relevant findings have spotted the existence of sperm in men with non-obstructive azoospermia by direct evaluation of testis biopsy specimens [109]. Testicular sperm extraction (TESE) surgery and intracytoplasmic sperm injection (ICSI), as part of the in vitro fertilization (IVF) cycle, were first introduced in 1995 for the treatment of non-obstructive azoospermic men [110, 111, 112]. The theoretical basis for attempting to retrieve spermatozoa for ICSI from the testes of men with apparent absence of spermatogenesis was based on early quantitative histological studies from testicle biopsy in fertile and infertile men [113, 114] (Figure 3.6). The technique of TESE-based ICSI was found to be successful in azoospermia in 60% of cases using only mature spermatids and spermatozoa [111, 115, 116]. The spermatogenesis in such cases is seen to be diffuse rather than regional, thus resulting in a great deal of testicular damage, and sometimes even limit successful patients to only one attempt [117]. Damage is sometimes minimized by using needle rather than open biopsy to obtain spermatozoa for ICSI [118]. However, control studies have shown that for difficult cases of non-obstructive azoospermia, where spermatogenesis is very meagre, needle biopsy is much less likely to find the rare foci of spermatogenesis for ICSI than open biopsy [119]. So far, there has been little effort to spatially map spermatogenesis in the testis of azoospermic men despite large amounts of testicular tissue being often removed during biopsy [115].

In order to reduce the amount of testicular tissue removed during TESE surgery, Schlegel et al. [120] have performed microdissection TESE surgery, where the scarce foci of normal spermatogenesis could often be detected directly under the operating microscope, and thereby, in some cases, only tiny portions of testicle needs to be removed. This highly invasive surgical procedure involves identifying seminiferous tubules carrying spermatozoa by visual examination of the infertile

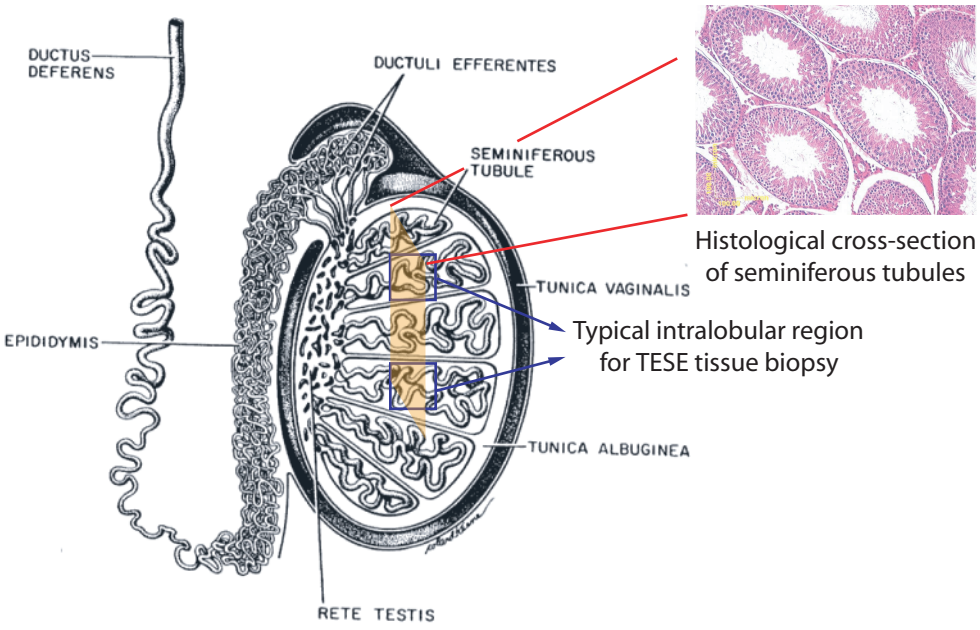

Figure 3.6: Sketch of the anatomy of the testis showing the arrangement of the seminiferous tubules leading into the convoluted epididymis. Histological cross-section (hematoxylin+eosin stain) of the seminiferous tubules and the typical region for tissue biopsy during TESE surgery are shown.

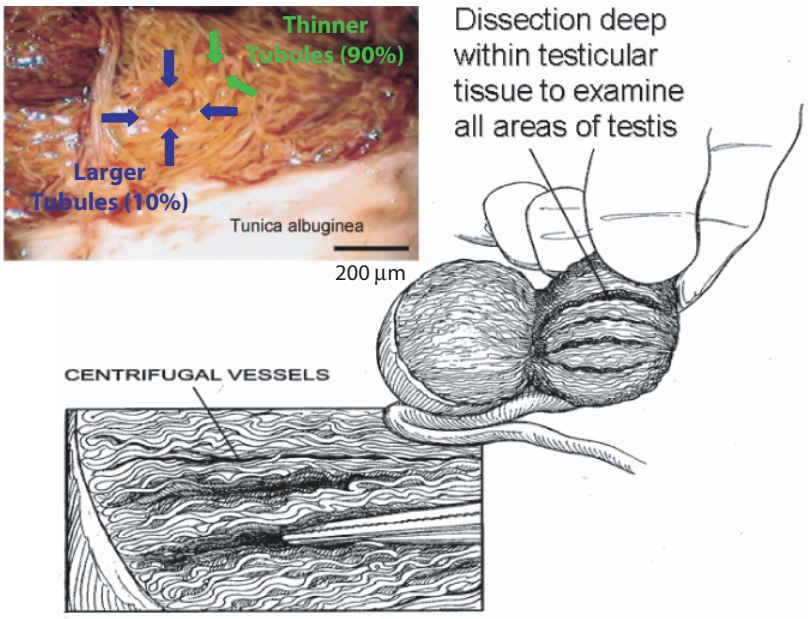

Figure 3.7: Sketch of the microdissection-TESE surgery showing the deep dissection of testicular tissue. Courtesy of Dr. Peter N. Schlegel, Weill Cornell Medical College, New York, NY.

testis under a microscope, and biopsy of the region of interest is performed (Figure 3.7). Tubules with low spermatogenesis have thinner walls and smaller diameter ($\approx$ 100 μm) as compared to healthy tubules ($\approx$ 200 μm). It has been observed that the larger sperm-producing tubules occupy only a fraction of the volume of the three-dimensional mass of tubules in the testis of an infertile male. Hence, dissection within the testis is necessary to search for healthy tubules embedded deep within the testis [120]. A minimally invasive tool for identification of regions of interest below the two-dimensional field of view of the microscope during microdissection-TESE surgery, will help reduce the loss of significant amount of tissue and can be used as a means to avoid vasculature in the testes. Information about the diameter and stiffness of the tubules in the depth direction without biopsy will help the surgeon make an informed decision about excision of tissue from a particular location, with a high probablity of locating tubules carrying spermatozoa.

Our hypothesis, proven in this work, is that by monitoring the tissue reaction force experienced by microprobes integrated to the ultrasonic horn actuator, inserted with 100-μm incision, the surgeon can measure the diameter, and stiffness of tubule walls encountered during the incision and subsequent penetration. By using the ultrasonic modality of the microprobe [41], the TESE surgery can be truly noninvasive by probing the organ from the outer surface, thus avoiding a large incision with a scalpel to examine the tissue. In this chapter, we demonstrate tubule dimension measurement in rat testis tissue *in vitro*, by insertion of silicon microprobes with integrated Wheatstone bridges formed by polysilicon strain gauges. Two microprobes with strain gauges are fabricated at the tip of the silicon ultrasonic horn actuator in order to increase the sampling of tubules and also to eliminate the Wheatstone bridge offset, thus increasing the SNR in force measurement. By way of modeling, expected tubule size measured by the microprobe is numerically simulated using the Monte Carlo method, and an analytical closed-form expression is derived for fitting the distribution of measured sizes.

3.3.2 Working principle

In this work, the silicon microprobes used are 4 mm long, 100 μm wide and 140 μm thick projecting outwards at the tip of the horn (Figure 3.2). To monitor the force sensed by the microprobes when puncturing the walls of the tubules, a set of four polysilicon resistors forming a Wheatstone bridge incorporated on both the microprobes was used as described in section 3.2. The tip of the microprobe has 2 sharp blade-like edges - a V-shaped edge on the top formed by the LPCVD nitride film and one at the bottom formed by silicon due to the anisotropic

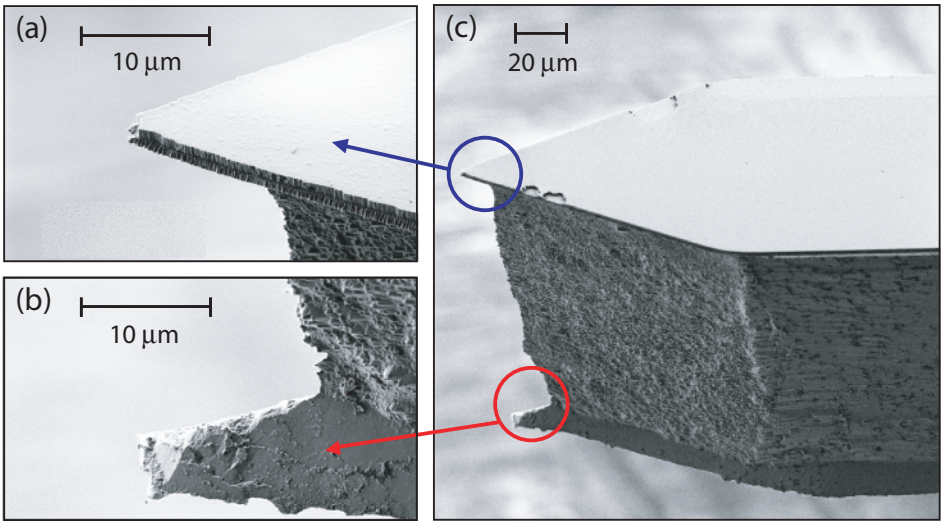

Figure 3.8: SEM images of (a) silicon nitride blade on top, (b) silicon blade at the bottom and (c) both blades on the tip of the microprobe.

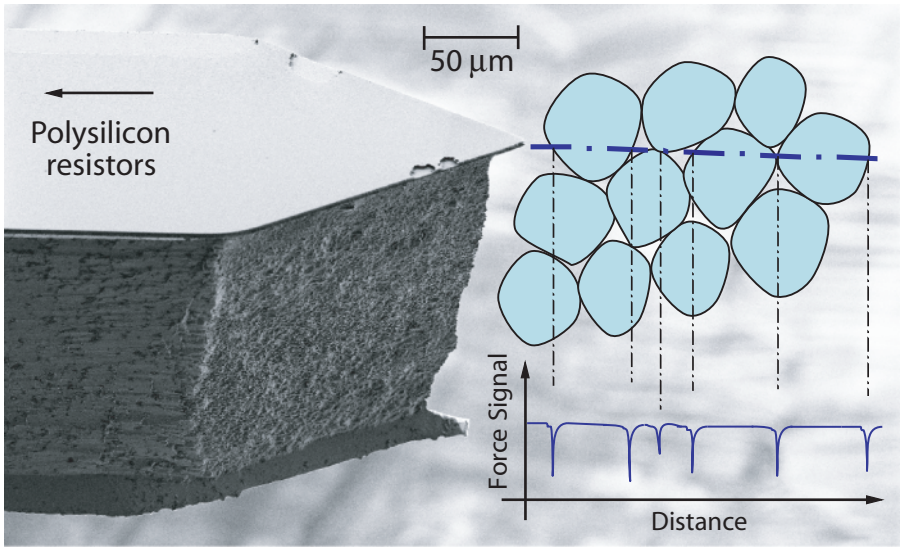

Figure 3.9: Sketch of the top blade (silicon nitride) on the microprobe tip penetrating the seminiferous tubules in the tissue and the expected force signal recording from the polysilicon resistors.

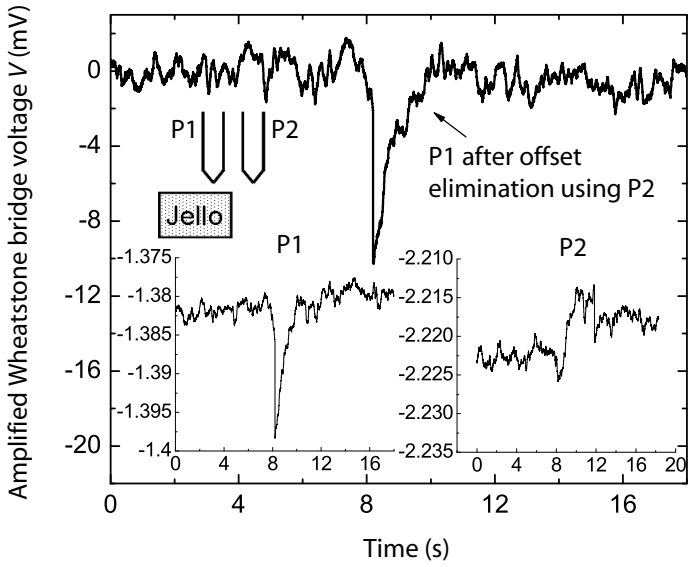

Figure 3.10: Offset elimination in signal of microprobe (P1) using the Wheatstone bridge offset of the 2^{nd} microprobe (P2), when probe P1 pierces a block of gelatin and the other does not.

backside-only KOH etch (Figure 3.8). When the top blade (silicon nitride) on the microprobe encounters the tubules, the strain experienced by the sense polysilicon resistors positioned on the microprobe near its clamped edge is due to a combination of pure-axial and bending-based compression of the microprobe. This compressive puncture force experienced by the top blade is recorded in the Wheatstone bridge voltage as voltage spikes (Figure 3.9). The bottom blade (silicon) when encountering tubules results in bending of the microprobe, and thus, in translating axial and tensile strain to the polysilicon resistors located on top of the device. From finite-element analysis, the force sensitivity of the bottom blade observed in the amplified Wheatstone bridge voltage was estimated to be 0.81 V/N. The microprobes are inserted into the tissue using a μ-manipulator with 0.2 μm precision (MP-285, Sutter Instruments, Inc.). The amplified Wheatstone bridge voltage is monitored which gives an estimate of the forces encountered by the microprobes using the force sensitivity of the microprobes (section 3.2).

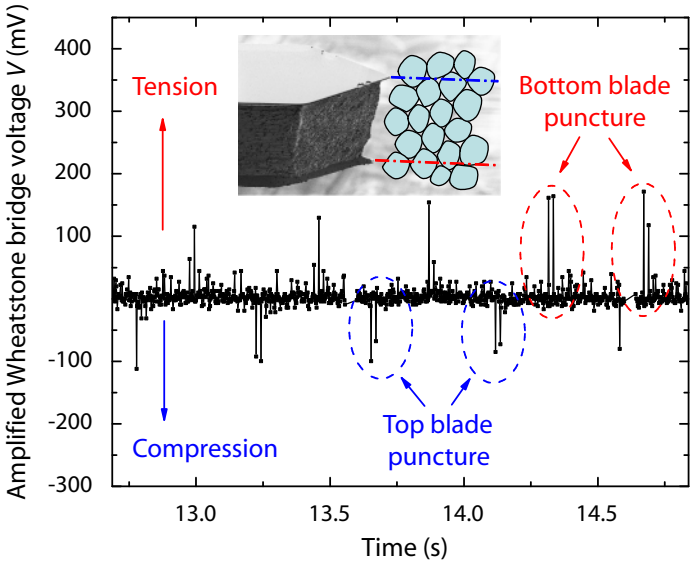

Figure 3.11: Detection of tubules (amplified Wheatstone bridge voltage versus time) in rat testis tissue by penetration with microprobe at a constant velocity of 100 μm/s. Cross-sectional sketch of microprobe penetrating the tubules is shown.

Since the two microprobes on the device are separated by a distance of 500 μm, the probability that both the microprobes will be cutting tubules at the same time is small. By monitoring the ratio of the Wheatstone bridge voltage in the two microprobes when both are not cutting tubules, the output voltage offset and drift of a microprobe when cutting a tubule can be eliminated in order to reduce noise, drift, loading etc. A controlled experiment was performed in which only one of the two probes was allowed to pierce a gelatin block. The offset of the probe piercing the gelatin (P1) was eliminated by using the recorded ratio of the offsets initially before penetration and the offset of the non-piercing probe P2 (Figure 3.10).

3.3.3 Proof-of-concept *in vitro* penetration experiments

The two microprobes were inserted *in vitro* to a depth of 2 mm into tissue excised from a healthy rat testis containing only seminiferous tubules at a velocity of 100

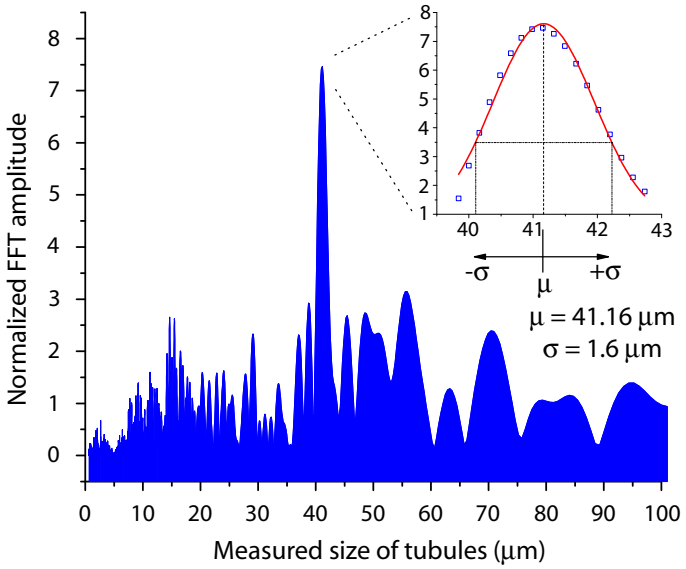

Figure 3.12: Normalized FFT amplitude of the time-domain force signal, with frequency modified to size of tubules measured by microprobe (x-axis), which is given by 100 μm/s$\times$[1/frequency].

μm/s. The bulk portion of the microprobe is intended to be thicker in order to be stiff enough to be used for penetrating the outer testicular muscle and connective tissue, and eventually reaching the seminiferous tubules. In addition, the thickness of the microprobe (140 μm) is chosen to be much larger than the diameter of the tubules in the tissue ($\approx$ 50 μm) so that the top and bottom blades encounter different tubules, thus increasing the number of tubules sampled per microprobe. Once inside the tissue, the blades on the microprobe puncture the tubules, and the puncture signature in the force signal is observed to be a negative spike (compression) for the top nitride blade and a positive spike (tension) for the bottom silicon blade (Figure 3.11). The puncture force can be calculated by measuring the magnitude of the spike due to the top nitride blade and dividing it by the estimated top-blade force sensitivity of the microprobe (-1.63 V/N). The range of voltage spike magnitudes in the Wheatstone bridge voltage suggests different kinds of punctures through tubules varying from maximum force when

puncturing along the diameter of the tubule to minimum force when seperating attached tubules.

Since the orientation and position of the tubular axis with respect to the path of puncture is random, the size measured by the microprobes can vary from a fraction to more than twice the diameter of the tubule. This measured size is calculated by multiplying the speed of puncture (100 μm/s) and the measured time between two consecutive puncture artifacts corresponding to the top nitride blade, since the tubules are densely packed wall-to-wall in the tissue. From the FFT (Fast-Fourier Transform) of the positive and negative spike data, we observe the maximum occurrence of a size measured corresponding to 41.1$\pm$1.6 μm (Figure 3.12). This was close to the visually measured average tubule diameter ($\approx$ 50 μm) in the tissue being probed. In order to detect the presence of tubules of two different diameters with different density of occurrence, it is crucial that we understand the distribution of sizes measured by the microprobe. Also, an analytical closed-form expression of the distrubution of sizes (discussed in the next section) would help determine, if statistically significant sizes are measured corresponding to the two different diameters, thus checking for false-positives.

3.3.4 Expected distribution of sizes measured using microprobe

Spermatogenesis occurs within a collection of U-shaped seminiferous tubules in the testis. The tubules are compartmentalized by connective tissue lobules in the testicular parenchyma. The tubules in each lobule are highly convoluted, closely packed and, start and end at the rete testis (Figure 3.6), which serves as the

reservoir for spermatozoa during ejaculation. If a constant volume of tissue is excised from the intralobular region at different locations of the testis (like in the TESE surgery), the orientation of the tubules found in the excised tissue is expected to be completely random. When the microprobe is inserted into a volume of testicular tissue containing only seminiferous tubules at a constant velocity and a fixed direction, the penetration of tubules by the blades on the microprobes will be in a uniformly random orientation with respect to the local axis of the tubule and at a uniformly random distance away from the axis. Assuming constant velocity of insertion and high sample set of sizes measured, the distribution of frequency of occurrence of path lengths traversed by the blade inside the tubules (the sizes measured by the microprobe) is derived here. Knowledge of the probability distribution of sizes measured by the microprobe when inserted in tissue is necessary to discern the existence of multiple populations of tubules with different diameters (in our case, thin and large diameters) in the testicular tissue being probed. For deriving an analytical expression for the expected distribution of sizes measured by the microprobes the framework is setup on the basis of a set of assumptions. In this section, the analytical expression is derived based on the assumptions made and finally the expression is verified by fitting the model to sizes measured by randomizing the orientation of the tubules using Monte Carlo simulations.

A. Assumptions

1. Tubules are assumed to be closely packed circular cylinders with a constant diameter (d). In the vicinity of the path of the microprobe, the cylinders are assumed to be right circular with a diameter much less than the thickness of the microprobe (140 μm).

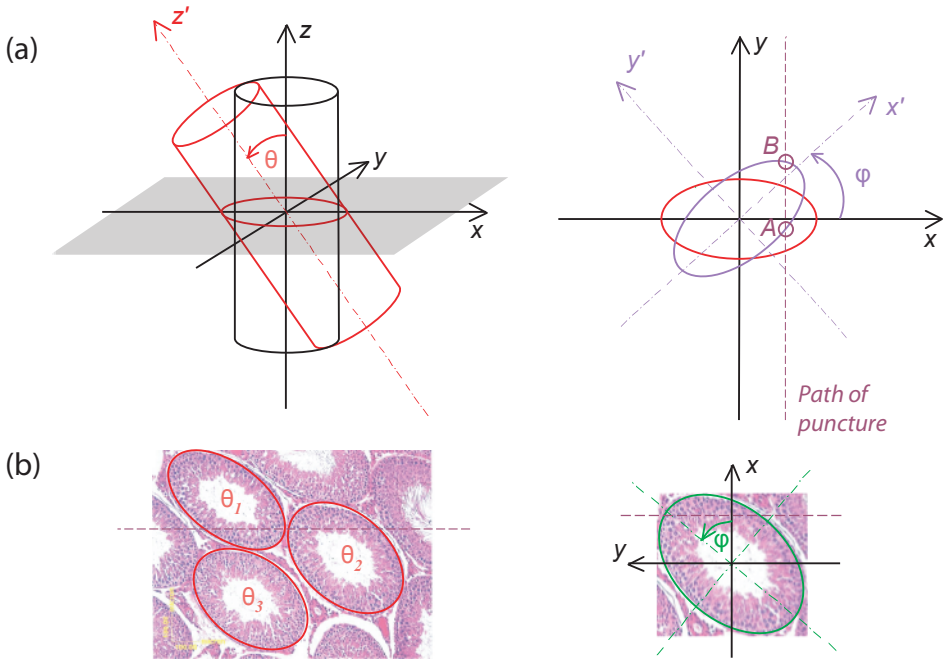

Figure 3.13: (a) Random orientation of tubule defined by angles θ and ϕ, being encountered by the microprobe (path of puncture of the blade) and size measured by microprobe = AB. (b) Histology slide of seminiferous tubules showing elliptical cross sections of the tubules and depiction of the path of puncture through the tubule.

2. Path of puncture is assumed to be a straight line with width and height (of the blade, in our case) much less than the diameter of the tubule. The puncture is assumed to be ideal with no compression artifact.

3. Penetration through successive cylindrical cross section of tubules is modeled by randomizing the orientation of the tubule and size measured by microprobe is quantified by measuring the length of the path of puncture inside the tubule.

B. Analytical expression

The analysis in this section has been adopted from Piefke [121], where chord length distribution of an ellipse is derived for different probability density of occurences

of the random variables considered. The size measured by the microprobe on penetration of a randomly oriented tubule is depicted as the length of the chord formed inside the tubule by the fixed path of penetration. In order to assume a randomly oriented right-circular cylinder, a cylinder with its axis in the z-direction is rotated by an angle θ about the z-axis. The cylinder is then further rotated such that its elliptical projection on the x-y plane is rotated by an angle ϕ (Figure 3.13a). The path of puncture is assumed to be a straight line parallel to the y-axis given by $x = p$. Histological cross sections of the tubules, obtained from microtome slicing of tissue and hematoxylin-eosin staining, reveals elliptical cross sections, and from the ratio of the minor and major axes, one can estimate the angle of orientation of the axis of the tubule with respect to the cutting plane (Figure 3.13b). The x-y plane can be assumed to be rotated by an angle ϕ with the axes along that of the ellipse formed by the projection of the cylinder. The path of puncture can be defined as a set of all straight lines G' such that

$$G' = \{(x, y);\ x \cdot cos\phi + y \cdot sin\phi = p\} \tag{3.1}$$

where $0 \leq \phi < 2\pi$, $0 \leq p$. To each line G there corresponds a point (p, ϕ, θ) in the parameter space such that

$$\Gamma = \left\{(p, \phi, \theta);\ 0 \leq p, 0 \leq \phi < 2\pi, -\frac{\pi}{2} < \theta < \frac{\pi}{2}\right\} \tag{3.2}$$

Let Q be the ellipse, G a random straight line, and $\Sigma(G)$ the length of the chord $Q \cap G$. We can define

$$H_\sigma = \{G \in G';\ \Sigma(G) \leq \sigma\} \tag{3.3}$$

for a given chord length $\sigma \geq 0$, and $\Gamma_\sigma = \Gamma(\mathrm{H}_\sigma)$. The probability distribution of the chord length Σ is described by the function $\mathrm{F}(\sigma) = \sigma(\mathrm{H}_\sigma)$. The probability

density function $f(\sigma)$ can be written as

$$f(\sigma) = \frac{d}{d\sigma} F(\sigma) \tag{3.4}$$

The probability distribution of the chord lengths F(σ) can be written as a function of the probability density of occurence $\rho(p, \phi, \theta)$

$$F(\sigma) = \int_{p} \int_{\theta} \int_{\phi} \rho(p, \phi, \theta)\, d\phi\, d\theta\, dp \tag{3.5}$$

Instead of integrating over p we wish to integrate over σ, the chord length of the line G defined by (p, ϕ)

$$F(\sigma) = \int_{0}^{\sigma} \iint_{K_{\sigma'}} \rho(p, \phi, \theta) \left| \frac{\partial p}{\partial \sigma'} \right| d\phi\, d\theta\, d\sigma' \tag{3.6}$$

where $K_{\sigma'}$ is the range of ϕ and θ values to which straight lines G with $\Sigma(G)$ $= \sigma'$ exist. Therefore

$$f(\sigma) = \iint_{K_{\sigma'}} \rho(p, \phi, \theta) \left| \frac{\partial p}{\partial \sigma} \right| d\phi\, d\theta \tag{3.7}$$

We need to quantify the probability density of occurence of p, ϕ and θ independently in order to find a closed form expression for $\rho(p, \phi, \theta)$. In our case, since the cylindrical tubule is randomly oriented, the angle ϕ in 3.1 can be assumed to be distributed uniformly over the range [0, 2π) for a given orientation of the axis of the cylinder θ. For a given angle ϕ, let $p_{max}(\phi)$ be the maximal value of p in 3.1 with $Q \cap G \neq \emptyset$; $p_{max}(\phi)$ is the p-value of the tangent. *Arithmetically* speaking, the value of p can be expected to be uniformly distributed over the range [0,$p_{max}(\phi)$). The angle of incision θ follows a uniform distribution of occurence. But the *geometric* probability distribution of occurence of θ, in order for an incision

to take place, is proportional to $\sin(\theta) \times \cos(\theta)$ [122, 123]: $\sin(\theta)$ dependence comes from the fact that as the angle of incision θ increases the probability of incision increases, and hence the probability density grows as $\sin(\theta)$ and, $\cos(\theta)$ dependence comes from the fact that as the angle of incision increases, the probability of number of tubules being cut decreases for a given length of incision in the tissue and hence the probability density is proportional $\cos(\theta)$. From the above, we can define the probability density of occurence $\rho(p, \phi, \theta)$ as

$$\rho(p, \phi, \theta) = \frac{\sin(\theta)\cos(\theta)}{p_{max}(\phi)} \tag{3.8}$$

The quantity $\rho(p, \phi, \theta)$ is not normalized and hence the probability density of chord lengths σ derived will need to be scaled by normalizing factor in order to get the conditional probability density. In order to quantify $\mathrm{p}_{max}(\phi)$ and $\left|\frac{\partial p}{\partial \sigma}\right|$ to solve 3.7, we define the ellipse Q to be

$$Q = \left\{ (x, y);\ \frac{x^2}{a^2} + \frac{y^2}{b^2} = 1 :\ b = \frac{d}{2},\ a = \frac{d}{2\cos(\theta)} \right\} \tag{3.9}$$

where $0 < b \leq a$ (without loss of generality) and d is the diameter of the tubule. The length of the chord σ formed by the intersection of the straight line 3.1 and the ellipse 3.9 can be calculated to be

$$\sigma = \frac{2ab}{A}\sqrt{A - p^2} \tag{3.10}$$

where $A = a^2(1 - sin^2(\theta)sin^2(\phi)) = p^2_{max}(\phi)$. From 3.10 we can write

$$\left|\frac{\partial p}{\partial \sigma}\right| = \frac{A^2\sigma}{(2ab)^2\sqrt{A - \left(\frac{A\sigma}{2ab}\right)^2}} \tag{3.11}$$

In order to evaluate 3.7 we need to determine K_σ. The chord length is maximal if $p = 0$ in 3.10. Hence, the maximal chord length for a given ϕ and θ is

$$\sigma_{max}(\phi) = \frac{2b}{\sqrt{1 - sin^2(\theta)sin^2(\phi)}} \tag{3.12}$$

Let ϕ and θ be fixed. Straight lines G with $\Sigma(G) = \sigma$ exist if and only if $\sigma \leq \sigma_{max}(\phi)$. Therefore $K_{\sigma'}$ can be proven to be

$$K_{\sigma'} = \begin{cases} \theta \in \left[\frac{-\pi}{2}, \frac{\pi}{2}\right];\ \phi \in [0, 2\pi) & \text{if } \sigma \leq 2b \\ \theta \in [\theta_0, \pi - \theta_0] \cup [\pi + \theta_0, 2\pi - \theta_0]; & \\ \phi \in [\phi_0, \pi - \phi_0] \cup [\pi + \phi_0, 2\pi - \phi_0] & \text{if } 2b < \sigma \leq 2a \\ \emptyset & \text{if } 2a < \sigma \end{cases} \tag{3.13}$$

with

$$\theta_0 = \arccos\left(\frac{2b}{\sigma}\right);\ \phi_0 = \arcsin\left(\frac{\sqrt{\sigma^2 - (2b)^2}}{\sigma \sin(\theta)}\right) \tag{3.14}$$

By substituting 3.8, 3.11 and 3.13, in the integral 3.7, we can write the analytical expression for the probability distribution for a measured size (σ) and fixed tubule diameter (d) as

$$f(\sigma) = \int_{\theta_o}^{\frac{\pi}{2}} \sin\theta \cos\theta \left(\frac{8\sigma}{\pi d^2} \int_{\phi_o}^{\frac{\pi}{2}} \sqrt{\frac{\left(1 - \left(\sin\theta \sin\phi\right)^2\right)^2}{1 - \left(\frac{\sigma}{d}\right)^2 \left(1 - \left(\sin\theta \sin\varphi\right)^2\right)}} \cdot d\phi \right) \cdot d\theta \tag{3.15}$$

where we define $\theta_0 = 0$ and $\phi_0 = 0$ for $\sigma \leq d$. The probability density function $f(\sigma)$ needs to be scaled by a normalizing factor in order to calculate the conditional probability density function.

C. Monte Carlo simulations

Monte Carlo simulations of sizes measured using the microprobe were done in MATLAB^{TM} by assuming random orientation of tubules of diameter $d = 100$ μm and measuring the chord lengths made by the path of puncture of the microprobe. The angle ϕ and p are assumed to be uniformly distributed between the limits

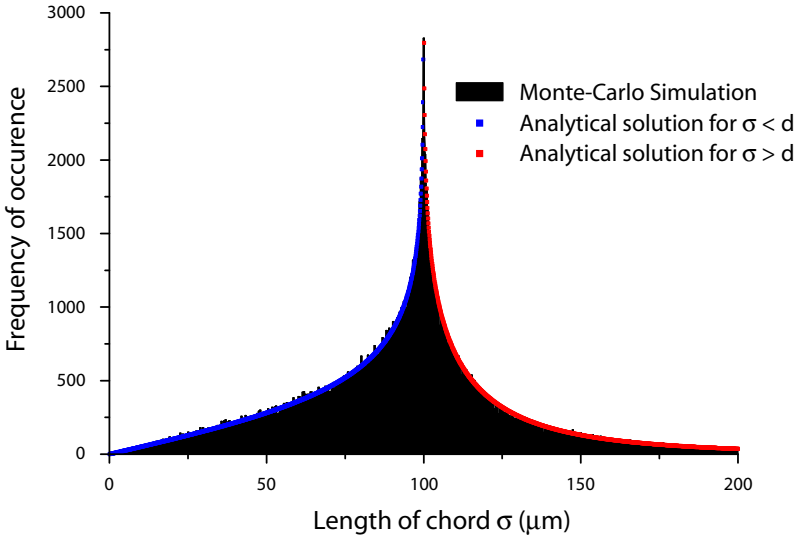

Figure 3.14: Binning of simulated (Monte Carlo) sizes measured by microprobe assuming the presence of thin tubules with diameter $d = 100$ μm. A scaled version of the probability density function (Eq. 3.15) is also plotted for $\sigma < d$ and $\sigma > d$.

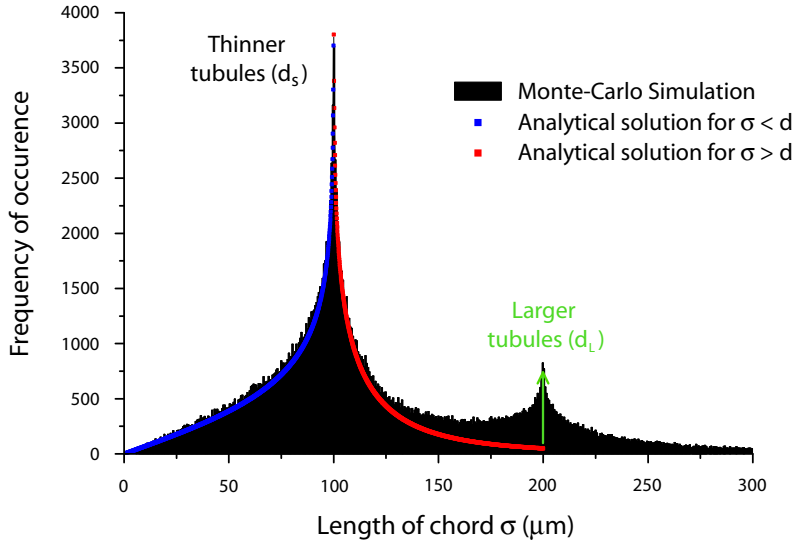

Figure 3.15: Binning of simulated (Monte Carlo) sizes measured by microprobe assuming the presence of mostly thinner ($d_S = 100$ μm) and few larger ($d_L = 200$ μm) tubules. Observed frequency of occurrence being greater than the analytically expected value (corresponding to the thinner tubule diameter) at $\sigma = d_L$ helps validate the presence of larger tubules.

[0,2π) and [0,$p_{max}(\phi)$), respectively. The incision angle θ is imposed with a probability distribution of $\sin(\theta) \times \cos(\theta)$ (geometric probability of occurrence) after generating uniformly distributed angles θ. The generated chord lengths (σ) are binned, and a histogram predicting the frequency of occurence of varied sizes measured (σ) is plotted (see Figure 3.14). The maximum frequency of occurence was seen to be at $\sigma = d$, diameter of the tubules. The histogram is essentially a non-normalized version of the probability density function (PDF) of the chord length σ. The probability density function$f(\sigma)$ from Eq. 3.15 when scaled and plotted along with the histogram proved to be a good fit (Figure 3.14).

In the practical scenario, the surgeon needs to be able to detect the presence of larger diameter tubules embedded within a mass of thinner diameter tubules. Knowledge about the probability distribution of measured sizes assuming an average diameter of tubules in the region of interest will help the surgeon detect the presence of larger fertile tubules embedded in the mass of thinner infertile tubules. Assuming a large set of sizes measured by probing multiple locations in a region of interest, if the tissue contains few larger tubules embedded in a mass of thinner tubules, then two peaks corresponding to the diameter of the thinner and larger tubules are expected when the measured sizes are binned. The peak for the thinner tubules is higher in magnitude than that of the larger tubules because of fewer large tubules. Two Monte Carlo simulations were performed with two different diameters, $d_S = 100$ and $d_L = 200$ μm, and the resulting chord lengths were plotted in a single histogram in Fig. 3.15. The frequency of occurrence of size equal to $d_L = 200$ m was intentionally adjusted to be only a fraction of that of $d_S = 100$ μm for purely illustrational purposes. If the observed frequency of occurrence at measured size equal to the larger tubule diameter (i.e., $\sigma = d_L$) is greater than the value calculated by using the scaled analytical expression of

the probability distribution function in Eq. 3.15 corresponding to the thinner tubule diameter (i.e., $f(d_S, \sigma = d_L)$), then the presence of larger tubules in the tissue is confirmed (Fig. 3.15). Thus, by sufficient sampling of tubules by the microprobe in a given region of interest, the surgeon can identify the presence of healthy tubules by using the analytical expression for the probability density of occurrence of measured sizes. To further validate the presence of larger tubules, the analytical expression in Eq. 3.15 for probability distribution of measured sizes corresponding to thinner and larger tubules (i.e. $f(d_S, \sigma) + f(d_L, \sigma)$) can be used to fit the frequency of occurrence of measured sizes.

3.3.5 Statistically significant microprobe metrology

In the ideal scenario, the analytical model for the expected probability distribution of sizes measured by the microprobes derived in the previous section will fit the data well if we have a large enough sample set, thus allowing for large histogram bin frequencies and small bin widths emulating a continuous curve. But practically speaking, given the limited probe insertion length and number of insertions, the surgeon will only be able to sample a finite number of sizes at a given location and, will need to discern the presence of larger diameter sperm-carrying tubules. Thus, a threshold sample size of measured-sizes needs to be determined, above which statistically significant determination of the average tubule diameter in the testicular tissue is possible. Knowledge of the threshold size will serve as an indicator to help the surgeon determine the minimum number of probe insertions required in a region of interest, to determine the presence of larger fertile tubules and make an informed decision about tissue excision. In this section, the distribution of experimentally measured sizes by the microprobes in the testicles

of a rat are described. Histological and morphological analysis of the seminiferous tubules is done to validate the experimental results. A new metric is presented for comparing the distribution of finite number of measured sizes by the microprobes to the analytical model, to determine the diameter of the tubules in the region of interest. An algorithm is described to automate this process for the surgeon to determine the presence of larger tubules in a region of interest in real-time during surgery.

A. Distribution of experimentally measured sizes by microprobes

A 60-week old adult male rat (Sprague-Dawley) is euthanized by the use of CO_2 inhalation. Both the testes are delivered by making a small incision ($\approx$ 1 cm) at the lower part of the organ. The outer layers of the testes are carefully dissected till the last layer (tunica albuginea) is intact (see Fig. 3.6), which holds the seminiferous tubules arranged in lobules intact. Once dissected the testes are immersed in PBS solution until the experiment is performed. The microprobes attached to the micro-manipulator is programmed using LabView to move a constant distance of 3 mm at a speed of 200 μm/s, and data is recorded at 2 kHz. In order to increase the sensitivity to tubules, the circuit described previously in this chapter is re-designed by modulating the bias voltage (V_{bias}, Fig. 3.3) by a 200 mV_{pp} 1 kHz sinusoidal signal, thus amplitude modulating (AM) the sensed strain signal in the Wheatstone bridge. Also, the microprobes used in the experiments were thinner (70 μm thick) compared to that described in section 3.2 in order to increase the probability of tubule penetration. The strain signal is amplified (G = 1000) and AM-demodulated using the sinusoidal signal. The demodulated signal is amplified again by a factor of 100. The overall increase in sensitivity using the new circuit is $\approx$ 1000 fold higher than the previous design. Due to the high strain sensitivity of

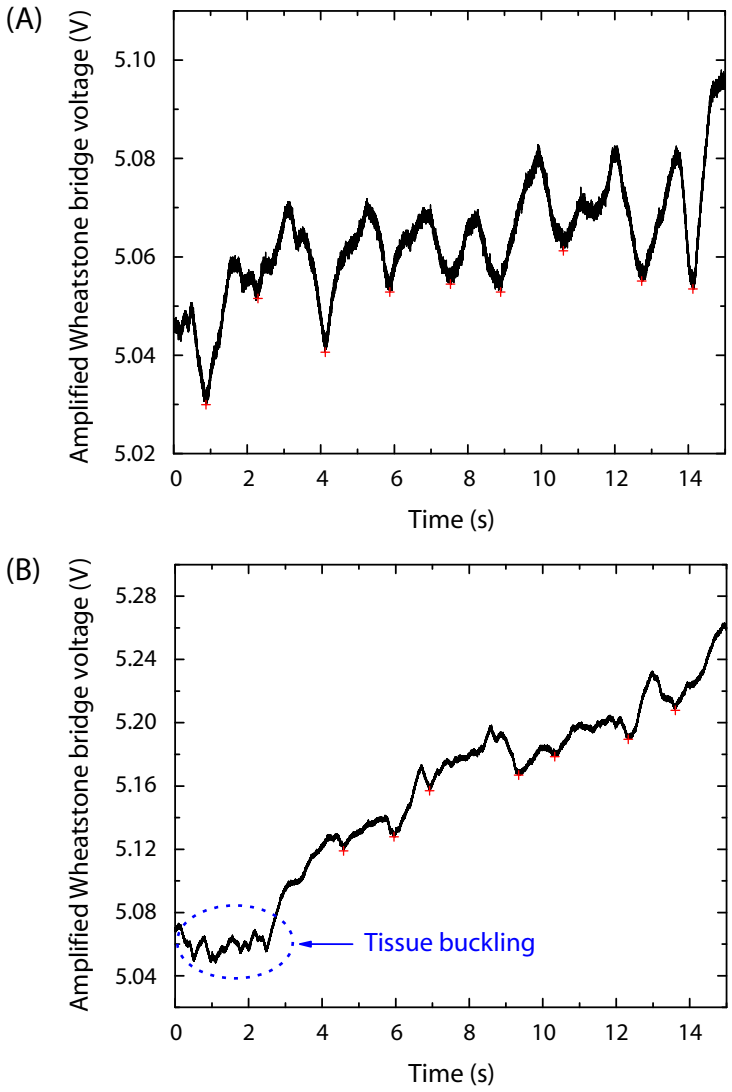

Figure 3.16: Strain signal from Wheatstone bridge depicting tubule puncture events (red crosses) during microprobe insertion into rat testis at a constant velocity of 200 μm/s for a depth of 3 mm. Two insertion experiment results are shown with (A) minimal and (B) substantial tissue buckling.

the circuit and the top blade, the compression signals from the top nitride blades (decrease in signal, Fig. 3.11) were predominant, and hence considered for size measurement. Before performing the microprobe insertion experiment, a small incision is made on the tunica albuginea of the whole intact testis exposing the seminiferous tubules underneath. Control measurements were done by recording the strain gauge signal for 5 seconds with the microprobes in air and in contact with tubules.

The microprobe insertion experiment is performed starting with the microprobe in contact with the seminiferous tubules. Once inside the tissue, the microprobes encounter and puncture through tubules as seen from the compression signatures in the signal in Figure 3.16. Since the insertion experiments are done on an intact testis by making a small incision on the outside, depending on the orientation of the exposed tissue with respect to the microprobes at times the tissue buckles and the signal is seen to have a steady increase/decrease due to the drag force of the tissue on the microprobes (Fig. 3.16B). When the orientation of the tissue is favorable, the puncture events are clean and easily identifiable (Fig. 3.16A). Irrespective of the orientation of the tissue, tubule puncture events are detected and the size measured is calculated by multiplying the speed of the microprobes (200 μm/s) to the time delay between 2 puncture events. 3 to 5 insertion experiments were done in multiple regions with local incisions made before microprobe entry. For every microprobe insertion experiment, 4 sizes were measured on an average. Experiments done on the testes tissue of 2 rats from the same litter were analyzed, and the size of the sample sets of measured sizes were N = 75 and 37. In order to appropriately bin the measured sizes (as part of a histogram) and to determine the bin corresponding to maximum occurring sizes, a MATLAB^{TM} code was written to choose the appropriate bin centers with the highest peak frequency, assuming

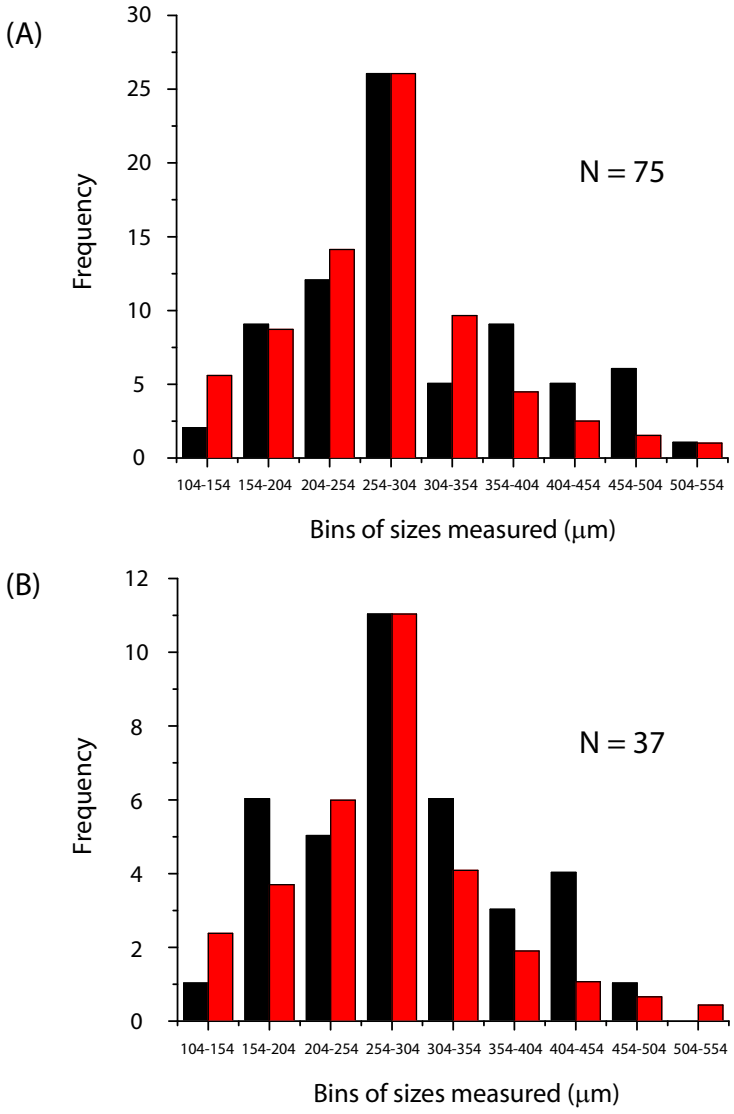

Figure 3.17: Histogram with experimentally measured sizes binned (black) using the optimized bin-center configuration, and the scaled histogram corresponding to the analytical probability density distribution (red) with diameter = 279 μm for (A) N = 75 and (B) N = 37.

the bin width to be constant and equal to 50 μm. The bin center corresponding to the maximum occurring peak is 279 μm for N = 75. Figure 3.17 shows the histogram corresponding to the two experiments along with the analytical fit integrated within the limits of the bins of the histogram and scaled to the highest occurring frequency in the histogram. The diameter of the tubules is assumed to be constant and equal to the bin center corresponding to the the maximum occurring frequency i.e. 279 μm. Since the sample size of measured sizes is limited, it can be observed that the experimental histogram follows the trend of the analytical model, but does not match up to it quite as well as the Monte Carlo simulations in Figure 3.14.

B. Area-Ratio metric

In order to establish a figure-of-merit given a sample size of measured-sizes by microprobes in an insertion experiment, an area-based metric is introduced. The ratio of the area under the histograms (using the trapezoidal rule) of the experimental data and the analytical fit scaled to the peak of the histogram is used. The basic idea behind the metric is to identify situations where the area-ratio is higher than that compared to when only smaller tubules present in the region, due to the presence of a second peak corresponding to a bin with a numerically higher bin center (i.e. corresponding to a larger tubule diameter). In order to use this metric after the sizes are measured and binned, the analytical fit for the probability distribution of measured sizes (Eq. 3.15) is integrated within the limits of the bins corresponding to the optimized bin center configuration, and scaled to the peak of the experimental histogram. Monte Carlo simulations (100 iterations) were performed to generate measured sizes at increasing sample sets of measured-sizes. Figure 3.18 shows the histogram of the Monte Carlo simulated sizes and the

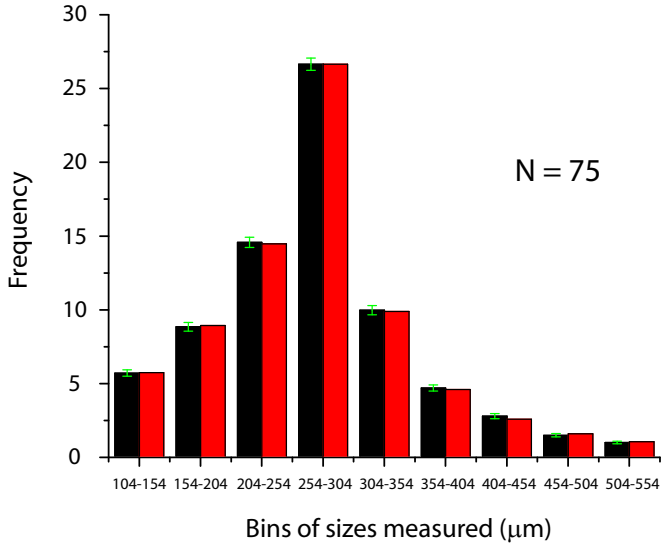

Figure 3.18: Histogram of Monte Carlo simulated measured sizes binned (black) using the optimized bin-center configuration, and the scaled analytical fit (red) with diameter = 279 μm for sample size of N = 75.

scaled analytical fit at N = 75, with binning performed using the optimized bin size corresponding to the experimental data for N = 75 (Fig. 3.17). By comparing the experimental and simulated histograms for N = 75, it can be observed that the values of the maximum peak are very close indicating that the sizes sampled by the microprobes are in accordance with the analytical model.

For a given testis once insertion experiments are performed in a few regions of interest, from the above analysis the size of the smaller tubules can be estimated and the corresponding optimized binning configuration is established. With this as the basis, when the surgeon performs microprobe metrology on a region of interest with larger tubules (say, 425 μm), the Area-Ratio metric should increase because of the presence of a relatively higher peak corresponding to the larger tubule size. In order to make a quantitative estimate of the concentration of larger tubules in the region of interest, Monte Carlo simulations were performed at different sample sizes (N = 0 to 200, 100 iterations each) for 3 cases where a) 50%, b) 75% and

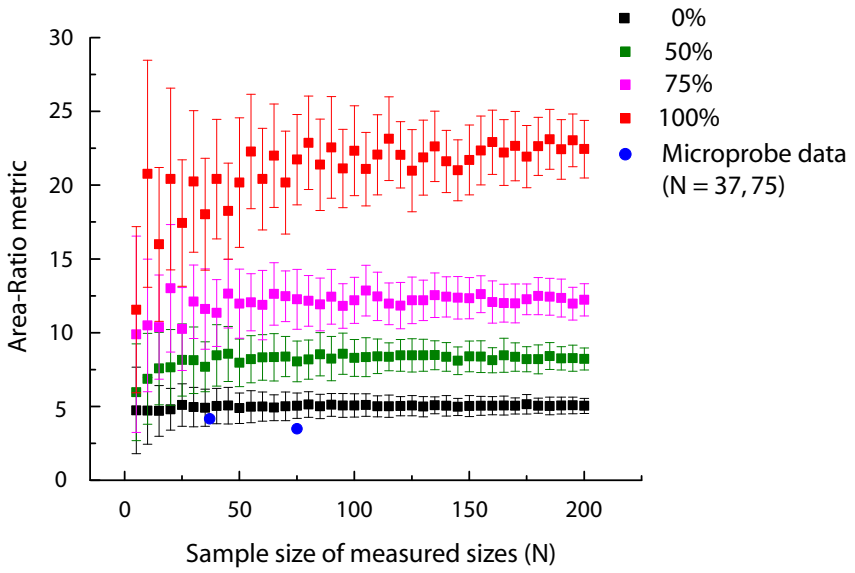

Figure 3.19: Area-Ratio metric plotted for Monte Carlo simulated measured sizes at varying sample sizes (N) corresponding to increasing percentages (0, 50, 75 and 100 %) of larger tubules sampled by the microprobes. The experimentally measured sizes for N = 37, 75 are also plotted on the curve for comparison.

c)100% of the sizes sampled were from the larger tubules (D = 425 μm). Figure 3.19 shows the plot of the Area-Ratio metric (error bar = 3σ, 100 iterations) corresponding to the varying percentage of larger tubules sampled for different sample sizes. The experimentally measured sizes by the microprobe at N = 37 and 75 can be observed to be very close to the simulated value, thus validating the Area-Ratio metric. To further illustrate the data at N = 75, the Area-Ratio metric using the simulated data is plotted against the percentage of larger tubules sampled and the corresponding histograms (using the optimized bin center configuration) of the simulated and analytical fit at 0, 25, 50, 75 and 100% (Figure 3.20). Also, the experimentally measured data using the microprobes at 0% is shown illustrating good correlation to the analytical model. From this illustration, it can be observed that as the percentage of larger tubules sampled is increased, the frequency in the bin corresponding to the larger tubule size increases and hence, the Area-Ratio

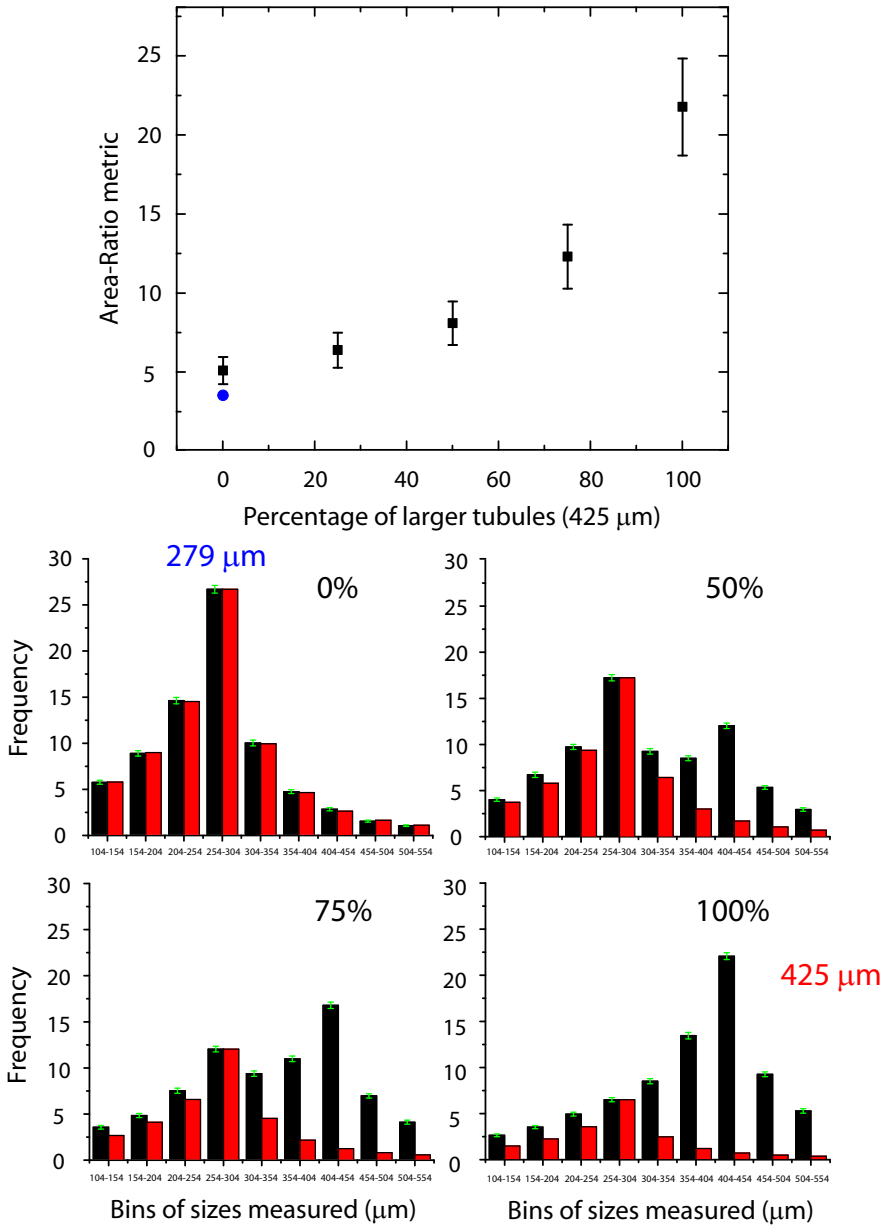

Figure 3.20: Top: Area-Ratio metric plotted for Monte Carlo simulated measured sizes at a sample size of N = 75 corresponding to increasing percentages (0, 25, 50, 75 and 100%) of larger tubules sampled by the microprobes. The metric corresponding to experimentally measured sizes for N = 75 is also plotted on the curve (blue circle). Bottom: Frequency histograms of Monte Carlo simulated and analytically estimated sizes corresponding to 0, 50, 75 and 100% is plotted.

metric is observed to increase. Based on the simulated data, the Area-Ratio metric for percentages between 0 to 25% and 25% to 50% are not significantly different from each other and hence, are indistinguishable. Nevertheless, an increase in percentage from 0 to 50% can be sensed. Once the Area-Ratio metric is simulated and calculated based on the size of the smaller tubule diameter and compared with the experimentally measured data, the surgeon can discern whether or not the present location is a region of interest. The final step would be to find the top two highest peaks in the histogram, which should correspond to the smaller and larger tubule diameters. By using the above metric tubule diameters can be estimated within 50 μm, which is well suited for microdissection TESE surgery where the difference between smaller infertile and larger fertile tubule diameters is known to be above 100 μm [124].

C. Histology of seminiferous tubules

The diameter of seminiferous tubules in a given volume of testicular tissue can be determined by means of morphological analysis of histological cross sections of the tissue. Since the tubules oriented in random directions in the tissue, are cut in a plane along the direction of motion of the microtome blade, the minor-axis length of the elliptical cross section of the tubules is equal to the diameter of the tubule [125]. Histology offers a two-dimensional view of the tissue cross section, thus making it easy to estimate the tubule diameter in the testicular tissue. After the microprobe insertion experiments, a small amount of tissue is excised from the lobule of the rat testis and fixed in modified Davidson's fluid (13.3% Ethyl Alcohol, 6.3% Acetic acid, 13.9% of 37% Formalin and 66.5% DI Water) [126]. After 3 days of fixation, the tissue was washed and embedded in a paraffin block. A total of 25 sections were made in the tissue using a microtome acquiring 1 slide every 50 μm,

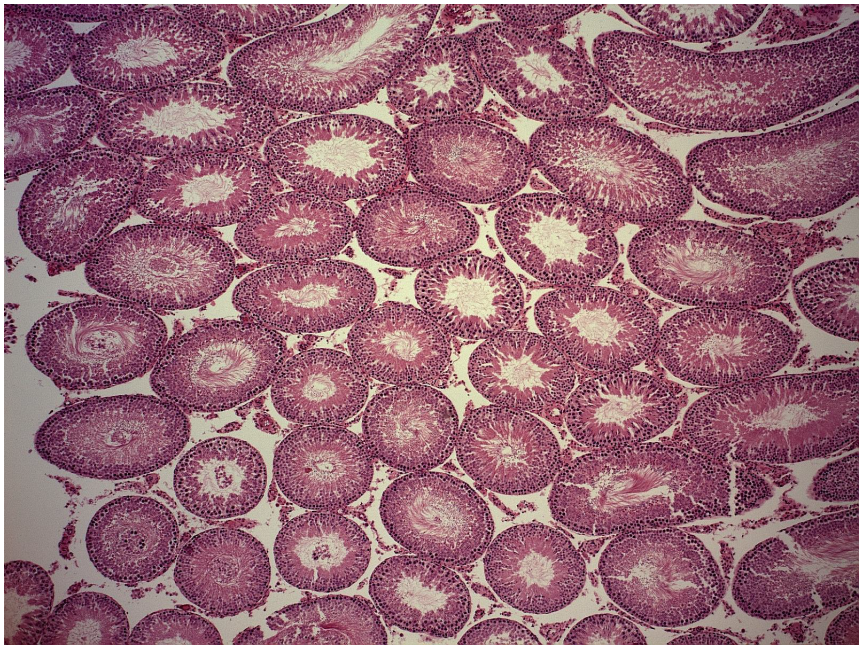

Figure 3.21: Hematoxylin and eosin stained slide of a 60-week old adult rat's lobular testis tissue fixed in modified Davidson's fluid, with elliptical cross-sections of the seminiferous tubules.

and hematoxylin and eosin staining was performed to visualize the tubule cross-sections. The slides were optically observed under a microscope and images were acquired using Microfire-C^{TM} camera (1600 $\times$ 1200 pixels, 1.85 μm/pixel) at 4X magnification (Fig. 3.21). In order to extract the minor diameter of the elliptical cross-sections observed in the slides, a segmentation-based algorithm was employed to capture the outline of the elliptical shapes (see Appendix C). Because of the presence of cells inside the elliptical cross-sections, for the sake of computation efficiency the region of interest is selected and cropped out of the image and the inside and outside of the ellipse was specified by free-hand sketch on the image (Fig. 3.22). After the segmentation is performed the outline of the ellipse is obtained and, the minor diameter was determined by fitting the outline to the general algebraic expression of an ellipse. With the help of this algorithm, the experimental data and the simulation-based Area-Ratio metric to estimate the

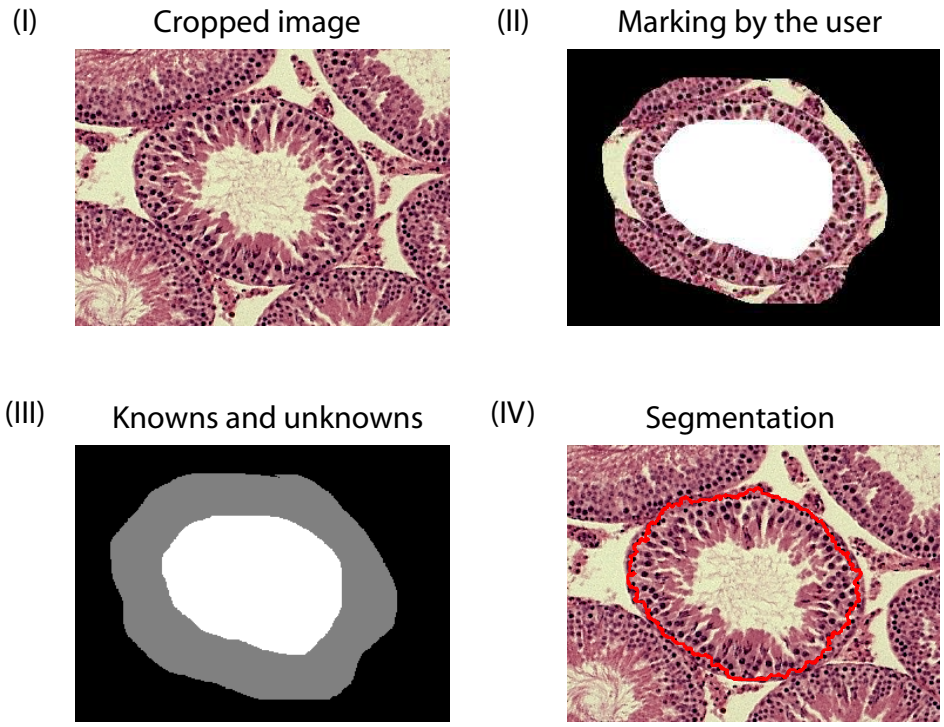

Figure 3.22: Demonstration of the segmentation algorithm in the following order - (I) crop image, (II) mark inside and outside of elliptical cross-section, (III) determining the knowns and unknowns of system, and (IV) segmentation of the image.

diameter of the tubules were validated by verifying the actual tubule diameter through histology. For the rat corresponding to a sample size N = 37 and 75, the diameter was measured to be 283.92±1.48 μm (N = 432) and 287.77±1.28 μm (N = 265) respectively. For both the experiments the optimized bin centers are very close to the histologically verified tubule diameters, hence by post-processing of the measured sizes, the analytical model and the Area-Ratio metric are validated.

3.3.6 Haptic interface and software development

The main essence of the work described in this chapter is that, by monitoring the tissue reaction force experienced by the microprobes when inserted into the testis, the surgeon can estimate the diameter of the seminiferous tubules in a three-dimensional volume beyond the field of view without tissue biopsy. This allows the surgeon to identify a region of interest (three-dimensional volume) in the testis which has a high probability of containing fertile sperm for ICSI. The microprobe when penetrating the tubules at a constant velocity provides a one-dimensional map of the tubules in the tissue, necessitating multiple insertions to be performed in a region of interest in order to estimate the average diameter of seminiferous tubules (highest occurring measured size) in a given volume of testicular tissue. In order to add a real-time dimension to the measurement, a joystick-based haptic interface was developed for the surgeon to be able to sense the microprobes penetrating the tubules in real-time.

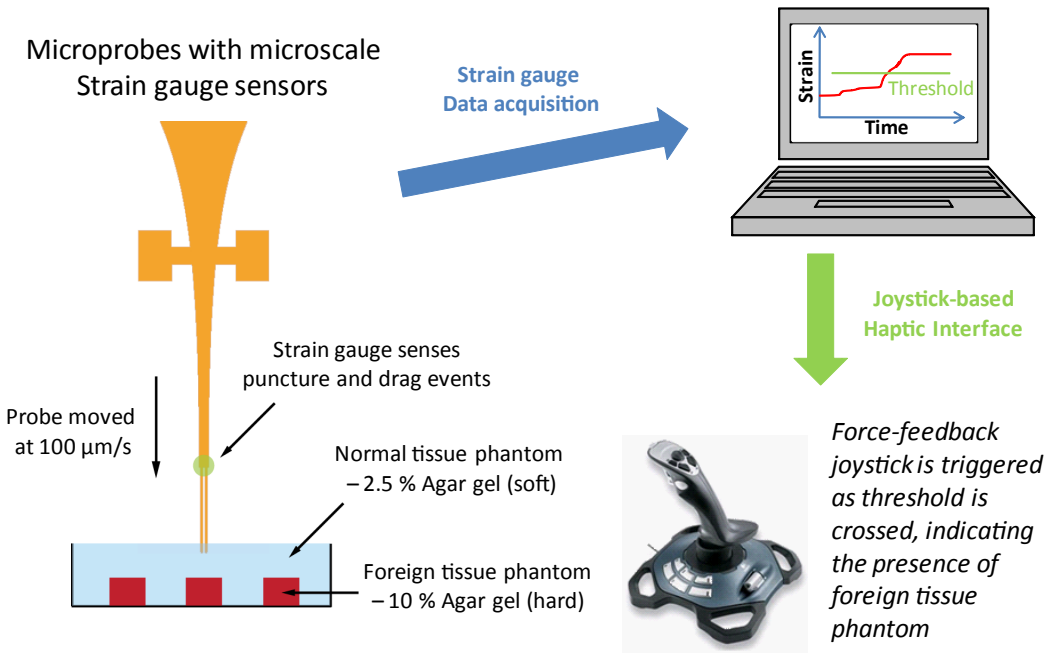

Figure 3.23: Microprobes with strain gauge sensors are penetrated into soft phantom tissue (2.5% agar gel) with relatively harder foreign phantom tissue (10% agar gel). The strain gauge data is acquired, analyzed and the joystick-based force feedback event is triggered when the strain signal crosses the threshold indicating the microprobes encoutering foreign tissue.

A. Framework of haptic interface

The haptic interface requires the microprobes to be moved by the micromanipulator, data from the strain gauge to be acquired, processed, plotted and the joystick (force-feedback) trigger events initiated in real-time. In order to achieve this a C++ based Windows software application was developed in Microsoft Visual Studio^{TM} (see Appendix D). A Labview^{TM} program was written to move the microprobes using a μmanipulator (MP285, WPI, Inc.) and corresponding header (Manipulator.h) and library (Manipulator.lib) files were compiled for interfacing in MS Visual studio. The output voltage from the Wheatstone bridge circuit corresponding to the strain gauge on the microprobe, is recorded using a NI USB-6251 (National Instruments, Inc.) data acquisition board at a sampling rate of 2 kHz. National Instruments DAQmx ANSI C development toolbox header files were included and predefined functions were used to set the data acquisition parameters and acquire data from the DAQ board. The strain gauge data is plotted in a separate window, the layout of which is programmed using National Instruments LabWindows CVI software and interfaced to the application being developed using header (myuir.h) and object (cbacks.obj) files. The strain gauge data is analyzed and the force feedback is triggered using a Logitech^{TM} Force 3D Pro joystick. DirectX programming (Microsoft Platform SDK) was used to interface with the joystick and trigger the force feedback events.

B. Preliminary experiments

The haptic interface and software was tested and proved by performing penetration experiments in phantom tissue samples (Fig. 3.23). The microprobes were inserted into soft tissue phantom (2.5% agar gel) with relatively harder phantom tissue (10%

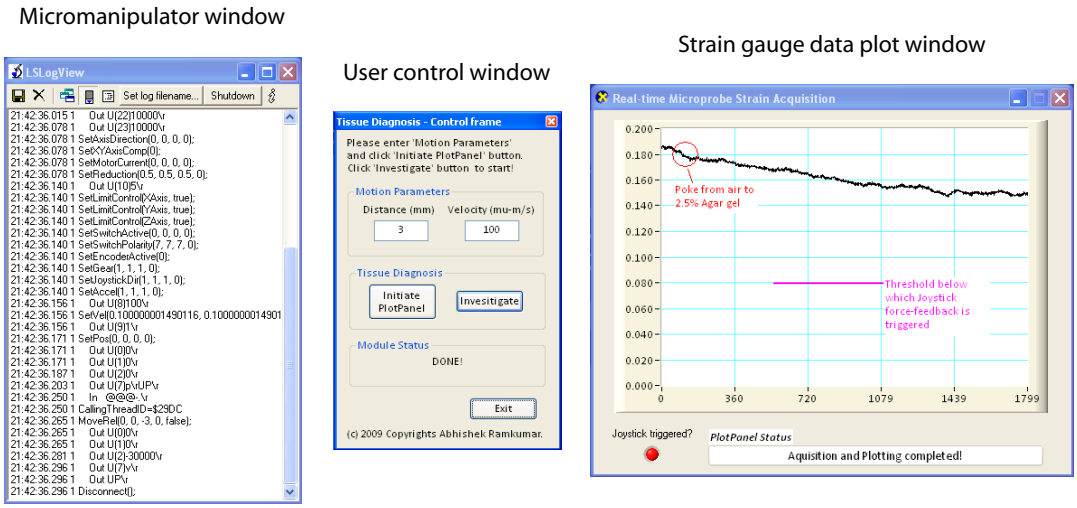

Figure 3.24: Software interface after the microprobes are inserted into soft phantom tissue (2.5% agar gel) with no hard foreign phantom tissue inside.

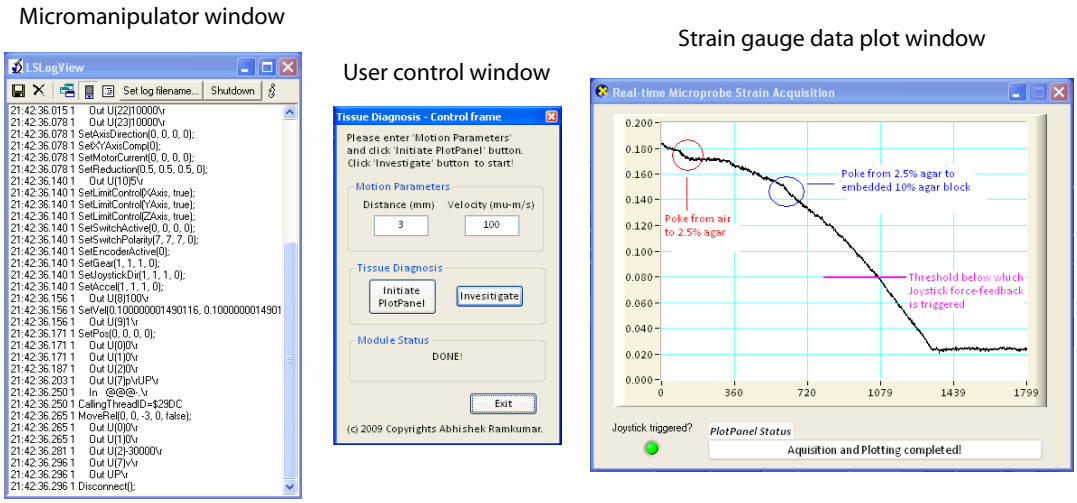

Figure 3.25: Software interface after the microprobes are inserted into soft phantom tissue (2.5% agar gel) with relatively hard foreign phantom tissue (10% agar gel) inside beneath the penetration site.

agar gel blocks) embedded inside. When the software is executed, the microprobes are inserted into the tissue by the micromanipulator and the strain gauge data is recorded, plotted and compared to a pre-determined threshold, in order to discern the presence of harder phantom tissue beneath the penetration site. Three main windows are displayed when the software is executed - micromanipulator status window, user control window to specify the motion parameters and run the experiment, and strain gauge data plot window. Figure 3.24 shows the software interface and the Wheatstone bridge output data when the microprobes are inserted into the soft phantom tissue with no hard phantom tissue underneath. As the microprobe is inserted into the soft tissue phantom the strain gauge senses drag forces experienced by the microprobe, hence the output voltage is seen to decrease steadily. When the microprobe is inserted into the soft tissue phantom with the harder phantom tissue underneath, the output voltage shows a clear inflection as the microprobe encounters the harder phantom tissue (Fig. 3.25). When the output voltage falls below the pre-determined threshold voltage (80 mV), the force-feedback on the joystick is triggered and the initiation is also indicated by a LED on the strain gauge plot window. Also, as the microprobe is inserted into the harder phantom the rate of decrease in output voltage due to the drag forces experienced is significantly higher, indicating a change in phantom tissue consistency. This rate of decrease of output voltage can be quantified and can be used as a figure of merit for measuring tissue consistency.

3.3.7 Conclusions and future work

In this work, a micromachined silicon ultrasonic microprobe with integrated force sensor and micro-blades is developed, and its potential for in-vitro microscale

tissue characterization has been demonstrated. The horn shape of the device in conjunction with the ultrasonic actuator helps in reducing tissue damage during incision. The force signal output recorded during insertion of the microprobe in rat testis tissue is used to estimate the diameter of the tubules in the tissue. This information is important for the surgeon to distinguish between tubules with (larger diameter) and without (smaller diameter) fertile sperm during Microdissection TESE surgery, enabling a microprobe-based assay for sperm viability. We propose the following future work to be done in order to assert the device's clinical relevance and reliability -

A. Rat study

The purpose of this study is to determine the feasibility of using microprobes to determine the stiffness of seminiferous tubules encountered and to estimate the diameter of the tubules encountered when inserted into a lobule of the testis of large number of rats. We propose two experiments to determine the viability of using microfabricated silicon microprobes for mechanical and spatial characterization of the seminiferous tubules in rodent testis tissue.

Experiment no. 1

Aim: To verify the viability of microprobes to monitor the increase in diameter of seminiferous tubules in testis tissue of rats with age.

Description of Pilot study: The increase in diameter and cell wall thickness (in our case, qualitatively measured as stiffness) of seminiferous tubules of the rat testis during postnatal development and ageing has been well studied [127, 128]. In this experiment, the intent is to verify the increase in tubule diameter and cell wall

thickness with age to that measured by the microprobes.

Control group - Four animals from each age group (5, 30 and 90 days) are euthanized and their testes excised. The entire testes are fixed and diced into blocks about 2 mm on a side. The histology of 5 μm microtome slices of tissue blocks are done using haematoxylin and eosin staining. The tubular diameter and wall thickess are obtained through image analysis of histological sections by using segmentation-based morphometry analysis (see Appendix C).

Experiment group - Four animals from each age group (5, 30 and 90 days) are euthanized and their testes excised. Multiple microprobe insertion experiments are performed in the testes to maximize the use of the organs, and the diameter of the tubules is estimated. Histology of two tissue blocks per testis is done in order to confirm that there is no gross variation in tubule diameter compared to the control group. The results from the control and experiment group are plotted against the age and the statistically viability of the microprobes is determined.

Experiment no. 2

Aim: To verify the viability of the microprobes to assess spermatozoa production in rats by detection of shrinkage of diameter of tubules by administering a drug called EDS (Ethane dimethane sulfonate).

Description of Pilot study: By administering Ethane dimethane sulfonate (EDS; kills Leydig cells), spermatozoa count, and therefore the diameter of seminiferous tubules decreases after 14 days [129, 130]. Subsequently (6 weeks later), spermatozoa production restarts and the diameter of tubules increases to the normal value. In this experiment, we intend to verify the variation in tubule diameter due to the drugs using our microprobes to assess the viability of detecting

drug-induced changes in tubule diameter.

Control group - Sixteen animals are given a single intraperitoneal injection of 2 ml normal saline at day 0 of the experiment to serve as the control group.

1. Four animals are euthanized and their testes excised at days 0 and 60 of the experiment respectively. Histology and morphometry of the entire testis is done and the diameter of the seminferous tubule is ascertained as described in the previous experiment.
2. Four animals are euthanized and their testes excised at days 0 and 60 respectively. Penetration of testis tissue with the microprobes is done as described in the previous experiment and the diameter of the tubules is estimated at days 0 and 60.

Experiment group - Sixteen animals are given a single intraperitoneal injection of EDS (75 mg/kg body weight dissolved in 0.5 ml of dimethyl sulfoxide (DMSO) and 1.5 ml of water) at day 0 of the experiment.

1. Four animals are euthanized and their testes excised at days 14 and 60 of the experiment respectively. Histology and morphometry of the entire testis is done and the diameter of the seminferous tubule is ascertained as described in the previous experiment.
2. Four animals are euthanized and their testes excised at days 14 and 60 respectively. Penetration of testis tissue with silicon needles is done as described in the previous experiment and the diameter of the tubules is estimated at days 14 and 60.

The diameter of the tubules from the histology of the drug-treated and untreated rats is plotted and compared to the diameter estimated by the penetration procedures using the Area-Ratio metric. Hence the viability of the microprobes to measure drug induced changes in testicular function is determined.

B. Device and DAQ-interface improvements

By incorporating the Wheatstone bridge electronics and intrumentation amplifier on the silicon horn, the metal line parasitics can be by-passed before amplification of the signal recorded, thus allowing for a higher signal-to-noise ratio. Electronics need to be developed for on-the-fly elimination of Wheatstone bridge offset voltage by using the ratio of baseline values of the two microprobes when not penetrating any tubules (Figure 3.10). Also a better mechanical characterization experiment needs to be designed, so that the mechanical response of the polysilicon resistors to forces applied only to the top and bottom blades can be measured. Along with the hardware, a user-friendly automated system needs to be developed to interpret the stiffness of the tubules sensed, and to make a dynamic histogram of the measured sizes. With this interface, the surgeon can get a sense of the size of tubules in the current location on-the-fly and can then decide whether to excise tissue or move to a different location.

3.4 Ultrasonic microprobe-based fluid viscosity measurement

3.4.1 Introduction

Viscosity of non-Newtonian fluids

A fluid is said to be Newtonian if the velocity achieved by the moving planes of the material is directly proportional to the tangential applied stress which provides the source of the motion. While many fluids exist that exhibit this property, most fluids in the real world do not behave in this idealized manner. Most fluids show a planar velocity trend that is not directly proportional to the load imposed, and are thus considered non-Newtonian [131]. This relationship between the imposed tangential stress and the rate of velocity of the moving planes or the rate of shear, defines a physical quantity called viscosity. For Newtonian fluids this quantity is a constant, while for non-Newtonian fluids the relationship is shear-rate dependent. Viscosity is the result of the tangential stress (τ) which produces a displacement (γ) in unit time between the two planes in which the fluid is situated:

$$\eta = \frac{\tau}{\dot{\gamma}} \tag{3.16}$$

where the rate of shear ($\dot{\gamma}$) is only applicable when the lines of shear are parallel and straight. This in turn gives a viscosity with units of mPa·s. Generally speaking water and air are Newtonian in behavior with any form of deviation insignificantly small for practical purposes. There are many other liquids for which the velocity of the quantity in Equation 3.16 is not constant for an applied stress, and as explained above these shear-rate dependent fluids are termed non-Newtonian. There is no

single constant viscosity value but rather the ratio of applied stress to rate of shear is called the *apparent viscosity*.

Several models exist to explain the properties of viscous fluids. These models compare the mechanical properties of the fluid to different series and parallel combinations of dashpots and springs. However, the models are generally limiting in relation to the general behavior of a real material as they (the materials) encompass many intermediate properties. The use of the mechanical models is a convenient way of visualizing the behavior of fluid. From these models various equations are derived in terms of applied stress and rate of shearing. The mechanical model of a viscous fluid is a dashpot assembly in which the fluid is unable to support any stress and the rate of shearing is directly related to the applied stress. In such a case a Newtonian fluid would be directly proportional to the applied stress and rate of shearing. To model a non-Newtonian fluid there is no direct proportionality, but rather a power-law relation:

$$\tau = K \cdot \gamma^n \tag{3.17}$$

The exponent n is a constant for a given fluid and for a Newtonian fluid is equal to 1, in which case the consistency parameter K is equal to the viscosity. Otherwise the value for K depends on both the nature of the material and the dimensions of τ and γ. Non-Newtownian fluid suspensions such as that of red blood cells appear to fit this relationship quite well, and by plotting the log of the viscosity against the log of the strain rate, Equation 3.16 can be manipulated to find the value for n because:

$$\eta(\gamma) = K \cdot \gamma^{n-1} \tag{3.18}$$

By fitting apparent viscosity data to this equation the value of n will give an

indication of the deviation of the fluid from Newtonian behavior. As n decreases from unity the pseudoplasticity of the material increases. This is a measure of the non-Newtonian properties of the fluid. In the plot of shear stress versus shear rate (flow curve) the slope of the line is the viscosity. In the case of a pseudoplastic fluid such as blood, the viscosity will not be constant but rather it will decrease with increasing shear rate. For example, at the higher hematocrits blood becomes more non-Newtonian. Thus the pseudoplasticity of blood should increase at higher hematocrits, which means that n should decrease with increases in hematocrit.

It is important to understand that the viscosity of a non-Newtonian fluid is not constant but is shear-rate dependent. As a result the Bingham plastic model utilizes the friction between the sliding surfaces. This model states that extension of the system is impossible unless the applied force exceeds the frictional force which is the yield stress of the material under shear. If the rate of shear is exactly proportional to the rate of extension then we have an idealized Bingham plastic, or in terms of fluids it should exhibit Newtonian behavior. However a modification of this model to apply to practical materials is the Casson equation proposed in 1959. The Casson Equation is as follows:

$$\sqrt{\tau} = \sqrt{\tau_0} + A \cdot \sqrt{\gamma} \tag{3.19}$$

By experimentation whole blood has been shown to follow the Casson equation. This model implies that there is a parameter τ_0 which represents the finite stress that must be applied to the fluid for flow to occur. The concept of yield stress which was originally developed for solids defines the stress at which irreversible physical changes occur to a body. In the Bingham plastic model this implies that for a viscous fluid such as blood, when sheared the planes of shear heal themselves once the stress has been removed. Measurements of yield stress are only available

with controlled shear stress viscometers. It must be kept in mind that τ_0 is a parameter of non-Newtonian fluids and Newtonian fluids will not exhibit any yield stress.

Blood

Blood is a heterogeneous suspension containing several different components. In the typical adult human blood is composed of approximately forty-five percent plasma, and the other fifty-five percent consists of a further heterogeneous mixture of cellular components. The major constituents of this formed element group include: red blood cells (RBCs) or erythrocytes, white blood cells (WBCs) or leukocytes, and platelets or thrombocytes. In normal human blood one cubic millimeter consists of approximately: 5 million red blood cells, 5,000 to 10,000 white blood cells, and 200,000 to 300,000 platelets. When the volume of blood being sheared is significantly greater than the volume of a single red blood cell, blood can be considered a homogeneous fluid. The concentration of white blood cells and platelets present in whole blood is normally so small when compared to that of the RBCs, that their presence likely contributes little to any viscous effects.

Red blood cells consist of a fine flexible membrane that surrounds the hemoglobin and is in healthy subjects biconcave in shape. In the study of fluid flow the shape of the suspended particles is of importance in relation to its reaction to an applied shear stress. If there is a suspension of rigid non-interacting particles at low concentration, the fluid may basically be considered Newtonian, since the effects of the suspending fluid undermine the overall effect of the particles. However, when the concentration of the particles increases mutual interference between the particles will occur and additional liquid will be prevented from flowing. Therefore

it should be seen for any fluid with formed particles that the viscosity will rise with the concentration. The flexibility of particles such as red cells will have a significant effect on the flow behavior of blood and particularly its non-Newtonian characteristics. It can be observed that at suitable concentrations and at very low shear rates the cells will deform so insignificantly, they will tend towards solid body behavior. This is the extension from which yield stress and n values are measured for the model of blood in respect to its solid body behavior. However, at high shear rates deformation of cells starts to affect its fluid flow behavior and with blood the non-Newtonian characteristics are nullified.

It is proposed that the flexibility of the RBCs plays an integral part in their ability to flow through the microcirculatory system. More important to this investigation, several researchers have postulated that the flexibility of these cells has great influence on the non-Newtonian properties of blood. The deformability of the red blood cell is crucial in its ability to pass through a capillary, since the diameter of the undeformed cell is slightly larger than the inner diameter of the capillary walls. This phenomenon adds to the complexity of the rheology of blood and makes accurate modeling of the medium difficult. Moreover, RBCs show the tendency to aggregate in such a fashion under low shear rates to form tubular looking structures resembling rolls of coins. These aggregations are called *rouleaux* and are theorized to play still another role in the rather unique rheological properties of blood. These rouleaux disperse at higher shear rates (above 50 s^{-1}) while at lower shear rates, the rouleaux remain intact and tend to have a greater influence on the viscosity of the blood. At dilute concentrations of RBCs the cells exhibit a smaller propensity for forming these relatively large flow impeding structures, and the suspension can be modeled as a homogeneous solution.

Measurement of blood viscosity

Medical diagnosis of disease often requires the viscosity of body fluids, most importantly that of blood [132]. Blood rheology in vivo can be used for prediction of blood flow through capillaries of varying sizes, while its in vitro rheology can be used for diagnosis and monitoring of diseases. Also, changes in blood rheology have been seen to contribute to or aggravate cardiovascular disorders such as myocardial infarction and hypertension [133, 134]. Clinical hemorheological tests measure the red blood cell (RBC or erythrocyte) aggregation by the erythrocyte sedimentation rate (ESR) and the plasma viscosity. Physiological conditions leading to alternation of plasma proteins (such as fibrinogen) results in a change in the ESR and plasma viscosity. Correlation to blood rheology can be used as a good indicator for prognosis, diagnosis and/or monitoring disease processes such as cancer, cardiovascular disease, etc. For example, inflammatory biomarkers (fibrinogen) and plasma viscosity have been observed to be significantly associated with death due to myocardial infarction or coronary heart disease [135]. Incidence of type 2 diabetes has been shown to be strongly related to high whole blood viscosity (WBV) [136], thus allowing a measure of blood viscosity to be a prognosis tool. Also, monitoring plasma viscosity can help in the prediction and diagnosis of plasma hyperviscosity syndrome and sickle cell disease [134]. Additionally, a measure of blood viscosity can help in monitoring interventions to alter blood viscosity such as diet, alcohol, pharmaceuticals etc.

As discussed previously, the RBCs in blood which compose about 35-40% of the volume are known to be deformable and contribute to the non-Newtonian nature of blood i.e. its viscoelastic behavior [137]. Whole blood viscosity (WBV) is observed to have shear-rate dependence due to the deformability of the RBCs.

This has been shown to have a strong correlation to hypertension [138]. Also, the blood volumes available from patients are small and must be analyzed quickly preferably without the addition of anticoagulants. The currently existing methods for clinical diagnosis and in vitro study of blood in laboratories, require large sample volumes (10s of ml) and involve the addition of anti-coagulants thus deviating from the true physiological state of blood [139, 140, 141, 142]. Also, the instruments being bulky pose a practical difficulty in order to have blood viscosity as a point-ofcare measurement for rapid on-site diagnosis. The most frequently used blood viscometers in laboratories are capillary tube, rotating and falling ball or needle viscometers. Rotational viscometers consist of one stationary element and one rotary element separated by a thin layer of fluid. As the rotary element is spun, the viscous forces of the fluid interact with both the rotating body and the stationary body, having the net effect of impeding the motion of the rotating body. Rotational viscometers can be further divided into one of two types, co-axial cylinder and cone-plate viscometers. The co-axial rotating cylinder viscometer consists of a cylinder, which houses a concentrically mounted solid cylinder. The outer cylinder is capable of forced rotation. To measure viscosity of fluids, the outer cylinder is rotated at a constant angular velocity. The viscous drag created by any fluid between the outer and inner cylinders is transmitted to the inner cylinder, and measured as a function of the angular displacement of the inner cylinder. Using the above discussed blood viscometers, it is difficult and labour intensive to measure the viscosity at different shear rates because usually some of the inherent characteristics of the device need to be modified (i.e. varying the rotation speed in rotating viscometers). There is a current need for low sample volume ($\approx 1\mu$l), rapid real-time measurement of rheological properties of whole blood and plasma (viscosity and coagulation) *in vitro* or *in vivo*. Such an instrument, together with

biosensors such as glucose measurement for diabetic patients, could serve as an invaluable tool for rapid diagnosis and monitoring of disease and blood function.

Acoustic wave sensors (piezoelectric crystals and electroceramics) have been used extensively in the measurement of fluid viscosity [143, 144, 145]. The physical properties of the fluid can be extracted from the change in resonant frequency, quality factor and the magnitude of vibration of a resonator. Thickness-shear mode (TSM) resonators have been reported to be used in blood rheological characterization such as viscosity and coagulation measurement. Since the acoustic shear wave thickness in the blood in contact with the TSM (high frequency) resonators is much smaller than the size of a RBC, only plasma viscosity can be measured and the effect of RBCs is not sensed [146, 147]. At the opposite extreme are low frequency resonant devices with high shear wave thickness that can become bulky, with the size approaching that of commercial tabletop viscometers. In this work, we present a mid-frequency (30-100 kHz) resonant viscosity sensor that generates high amplitude motion (less than 1 μm) via non-linear coupling between longitudinal to transverse motion to measure fluid viscosity with a self-calibrating immersion depth sensor. This instrument is likely to be clinically suitable, as a probe that can be easily inserted in microliters of sample collected from patients, such as a drop of blood (Fig. 3.26). We have also demonstrated that high-amplitude horn-shaped longitudinal mode resonators quality factor is sensitive to fluid viscosity into which the probes are inserted [148]. However, this capability is limited as it is not easy to measure how much of the probe is inserted into the fluid and, the shear-rate dependent fluid viscosity cannot be distinguished. Here we demonstrate fluid viscosity measurement by monitoring the viscous damping of non-linear flexural vibrations of the microprobes, induced by the $\lambda/2$ longitudinal resonance of silicon horn actuators. Real-time coagulation in a rat-blood droplet

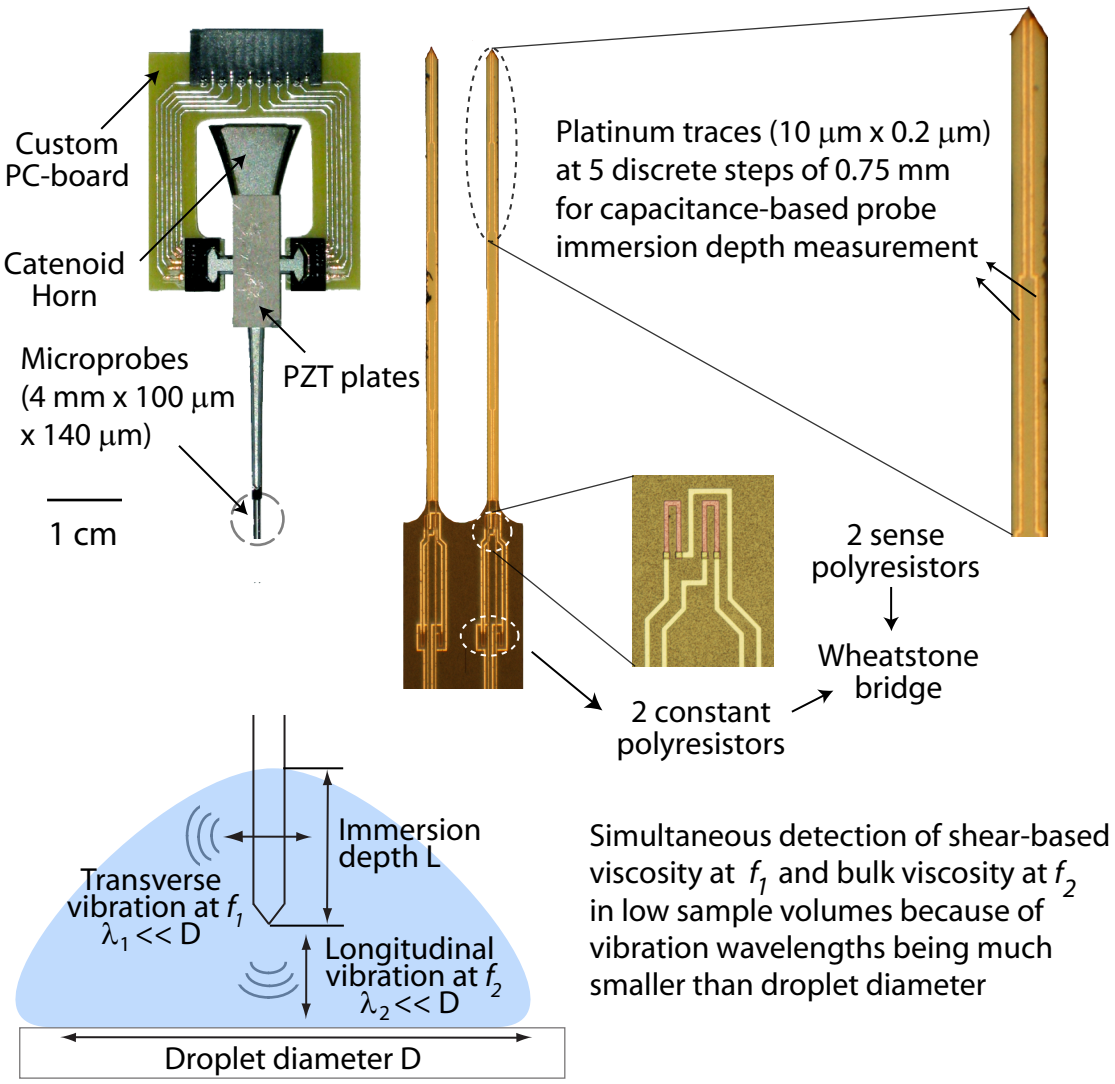

Figure 3.26: Top: Optical photograph of the fabricated device. The piezoresistors ($\approx$ 9 kΩ) are located at the junction of the horn and the microprobe to sense the ultrasound induced strain oscillations. Bottom: The probes can be used for multi-sensing viscosity (bulk and shear) measurements in μ-droplet fluid samples at a specific immersion depth.

(≈ 5 μl) as a function of time is measured by monitoring the resonance frequency of the flexural vibration. This demonstrates the sensors applicability as a rapid blood coagulation sensor alongside measuring whole blood viscosity. Furthermore, since the viscosity is a strong function of probe insertion depth, we have integrated capacitance-based immersion depth sensors for selfcalibration of probe depth, or fluid immersion, of the ultrasonic viscometer.

3.4.2 Working principle

In this work, the catenoid horn is 4 cm long, with shank-to-tip area ratio 10:1, and a longitudinal $\lambda/2$ resonance at 110 kHz, with two silicon microprobes 4 mm long, 100 μm long wide and, 70 and 140 μm thick projecting outwards at the tip of the horn (Figure 3.26). The polysilicon strain gauges sense the ultrasonic strain generated in the microprobe when the horn is actuated. As discussed earlier, polysilicon strain gauges are connected in a Wheatstone bridge configuration, are integrated at the junction of the horn and the microprobe to measure the longitudinal and flexural oscillating motion (Fig. 3.27). The silicon horn actuated at its $\lambda/2$ longitudinal resonance (109.8 kHz) exerts longitudinal strain at the tip of the horn, and induces a non-linear flexural vibration mode (30.4 kHz) in the microprobes. From the Fast-Fourier Transform (FFT) of the amplified Wheatstone bridge voltage, the magnitude of vibration corresponding to both the oscillation frequencies is measured (Fig. 3.27A). A 2D laser Doppler vibrometer scan of microprobes indicates a mode with three displacement nodes with $\lambda \approx$ 2.83mm (Fig. 3.27B). Immersion depth calibration is implemented by measuring the capacitance at discrete steps, which provide distinct motion artifacts as the liquid with the much higher dielectric constant surrounds the traces. The distance

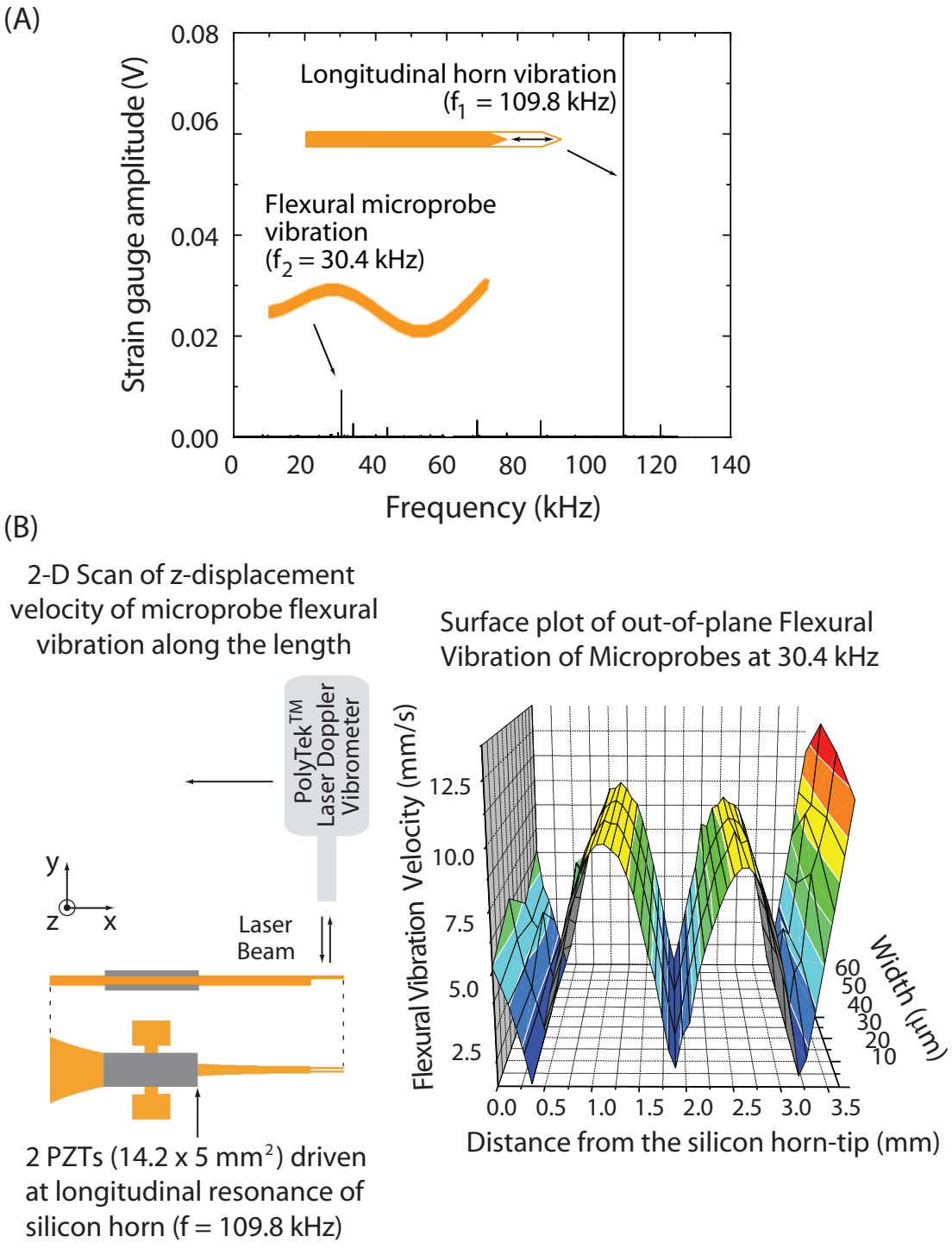

Figure 3.27: (A) Frequency spectrum of Wheatstone bridge voltage showing the longitudinal and flexural vibration (B) 2D laser Doppler vibrometer measurement of microprobes flexural displacement and surface plot along the length of the microprobes indicating the mode shape with 3 nodes.

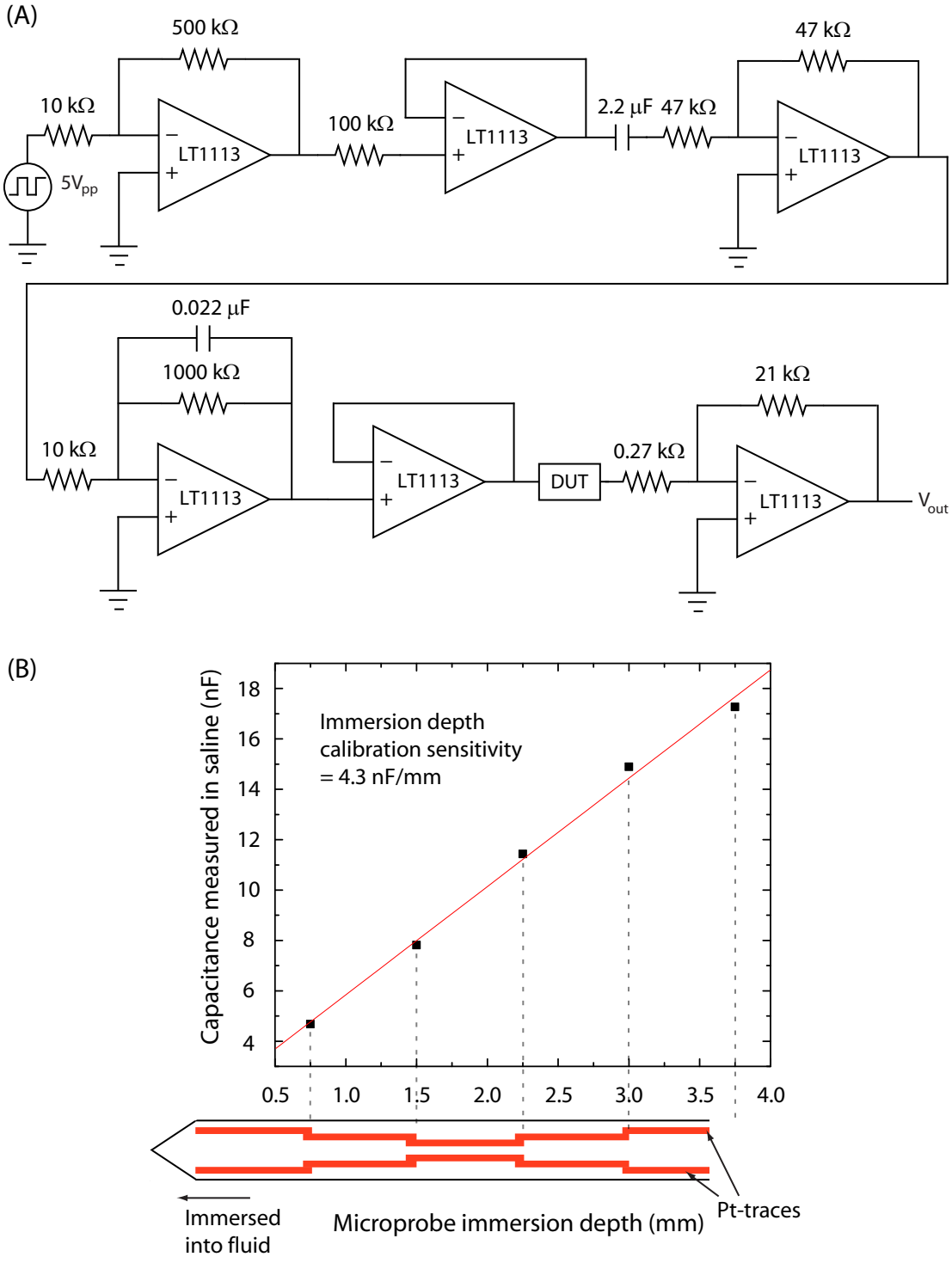

Figure 3.28: Capacitance-based calibration of microprobe immersion depth in physiological saline (0.9% w/v NaCl). (A) Platinum electrode-electrolyte capacitance (DUT) measuring circuit. (B) Platinum traces (10 μm wide and 0.2 μm thick) have discrete steps of 0.75 mm and capacitance is measured at every step.

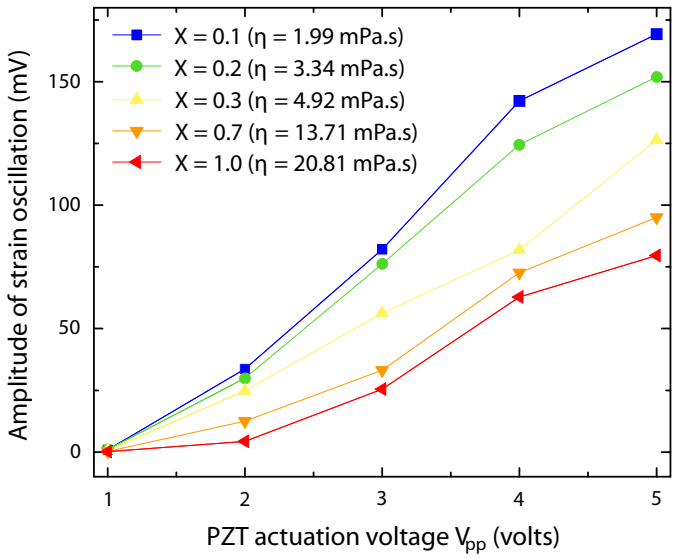

Figure 3.29: Variation of peak-to-peak amplitude of strain oscillation with PZT actuation voltage V_{pp}, when the microprobe is immersed in aqueous solutions of ethylene glycol with mole fraction (X) varying from 0.1 to 1.0.

coding capacitance is formed by platinum traces (10 μm wide and 0.2 μm thick) co-fabricated on the microprobes (Fig. 3.26). Figure 3.28A shows capacitance measurement circuitry with one lead of the Device Under Test (DUT) to be the platinum trace and the other to a Ag/AgCl electrode immersed in physiological saline solution (0.9% w/v NaCl). Figure 3.28B depicts the linear dependence of the capacitance signal with increasing depth of immersion of the microprobes in saline solution (sensitivity = 4.3 nF/mm).

3.4.3 Viscosity measurement of ethylene glycol

A. Longitudinal vibration damping

Since the polysilicon (sense) resistors on the microprobe are not matched, there is a non-zero dc component across the output terminals of the Wheatstone bridge.

When the silicon horn is actuated, the microprobe undergoes longitudinal and flexural motion, and strain corresponding to each is sensed across the piezoresistors. The peak-to-peak amplitude of the longitudinal vibration is monitored when the microprobe is immersed (2 mm) in aqueous solutions with varying mole fractions of ethylene glycol ($X = 0.1$ to 1.0). The viscosity of aqueous solutions with different mole fractions of ethylene glycol is well characterized [149]. The variation of strain oscillation with PZT drive varying from 1 to 5 V_{pp} is also monitored when immersed in the different solutions. It is observed that as the PZT actuation voltage is increased, the amplitude of strain oscillation increases because of the increased horn tip displacement (i.e. increased strain on the polysilicon resistors) [9]. It also tends to saturate at high PZT actuation voltages (≈ 7 V_{pp}). At a given PZT voltage, as the viscosity of the fluid surrounding the microprobe is increased, the strain oscillation amplitude is observed to decrease because of the increased viscous damping (Figure 3.29). By deriving the value for the damping coefficient, it has been observed that the fluid damping is proportional to the square root of the viscosity [150, 151]. The amplitude of strain oscillation is observed to be inversely proportional to the square root of viscosity (Figure 3.30) at a given PZT actuation (in this case, 3 V_{pp}).

B. Flexural vibration damping

In order to characterize the viscosity sensor the microprobes were immersed in ethylene glycol solutions of varying viscosity, and the damping in microprobe flexural vibration was monitored at a fixed drive voltage. The vibration amplitude is monitored as the microprobes are immersed in the liquid at different immersion depths and is observed at increasing PZT actuation voltages (1-10 V_{pp}). Resonance frequency changes were also measured but, for ease of characterization, amplitude

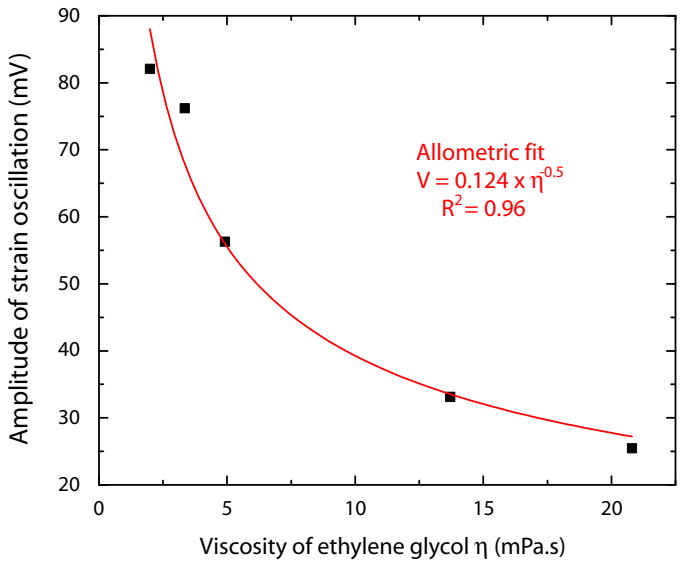

Figure 3.30: Variation of peak-to-peak amplitude of strain oscillation with viscosity under PZT actuation of 3 V_{pp}. Allometric curve-fit $V = 0.124 \times \eta^{-0.5}$ is also shown ($R^2 = 0.96$).

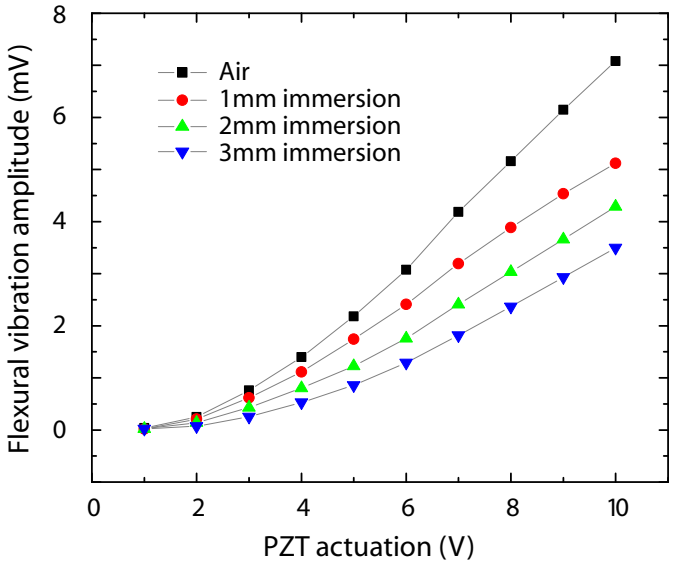

Figure 3.31: Amplitude of microprobe flexural vibration in DI water as compared to air, at increasing PZT actuation voltages for varying immersion depths of microprobe (1 to 3 mm).

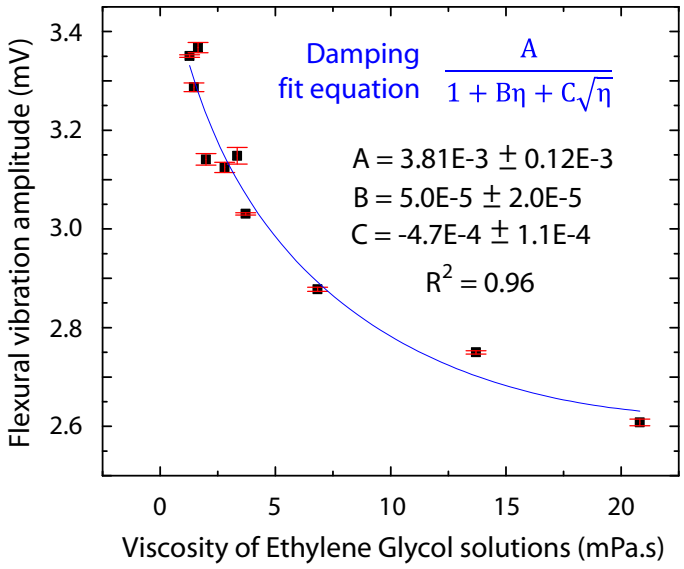

Figure 3.32: Damping of microprobe vibration in ethylene glycol solutions (2 mm immersed) of varying viscosities at 8 V_{pp} PZT actuation. The viscous damping of the microprobe is modeled assuming the immersed part of the microprobe to be an oscillating sphere.

changes were used. With increasing immersion depth of microprobes in DI water the damping is observed to increase with increasing contact with fluid (Fig. 3.31). Figure 3.32 shows the decrease in vibration amplitude at 8 V_{pp} PZT actuation as the microprobe is immersed (2 mm) in ethylene glycol solutions of varying viscosities. As a first approximation, the viscous fluid damping of the microprobe is modeled by assuming the immersed-part of the vibrating probe to be an oscillating sphere immersed in a liquid [152], and the damping model is shown to agree reasonably to the data in Figure 3.32. The parameters in the model are dependent on the microprobe mass and geometry, and the immersion depth. Therefore, wide range of viscosities can be accurately measured, with high sensitivity in the whole blood viscosity regime (0 to 5 mPa·s), by monitoring the amplitude of the vibration in the device at different immersion depths, both capabilities integrated on the device.

Calibration of the viscosity sensor using a liquid (such as ethylene glycol) with a standardized viscosity at a given temperature and, also the quality of the analytical damping models fit to the data can be used as a figure of merit to determine the viability of the device for re-use.

3.4.4 Rat whole blood coagulation

Whole blood from a Sprague-Dawley rat (44 weeks old) without addition of anti-coagulants was extracted by exsanguination. The flexural vibration frequency is monitored with the microprobe immersed in a blood drop ($\approx 5\ \mu$l) at a depth of ≈ 1 mm. The hypothesis is that, initially the red blood cells (RBCs) coat the microprobe, lying within the shear thickness and thus loading the vibration by reducing its frequency (Fig. 3.33, Phase I). The blood coagulation cycle ramps up with the formation of blood clots (coagulated RBCs) with sizes larger than the acoustic shear thickness, and thus reducing the loading resulting in a steady increase in the vibration frequency (Fig. 3.33, Phase II). Finally, the blood coagulation cycle ends at ≈ 430 seconds which is close to that observed in literature [147]. The residual damping observed at the end of the coagulation cycle is mostly due to the plasma, few RBCs and the fibrous network of clots formed (Fig. 3.33, Phase III). The microprobe was cleaned after the measurement by immersion in dilute bleach solution and actuating the PZT at 20 V_{pp}, and the frequency and amplitude of vibration returned to the initial baseline values.

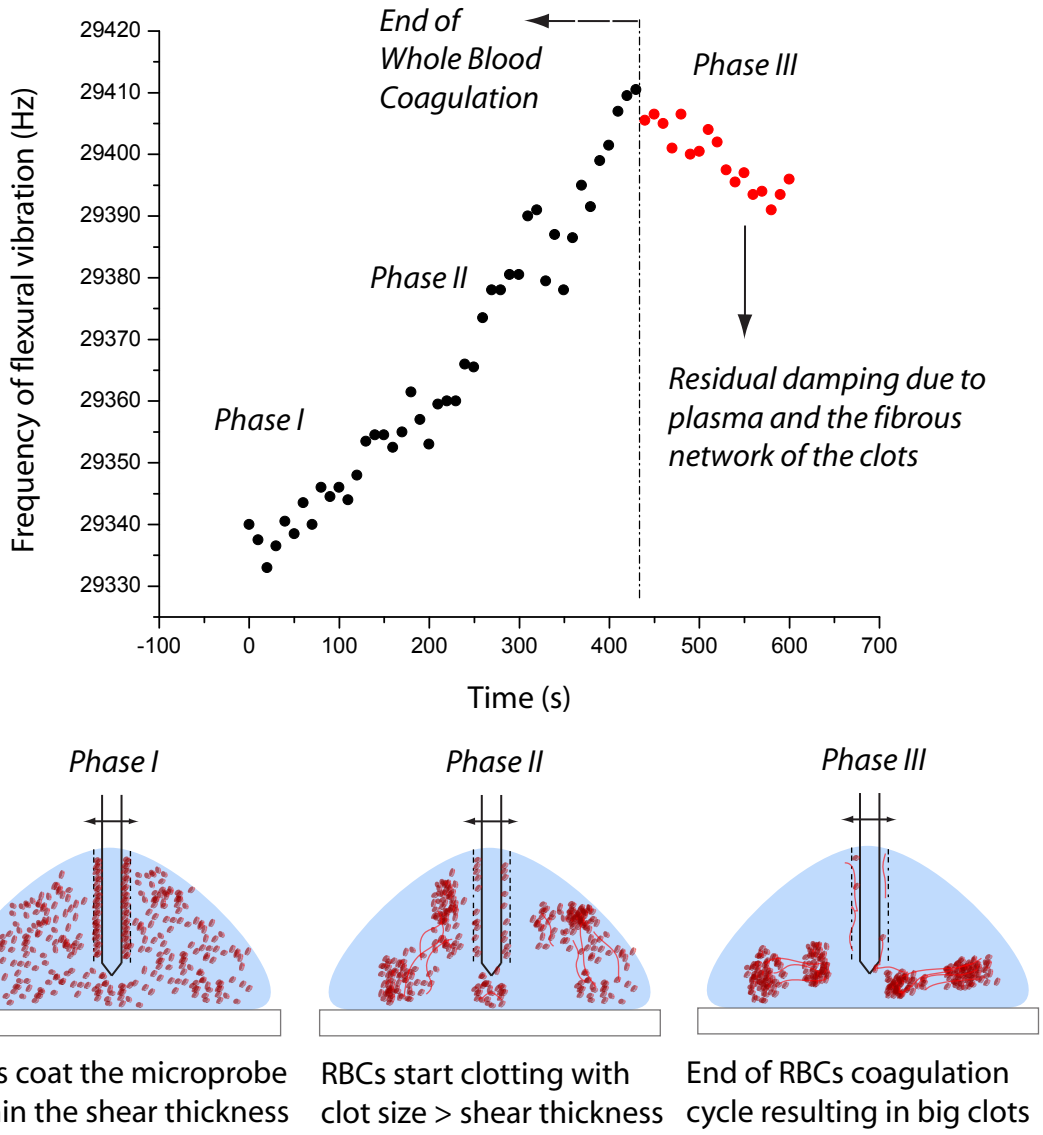

Figure 3.33: Frequency variation of microprobe flexural vibration in $\approx$ 5 μl drop of whole rat blood ($\approx$ 1 mm immersed) at 10 V_{pp} PZT actuation. *Phase I:* The red blood cells (RBCs) coat the microprobe within the shear thickness ($\approx$ 4 μm) and load the vibration frequency reducing it; *Phase II:* The blood starts to coagulate with the RBCs coaguating with clot sizes bigger than the shear thickness, thus reducing the vibration loading (thus, increasing the frequency); *Phase III:* End of blood coagulation with the formation of fibrous structures and large clots.

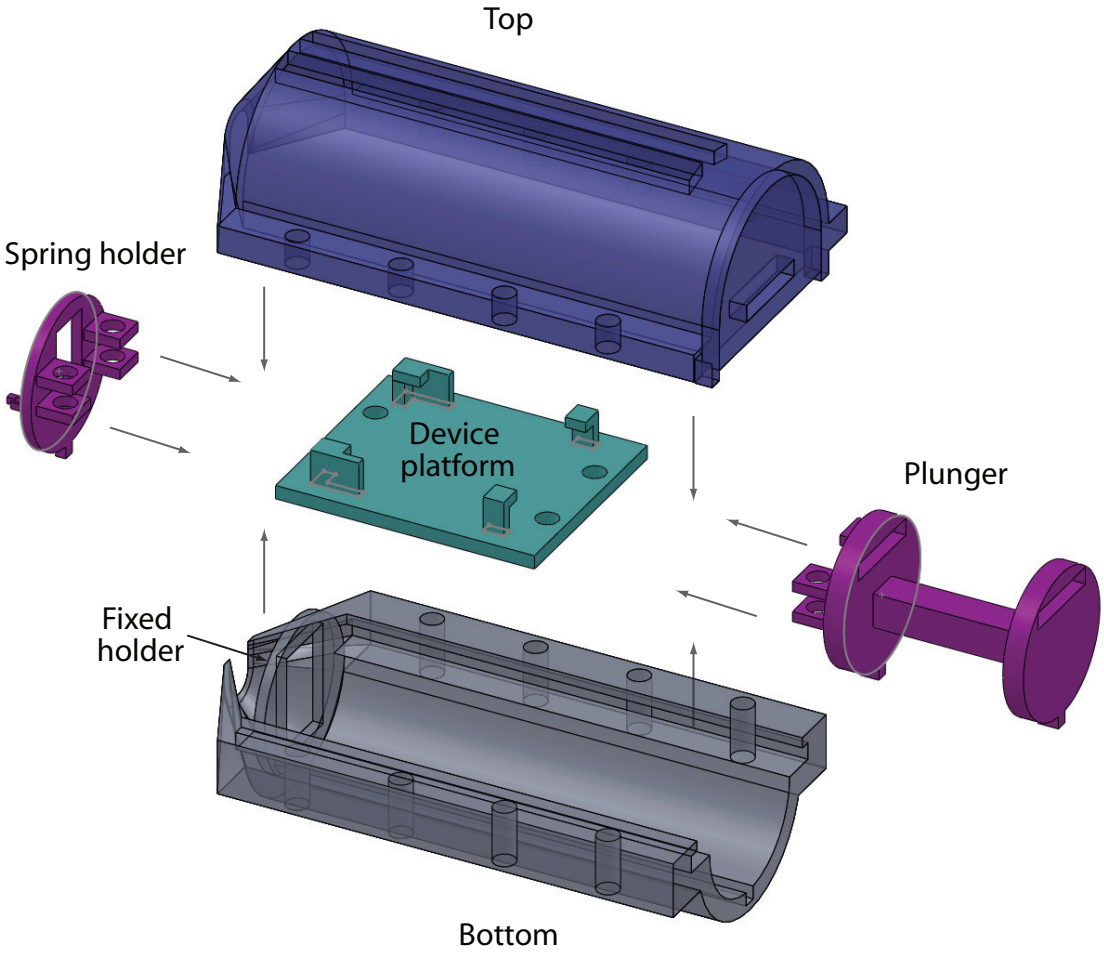

Figure 3.34: Schematic of the prototype assembly and its parts made in Solidworks^{TM}. The prototype is envisioned to be hand-held with the microprobes and PCB assembled on the *device platform*, and the viscosity measurement performed on small samples when the microprobes are engaged by using the *plunger* and *spring* assembly.

(A)

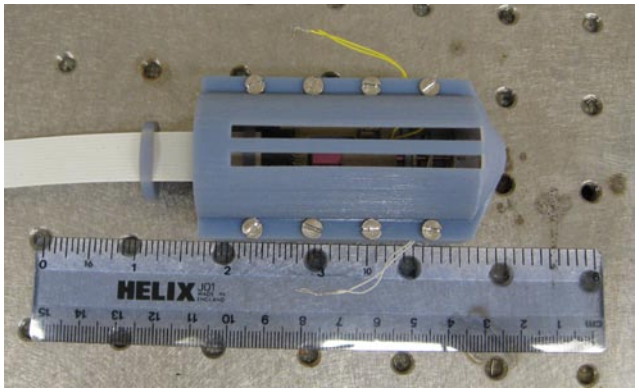

(B)

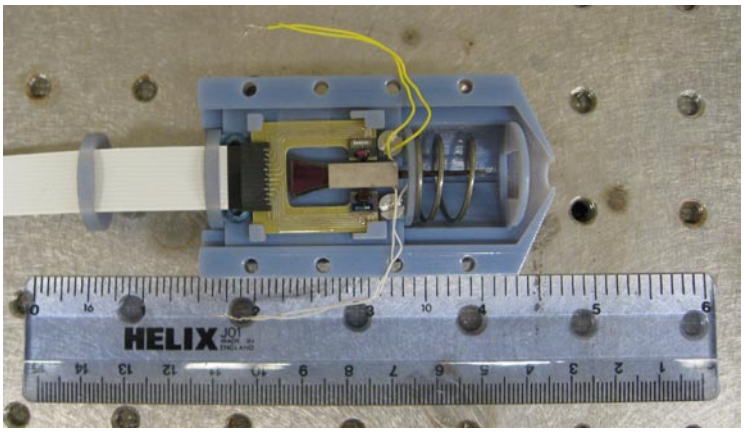

Figure 3.35: Optical photograph of the prototype assembly with PCB and microprobes.

3.4.5 Prototype and software development

A prototype was developed with the vision of having the device and its electronics on a hand-held platform, which can be used to measure fluid viscosity in droplets conveniently. The prototype consists of 5 discrete components which are assembled together with screws - *device platform, sping holder, plunger, top and bottom* (Fig. 3.34). The files were made in Solidworks^{TM} and given to Xpress3D, Inc. for building the three dimensional parts by building layers upon layer of material (Polycarbonate, PJET^{TM}). The device platform is designed to have fixed clamps tailored to the size of the PCB, in order to hold the PCB with the device in position (Fig. 3.26). The plunger is screwed on to the back of the PCB on the device platform, with a provision for cables from the PCB to be routed to the electronics board. The spring holder is screwed on to the front of the PCB with the microprobes on the PCB protruding through a rectangular hole on the holder. The spring holder, device platform and plunger once assembled are inserted into the bottom component which has a groove built into it. A steel spring is inserted between the fixed holder incorporated on the bottom component, and the spring holder (see Figure 3.35B). The spring hold is built with clamps (on the side opposite to that of the PCB) for the spring to be held in place. The length of the spring can be adjusted to ensure that the microprobes on the device holder protrude (entire length) through the front of the assembly, when the plunger is engaged compressing the spring. The top component is then placed on the bottom component and screwed in place (see Figure 3.35A). It is provided with grooves running through its length to allow for connections to the PZTs on the device.

A software interface was developed to record ultrasonic vibrational strain (longitudinal and flexural) data from the strain gauge, process the data (FFT)

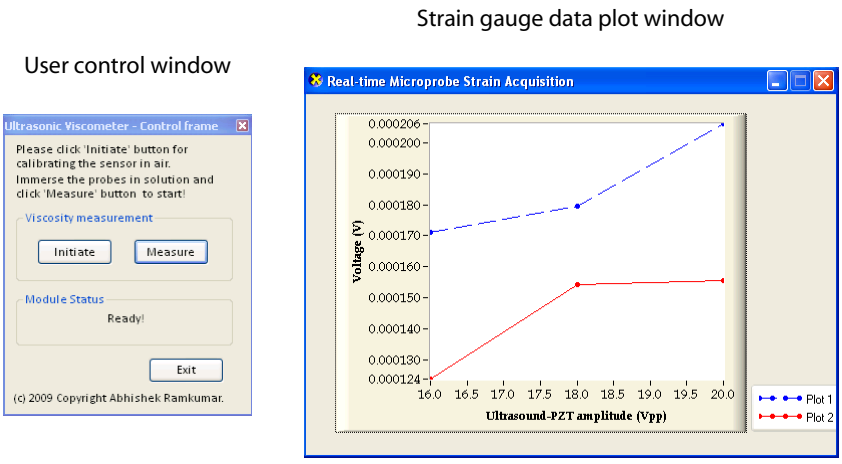

Figure 3.36: Software interface after the flexural vibration amplitude at varying Ultrasound-PZT actuation voltages measured in air, and when the microprobes are immersed ($\approx$ 2 mm) in DI water.

and plot the magnitude of the ultrasonic strain at a particular frequency as a function of PZT drive voltage in air and when immersed in solution. For real-time processing, a C++ based Windows-based software application was developed in Microsoft Visual Studio^{TM} (see Appendix E). In order to get meaningful data for the ultrasonic strain at high-frequencies, the output voltage from the Wheatstone bridge circuit corresponding to the strain gauge on the microprobe, is recorded using a NI USB-6251 (National Instruments, Inc.) data acquisition board for a period of 2 seconds at a sampling rate of 2 MHz. A Labview^{TM} program was written to set the PZT drive voltage using *Agilent^{TM} 33250A Arbitrary Waveform Generator* (Agilent, Inc.) via a GPIB interface, and corresponding header (VppSet.h) and library (VppSet.lib) files were compiled for interfacing in MS Visual studio. National Instruments^{TM} DAQmx ANSI C development toolbox header files were included and predefined functions were used to set the data acquisition parameters and acquire data from the DAQ board. The FFT of the data is performed using an open-source package *fftw* - the corresponding header

(fftw3.h) and library (libfftw.lib) files were included in the VC++ project and the predefined FFT function in the package was used. The FFT data generated is then sorted to find the peak corresponding to the longitudinal ($\approx$ 110 kHz) and flexural ($\approx$ 30 kHz) vibration. The strain gauge data is plotted in a separate window, the layout of which is programmed using National Instruments^{TM} LabWindows CVI software and interfaced to the application being developed using header (myuir.h) and object (cbacks.obj) files. The strain gauge data is processed to determine the magnitude of the flexural ultrasonic strain (from FFT) at different PZT drive voltages in air and when immersed in solution, and the data is plotted as a function of the actuation voltages. The microprobe in the hand-held prototype assembly when immersed ($\approx$ 2 mm immersion depth) in DI-water, damps the flexural vibration at different PZT actuation voltages (Plot 2 in Fig. 3.36) when compared to that measured in air (Plot 1 in Fig. 3.36).

3.4.6 Conclusions and future work

From the above experiments, we have demonstrated fluid viscosity measurement by monitoring the longitudinal and flexural vibrations of the immersed microprobes, with precise control of the depth of immersion. Since the acoustic shear thickness of the flexural vibration is close to the size of a RBC [152], the viscous damping was influenced by the RBCs, thus enabling the measurement of whole blood viscosity. Also, by varying the PZT actuation voltage the microprobe flexural vibration rate can be varied, and hence shear rate dependence of whole blood viscosity can be measured. In addition, the damping in the silicon horns longitudinal vibration (109.8 kHz) having a shear thickness (inversely proportional to the square root of frequency) much smaller than the size of a RBC will allow for measurement

of blood plasma viscosity [148]. Since the shear (non-linear vibration) and bulk (silicon horns $\lambda/2$ longitudinal resonance) damping can be observed at two different frequencies, we can simultaneously measure the plasma (bulk) and whole (shear-rate dependent) blood viscosity in low-sample volumes ($\approx$ 1-3 μl). Also, the natural and drug induced blood coagulation cascade can be precisely monitored as a function of time. With the help of the prototype and software developed, blood viscosity measurement can be done on the bed-side allowing for quick diagnosis and detection of diseases.

In the future, work needs to be done on circuitry to monitor the change in frequency (f_0) and quality factor ($f_0/\Delta f$) of the flexural and longitudinal vibrations of the microprobes when immersed in a fluid. This will allow us to achieve higher sensitivity when measuring fluid viscosity. Also, FEM based analysis of the local shear-rate at the microprobe-sample interface needs to be done, in order to be able to compare the viscosities measured using the microprobes with that of standardized rheometers. In other words, an expression of shear rate τ as a function of PZT drive V_{pp} for the microprobe needs to be derived. Once the shear rate τ is known, the viscosity of blood samples can be measured as a function of PZT drive. The control experiment would be to measure the viscosity of ethylene glycol samples as a function of PZT drive - the measurement is expected to be constant, since ethylene glycol is a Newtonian fluid.

APPENDIX A

ANSYS CODE FOR ULTRASONIC HORN WITH MICROPROBES

The following is the ANSYS^{TM} code for analyzing the mechanical motion of the microprobes when the silicon horn is actuated at its $\lambda/2$ longitudinal resonance:

```
!! CATENARY HORN PROBE FOR CARDIAC RECORDINGS
!! 40mm long horn, 10 mm:1 mm end-to-tip width ratio.
FINISH
/CLEAR
/CWD, "C:\AnsysDump"
/Title, Catenary Horn Plate
/PREP7   ! /PREP7: Enters the model creation preprocessor.
/UNIT,SI
/TRIAD,LBOT ! /TRIAD: Display triad in lower left screen corner
SMART,ON ! SMART: Smart Meshing
!----------------------
! MATERIAL PROPERTIES
!----------------------
ET,1,SOLID95 ! ET: Defines a local element from element library
! SOLID95 is a 3-D 8-node solid element
MP,EX,1,190e9 ! MP: Defines a linear material property as a constant
! or a function
MP,NUXY,1,0.25 ! temperature. EX - Elastic Moduli, NUXY - Minor
! Poisson's ratio
MP,DENS,1,2300   ! and DENS - Mass Density
!---------------------------------------
```

```
! DEVICE DIMENSIONS AND SHAPE DEFINITION
!---------------------------------------
! HORN SHAPE
LEN=40E-3 ! Horn Length
W0=10E-3 ! End Width
W1=1E-3 ! Tip Width
DX=w1 ! 'NOFPX-1' divisions in the horn part, 1mm each
NOFPX=(LEN)/DX+1
ALPHA=45.4612 ! ALPHA=ACOSH(SQRT(W0/W1))/LEN
*DO,II,1,NOFPX ! Define keypoints for the upper half of the horn
XX=(II-1)*DX
YY=W1*COSH(ALPHA*(LEN-XX))**2/2
K,0,XX,YY,0
K,0,XX,0,0
*ENDDO
*DO,II,1,NOFPX-1 ! Define areas of upper half of horn by Keypoints
A,2*II-1,2*II,2*(II+1),2*(II+1)-1
*ENDDO
! DUMMY DEVICE ON TOP
*DO,II,1,NOFPX ! Define keypoints for the upper half of the horn
XX=(II-1)*DX
YY=W1*COSH(ALPHA*(LEN-XX))**2/2
K,0,XX,YY,5E-4
K,0,XX,0,5E-4
*ENDDO
*DO,II,1,NOFPX-1 ! Define areas of upper half of horn by Keypoints
```

```
A,82+2*II-1,82+2*II,82+2*(II+1),82+2*(II+1)-1
*ENDDO
K,10001,0,0,0 ! K: Defines a Keypoint.
K,10002,0,0,-5E-4
L,10001,10002 ! L: Defines a line between two keypoints.

ASEL,s,loc,z,0,1E-4    ! ASEL: Selects a subset of areas.
AADD,ALL ! AADD: Adds separate areas to create a single area.
VDRAG,ALL,0,0,0,0,0,243 ! VDRAG: Generates volumes
K,10003,0,0,5E-4 ! K: Defines a Keypoint.
L,10003,10002 ! L: Defines a line between two keypoints.
ASEL,s,loc,z,5E-4, 6E-4 ! ASEL: Selects a subset of areas.
AADD,ALL     ! AADD: Adds separate areas to create a single area.
VDRAG,ALL,0,0,0,0,0,369 ! VDRAG: Generates volumes
VSEL,ALL
VADD,ALL
! CLAMP FOR THE LONGITUDINAL NODE WITH EARS
NODEX=15.57E-3 ! COORDINATES OF THE DISPLACEMENT NODE
NODEY=0
NODEZ=0
CW=1.962E-3 ! DIMENSIONS OF THE CLAMP BAR
CH=15E-3
EW=5.776E-3 ! DIMENSIONS OF THE HORN'S EARS
EH=3.755E-3
K,50001,NODEX-CW/2,NODEY+CH/2,NODEZ
K,50002,NODEX+CW/2,NODEY+CH/2,NODEZ
```

```
K,50003,NODEX+CW/2,NODEY,NODEZ
K,50004,NODEX-CW/2,NODEY,NODEZ
A,50001,50002,50003,50004
K,50005,NODEX-EW/2,NODEY+CH/2,NODEZ
K,50006,NODEX+EW/2,NODEY+CH/2,NODEZ
K,50007,NODEX+EW/2,NODEY+CH/2-EH,NODEZ
K,50008,NODEX-EW/2,NODEY+CH/2-EH,NODEZ
A,50005,50006,50007,50008
ASEL,s,loc,x, NODEX-EW/2, NODEX+EW/2
ASEL,r,loc,z,0,1E-4
BOPTN,KEEP,NO
AOVLAP,ALL
AADD,ALL ! AADD: Adds separate areas to create a single area.
VDRAG,ALL,0,0,0,0,0,243 ! VDRAG: Generates volumes
! CURVE LEADING TO MICROPROBES
R=15E-5 ! Radius of curvature leading into microprobes
DX2=15E-6
NOFPX2=R/DX2 + 1 ! 'NOFPX2' divisions in the curved part, 15E-6 each
*DO,II2,1,NOFPX2
XX2=LEN+(II2-1)*DX2
YY2a=(W1/2) - SQRT((R**2 - (XX2- (LEN+R))**2))
YY2b=SQRT((R**2 - (XX2-(LEN+R))**2))
K, (100000+4*(II2-1)+1),XX2,YY2a,-1.5E-4
K, (100000+4*(II2-1)+1)+1,XX2,YY2b,-1.5E-4
K, (100000+4*(II2-1)+1)+2,XX2,YY2a,0
K, (100000+4*(II2-1)+1)+3,XX2,YY2b,0
```

```
*ENDDO
! Define areas of the upper half of the microprobe by Keypoints
*DO,II2,1,NOFPX2-1
V,(100000+4*(II2-1)+1),(100000+4*(II2-1)+1)+1,
(100000+4*(II2-1)+1)+3, (100000+4*(II2-1)+1)+2,
(100000+4*(II2)+1),(100000+4*(II2)+1)+1,
(100000+4*(II2)+1)+3,(100000+4*(II2)+1)+2
*ENDDO
BLOCK, LEN+R, LEN+R+9.65E-3, R, R+2E-4,0,-1.5E-4
K,10004, LEN+R+9.65E-3, R+2E-4,0
K,10005, LEN+R+9.65E-3, R,0
K,10006, LEN+R+9.65E-3+2E-4, R+1E-4,0
K,10007, LEN+R+9.65E-3, R+2E-4,-1.5E-4
K,10008, LEN+R+9.65E-3, R, -1.5E-4
K,10009, LEN+R+9.65E-3+2E-4, R+1E-4, -1.5E-4
V,10004,10005,10006,10007,10008,10009
VSEL,ALL
VADD,ALL
VSYMM,Y,ALL
VSEL,ALL
VADD,ALL
!----------
! MESHING
!----------
VATT,1,,1
MSHKEY,0
```

```
MSHAPE,1
MOPT,TETEXPND,2
FINISH  ! FINISH: Exits normally from a processor.
!---------------------
! SOLUTION PROCESSOR
!---------------------
/SOLU ! /SOLU: Enters the solution processor.
ANTYPE,MODAL! ANTYPE: Specifies the analysis type.
RIGID,ALL ! RIGID: Specifies known rigid body modes of the model.
! CLAMP DISPLACEMENT AT TIP OF MICROPROBES
!nsel,s,loc,x, LEN+R+4.65E-3+2E-4, LEN+R+4.65E-3+2E-4
!d,all,ux,0.0
!d,all,uy,0.0
!d,all,uz,0.0
! CLAMPING THE LONGITUDINAL NODE
nsel,s,loc,y, NODEY+CH/2-EH, NODEY+CH/2 ! clamp displacement
nsel,r,loc,x, NODEX-EW/2, NODEX+EW/2
d,all,ux,0.0
d,all,uy,0.0
d,all,uz,0.0
nsel,s,loc,y, -NODEY-CH/2+EH, -NODEY-CH/2 ! clamp displacement
nsel,r,loc,x, NODEX-EW/2, NODEX+EW/2
d,all,ux,0.0
d,all,uy,0.0
d,all,uz,0.0
NSEL,ALL ! NSEL: Selects a subset of nodes.
```

```
!MODOPT,SUBSP,40 ! MODOPT: Specifies modal analysis options.
!MXPAND,40,,,YES ! MXPAND: Specifies the number of modes to expand
! and write for a modal or buckling analysis.
MODOPT,LANB,5,1e5,1.2e5
MXPAND,5,,,YES
SOLVE ! SOLVE: Solve a solution.
FINISH ! FINISH: Exits normally from a processor.
!------------------
! POST-PROCESSING
!------------------
/POST1 ! /POST1: Enters the database results postprocessor.
SET,NEAR,,,0,110000
! SET: Defines the data set to be read from the results file.
PLNSOL,U,x,2 ! PLNSOL: Displays results as continuous contours.
/WAIT,3 ! /WAIT: Causes a delay before the next command.
```

APPENDIX B

MATHEMATICA CODE FOR MODELING ELECTRODE-ELECTROLYTE INTERFACE IMPEDANCE

B.1 Platinum wire

The following is the Mathematica^{TM} code for emperically modeling the experimentally measured Pt-wire and electrolyte interfacial impedance using the standard three-electrode system (Figure 2.17). The emperical fit to the experimental data (with error bars) allows us to extract the parameters of the equivalent circuit as shown in Figure 2.18:

B.1.1 Modulus of Impedance

```
xy =
ReadList[
"C:\\Documents and Settings\\Abhishek\\Desktop\\Modelling
Electrolyte-Electrode
Interface\\Ptwire_meanModZ_300KHzto10mHz_1mV.txt",
Table[Number, {2}]];

xyerror =
ReadList[
"C:\\Documents and Settings\\Abhishek\\Desktop\\Modelling
Electrolyte-Electrode
Interface\\Ptwire_errModZ_300KHzto10mHz_1mV.txt"];
```

$$\text{Delta}[\omega\_] := \left(q^{-\beta} + \text{Rct}\omega^{\beta}\text{Cos}\left[\frac{\beta * \text{Pi}}{2}\right]\right)^2 + \left(\text{Rct}\omega^{\beta}\text{Sin}\left[\frac{\beta * \text{Pi}}{2}\right]\right)^2$$

$$\text{RE}[\omega\_] := \frac{\text{Rct}q^{-\beta}\left(q^{-\beta} + \text{Rct}\omega^{\beta}\text{Cos}\left[\frac{\beta * \text{Pi}}{2}\right]\right)}{\text{Delta}[\omega]} + \text{Rs}$$

$$\text{XE}[\omega\_] := \frac{\text{Rct}^2 q^{-\beta}\omega^{\beta}\text{Sin}\left[\frac{\beta * \text{Pi}}{2}\right]}{\text{Delta}[\omega]}$$

$$G[\omega\_] := \text{RE}[\omega] - \text{XE}[\omega] I$$

$$\text{modG}[\omega\_, \text{q}\_, \beta\_, \text{Rct}\_, \text{Rs}\_] :=$$
$$\text{Log}\left[10, \text{Sqrt}\left[\left(\frac{\text{Rct}q^{-\beta}\left(q^{-\beta} + \text{Rct}\omega^{\beta}\text{Cos}\left[\frac{\beta * \text{Pi}}{2}\right]\right)}{\left(q^{-\beta} + \text{Rct}\omega^{\beta}\text{Cos}\left[\frac{\beta * \text{Pi}}{2}\right]\right)^2 + \left(\text{Rct}\omega^{\beta}\text{Sin}\left[\frac{\beta * \text{Pi}}{2}\right]\right)^2} + \text{Rs}\right)^2 + \left(\frac{\text{Rct}^2 q^{-\beta}\omega^{\beta}\text{Sin}\left[\frac{\beta * \text{Pi}}{2}\right]}{\left(q^{-\beta} + \text{Rct}\omega^{\beta}\text{Cos}\left[\frac{\beta * \text{Pi}}{2}\right]\right)^2 + \left(\text{Rct}\omega^{\beta}\text{Sin}\left[\frac{\beta * \text{Pi}}{2}\right]\right)^2}\right)^2\right]\right]$$

```
Needs["NonlinearRegression`"]
```

```
nr = NonlinearRegress [xy, {modG [2π10^f, q, β, Rct, Rs]} ,
{{q, 6.01518*^-8}, {β, 0.92535}, {Rct, 13.364466*^6}, {Rs, 57.25}},
f, Weights → xyerror, ConfidenceLevel → .99]
```

```
nrmodel = modG [2π10^f, q, β, Rct, Rs] ;
Evaluate[nrmodel/.Last[First[nr]]];
modelf =
```

Function [{f}, Evaluate [modG [$2\pi 10^f, q, \beta$, Rct, Rs] /.Last[First[nr]]]] ;

Plot[modelf[f], {$f, -2, 6$}, Epilog → Map[Point, xy]]

B.1.2 Phase of Impedance

xy =

ReadList[

"C:\\Documents and Settings\\Abhishek\\Desktop\\Modelling

Electrolyte-Electrode

Interface\\Ptwire_meanPhase_300KHzto10mHz_1mV.txt",

Table[Number, {2}]];

xyerror =

ReadList[

"C:\\Documents and Settings\\Abhishek\\Desktop\\Modelling

Electrolyte-Electrode

Interface\\Ptwire_errPhase_300KHzto10mHz_1mV.txt"];

(*Rs=25*)

$$\text{Delta}[\omega\_]:=\left(q^{-\beta}+\text{Rct}\omega^{\beta}\text{Cos}\left[\frac{\beta*\text{Pi}}{2}\right]\right)^2+\left(\text{Rct}\omega^{\beta}\text{Sin}\left[\frac{\beta*\text{Pi}}{2}\right]\right)^2$$

$$\text{RE}[\omega\_]:=\frac{\text{Rct}q^{-\beta}\left(q^{-\beta}+\text{Rct}\omega^{\beta}\text{Cos}\left[\frac{\beta*\text{Pi}}{2}\right]\right)}{\text{Delta}[\omega]}+\text{Rs}$$

$$\mathrm{XE}[\omega\_]:=\frac{\mathrm{Rct}^2 q^{-\beta}\omega^{\beta}\mathrm{Sin}\left[\frac{\beta*\mathrm{Pi}}{2}\right]}{\mathrm{Delta}[\omega]}$$

$$G[\omega\_]:=\mathrm{RE}[\omega]-\mathrm{XE}[\omega]I$$

$$\mathrm{phaseG}[\omega\_, \mathrm{q}\_, \beta\_, \mathrm{Rct}\_, \mathrm{Rs}\_]:=$$
$$\frac{180}{\pi}\mathrm{ArcTan}\left[-\frac{\left(\frac{\mathrm{Rct}^2 q^{-\beta}\omega^{\beta}\mathrm{Sin}\left[\frac{\beta*\mathrm{Pi}}{2}\right]}{\left(q^{-\beta}+\mathrm{Rct}\omega^{\beta}\mathrm{Cos}\left[\frac{\beta*\mathrm{Pi}}{2}\right]\right)^2+\left(\mathrm{Rct}\omega^{\beta}\mathrm{Sin}\left[\frac{\beta*\mathrm{Pi}}{2}\right]\right)^2}\right)}{\left(\frac{\mathrm{Rct}q^{-\beta}\left(q^{-\beta}+\mathrm{Rct}\omega^{\beta}\mathrm{Cos}\left[\frac{\beta*\mathrm{Pi}}{2}\right]\right)}{\left(q^{-\beta}+\mathrm{Rct}\omega^{\beta}\mathrm{Cos}\left[\frac{\beta*\mathrm{Pi}}{2}\right]\right)^2+\left(\mathrm{Rct}\omega^{\beta}\mathrm{Sin}\left[\frac{\beta*\mathrm{Pi}}{2}\right]\right)^2}+\mathrm{Rs}\right)}\right]$$

```
Needs["NonlinearRegression`"]

nr = NonlinearRegress[xy,
{phaseG [2π10^f, q, β, Rct, Rs] , q > 0} ,
{{q, 1.9984623127399138*^-7}, {β, "0.90808"},
{Rct, "1.89082" × 10^"7"}, {Rs, "57.6129"}}, f,
Weights → xyerror, ConfidenceLevel → .99]

nrmodel = phaseG [2π10^f, q, β, Rct, "56.4696"] ;
Evaluate[nrmodel/.Last[First[nr]]];
modelf =
Function[{f},
Evaluate [phaseG [2π10^f, q, β, Rct, "56.4696"] /.
Last[First[nr]]]];
Plot[modelf[f], {f, −2, 6}, Epilog → Map[Point, xy]]
```

B.2 Platinum electrode on silicon microprobe

The following is the Mathematica^{TM} code for emperically modeling the experimentally measured interfacial impedance between the Pt-electrode on the silicon microprobe and electrolyte, using the standard three-electrode system (Figure 2.17). The emperical fit to the experimental data (with error bars) allows us to extract the parameters of the equivalent circuit as shown in Figure 2.19:

B.2.1 Modulus of Impedance

```
xy =
ReadList[
"C:\\Documents and Settings\\Abhishek\\Desktop\\Modelling
Electrolyte-Electrode
Interface\\SiliconMicroprobe_meanModZ_300KHzto10mHz_1mV.txt",
Table[Number, {2}]];

xyerror =
ReadList[
"C:\\Documents and Settings\\Abhishek\\Desktop\\Modelling
Electrolyte-Electrode
Interface\\SiliconMicroprobe_errModZ_300KHzto10mHz_1mV.txt"];

Delta[ω_, q_, β_, Rct_, Rs_]:= (q^-β + Rctω^βCos [β*Pi/2])^2 + (Rctω^βSin [β*Pi/2])^2
```

$$\mathrm{RE}[\omega\_, \mathrm{q}\_, \beta\_, \mathrm{Rct}\_, \mathrm{Rs}\_] := \frac{\mathrm{Rct} q^{-\beta}\left(q^{-\beta} + \mathrm{Rct}\omega^{\beta}\mathrm{Cos}\left[\frac{\beta * \mathrm{Pi}}{2}\right]\right)}{\mathrm{Delta}[\omega, q, \beta, \mathrm{Rct}, \mathrm{Rs}]} + \mathrm{Rs}$$

$$\mathrm{XE}[\omega\_, \mathrm{q}\_, \beta\_, \mathrm{Rct}\_, \mathrm{Rs}\_] := \frac{\mathrm{Rct}^2 q^{-\beta}\omega^{\beta}\mathrm{Sin}\left[\frac{\beta * \mathrm{Pi}}{2}\right]}{\mathrm{Delta}[\omega, q, \beta, \mathrm{Rct}, \mathrm{Rs}]}$$

$$G[\omega\_, \mathrm{q}\_, \beta\_, \mathrm{Rct}\_, \mathrm{Rs}\_] := \mathrm{RE}[\omega, q, \beta, \mathrm{Rct}, \mathrm{Rs}] - \mathrm{XE}[\omega, q, \beta, \mathrm{Rct}, \mathrm{Rs}] I$$

$$\mathrm{modG}[\omega\_, \mathrm{q}\_, \beta\_, \mathrm{Rct}\_, \mathrm{Rs}\_] :=$$
$$\mathrm{Log}\left[10, \mathrm{Sqrt}\left[\left(\frac{\mathrm{Rct} q^{-\beta}\left(q^{-\beta} + \mathrm{Rct}\omega^{\beta}\mathrm{Cos}\left[\frac{\beta * \mathrm{Pi}}{2}\right]\right)}{\left(q^{-\beta} + \mathrm{Rct}\omega^{\beta}\mathrm{Cos}\left[\frac{\beta * \mathrm{Pi}}{2}\right]\right)^2 + \left(\mathrm{Rct}\omega^{\beta}\mathrm{Sin}\left[\frac{\beta * \mathrm{Pi}}{2}\right]\right)^2} + \mathrm{Rs}\right)^2 + \left(\frac{\mathrm{Rct}^2 q^{-\beta}\omega^{\beta}\mathrm{Sin}\left[\frac{\beta * \mathrm{Pi}}{2}\right]}{\left(q^{-\beta} + \mathrm{Rct}\omega^{\beta}\mathrm{Cos}\left[\frac{\beta * \mathrm{Pi}}{2}\right]\right)^2 + \left(\mathrm{Rct}\omega^{\beta}\mathrm{Sin}\left[\frac{\beta * \mathrm{Pi}}{2}\right]\right)^2}\right)^2\right]\right]$$

```
Needs["NonlinearRegression`"]

nr = NonlinearRegress [xy, {modG [2π10^f, q, β, Rct, Rs]},
{{q, 6.41681*^-11}, {β, 0.9002}, {Rct, 5.375248028*^9}, {Rs, 9077}},
f, Weights → xyerror, ConfidenceLevel → .99]

nrmodel = modG [2π10^f, q, β, Rct, Rs] ;
Evaluate[nrmodel/.Last[First[nr]]];
modelf =
Function [{f}, Evaluate [modG [2π10^f, q, β, Rct, Rs] /.Last[First[nr]]]] ;
Plot[modelf[f], {f, −2, 6}, Epilog → Map[Point, xy]]
```

B.2.2 Phase of Impedance

```
xy =
ReadList[
"C:\\Documents and Settings\\Abhishek\\Desktop\\Modelling
Electrolyte-Electrode
Interface\\SiliconMicroprobe_meanPhase_300KHzto10mHz_1mV.txt",
Table[Number, {2}]];

xyerror =
ReadList[
"C:\\Documents and Settings\\Abhishek\\Desktop\\Modelling
Electrolyte-Electrode
Interface\\SiliconMicroprobe_errPhase_300KHzto10mHz_1mV.txt"];
```

$$\text{Delta}[\omega\_] := \left(q^{-\beta} + \text{Rct}\omega^{\beta}\text{Cos}\left[\frac{\beta*\text{Pi}}{2}\right]\right)^2 + \left(\text{Rct}\omega^{\beta}\text{Sin}\left[\frac{\beta*\text{Pi}}{2}\right]\right)^2$$

$$\text{RE}[\omega\_] := \frac{\text{Rct}q^{-\beta}\left(q^{-\beta}+\text{Rct}\omega^{\beta}\text{Cos}\left[\frac{\beta*\text{Pi}}{2}\right]\right)}{\text{Delta}[\omega]} + \text{Rs}$$

$$\text{XE}[\omega\_] := \frac{\text{Rct}^2 q^{-\beta}\omega^{\beta}\text{Sin}\left[\frac{\beta*\text{Pi}}{2}\right]}{\text{Delta}[\omega]}$$

$$G[\omega\_] := \text{RE}[\omega] - \text{XE}[\omega]I$$

```
phaseG[ω_, q_, β_, Rct_, Rs_]:=
```

$$\frac{180}{\pi}\text{ArcTan}\left[-\frac{\left(\frac{\text{Rct}^2 q^{-\beta}\omega\beta\text{Sin}\left[\frac{\beta*\text{Pi}}{2}\right]}{\left(q^{-\beta}+\text{Rct}\omega\beta\text{Cos}\left[\frac{\beta*\text{Pi}}{2}\right]\right)^2+\left(\text{Rct}\omega\beta\text{Sin}\left[\frac{\beta*\text{Pi}}{2}\right]\right)^2}\right)}{\left(\frac{\text{Rct}q^{-\beta}\left(q^{-\beta}+\text{Rct}\omega\beta\text{Cos}\left[\frac{\beta*\text{Pi}}{2}\right]\right)}{\left(q^{-\beta}+\text{Rct}\omega\beta\text{Cos}\left[\frac{\beta*\text{Pi}}{2}\right]\right)^2+\left(\text{Rct}\omega\beta\text{Sin}\left[\frac{\beta*\text{Pi}}{2}\right]\right)^2}+\text{Rs}\right)}\right]$$

```
Needs["NonlinearRegression`"]


nr = NonlinearRegress[xy,
{phaseG [2π10^f, q, β, Rct, Rs] , q > 0} ,
{{q, 9.367480570109006*^-11}, {β, "0.896298"},
{Rct, "5.79043" × 10^"9"}, {Rs, "7671.11"}}, f,
Weights → xyerror, ConfidenceLevel → .99]


nrmodel = phaseG [2π10^f, q, β, Rct, Rs] ;
Evaluate[nrmodel/.Last[First[nr]]];
modelf =
Function[{f},
Evaluate [phaseG [2π10^f, q, β, Rct, Rs] /.Last[First[nr]]] ;
Plot[modelf[f], {f, −2, 6}, Epilog → Map[Point, xy]]
```

APPENDIX C

MORPHOLOGICAL ANALYSIS OF HISTOLOGICAL CROSS-SECTIONS OF SEMINIFEROUS TUBULES

The MATLAB^{TM} code for morphological analysis of histological cross-sections of testicular tissue containing seminiferous tubules is described in this appendix:

```
%Prior to running the program, please download 2 files the
%following links and include the paths of the file in MATLAB -
%http://eslab.bu.edu/software/graphanalysis
%/graphAnalysisToolbox-1.0.tar.gz and
%http://www.cns.bu.edu/\%7Elgrady/random_walker_matlab_code.zip.

clc
close all
clear
cd 'C:\Histology\'
p = dir;
N = size(p);
N = N(1);

cnt = 0; % Counter for tubule_radius vector
for fcnt = 1:N-1 % Files loop
next = 'y';

while next == 'y' %Ellipses loop
```

```
close all
I = double(imread(strcat('C:\Histology\',p(fcnt+8).name)));
M  = max(max(max(I)));
I = I/M;

disp('Current file being analyzed:');
p(fcnt+8).name

%% CROPPING THE IMAGE
imshow(I);
title(' Crop image by drawing a rectangle and double-click
to confirm.');
h = imrect;
position = round(wait(h)); % getting vertices of the rectangle;
close all;

I = I(position(2):position(2)+position(4),
position(1):position(1)+position(3),:);
[X,Y,F] = size(I);

%% GENERATING TRIMAP
trimap = 0.5*ones(X,Y);

close all;
imshow(I);
```

```
title('Please trace inside the cell.
   Note everything INSIDE this will be marked as cell');
h = imfreehand(gca);
position = wait(h);
bwf = poly2mask(position(:,1),position(:,2),X,Y);
trimap(find(bwf==1))=1;

close all;
imshow(I);
title('Please trace outside the cell.
 Note everything OUTSIDE this will be marked as background');
h = imfreehand(gca);
position = wait(h);
bwg = poly2mask(position(:,1),position(:,2),X,Y);
trimap(find(bwg==0))=0;

%% SEGMENTATION
seeds = find(trimap~=0.5); % seeds are the pixels marked by user
labels = trimap(seeds); %labels are what user calls these regions
mask = random_walker(I,seeds,labels);
mask = mask-min(min(mask));

% These few lines for generating J are just for
% visualization purpose.
J = I;
for i=1:3
```

```
    K = I(:,:,i);
    K(find(trimap==1))=1;
    K(find(trimap==0))=0;
    J(:,:,i)=K;
end

subplot(2,2,1); imshow(I); title('Cropped image');
subplot(2,2,2); imshow(J); title('Marking by the user');
subplot(2,2,3); imshow(trimap); title('Knowns and unknowns');
subplot(2,2,4); imshow(I); hold on;
pts = contour(mask, [0.5 0.5], 'r');
title('Segmentation'); %%% we are now extracting boundary points

%% ELLIPSE FITTING
%%%%%% It is useful to refer to the following reference:
%%%%%% http://mathworld.wolfram.com/Ellipse.html
pts = pts(:,2:end); %% the first entry is to be discarded
%%% AN ellipse is of the form ax^2 + 2bxy + cy^2 + 2dx + 2fy + g;
%%% We shall estimate that now

[X,Y,F] = size(I);
x = pts(1,:)'; %%% scaling the points between 0 and 1
y = pts(2,:)'; %%% scaling the points between 0 and 1

D = [x.^2 x.*y y.^2 x y ones(size(x))]; %CREATE MATRIX OF MONOMIALS
A = D(:,1:end-1);
```

```
B = D(:,end);
v = -A\B;

a = v(1);
b = v(2)/2;
c = v(3);
d = v(4)/2;
f = v(5)/2;
g = 1;

%%  ELLIPSE VERIFICATION
crit1 = det([a b d; b c f; d f g]);
crit2 = det([a b; b c]);
crit3 = a+b;

if ((crit2>0) && (crit1/crit3 <0))
    disp('Criteria checked and valid ellipse detected');
else
    disp('Criteria checked and invalid ellipse detected');
end

%% CALCULATION OF THE AXES LENGTH

nr = 2*(a*f*f +c*d*d + g*b*b - 2*b*d*f - a*c*g);
dr1 = b*b-a*c;
dr2 = sqrt((a-c)^2 + 4*b^2);
```

```
dr3 = -(a+c);

major_axis_length = 2*sqrt(nr/(dr1*(dr3+dr2)));
minor_axis_length = 2*sqrt(nr/(dr1*(dr3-dr2)));

if cnt == 0
    tubule_radius = minor_axis_length
else
    tubule_radius = [tubule_radius minor_axis_length]
end
cnt = cnt+1;

next = input('Continue analyzing same image? (y/n) [y] ', 's');
if isempty(next)
    next = 'y';
end

end % Ellipses loop end

end % Files loop end

save histology_results.mat
```

APPENDIX D

MICROSOFT VISUAL STUDIO CODE FOR STRAIN GAUGE-BASED FORCE FEEDBACK

The WINAPI project created in Microsoft Visual Studio required 3 types of files for successfully compiling and creating the software - Header, Resource and Source files. Aside from the above mentioned file types other files such as .obj and .lib files are needed for successfully compiling the project. The following sections describe the codes corresponding to the different types of files required:

D.1 Header files

D.1.1 Manipulator.h

```
#include "extcode.h"
#pragma pack(push)
#pragma pack(1)
#ifdef __cplusplus
extern "C" {
#endif
void __stdcall ManipulatorMotion(double DistanceToBeProbedInMm,
double VelocityXYZInRevSecMmSec);
long __cdecl LVDLLStatus(char *errStr, int errStrLen, void *module);
#ifdef __cplusplus
} // extern "C"
#endif
```

```
#pragma pack(pop)
```

D.1.2 myuir.h

```
/*****************************************************************/
/* LabWindows/CVI User Interface Resource (UIR) Include File     */
/* Copyright (c) National Instruments 2009. All Rights Reserved. */
/*                                                               */
/* WARNING: Do not add to, delete from, or otherwise modify the  */
/*          contents of this include file.                       */
/*****************************************************************/
#include <userint.h>
#ifdef __cplusplus
    extern "C" {
#endif
     /* Panels and Controls: */
#define  PANEL                           1
#define  PANEL_STATUS                    2
#define  PANEL_THRESHOLD                 3
#define  PANEL_STRIPCHART                4
#define  PANEL_JoystickLED               5
     /* Menu Bars, Menus, and Menu Items: */
          /* (no menu bars in the resource file) */
     /* (no callbacks specified in the resource file) */
#ifdef __cplusplus
    }
```

```
#endif
```

D.1.3 resource.h

```
//{{NO_DEPENDENCIES}}
// Microsoft Visual C++ generated include file.
// Used by FFbackAPI.rc
//
#define IDD_FORCE_FEEDBACK              102
#define IDI_MAIN                        102
#define IDC_CLOSE                       1000
#define IDC_BUTTON1                     1001
#define IDC_EDIT1                       1008
#define IDC_BUTTON3                     1010
#define IDC_BUTTON2                     1011
#define IDC_BUTTON4                     1012
#define IDC_BUTTON5                     1013
#define IDC_BUTTON6                     1016
#define IDC_EDIT2                       1018
#define IDC_EDIT3                       1019
#define IDC_ANIMATE1                    1023
// Next default values for new objects
//
#ifdef APSTUDIO_INVOKED
#ifndef APSTUDIO_READONLY_SYMBOLS
#define _APS_NEXT_RESOURCE_VALUE        104
```

```
#define _APS_NEXT_COMMAND_VALUE         40001
#define _APS_NEXT_CONTROL_VALUE         1024
#define _APS_NEXT_SYMED_VALUE           101
#endif
#endif
```

D.2 Resource files

D.2.1 FFBackAPI.rc

```
// Microsoft Visual C++ generated resource script.
//
#include "resource.h"
#define APSTUDIO_READONLY_SYMBOLS
////////////////////////////////////////////////////////////////////
//
// Generated from the TEXTINCLUDE 2 resource.
//
#include "afxres.h"
////////////////////////////////////////////////////////////////////
#undef APSTUDIO_READONLY_SYMBOLS
////////////////////////////////////////////////////////////////////
// English (U.S.) resources
#if !defined(AFX_RESOURCE_DLL) || defined(AFX_TARG_ENU)
#ifdef _WIN32
```

```
LANGUAGE LANG_ENGLISH, SUBLANG_ENGLISH_US
#pragma code_page(1252)
#endif //_WIN32
//////////////////////////////////////////////////////////////////////
//
// RT_MANIFEST
//
1                       RT_MANIFEST             "ffconst.manifest"
//////////////////////////////////////////////////////////////////////
//
// Dialog
//
IDD_FORCE_FEEDBACK DIALOGEX 250, 75, 163, 201
STYLE DS_SETFONT | DS_MODALFRAME | DS_SETFOREGROUND | WS_POPUP |
WS_CAPTION | WS_SYSMENU
EXSTYLE WS_EX_PALETTEWINDOW
CAPTION "Tissue Diagnosis - Control frame"
FONT 9, "Calibri", 400, 0, 0x0
BEGIN
    DEFPUSHBUTTON   "Exit",IDCANCEL,97,169,50,14
    LTEXT           "Please enter 'Motion Parameters'",
    IDC_STATIC,7,4,135,8
    LTEXT           "and click 'Initiate PlotPanel' button.",
    IDC_STATIC,7,12,132,8
    EDITTEXT        IDC_EDIT1,13,142,136,16,ES_CENTER |
    ES_MULTILINE | ES_AUTOHSCROLL | ES_READONLY | NOT WS_BORDER
```

```
    PUSHBUTTON      "Invesitigate",IDC_BUTTON2,87,101,50,14,
    BS_CENTER
    PUSHBUTTON      "Initiate PlotPanel",IDC_BUTTON1,23,97,50,23,
    BS_CENTER | BS_MULTILINE
    LTEXT           "Click 'Investigate' button  to start!",
    IDC_STATIC,8,20,132,8
    GROUPBOX        "Motion Parameters",IDC_STATIC,8,35,144,45
    GROUPBOX        "Module Status",IDC_STATIC,9,132,144,30
    EDITTEXT        IDC_EDIT2,27,57,40,13,ES_CENTER | ES_AUTOHSCROLL
    EDITTEXT        IDC_EDIT3,94,57,40,13,ES_CENTER | ES_AUTOHSCROLL
    LTEXT           "Distance (mm)",IDC_STATIC,19,46,54,8
    LTEXT           "Velocity (mu-m/s)",IDC_STATIC,81,46,65,8
    GROUPBOX        "Tissue Diagnosis",IDC_STATIC,9,86,144,40
    LTEXT           "(c) 2009 Copyright Abhishek Ramkumar.",
    IDC_STATIC,7,188,149,8
END
#ifdef APSTUDIO_INVOKED
//////////////////////////////////////////////////////////////////////
//
// TEXTINCLUDE
//
1 TEXTINCLUDE
BEGIN
    "resource.h\0"
END
2 TEXTINCLUDE
```

```
BEGIN
    "#include ""afxres.h""\r\n"
    "\0"
END
3 TEXTINCLUDE
BEGIN
    "\r\n"
    "\0"
END
#endif    // APSTUDIO_INVOKED
////////////////////////////////////////////////////////////////////////
//
// Icon
//
// Icon with lowest ID value placed first to ensure application icon
// remains consistent on all systems.
IDI_MAIN                ICON                    "..\\directx.ico"
////////////////////////////////////////////////////////////////////////
//
// DESIGNINFO
//
#ifdef APSTUDIO_INVOKED
GUIDELINES DESIGNINFO
BEGIN
    IDD_FORCE_FEEDBACK, DIALOG
    BEGIN
```

```
        RIGHTMARGIN, 162
        BOTTOMMARGIN, 200
    END
END
#endif    // APSTUDIO_INVOKED
#endif    // English (U.S.) resources
/////////////////////////////////////////////////////////////////////////
#ifndef APSTUDIO_INVOKED
/////////////////////////////////////////////////////////////////////////
//
// Generated from the TEXTINCLUDE 3 resource.
//
/////////////////////////////////////////////////////////////////////////
#endif    // not APSTUDIO_INVOKED
```

D.3 Source files

D.3.1 FFBackAPI.cpp

```
//-----------------------------------------------------------------
// File: FFbackAPI.cpp
//
// Desc: Demonstrates an application which sets a force feedback
//       constant force determined by stiffness of the tissue
//  encountered by Ultrasonic Microprobes.
```

```
// Copyright (c) Ramkumar Abhishek, Cornell University. All rights
// reserved.
//-----------------------------------------------------------------------
#define STRICT
#define DIRECTINPUT_VERSION 0x0800
#include <stdio.h>
#include <tchar.h>
#include <windows.h>
#include <windowsx.h>
#include <commctrl.h>
#include <basetsd.h>
#include <mmsystem.h>
#include <dinput.h>
#include <math.h>
#include <time.h> // for wait function
#include <string.h>
#pragma warning( disable : 4996 ) // disable deprecated warning
#include <strsafe.h>
#pragma warning( default : 4996 )
#include "resource.h"
#if defined(DEBUG) | defined(_DEBUG)
#include <crtdbg.h>
#endif

// Labview header files
//CVI User Interface Resource (UIR)
```

```
#include <cvirte.h>
#include <userint.h>
#include <ansi_c.h>
#include "myuir.h"

// NIDAQmx
#include <formatio.h>
#include <NIDAQmx.h>

// Manipulator Header file
#include "Manipulator.h"

//---------------------------------------------------------------
// Function prototypes
//---------------------------------------------------------------
//Joystick
INT_PTR CALLBACK MainDlgProc( HWND hDlg, UINT msg, WPARAM wParam,
 LPARAM lParam );
BOOL CALLBACK EnumFFDevicesCallback( const DIDEVICEINSTANCE* pInst,
 VOID* pContext );
BOOL CALLBACK EnumAxesCallback( const DIDEVICEOBJECTINSTANCE*
pdidoi, VOID* pContext );
HRESULT InitDirectInput( HWND hDlg );
VOID FreeDirectInput();
HRESULT JoystickTrigger( HWND hDlg, double x );
INT CoordToForce( INT x );
```

```
HRESULT SetDeviceForcesXY();


//-----------------------------------------------------------------
// Defines, constants, and global variables
//-----------------------------------------------------------------
#define SAFE_DELETE(p)  { if(p) { delete (p);     (p)=NULL; } }
#define SAFE_RELEASE(p) { if(p) { (p)->Release(); (p)=NULL; } }
#define FEEDBACK_WINDOW_X       20
#define FEEDBACK_WINDOW_Y       60
#define FEEDBACK_WINDOW_WIDTH   200
#define windowLength 1800
//Joystick
LPDIRECTINPUT8          g_pDI = NULL;
LPDIRECTINPUTDEVICE8    g_pDevice = NULL;
LPDIRECTINPUTEFFECT     g_pEffect = NULL;
BOOL                    g_bActive = TRUE;
DWORD                   g_dwNumForceFeedbackAxis = 0;
INT                     g_nXForce;
INT                     g_nYForce;
DWORD                   g_dwLastEffectSet;
HWND hDlg_global;
//NIDAQmx
TaskHandle taskHandle=0;
int filewritestatus = -1, k = 0;
double flag = 0;
long duration = 0, BeforeTime, AfterTime, N = 500;
```

```
int32 DAQmxErrorFlag, DAQmxDoneAcquire;
size_t nSize;
wchar_t *display;
//Labview Plotting
static int panelHandle, counter;
static int numButtonPresses = 0;
static char msgString[100];
#define NBLEFT  100
static double dataArray[50];

//--------------------------------------------------------------------
// Name: WinMain()
// Desc: Entry point for the application.  Since we use a simple
//       dialog for user interaction we don't need to pump messages.
//--------------------------------------------------------------------
INT WINAPI WinMain( HINSTANCE hInst, HINSTANCE, LPSTR, INT )
{
    // Enable run-time memory check for debug builds.
#if defined(DEBUG) | defined(_DEBUG)
    _CrtSetDbgFlag( _CRTDBG_ALLOC_MEM_DF | _CRTDBG_LEAK_CHECK_DF );
#endif
    InitCommonControls();
InitCVIRTE (hInst, 0, 0);
    // Display the main dialog box.
    DialogBox( hInst, MAKEINTRESOURCE( IDD_FORCE_FEEDBACK ), NULL,
     MainDlgProc );
```

```
    return 0;
}

//-----------------------------------------------------------------
// Name: MainDlgProc
// Desc: Handles dialog messages
//-----------------------------------------------------------------
INT_PTR CALLBACK MainDlgProc( HWND hDlg, UINT msg, WPARAM wParam,
 LPARAM lParam )
{
    switch( msg )
    {
        case WM_INITDIALOG:
            if( FAILED( InitDirectInput( hDlg ) ) )
            {
        MessageBox( NULL,_T( "Error Initializing DirectInput " )
                        _T( "The sample will now exit." ),
                        _T( "FFConst" ), MB_ICONERROR | MB_OK );
            EndDialog( hDlg, 0 );
            }
            // Init the time of the last force feedback effect
            g_dwLastEffectSet = timeGetTime();
SetWindowText(GetDlgItem(hDlg, IDC_EDIT1),_T("Waiting for
 Motion Parameters..."));
            break;
        case WM_COMMAND:
```

```
            switch( LOWORD( wParam ) )
            {
                case IDCANCEL:
DAQmxStopTask(taskHandle);
DAQmxClearTask(taskHandle);
EndDialog( hDlg, 0 );
KillTimer( hDlg, 0 );
FreeDirectInput();
CloseHandle(hSerial);
QuitUserInterface (0);
    DiscardPanel (panelHandle);
    CloseCVIRTE ();
                    break;
case IDC_BUTTON1:
SetWindowText(GetDlgItem(hDlg, IDC_EDIT1),_T("Loading
 PlotPanel..."));
panelHandle = LoadPanel (0, "myuir.uir", PANEL);
if(panelHandle <0)
{
MessagePopup("Error", "Unable to load myuir.uir, make
sure it is in the same directory as this executable.");
}
DisplayPanel (panelHandle);
SetCtrlAttribute (panelHandle, PANEL_STRIPCHART,
 ATTR_POINTS_PER_SCREEN, windowLength);
SetCtrlVal (panelHandle, PANEL_STATUS, "\nMicroprobe
```

```
 Strain Gauge PlotPanel and Joystick Initialized!");
SetCtrlAttribute (panelHandle, PANEL_JoystickLED,
 ATTR_ON_COLOR, VAL_GREEN);
SetCtrlAttribute (panelHandle, PANEL_JoystickLED,
 ATTR_OFF_COLOR, VAL_RED);
SetWindowText(GetDlgItem(hDlg, IDC_EDIT1),_T("Motion
 Stage, Strain Gauge and Joystick ready!"));
SetCtrlVal (panelHandle, PANEL_THRESHOLD, "\n80 mV
 below initial baseline");
break;

case IDC_BUTTON2:
SetWindowText(GetDlgItem(hDlg, IDC_EDIT1),_T("Initializing
 Motion stage..."));
g_pDevice->Acquire();
SetCtrlVal (panelHandle, PANEL_JoystickLED, 0);
double distance,velocity,LVflag,datapoint;
float velocity_float;
float64 data1,datasave[windowLength][2];
distance = -1.0*(GetDlgItemInt(hDlg, IDC_EDIT2, NULL,
 FALSE));
velocity = GetDlgItemInt(hDlg, IDC_EDIT3, NULL, FALSE);
velocity_float = 0.001*velocity;
ManipulatorMotion(distance, velocity_float);
SetCtrlVal (panelHandle, PANEL_STATUS, "\nAquiring
 Microprobe Strain Gauge data...");
```

```
ClearStripChart (panelHandle, PANEL_STRIPCHART);
flag = 0;
DAQmxLoadTask ("ai0_1data", &taskHandle);
DAQmxErrorFlag = DAQmxStartTask(taskHandle);
for (int cnt = 0; cnt < windowLength; cnt++)
{
BeforeTime = timeGetTime();
if ( cnt == 0 )
datasave[cnt][0] = (float64) timeGetTime();
else
datasave[cnt][0] = (float64) timeGetTime()
 - datasave[0][0];
DAQmxDoneAcquire = DAQmxReadAnalogScalarF64(taskHandle,
10.0,&data1,NULL);
datapoint = data1;
datasave[cnt][1] = data1;
if ( (datasave[0][1] - data1 > 0.015) & (cnt != 0) )
LVflag = 1;
else
LVflag = 0;
if ( LVflag-flag == 1 )
{
JoystickTrigger( hDlg, LVflag );
SetCtrlVal (panelHandle, PANEL_JoystickLED, 1);
}
flag = LVflag;
```

```
PlotStripChartPoint (panelHandle, PANEL_STRIPCHART,
 datapoint);
AfterTime = timeGetTime();
if ( cnt == 0 )
duration = AfterTime - BeforeTime;
else
duration = duration + (AfterTime - BeforeTime);
Sleep(20);
}
DAQmxStopTask(taskHandle);
DAQmxClearTask(taskHandle);
datasave[0][0] = 0;
filewritestatus = ArrayToFile("C:/DATA/data.txt",
 &datasave, VAL_DOUBLE, 2*windowLength, 2,
  VAL_DATA_MULTIPLEXED, VAL_GROUPS_AS_COLUMNS,
   VAL_SEP_BY_TAB, 0, VAL_ASCII, VAL_TRUNCATE);
fflush(stdout);
SetCtrlVal (panelHandle, PANEL_STATUS, "\nAquisition
 and Plotting completed!");
SetWindowText(GetDlgItem(hDlg, IDC_EDIT1),_T("DONE!"));
break;
                default:
                    return FALSE; // Message not handled
            }
            break;
```

```
        case WM_DESTROY:
            // Cleanup everything
            EndDialog( hDlg, 0 );
KillTimer( hDlg, 0 );
FreeDirectInput();
CloseHandle(hSerial);
QuitUserInterface (0);
DiscardPanel (panelHandle);
CloseCVIRTE ();
            break;
        default:
            return FALSE; // Message not handled
    }
    return TRUE; // Message handled
}

//-----------------------------------------------------------------------
// Name: InitDirectInput()
// Desc: Initialize the DirectInput variables.
//-----------------------------------------------------------------------
HRESULT InitDirectInput( HWND hDlg )
{
    DIPROPDWORD dipdw;
    HRESULT hr;

    // Register with the DirectInput subsystem and get a pointer
```

```
    // to a IDirectInput interface we can use.
    if( FAILED( hr = DirectInput8Create( GetModuleHandle( NULL ),
     DIRECTINPUT_VERSION, IID_IDirectInput8, (VOID**)&g_pDI, NULL)))
    {
        return hr;
    }
    // Look for a force feedback device we can use
    if( FAILED( hr = g_pDI->EnumDevices( DI8DEVCLASS_GAMECTRL,
                                EnumFFDevicesCallback, NULL,
                                DIEDFL_ATTACHEDONLY |
                                DIEDFL_FORCEFEEDBACK ) ) )
    {
        return hr;
    }
    if( NULL == g_pDevice )
    {
        MessageBox( NULL, _T( "Force feedback device not found. " )
                          _T( "The sample will now exit." ),
                          _T( "FFConst" ), MB_ICONERROR | MB_OK );
        EndDialog( hDlg, 0 );
        return S_OK;
    }
// Set the data format to "simple joystick" - a predefined data
// format. A data format specifies which controls on a device we
// are interested in, and how they should be reported.
//
```

```
// This tells DirectInput that we will be passing a DIJOYSTATE
// structure to IDirectInputDevice8::GetDeviceState(). Even though
// we won't actually do it in this sample. But setting the data
// format is important so that the DIJOFS_* values work properly.
    if( FAILED( hr = g_pDevice->SetDataFormat( &c_dfDIJoystick ) ) )
        return hr;

// Set the cooperative level to let DInput know how this device
// should interact with the system and with other DInput
// applications.
// Exclusive access is required in order to perform force feedback.
    if( FAILED( hr = g_pDevice->SetCooperativeLevel( hDlg,
                                            DISCL_EXCLUSIVE |
                                            DISCL_FOREGROUND ) ) )
    {
        return hr;
    }
    // Since we will be playing force feedback effects, we should
    // disable the auto-centering spring.
    dipdw.diph.dwSize = sizeof( DIPROPDWORD );
    dipdw.diph.dwHeaderSize = sizeof( DIPROPHEADER );
    dipdw.diph.dwObj = 0;
    dipdw.diph.dwHow = DIPH_DEVICE;
    dipdw.dwData = FALSE;
    if( FAILED( hr = g_pDevice->SetProperty( DIPROP_AUTOCENTER,
     &dipdw.diph ) ) )
```

```
        return hr;
    // Enumerate and count the axes of the joystick
    if( FAILED( hr = g_pDevice->EnumObjects( EnumAxesCallback,
                ( VOID* )&g_dwNumForceFeedbackAxis, DIDFT_AXIS ) ) )
        return hr;
    // This simple sample only supports one or two axis joysticks
    if( g_dwNumForceFeedbackAxis > 2 )
        g_dwNumForceFeedbackAxis = 2;
    // This application needs only one effect: Applying raw forces.
    DWORD rgdwAxes[2] = { DIJOFS_X, DIJOFS_Y };
    LONG rglDirection[2] = { 0, 0 };
    DICONSTANTFORCE cf = { 0 };
    DIEFFECT eff;
    ZeroMemory( &eff, sizeof( eff ) );
    eff.dwSize = sizeof( DIEFFECT );
    eff.dwFlags = DIEFF_CARTESIAN | DIEFF_OBJECTOFFSETS;
    //eff.dwDuration = 100000;
  eff.dwDuration = INFINITE;
    eff.dwSamplePeriod = 0;
    eff.dwGain = DI_FFNOMINALMAX;
    eff.dwTriggerButton = DIEB_NOTRIGGER;
    eff.dwTriggerRepeatInterval = 0;
    eff.cAxes = g_dwNumForceFeedbackAxis;
    eff.rgdwAxes = rgdwAxes;
    eff.rglDirection = rglDirection;
    eff.lpEnvelope = 0;
```

```
    eff.cbTypeSpecificParams = sizeof( DICONSTANTFORCE );
    eff.lpvTypeSpecificParams = &cf;
    eff.dwStartDelay = 0;
    // Create the prepared effect
    if( FAILED( hr = g_pDevice->CreateEffect( GUID_ConstantForce,
        &eff, &g_pEffect, NULL ) ) )
    {
        return hr;
    }
    if( NULL == g_pEffect )
        return E_FAIL;
    return S_OK;
}


//-----------------------------------------------------------------------
// Name: EnumAxesCallback()
// Desc: Callback function for enumerating the axes on a joystick
//       and counting each force feedback enabled axis
//-----------------------------------------------------------------------
BOOL CALLBACK EnumAxesCallback(const DIDEVICEOBJECTINSTANCE* pdidoi,
                               VOID* pContext )
{
    DWORD* pdwNumForceFeedbackAxis = ( DWORD* )pContext;
    if( ( pdidoi->dwFlags & DIDOI_FFACTUATOR ) != 0 )
        ( *pdwNumForceFeedbackAxis )++;
    return DIENUM_CONTINUE;
```

```
}


//-----------------------------------------------------------------
// Name: EnumFFDevicesCallback()
// Desc: Called once for each enumerated force feedback device. If
//       we find one, create a device interface on it so we can play
//  with it.
//-----------------------------------------------------------------
BOOL CALLBACK EnumFFDevicesCallback( const DIDEVICEINSTANCE* pInst,
                                     VOID* pContext )
{
    LPDIRECTINPUTDEVICE8 pDevice;
    HRESULT hr;
    // Obtain an interface to the enumerated force feedback device.
    hr = g_pDI->CreateDevice( pInst->guidInstance, &pDevice, NULL );

    // If it failed, then we can't use this device for some
    // bizarre reason.  (Maybe the user unplugged it while we
    // were in the middle of enumerating it.)
    if( FAILED( hr ) )
        return DIENUM_CONTINUE;
    // We successfully created an IDirectInputDevice8.
    // So stop looking for another one.
    g_pDevice = pDevice;
    return DIENUM_STOP;
}
```

```
//-----------------------------------------------------------------
// Name: FreeDirectInput()
// Desc: Initialize the DirectInput variables.
//-----------------------------------------------------------------
VOID FreeDirectInput()
{
    // Unacquire the device one last time just in case
    // the app tried to exit while the device is still acquired.
    if( g_pDevice )
        g_pDevice->Unacquire();
    // Release any DirectInput objects.
    SAFE_RELEASE( g_pEffect );
    SAFE_RELEASE( g_pDevice );
    SAFE_RELEASE( g_pDI );
}


//-----------------------------------------------------------------
// Name: JoystickTrigger()
// Desc: Starts the Joystick task defined in InitDirectInput
//-----------------------------------------------------------------
HRESULT JoystickTrigger( HWND hDlg, double x )
{
    HRESULT hr;
    DWORD dwCurrentTime;
```

```
    if( NULL == g_pEffect )
        return S_OK;
        dwCurrentTime = timeGetTime();
        if( dwCurrentTime - g_dwLastEffectSet < 100 )
        {
            // Don't allow setting effect more often than
            // 100ms since every time an effect is set, the
            // device will jerk.
            return S_OK;
        }

        g_dwLastEffectSet = dwCurrentTime;
        g_nXForce = 0;
g_nYForce = -DI_FFNOMINALMAX;
        if( FAILED( hr = SetDeviceForcesXY() ) )
            return hr;
    return S_OK;
}

//-----------------------------------------------------------------
// Name: CoordToForce()
// Desc: Convert a coordinate 0 <= nCoord <= FEEDBACK_WINDOW_WIDTH
//       to a force value in the range -DI_FFNOMINALMAX to
//  +DI_FFNOMINALMAX.
//-----------------------------------------------------------------
INT CoordToForce( INT nCoord )
```

```
{
    INT nForce = MulDiv( nCoord, 2 * DI_FFNOMINALMAX,
     FEEDBACK_WINDOW_WIDTH )- DI_FFNOMINALMAX;

    // Keep force within bounds
    if( nForce < -DI_FFNOMINALMAX )
        nForce = -DI_FFNOMINALMAX;

    if( nForce > +DI_FFNOMINALMAX )
        nForce = +DI_FFNOMINALMAX;

    return nForce;
}

//-----------------------------------------------------------------
// Name: SetDeviceForcesXY()
// Desc: Apply the X and Y forces to the effect we prepared.
//-----------------------------------------------------------------
HRESULT SetDeviceForcesXY()
{
    // Modifying an effect is basically the same as creating a new
    // one, except you need only specify the parameters you are
    // modifying
    LONG rglDirection[2] = { 0, 0 };
    DICONSTANTFORCE cf;
    if( g_dwNumForceFeedbackAxis == 1 )
```

```
{
    // If only one force feedback axis, then apply only one
    //  direction and keep the direction at zero
    cf.lMagnitude = g_nXForce;
    rglDirection[0] = 0;
}
else
{
    // If two force feedback axis, then apply magnitude from
    // both directions
    rglDirection[0] = g_nXForce;
    rglDirection[1] = g_nYForce;
    cf.lMagnitude = ( DWORD )sqrt( ( double )g_nXForce *
     ( double )g_nXForce + ( double )g_nYForce *
     ( double )g_nYForce );
}
DIEFFECT eff;
ZeroMemory( &eff, sizeof( eff ) );
eff.dwSize = sizeof( DIEFFECT );
eff.dwFlags = DIEFF_CARTESIAN | DIEFF_OBJECTOFFSETS;
eff.cAxes = g_dwNumForceFeedbackAxis;
eff.rglDirection = rglDirection;
eff.lpEnvelope = 0;
eff.cbTypeSpecificParams = sizeof( DICONSTANTFORCE );
eff.lpvTypeSpecificParams = &cf;
eff.dwStartDelay = 0;
```

```
    // Now set the new parameters and start the effect immediately.
    return g_pEffect->SetParameters( &eff, DIEP_DIRECTION |
                                     DIEP_TYPESPECIFICPARAMS |
                                     DIEP_START );
}
```

APPENDIX E

MICROSOFT VISUAL STUDIO CODE FOR STRAIN GAUGE-BASED FLUID VISCOSITY MEASUREMENT

The WINAPI project created in Microsoft Visual Studio required 3 types of files for successfully compiling and creating the software - Header, Resource and Source files. Aside from the above mentioned file types other files such as .obj and .lib files are needed for successfully compiling the project. The following sections describe the codes corresponding to the different types of files required:

E.1 Header files

E.1.1 fftw3.h

```
/*
 *Copyright (c) 2003, 2007-8 Matteo Frigo
 *Copyright (c) 2003, 2007-8 Massachusetts Institute of Technology
 *
 *The following statement of license applies *only* to this header
 *file, and *not* to the other files distributed with FFTW or
 *derived therefrom:
 *
 *Redistribution and use in source and binary forms, with or without
 *modification, are permitted provided that the following conditions
 *are met:
 *
```

```
 *1.Redistributions of source code must retain the above copyright
 *  notice, this list of conditions and the following disclaimer.
 *
 *2.Redistributions in binary form must reproduce the above
 *  copyright notice, this list of conditions and the following
 *  disclaimer inthe documentation and/or other materials provided
 *  with the distribution.
 *
  *THIS SOFTWARE IS PROVIDED BY THE AUTHOR ‘‘AS IS’’ AND ANY EXPRESS
 *OR IMPLIED WARRANTIES, INCLUDING, BUT NOT LIMITED TO, THE IMPLIED
 *WARRANTIES OF MERCHANTABILITY AND FITNESS FOR A PARTICULAR PURPOSE
 *ARE DISCLAIMED. IN NO EVENT SHALL THE AUTHOR BE LIABLE FOR ANY
 *DIRECT, INDIRECT, INCIDENTAL, SPECIAL, EXEMPLARY, OR CONSEQUENTIAL
 *DAMAGES (INCLUDING, BUT NOT LIMITED TO, PROCUREMENT OF SUBSTITUTE
 *GOODS OR SERVICES; LOSS OF USE, DATA, OR PROFITS; OR BUSINESS
 *INTERRUPTION) HOWEVER CAUSED AND ON ANY THEORY OF LIABILITY,
 *WHETHER IN CONTRACT, STRICT LIABILITY, OR TORT (INCLUDING
 *NEGLIGENCE OR OTHERWISE) ARISING IN ANY WAY OUT OF THE USE OF THIS
 *SOFTWARE, EVEN IF ADVISED OF THE POSSIBILITY OF SUCH DAMAGE.
 */
/************************ NOTE TO USERS ****************************
 *
 *                  THIS IS A HEADER FILE, NOT A MANUAL
 *
 *    If you want to know how to use FFTW, please read the manual,
 *    online at http://www.fftw.org/doc/ and also included with
```

```
 *    FFTW. For a quick start, see the manual's tutorial section.
 *
 *   (Reading header files to learn how to use a library is a habit
 *    stemming from code lacking a proper manual.  Arguably, it's a
 *    *bad* habit in most cases, because header files can contain
 *    interfaces that are not part of the public, stable API.)
 *
 ****************************************************************/
#ifndef FFTW3_H
#define FFTW3_H
#include <stdio.h>
#ifdef __cplusplus
extern "C"
{
#endif /* __cplusplus */
/* If <complex.h> is included, use the C99 complex type.  Otherwise
   define a type bit-compatible with C99 complex */
#if !defined(FFTW_NO_Complex) && defined(_Complex_I) &&
 defined(complex) && defined(I)
#  define FFTW_DEFINE_COMPLEX(R, C) typedef R _Complex C
#else
#  define FFTW_DEFINE_COMPLEX(R, C) typedef R C[2]
#endif
#define FFTW_CONCAT(prefix, name) prefix ## name
#define FFTW_MANGLE_DOUBLE(name) FFTW_CONCAT(fftw_, name)
#define FFTW_MANGLE_FLOAT(name) FFTW_CONCAT(fftwf_, name)
```

```
#define FFTW_MANGLE_LONG_DOUBLE(name) FFTW_CONCAT(fftwl_, name)
/* IMPORTANT: for Windows compilers, you should add a line
        #define FFTW_DLL
  here and in kernel/ifftw.h if you are compiling/using FFTW as a
  DLL, in order to do the proper importing/exporting, or
  alternatively compile with -DFFTW_DLL or the equivalent
  command-line flag.  This is not necessary under MinGW/Cygwin,
  where libtool does the imports/exports automatically. */
#if defined(FFTW_DLL) && (defined(_WIN32) || defined(__WIN32__))
   /* annoying Windows syntax for shared-library declarations */
# if defined(COMPILING_FFTW)/*defined in api.h when compiling FFTW*/
#    define FFTW_EXTERN extern __declspec(dllexport)
# else /* user is calling FFTW; import symbol */
#    define FFTW_EXTERN extern __declspec(dllimport)
# endif
#else
#  define FFTW_EXTERN extern
#endif
enum fftw_r2r_kind_do_not_use_me {
     FFTW_R2HC=0, FFTW_HC2R=1, FFTW_DHT=2,
     FFTW_REDFT00=3, FFTW_REDFT01=4, FFTW_REDFT10=5, FFTW_REDFT11=6,
     FFTW_RODFT00=7, FFTW_RODFT01=8, FFTW_RODFT10=9, FFTW_RODFT11=10
};
struct fftw_iodim_do_not_use_me {
     int n;                       /* dimension size */
     int is; /* input stride */
```

```
     int os; /* output stride */
};
#include <stddef.h> /* for ptrdiff_t */
struct fftw_iodim64_do_not_use_me {
     ptrdiff_t n;                       /* dimension size */
     ptrdiff_t is; /* input stride */
     ptrdiff_t os; /* output stride */
};
/*
  huge second-order macro that defines prototypes for all API
  functions.  We expand this macro for each supported precision
  X: name-mangling macro
  R: real data type
  C: complex data type
*/
#define FFTW_DEFINE_API(X, R, C)    \
FFTW_DEFINE_COMPLEX(R, C);    \
typedef struct X(plan_s) *X(plan);    \
typedef struct fftw_iodim_do_not_use_me X(iodim);    \
typedef struct fftw_iodim64_do_not_use_me X(iodim64);    \
typedef enum fftw_r2r_kind_do_not_use_me X(r2r_kind);    \
FFTW_EXTERN void X(execute)(const X(plan) p);    \
FFTW_EXTERN X(plan) X(plan_dft)(int rank, const int *n,   \
    C *in, C *out, int sign, unsigned flags);    \
FFTW_EXTERN X(plan) X(plan_dft_1d)(int n, C *in, C *out, int sign,\
       unsigned flags);    \
```

```
FFTW_EXTERN X(plan) X(plan_dft_2d)(int n0, int n1,   \
       C *in, C *out, int sign, unsigned flags);    \
FFTW_EXTERN X(plan) X(plan_dft_3d)(int n0, int n1, int n2,  \
       C *in, C *out, int sign, unsigned flags);    \
FFTW_EXTERN X(plan) X(plan_many_dft)(int rank, const int *n,\
                         int howmany,   \
                         C *in, const int *inembed,   \
                         int istride, int idist,   \
                         C *out, const int *onembed,   \
                         int ostride, int odist,   \
                         int sign, unsigned flags);    \
FFTW_EXTERN X(plan) X(plan_guru_dft)(int rank, const X(iodim)*dims,\
 int howmany_rank,   \
 const X(iodim) *howmany_dims,   \
 C *in, C *out,   \
 int sign, unsigned flags);    \
FFTW_EXTERN X(plan) X(plan_guru_split_dft)(int rank, \
 const X(iodim) *dims, int howmany_rank,   \
 const X(iodim) *howmany_dims,   \
 R *ri, R *ii, R *ro, R *io,   \
 unsigned flags);    \
FFTW_EXTERN X(plan) X(plan_guru64_dft)(int rank,   \
                         const X(iodim64) *dims,   \
 int howmany_rank,   \
 const X(iodim64) *howmany_dims,   \
 C *in, C *out,   \
```

```
 int sign, unsigned flags);    \
FFTW_EXTERN X(plan) X(plan_guru64_split_dft)(int rank,   \
                         const X(iodim64) *dims,   \
 int howmany_rank,   \
 const X(iodim64) *howmany_dims,   \
 R *ri, R *ii, R *ro, R *io,   \
 unsigned flags);    \
FFTW_EXTERN void X(execute_dft)(const X(plan) p, C *in, C *out);\
FFTW_EXTERN void X(execute_split_dft)(const X(plan) p,R *ri,R *ii,\
                                      R *ro, R *io);    \
FFTW_EXTERN X(plan) X(plan_many_dft_r2c)(int rank, const int *n,\
                            int howmany,   \
                            R *in, const int *inembed,   \
                            int istride, int idist,   \
                            C *out, const int *onembed,   \
                            int ostride, int odist,   \
                            unsigned flags);    \
FFTW_EXTERN X(plan) X(plan_dft_r2c)(int rank, const int *n,  \
                        R *in, C *out, unsigned flags);    \
FFTW_EXTERN X(plan) X(plan_dft_r2c_1d)(int n,R *in,C *out, \
  unsigned flags);    \
FFTW_EXTERN X(plan) X(plan_dft_r2c_2d)(int n0, int n1,   \
   R *in, C *out, unsigned flags);    \
FFTW_EXTERN X(plan) X(plan_dft_r2c_3d)(int n0, int n1,   \
   int n2,   \
   R *in, C *out, unsigned flags);    \
```

```
FFTW_EXTERN X(plan) X(plan_many_dft_c2r)(int rank, const int *n,\
     int howmany,   \
     C *in, const int *inembed,   \
     int istride, int idist,   \
     R *out, const int *onembed,   \
     int ostride, int odist,   \
     unsigned flags);    \
FFTW_EXTERN X(plan) X(plan_dft_c2r)(int rank, const int *n,   \
                         C *in, R *out, unsigned flags);    \
FFTW_EXTERN X(plan) X(plan_dft_c2r_1d)(int n,C *in,R *out,\
unsigned flags); \
FFTW_EXTERN X(plan) X(plan_dft_c2r_2d)(int n0, int n1,   \
   C *in, R *out, unsigned flags);    \
FFTW_EXTERN X(plan) X(plan_dft_c2r_3d)(int n0, int n1,   \
   int n2,   \
   C *in, R *out, unsigned flags);    \
FFTW_EXTERN X(plan) X(plan_guru_dft_r2c)(int rank,   \
     const X(iodim)*dims, int howmany_rank,   \
     const X(iodim) *howmany_dims,   \
     R *in, C *out,   \
     unsigned flags);    \
FFTW_EXTERN X(plan) X(plan_guru_dft_c2r)(int rank,    \
     const X(iodim) *dims, int howmany_rank,   \
     const X(iodim) *howmany_dims,   \
     C *in, R *out,   \
     unsigned flags);    \
```

```
FFTW_EXTERN X(plan) X(plan_guru_split_dft_r2c)(    \
                            int rank, const X(iodim) *dims,\
     int howmany_rank,   \
     const X(iodim) *howmany_dims,   \
     R *in, R *ro, R *io,   \
     unsigned flags);    \
FFTW_EXTERN X(plan) X(plan_guru_split_dft_c2r)(    \
                            int rank, const X(iodim) *dims,\
     int howmany_rank,   \
     const X(iodim) *howmany_dims,   \
     R *ri, R *ii, R *out,   \
     unsigned flags);    \
FFTW_EXTERN X(plan) X(plan_guru64_dft_r2c)(int rank,   \
                            const X(iodim64) *dims,   \
     int howmany_rank,   \
     const X(iodim64) *howmany_dims,   \
     R *in, C *out,   \
     unsigned flags);    \
FFTW_EXTERN X(plan) X(plan_guru64_dft_c2r)(int rank,   \
                            const X(iodim64) *dims,   \
     int howmany_rank,   \
     const X(iodim64) *howmany_dims,   \
     C *in, R *out,   \
     unsigned flags);    \
FFTW_EXTERN X(plan) X(plan_guru64_split_dft_r2c)(    \
                            int rank, const X(iodim64) *dims, \
```

```
     int howmany_rank,   \
     const X(iodim64) *howmany_dims,   \
     R *in, R *ro, R *io,   \
     unsigned flags);    \
FFTW_EXTERN X(plan) X(plan_guru64_split_dft_c2r)(    \
                              int rank, const X(iodim64) *dims, \
     int howmany_rank,   \
     const X(iodim64) *howmany_dims,   \
     R *ri, R *ii, R *out,   \
     unsigned flags);    \
FFTW_EXTERN void X(execute_dft_r2c)(const X(plan) p,R *in,C *out);\
FFTW_EXTERN void X(execute_dft_c2r)(const X(plan) p,C *in,R *out);\
FFTW_EXTERN void X(execute_split_dft_r2c)(const X(plan) p,   \
                                          R *in, R *ro, R *io);  \
FFTW_EXTERN void X(execute_split_dft_c2r)(const X(plan) p,   \
                                          R *ri, R *ii, R *out); \
FFTW_EXTERN X(plan) X(plan_many_r2r)(int rank, const int *n, \
                          int howmany,   \
                          R *in, const int *inembed,   \
                          int istride, int idist,   \
                          R *out, const int *onembed,   \
                          int ostride, int odist,   \
                          const X(r2r_kind) *kind, unsigned flags);\
FFTW_EXTERN X(plan) X(plan_r2r)(int rank, const int *n, R *in,  \
                       R *out, const X(r2r_kind) *kind, \
   unsigned flags);    \
```

```
FFTW_EXTERN X(plan) X(plan_r2r_1d)(int n, R *in, R *out,   \
                      X(r2r_kind) kind, unsigned flags);    \
FFTW_EXTERN X(plan) X(plan_r2r_2d)(int n0, int n1, R *in, R *out,\
                      X(r2r_kind) kind0, X(r2r_kind) kind1,  \
                      unsigned flags);    \
FFTW_EXTERN X(plan) X(plan_r2r_3d)(int n0, int n1, int n2,    \
                      R *in, R *out, X(r2r_kind) kind0,   \
                      X(r2r_kind) kind1, X(r2r_kind) kind2,  \
                      unsigned flags);    \
FFTW_EXTERN X(plan) X(plan_guru_r2r)(int rank,const X(iodim) *dims,\
                        int howmany_rank,   \
                        const X(iodim) *howmany_dims,   \
                        R *in, R *out,   \
                        const X(r2r_kind) *kind, unsigned flags);\
FFTW_EXTERN X(plan) X(plan_guru64_r2r)(int rank,    \
                        const X(iodim64) *dims, int howmany_rank,\
                        const X(iodim64) *howmany_dims,   \
                        R *in, R *out,   \
                        const X(r2r_kind) *kind, unsigned flags);\
FFTW_EXTERN void X(execute_r2r)(const X(plan) p, R *in, R *out);\
FFTW_EXTERN void X(destroy_plan)(X(plan) p);    \
FFTW_EXTERN void X(forget_wisdom)(void);    \
FFTW_EXTERN void X(cleanup)(void);    \
FFTW_EXTERN void X(set_timelimit)(double);    \
FFTW_EXTERN void X(plan_with_nthreads)(int nthreads);    \
FFTW_EXTERN int X(init_threads)(void);    \
```

```
FFTW_EXTERN void X(cleanup_threads)(void);    \
FFTW_EXTERN void X(export_wisdom_to_file)(FILE *output_file);    \
FFTW_EXTERN char *X(export_wisdom_to_string)(void);    \
FFTW_EXTERN void X(export_wisdom)(  \
                void (*write_char)(char c, void *), void *data);\
FFTW_EXTERN int X(import_system_wisdom)(void);    \
FFTW_EXTERN int X(import_wisdom_from_file)(FILE *input_file);    \
FFTW_EXTERN int X(import_wisdom_from_string)(  \
const char *input_string);    \
FFTW_EXTERN int X(import_wisdom)(int (*read_char)(void *),  \
void *data);    \
FFTW_EXTERN void X(fprint_plan)(const X(plan) p, \
FILE *output_file);    \
FFTW_EXTERN void X(print_plan)(const X(plan) p);    \
FFTW_EXTERN void *X(malloc)(size_t n);    \
FFTW_EXTERN void X(free)(void *p);    \
FFTW_EXTERN void X(flops)(const X(plan) p,   \
                          double *add, double *mul, double *fmas);\
FFTW_EXTERN double X(estimate_cost)(const X(plan) p);    \
FFTW_EXTERN const char X(version)[];    \
FFTW_EXTERN const char X(cc)[];    \
FFTW_EXTERN const char X(codelet_optim)[];
/* end of FFTW_DEFINE_API macro */
FFTW_DEFINE_API(FFTW_MANGLE_DOUBLE, double, fftw_complex)
FFTW_DEFINE_API(FFTW_MANGLE_FLOAT, float, fftwf_complex)
FFTW_DEFINE_API(FFTW_MANGLE_LONG_DOUBLE, long double, fftwl_complex)
```

```
#define FFTW_FORWARD (-1)
#define FFTW_BACKWARD (+1)
#define FFTW_NO_TIMELIMIT (-1.0)
/* documented flags */
#define FFTW_MEASURE (0U)
#define FFTW_DESTROY_INPUT (1U << 0)
#define FFTW_UNALIGNED (1U << 1)
#define FFTW_CONSERVE_MEMORY (1U << 2)
#define FFTW_EXHAUSTIVE (1U << 3) /* NO_EXHAUSTIVE is default */
#define FFTW_PRESERVE_INPUT (1U << 4) /*cancels FFTW_DESTROY_INPUT*/
#define FFTW_PATIENT (1U << 5) /* IMPATIENT is default */
#define FFTW_ESTIMATE (1U << 6)
/* undocumented beyond-guru flags */
#define FFTW_ESTIMATE_PATIENT (1U << 7)
#define FFTW_BELIEVE_PCOST (1U << 8)
#define FFTW_NO_DFT_R2HC (1U << 9)
#define FFTW_NO_NONTHREADED (1U << 10)
#define FFTW_NO_BUFFERING (1U << 11)
#define FFTW_NO_INDIRECT_OP (1U << 12)
#define FFTW_ALLOW_LARGE_GENERIC (1U << 13)
/* The above statement: NO_LARGE_GENERIC is default */
#define FFTW_NO_RANK_SPLITS (1U << 14)
#define FFTW_NO_VRANK_SPLITS (1U << 15)
#define FFTW_NO_VRECURSE (1U << 16)
#define FFTW_NO_SIMD (1U << 17)
#define FFTW_NO_SLOW (1U << 18)
```

```
#define FFTW_NO_FIXED_RADIX_LARGE_N (1U << 19)
#define FFTW_ALLOW_PRUNING (1U << 20)
#define FFTW_WISDOM_ONLY (1U << 21)
#ifdef __cplusplus
}  /* extern "C" */
#endif /* __cplusplus */
#endif /* FFTW3_H */
```

E.1.2 myuir.h

```
/*****************************************************************/
/* LabWindows/CVI User Interface Resource (UIR) Include File     */
/* Copyright (c) National Instruments 2009. All Rights Reserved.  */
/*                                                               */
/* WARNING: Do not add to, delete from, or otherwise modify the   */
/*          contents of this include file.                       */
/*****************************************************************/
#include <userint.h>
#ifdef __cplusplus
    extern "C" {
#endif
/* Panels and Controls: */
#define  PANEL                           1
#define  PANEL_GRAPH                     2
/* Menu Bars, Menus, and Menu Items: */
/* (no menu bars in the resource file) */
```

```
/* (no callbacks specified in the resource file) */
#ifdef __cplusplus
    }
#endif
```

E.1.3 VppSet.h

```
#include "extcode.h"
#pragma pack(push)
#pragma pack(1)
#ifdef __cplusplus
extern "C" {
#endif
void __stdcall VppSet(long Vpp);
long __cdecl LVDLLStatus(char *errStr, int errStrLen, void *module);
#ifdef __cplusplus
} // extern "C"
#endif
#pragma pack(pop)
```

E.1.4 resource.h

```
//{{NO_DEPENDENCIES}}
// Microsoft Visual C++ generated include file.
// Used by FFbackAPI.rc
#define IDD_FORCE_FEEDBACK              102
```

```
#define IDI_MAIN                        102
#define IDC_CLOSE                       1000
#define IDC_BUTTON1                     1001
#define IDC_EDIT1                       1008
#define IDC_BUTTON3                     1010
#define IDC_BUTTON2                     1011
#define IDC_BUTTON4                     1012
#define IDC_BUTTON5                     1013
#define IDC_BUTTON6                     1016
#define IDC_EDIT2                       1018
#define IDC_EDIT3                       1019
#define IDC_ANIMATE1                    1023
#define IDC_SPLIT1                      1025
// Next default values for new objects
#ifdef APSTUDIO_INVOKED
#ifndef APSTUDIO_READONLY_SYMBOLS
#define _APS_NEXT_RESOURCE_VALUE        104
#define _APS_NEXT_COMMAND_VALUE         40001
#define _APS_NEXT_CONTROL_VALUE         1026
#define _APS_NEXT_SYMED_VALUE           101
#endif
#endif
```

E.2 Resource files

E.2.1 FFbackAPI.rc

```
// Microsoft Visual C++ generated resource script.
#include "resource.h"
#define APSTUDIO_READONLY_SYMBOLS
//////////////////////////////////////////////////////////////////////
// Generated from the TEXTINCLUDE 2 resource.
#include "afxres.h"
//////////////////////////////////////////////////////////////////////
#undef APSTUDIO_READONLY_SYMBOLS
//////////////////////////////////////////////////////////////////////
// English (U.S.) resources
#if !defined(AFX_RESOURCE_DLL) || defined(AFX_TARG_ENU)
#ifdef _WIN32
LANGUAGE LANG_ENGLISH, SUBLANG_ENGLISH_US
#pragma code_page(1252)
#endif //_WIN32
//////////////////////////////////////////////////////////////////////
// RT_MANIFEST
1                       RT_MANIFEST             "ffconst.manifest"
//////////////////////////////////////////////////////////////////////
// Dialog
IDD_FORCE_FEEDBACK DIALOGEX 250, 75, 163, 158
STYLE DS_SETFONT | DS_MODALFRAME | DS_SETFOREGROUND | WS_POPUP |
```

```
 WS_CAPTION | WS_SYSMENU
EXSTYLE WS_EX_PALETTEWINDOW
CAPTION "Ultrasonic Viscometer - Control frame"
FONT 9, "Calibri", 400, 0, 0x0
BEGIN
    DEFPUSHBUTTON   "Exit",IDCANCEL,95,126,50,14
    LTEXT           "Please click 'Initiate' button for",IDC_STATIC,
     7,4,135,8
    LTEXT           "calibrating the sensor in air.",IDC_STATIC,7,
     12,132,8
    EDITTEXT        IDC_EDIT1,12,100,136,16,ES_CENTER | ES_MULTILINE
       | ES_AUTOHSCROLL | ES_READONLY | NOT WS_BORDER
    PUSHBUTTON      "Measure",IDC_BUTTON2,85,59,50,15,BS_CENTER
    PUSHBUTTON      "Initiate",IDC_BUTTON1,21,59,50,15,BS_CENTER
     | BS_MULTILINE
    LTEXT           "Immerse the probes in solution and",IDC_STATIC,
     7,21,132,8
    GROUPBOX        "Module Status",IDC_STATIC,7,89,144,30
    GROUPBOX        "Viscosity measurement",IDC_STATIC,7,43,144,40
    LTEXT           "(c) 2009 Copyright Ramkumar Abhishek.",
     IDC_STATIC,5,145,149,8
    LTEXT           "click 'Measure' button  to start!",IDC_STATIC,
     7,29,132,8
END
#ifdef APSTUDIO_INVOKED
//////////////////////////////////////////////////////////////////
```

```
// TEXTINCLUDE

1 TEXTINCLUDE

BEGIN

    "resource.h\0"

END

2 TEXTINCLUDE

BEGIN

    "#include ""afxres.h""\r\n"

    "\0"

END

3 TEXTINCLUDE

BEGIN

    "\r\n"

    "\0"

END

#endif    // APSTUDIO_INVOKED

/////////////////////////////////////////////////////////////////////////

// Icon

// Icon with lowest ID value placed first to ensure application icon

// remains consistent on all systems.

IDI_MAIN                ICON                    "..\\directx.ico"

/////////////////////////////////////////////////////////////////////////

// DESIGNINFO

#ifdef APSTUDIO_INVOKED

GUIDELINES DESIGNINFO

BEGIN
```

```
    IDD_FORCE_FEEDBACK, DIALOG
    BEGIN
        RIGHTMARGIN, 162
        BOTTOMMARGIN, 156
    END
END
#endif    // APSTUDIO_INVOKED
#endif    // English (U.S.) resources
/////////////////////////////////////////////////////////////////////////
#ifndef APSTUDIO_INVOKED
/////////////////////////////////////////////////////////////////////////
// Generated from the TEXTINCLUDE 3 resource.
/////////////////////////////////////////////////////////////////////////
#endif    // not APSTUDIO_INVOKED
```

E.3 Source files

E.3.1 ViscosityAPI.cpp

```
//-----------------------------------------------------------------
// File: FFbackAPI.cpp
//
// Desc: Demonstrates an application which measures the flexural
//       vibration damping of Ultrasonic microprobes  when immersed
//  in a fluid compared to that in air.
```

```
// Copyright (c) Ramkumar Abhishek, Cornell University. All rights
// reserved.
//-----------------------------------------------------------------
#define STRICT
#define DIRECTINPUT_VERSION 0x0800
#include <stdio.h>
#include <tchar.h>
#include <windows.h>
#include <windowsx.h>
#include <commctrl.h>
#include <basetsd.h>
#include <mmsystem.h>
#include <dinput.h>
#include <math.h>
#include <time.h> // for wait function
#include <string.h>
#pragma warning( disable : 4996 ) // disable deprecated warning
#include <strsafe.h>
#pragma warning( default : 4996 )
#include "resource.h"
#if defined(DEBUG) | defined(_DEBUG)
#include <crtdbg.h>
#endif
// Labview header files
//CVI User Interface Resource (UIR)
#include <cvirte.h>/* needed if linking .exe in external compiler*/
```

```
#include <userint.h>
#include <ansi_c.h>
#include "myuir.h"
// NIDAQmx
#include <formatio.h>
#include <NIDAQmx.h>
// FFTW Header file
#include "fftw3.h"
// Agilent Vpp Set Header file
#include "VppSet.h"
//---------------------------------------------------------------
// Function prototypes
//---------------------------------------------------------------
//Joystick
INT_PTR CALLBACK MainDlgProc( HWND hDlg, UINT msg, WPARAM wParam,
 LPARAM lParam );
VOID FFTViscosity();
//---------------------------------------------------------------
// Defines, constants, and global variables
//---------------------------------------------------------------
#define SAFE_DELETE(p)  { if(p) { delete (p);     (p)=NULL; } }
#define SAFE_RELEASE(p) { if(p) { (p)->Release(); (p)=NULL; } }
#define FEEDBACK_WINDOW_X       20
#define FEEDBACK_WINDOW_Y       60
#define FEEDBACK_WINDOW_WIDTH   200
#define windowLength 1800
```

```
//NIDAQmx
TaskHandle taskHandle=0;
int filewritestatus = -1, k = 0;
double flag = 0;
long duration = 0, BeforeTime, AfterTime, N = 500;
int32 DAQmxErrorFlag, DAQmxDoneAcquire;
size_t nSize;
wchar_t *display;
//Labview Plotting
static int panelHandle, counter;
static int numButtonPresses = 0;
static char msgString[100];
#define NBLEFT  100
static double dataArray[50];
double x[3],y[3];

//--------------------------------------------------------------------
// Name: WinMain()
// Desc: Entry point for the application.  Since we use a simple
//       dialog for user interaction we don't need to pump messages.
//--------------------------------------------------------------------
INT WINAPI WinMain( HINSTANCE hInst, HINSTANCE, LPSTR, INT )
{
    // Enable run-time memory check for debug builds.
#if defined(DEBUG) | defined(_DEBUG)
    _CrtSetDbgFlag( _CRTDBG_ALLOC_MEM_DF | _CRTDBG_LEAK_CHECK_DF );
```

```
#endif
    InitCommonControls();
InitCVIRTE (hInst, 0, 0);
    // Display the main dialog box.
    DialogBox( hInst, MAKEINTRESOURCE( IDD_FORCE_FEEDBACK ), NULL,
     MainDlgProc );
    return 0;
}

//--------------------------------------------------------------------
// Name: MainDlgProc
// Desc: Handles dialog messages
//--------------------------------------------------------------------
INT_PTR CALLBACK MainDlgProc( HWND hDlg, UINT msg, WPARAM wParam,
 LPARAM lParam )
{
    switch( msg )
    {
        case WM_INITDIALOG:
SetWindowText(GetDlgItem(hDlg, IDC_EDIT1),_T("Hello!"));
            break;
        case WM_COMMAND:
            switch( LOWORD( wParam ) )
            {
        case IDCANCEL:
DAQmxStopTask(taskHandle);
```

```
DAQmxClearTask(taskHandle);
EndDialog( hDlg, 0 );
KillTimer( hDlg, 0 );
QuitUserInterface (0);
    DiscardPanel (panelHandle);
  CloseCVIRTE ();
                    break;
case IDC_BUTTON1:
SetWindowText(GetDlgItem(hDlg, IDC_EDIT1),_T("
 Calibrating sensor in air, please wait..."));
panelHandle = LoadPanel (0, "myuir.uir", PANEL);
if(panelHandle <0)
{
MessagePopup("Error", "Unable to load myuir.uir, make
sure it is in the same directory as this executable.");
}
DisplayPanel (panelHandle);
FFTViscosity();
PlotXY(panelHandle, PANEL_GRAPH, &x, &y, 3, VAL_DOUBLE,
VAL_DOUBLE, VAL_CONNECTED_POINTS, VAL_SOLID_CIRCLE,
VAL_DASH, 1, VAL_BLUE);
SetWindowText(GetDlgItem(hDlg, IDC_EDIT1),_T("Ready!"));
break;

case IDC_BUTTON2:
SetWindowText(GetDlgItem(hDlg, IDC_EDIT1),_T("Measuring
```

```
viscosity, please wait..."));
FFTViscosity();
PlotXY(panelHandle, PANEL_GRAPH, &x, &y, 3, VAL_DOUBLE,
VAL_DOUBLE, VAL_CONNECTED_POINTS, VAL_SOLID_CIRCLE,
VAL_SOLID, 1, VAL_RED);
SetWindowText(GetDlgItem(hDlg, IDC_EDIT1),_T("Ready!"));
          break;

        default:
          return FALSE; // Message not handled
          }
          break;

        case WM_DESTROY:
          // Cleanup everything
          EndDialog( hDlg, 0 );
KillTimer( hDlg, 0 );
FreeDirectInput();
QuitUserInterface (0);
DiscardPanel (panelHandle);
CloseCVIRTE ();
            break;
        default:
            return FALSE; // Message not handled
    }
    return TRUE; // Message handled
```

```
}


VOID FFTViscosity()
{
int NF, Fs;
NF = 2000000;
Fs = 1000000;
int32 datasize, count;
double *data_double,*Magnitude,plotdata[2000],max[3][2],maxr;
data_double = new double[NF];
Magnitude = new double[(Fs/2)+1];
fftw_complex *out;
out = (fftw_complex*) fftw_malloc(sizeof(fftw_complex) * NF);
float64 *datadump;
datadump = (float64*) malloc(sizeof(float64)*100000);
fftw_plan p;
DAQmxLoadTask ("ai0", &taskHandle1);
DAQmxErrorFlag = DAQmxStartTask(taskHandle1);
DAQmxSetBufferAttribute(taskHandle1,100000000);
for ( int vcnt = 0; vcnt < 3; vcnt++)
{
VppSet(2*(vcnt+8));
maxr = 0;
for (int rcnt = 0; rcnt < 3; rcnt++)
{
for (int icnt = 0; icnt < 20; icnt++)
```

```
{
DAQmxDoneAcquire = DAQmxReadAnalogF64(taskHandle1,
100000,10.0,DAQmx_Val_GroupByChannel,datadump,NF,
&datasize,NULL);
for (int jcnt = 0; jcnt < 100000; jcnt++)
{
data_double[icnt*100000 + jcnt] = datadump[jcnt];
count = icnt*100000 + jcnt;
}
}
p = fftw_plan_dft_r2c_1d(Fs, data_double, out, FFTW_ESTIMATE);
fftw_execute(p); /* repeat as needed */
for ( int j = 0; j<(Fs/2)+1; j++ )
Magnitude[j] = sqrt( ((out[j][0])*(out[j][0])) +
 ((out[j][1])*(out[j][1])) ) / Fs;
for ( int k = 29000; k < 30000; k++)
{
if ( k == 29000)
{max[vcnt][1] = Magnitude[k];}
plotdata[k-29000] = Magnitude[k];
if ( Magnitude[k] > max[vcnt][1] )
{
max[vcnt][1] = Magnitude[k];
max[vcnt][0] = k;
}
}
```

```
maxr = maxr + max[vcnt][1];
}
max[vcnt][1] = maxr/3;
maxr = 0;
if ( vcnt == 0 )
filewritestatus = ArrayToFile("C:/ViscosityFFTpeak.txt",
&plotdata, VAL_DOUBLE, 2000, 1, VAL_DATA_MULTIPLEXED,
VAL_GROUPS_AS_COLUMNS, VAL_SEP_BY_TAB, 0, VAL_ASCII,
VAL_TRUNCATE);
else
filewritestatus = ArrayToFile("C:/ViscosityFFTpeak.txt",
&plotdata, VAL_DOUBLE, 2000, 1, VAL_DATA_MULTIPLEXED,
VAL_GROUPS_AS_COLUMNS, VAL_SEP_BY_TAB, 0, VAL_ASCII,
VAL_APPEND);
}
fftw_destroy_plan(p);
fftw_free(out);
fflush(stdout);
DAQmxStopTask(taskHandle1);
DAQmxClearTask(taskHandle1);
filewritestatus = ArrayToFile("C:/ViscosityFFTpeak.txt",
&max, VAL_DOUBLE, 6, 2, VAL_DATA_MULTIPLEXED,
VAL_GROUPS_AS_COLUMNS, VAL_SEP_BY_TAB, 0, VAL_ASCII,
VAL_TRUNCATE);
for ( int k = 0; k < 3; k++ )
{
```

```
x[k] = 2*(k+8);

y[k] = max[k][1];

}

}
```

BIBLIOGRAPHY

[1] A. Lal, *Micromachined Silicon Ultrasonic Longitudinal-Mode Actuators: Theory and Applications to Surgery, Pumping, and Atomization.* A dissertation submitted in partial fulfilment of requirements for Doctor of Philosophy, (Electrical Engineering and Computer Sciences) at University of California, Berkeley, 1996.

[2] A. G. Kleber and Y. Rudy, "Basic mechanisms of cardiac impulse propagation and associated arrhythmias," *Physiological Reviews*, vol. 84, no. 2, pp. 431–488, 2004.

[3] P. Kohl and F. Sachs, "Mechanoelectric feedback in cardiac cells," *Phil. Trans. R. Soc. Lond. A*, vol. 359, pp. 1173–1185, 2001.

[4] G. P. Stacy, R. L. Jobe, K. Taylor, and D. E. Hansen, "Stretch-induced depolarizations as a trigger of arrhythmias in isolated canine left ventricles," *Am. J. Physiol.*, vol. 263, pp. H613–H621, 1992.

[5] C.-. R. Kong, N. Bursac, and L. Tung, "Mechanoelectrical excitation by fluid jets in monolayers of cultured cardiac myocytes," *J. Appl. Physiol.*, vol. 98, pp. 2328–2336, 2005.

[6] F. V. Hunt, "Stress and strain limits on the attainable velocity in mechanical vibration," *J. Acoust. Soc. Am*, vol. 32, no. 9, pp. 1123–1128, 1960.

[7] A. Lal and R. M. White, "Silicon microfabricated horns for power ultrasonics," *Sens. Act. A*, vol. 54, no. 1-3, pp. 542–546, 1996.

[8] K. F. Graff, *Wave motion in elastic solids.* Ohio state university press, 1975.

[9] X. Chen, *Micromachined ultrasonic actuators for biomedical applications: surgical tools, cardiac microprobes, and microfluidic actuation.* A dissertation submitted in partial fulfilment of requirements for Doctor of Philosophy, (Electrical and Computer Engineering) at Cornell University, 2006.

[10] L. G. Merkulov, "Design of ultrasonic concentrators," *Soviet Physics. Acoustics. (English translation)*, vol. 3, pp. 245–255, 1957.

[11] E. Eisner, "Complete solutions of the webster horn equation," *J. Acoust. Soc. Am*, vol. 41, p. 1126, 1967.

[12] B. Alberts, D. Bray, J. Lewis, M. Raff, K. Roberts, and J. Watson, *The Cell.* Garland Publishing, 1994.

[13] D. M. Bers, *Excitation-Contraction Coupling and Cardiac Contractile Force.* London, UK: Kluwer Academic, 2001.

[14] Heart disease and stroke statistics, 2005, american heart association (aha). [Online]. Available: http://www.americanheart.org/presenter.jhtml?identifier=3000090

[15] M. A. Allessie, F. I. M. Bonke, and F. J. C. Schopman, "Circus movement in a rabbit atrial muscle as a mechanism of tachycardia," *Circ. Res.*, vol. 33, pp. 54–77, 1973.

[16] J. M. Davidenko, A. M. Pertsov, R. Salomonsz, W. Baxter, and J. Jalife, "Stationary and drifting spiral waves of excitation in isolated cardiac muscle," *Nature*, vol. 355, pp. 349–351, 1992.

[17] I. R. Efimov, V. Sidorov, Y. Cheng, and B. Wollenzier, "Evidence of 3d scroll waves with ribbon-shaped filament as a mechanism of ventricular tachycardia in the isolated rabbit heart," *J. Cardiovasc. Electrophysiol.*, vol. 10, pp. 1452–1462, 1999.

[18] C. Bonometti, C. Hwang, D. Hough, J. J. Lee, M. C. Fishbein, H. S. Karagueuzian, and P. S. Chen, "Interaction between strong electrical stimulation and re-entrant wavefronts in canine ventricular fibrillation," *Circ. Res.*, vol. 77, pp. 407–416, 1995.

[19] F. X. Witkowski, L. J. Leon, P. A. Penkoske, W. R. Giles, M. L. Spano, W. L. Ditto, and A. T. Winfree, "Spatiotemporal evolution of ventricular fibrillation," *Nature*, vol. 392, no. 5, pp. 78–82, 1998.

[20] J. Chen, R. Mandapati, O. Berefeld, A. C. Skanes, and J. Jalife, "High-frequency periodic sources underlie ventricular fibrillation in the isolated rabbi heart," *Circ. Res.*, vol. 86, no. 1, pp. 86–93, 2000.

[21] V. N. Bitkashev, A. V. Holden, S. F. Mironov, A. M. Pertsov, and A. V. Zaitsev, "Three-dimensional aspects of re-entry in experimental

and numerical models of ventricular fibrillation," *International Journal of Bifurcation and Chaos*, vol. 9, no. 4, pp. 695–704, 1999.

[22] A. T. Winfree, "Electrical turbulence in three-dimensional heart muscle," *Science*, vol. 266, pp. 1003–1006, 1994.

[23] P. S. Chen, P. D. Wolf, E. G. Dixon, N. D. Danieley, D. W. Smith, and R. E. Idker, "Mechanism of ventricular vulnerability to single premature stimuli in open chest dogs," *Circ. Res.*, vol. 62, pp. 1191–1209, 1988.

[24] K. Najafi, K. D. Wise, and T. Mochizuki, "A high-yield ic-compatible multichannel recording array," *IEEE Trans. Electron Devices*, vol. 32, no. 7, pp. 1206–1211, 1985.

[25] K. Najafi and K. D. Wise, "A high-yield ic-compatible multi-channel recording array," *IEEE J. Solid-State Circuits*, vol. 21, no. 6, pp. 1035–1044, 1986.

[26] G. Ensell, D. Banks, D. Ewins, W. Balachandran, and P. Richards, "Silicon-based microelectrodes for neurophysiology fabricated using a gold metallization/nitride passivation system," *IEEE J. Microelectromech. Syst.*, vol. 5, no. 2, pp. 117–121, 1996.

[27] D. T. Kewley, M. D. Hills, D. A. Borkholder, I. E. Opris, N. I. Maluf, C. W. Stormemnt, J. M. Bower, and G. T. A. Kovacs, "Plasma-etched neural probes," *Sens. Act. A.*, vol. 58, pp. 27–35, 1997.

[28] T. H. Yoon, E. J. Hwang, D. Y. Shin, S. I. Park, S. J. Oh, and S. C. Jung, "A micromachined silicon depth probe for multichannel neural recording," *IEEE Trans. Biomed. Eng.*, vol. 47, no. 8, pp. 1082–1087, 2000.

[29] K. Najafi, "Solid-state microsensors for cortical recordings," *IEEE Eng. Med. Biol. Mag.*, vol. 13, no. 3, pp. 375–387, 1994.

[30] K. Najafi and J. F. Hetke, "Strength characterization of silicon in neurophysiological tissues," *IEEE Trans. Biomed. Eng.*, vol. 37, no. 5, pp. 474–481, 1990.

[31] H. Yamada and F. G. Evans, *Strength of biological materials*. Baltimore, MD: The Williams and Wilkins Company, 1970.

[32] A. Lal, "Silicon-based surgical tools," in *Proceedings of the 20th Annual IEEE*

International Conference on Engineering and Medicine in Biology Society (EMBS'98), Hong Kong, China, 1998, pp. 2785–2790.

[33] X. Chen and A. Lal, "Micromachined ultrasonic ophthalmic microsurgical tool with integrated pressure sensor," in *Proceedings of the 11th Annual IEEE International Conference on Solid-State Sensors and Actuators (Transducers'01)*, Munich, Germany, 2001, pp. 427–430.

[34] I. S. Son, A. Lal, B. Hubbard, and T. Olsen, "A multifunctional silicon-based microscale surgical system," *Sens. Act. A.*, vol. 91, pp. 351–356, 2001.

[35] K. S. Suslick, *Ultrasound - Its Chemical, Physical and Biological Effects.* New York, NY: VCH Publishers, 1988.

[36] L. Frizell, "Therapeutic ultrasound," in *Short course at the IEEE Ultrasonic Symposium*, San Antonio, USA, 1996.

[37] J. Tautz, F. Roces, and B. Holldobler, "Use of a sound-based vibratome by leaf-cutting ants," *Science*, vol. 267, pp. 84–87, 1995.

[38] Y. C. Fung, *Biomechanics- Mechanical Properties of Living Tissues.* Michigan, USA: Springer-Verlag, 1993.

[39] M. K. Nabibekov, B. D. Plyushchenkov, and I. Y. Sarikisov, "Study of ultrasonic cutting of soft biotissues," *Mekhanika Komozitnykh Materialov (Mechanics of Composite Materials)*, vol. 3, pp. 519–524, 1980.

[40] ——, "Methods for raising the efficiency of the ultrasonic cutting of soft biological tissues," *Mekhanika Komozitnykh Materialov (Mechanics of Composite Materials)*, vol. 4, pp. 703–707, 1980.

[41] X. Chen, A. Lal, M. L. Riccio, and R. F. G. Jr., "Ultrasonically actuated silicon microprobes for cardiac signal recording," *IEEE Trans. Biomed. Eng.*, vol. 53, no. 8, pp. 1665–1671, 2006.

[42] L. A. Geddes, "Historical evolution of circuit models for the electrode-electrolyte interface," *Ann. Biomed. Eng.*, vol. 25, pp. 1–14, 1997.

[43] G. T. A. Kovacs, *Enabling Technologies for Cultured Neural Networks.* London, U.K.: Academic Press, 1988, pp. 121–165.

[44] E. T. McAdams and J. Jossinet, "Physical interpretation of schwan's limit voltage of linearity," *Med. Biol. Eng. Comp.*, vol. 32, pp. 126–130, 1994.

[45] D. C. Grahame, "Mathematical theory of the faradaic admittance," *J. Electrochem. Soc.*, vol. 99, pp. 370C–385C, 1952.

[46] A. J. Bard and L. R. Faulkner, *Electrochemical Methods*. New York, NY: Wiley, 2001.

[47] J. O. Bockris and A. K. N. Reddy, *Modern electrochemistry*. New York, NY: Plenum, 1970.

[48] S.-M. Kang and Y. Leblebigi, *CMOS digital integrated circuits*. MCGraw-Hill, 1999.

[49] T. Sakurai and K. Tamaru, "Simple formulas for two- and three-dimensional capacitances," *IEEE Trans. Electron Devices*, vol. 30, no. 2, pp. 183–185, 1983.

[50] X. Qi, B. Kleveland, Z. Yu, S. Wong, R. Dutton, and T. Young, "On-chip inductance modeling of vlsi interconnects," in *Digest of Technical Papers -IEEE International Solid-State Circuits Conference*, San Francisco, USA, 2000, pp. 172–173.

[51] W. Franks, I. Schenker, P. Schmutz, and A. Hierlemann, "Impedance characterization and modeling of electrode for biomedical applications," *IEEE Trans. Biomed. Eng.*, vol. 52, no. 7, pp. 1295–1302, 2005.

[52] E. T. McAdams, A. Lackermeier, J. A. McLaughlin, D. Macken, and J. Jossinet, "The linear and nonlinear electrical properties of the electrodeelectrolyte interface," *Biosen. Bioelectron.*, vol. 10, pp. 67–74, 1995.

[53] W. A. Franks, *Towards Monolithic CMOS Cell-Based Biosensors*. A dissertation submitted in partial fulfilment of requirements for Doctor of Philosophy, at Eidgenoessische Technische Hochschule (ETH), Zurich, Switzerland, 2005.

[54] M. L. Riccio, M. L. Koller, and R. F. J. Gilmour, "The linear and nonlinear electrical properties of the electrode-electrolyte interface," *Circ. Res.*, vol. 84, pp. 955–963, 1999.

[55] B. J. Caldwell, B. S. Hon, I. J. Legrice, D. A. Hooks, D. C. S. Tai, A. J.

Pullan, and B. Smaill, "Intramural measurement of transmembrane potential in the isolated pig heart: validation of a novel technique," *J. Cardiovas. electrophys.*, vol. 16, no. 9, pp. 1001–1010, 2005.

[56] M. L. Pressler, P. N. Munster, and X. D. Huang, "Gap junction distribution in the heart: functinal relevance," in *Cardiac Electrophysiology: from Cell to Bedside*. Philadelphia, PA: W. B. Saunders Company, 1995, p. 148.

[57] C. H. Luo and Y. Rudy, "A model of the ventricular cardiac action potential. depolarization, repolarization, and their interaction," *Circ. Res.*, vol. 68, pp. 1501–1526, 1991.

[58] C. Gold, D. A. Henze, C. Koch, and G. Buzsaki, "On the origin of the extracellular action potential waveform: a modeling study," *J. Neurophys.*, vol. 95, pp. 3113–3128, 2006.

[59] H. V. Huikuri, A. Castellanos, and R. J. Myerburg, "Sudden death due to cardiac arrhythmias," *N. Engl. J. Med.*, vol. 345, p. 14731482, 2001.

[60] C. Veltmann, M. Borggrefe, R. Schimpf, and C. Wolpert, "Fatal inappropriate icd shock," *J. Cardio. Electrophysiol.*, vol. 18, no. 3, pp. 326–328, 2007.

[61] E. B. Schron, D. V. Exner, Q. Yao, L. S. Jenkins, J. S. Steinberg, J. R. Cook, S. P. Kutalek, P. L. Friedman, R. S. Bubien, R. L. Page, and J. Powell, "Quality of life in the antiarrhythmics versus implantable defibrillators trial: impact of therapy and influence of adverse symptoms and defibrillator shocks," *Circulation*, vol. 105, no. 5, pp. 589–594, 2002.

[62] F. Guharay and F. Sachs, "Stretch-activated single ion channel currents in tissue-cultured embryonic check skeletal muscle," *J. Physiol.*, vol. 352, pp. 685–701, 1984.

[63] A. Fabiato and F. Fabiato, "Dependence of contractile activation of skinned cardiac cells on the sarcomere length," *Nature*, vol. 256, pp. 53–56, 1975.

[64] H. Hu and F. Sachs, "Mechanically activated currents in chick heart cells," *J. Membrane Biol.*, vol. 154, pp. 205–216, 1996.

[65] G. C. L. Bett and F. Sachs, "Activation and inactivation of mechanosensitive currents in the chick heart," *J. Membrane Biol.*, vol. 173, pp. 237–254, 2000.

[66] F. Sachs, "Mechanical transduction by ion channels: how forces reach the channel," in *Cytoskeletal regulation of membrane function: Society of General Physiologists 50th Ann. Symp.*, Marine Biological Laboratory, Woods Hole, MA, 1996, pp. 209–218.

[67] T. Zeng, G. C. L. Bett, and F. Sachs, "Stretch-activated whole cell currents in adult rat cardiac myocytes," *Am. J. Physiol.*, vol. 278, pp. H548–H557, 2000.

[68] W. Craelius, "Stretch-activation of rat cardiac myocytes," *Exp. Phys.*, vol. 78, pp. 411–423, 1993.

[69] P. Kohl, J. Y. L. Guennec, and E. White, "Diastolic (dys-) function and electrophysiology," *Cardiol. Clin. North America*, vol. 18, no. 3, pp. 637–651, 2000.

[70] E. White, J. Y. L. Guennec, J. M. Nigretto, F. Gannier, J. A. Argibay, and D. Garnier, "The effects of increasing cell length on auxotonic contractions; membrane potential and intracellular calcium transients in single guinea-pig ventricular myocytes," *Exp. Physiol.*, vol. 78, pp. 65–78, 1993.

[71] M. Zabel, B. S. Koller, F. Sachs, and M. R. Franz, "Stretch-induced voltage changes in the isolated beating heart: importance of the timing of stretch and implications for stretch-activated ion channels," *Cardiovasc. Res.*, vol. 32, pp. 120–130, 1996.

[72] J. Boland and J. Troquet, "Intracellular action potential changes induced in both ventricles of the rat by an acute right ventricular pressure overload," *Cardiovasc. Res.*, vol. 14, pp. 735–740, 1980.

[73] B. B. Lerman, D. Burkhoff, D. T. Yue, M. R. Franz, and K. Sagawa, "Mechano-electrical feedback: Independent role of preload and contractility in modulation of canine ventricular excitability," *J. Clin. Invest.*, vol. 76, pp. 1843–1850, 1985.

[74] M. R. Franz, R. Cima, D. Wang, D. Profitt, and R. Kurz, "Electrophysiological effects of myocardial stretch and mechanical determinants of stretch-activated arrhythmias," *Circulation*, vol. 86, no. 3, pp. 968–978, 1992.

[75] P. Kohl, A. G. Kamkin, I. S. Kiseleva, and D. Noble, "Mechanosensitive fibroblasts in the sino-atrial node region of rat heart: interaction with cardiomyocytes with possible role," *Exp. Physiol.*, vol. 79, pp. 943–956, 1994.

[76] F. Gannier, E. White, D. Garnier, and J. Y. L. Guennec, "A possible mechanism for large stretch-induced increase in [ca2+]i in isolated guinea-pig ventricular myocytes," *Cardiovasc. Res.*, vol. 32, pp. 158–167, 1996.

[77] F. Sachs, "Modelling mechanical-electrical transduction in the heart," in *Cell mechanics and cellular engineering*. Springer-Verlag, 1994, pp. 308–328.

[78] T. L. Reimer, E. A. Sobie, and L. Tung, "Stretch-induced changes in arrythmogenesis and excitability in experimentally based heart cell models," *Am. J. Physiol.*, vol. 275, pp. H431–H442, 1998.

[79] P. Kohl, K. Day, and D. Noble, "Cellular mechanism of cardiac mechanoelectric feedback in a mathematical model," *Can. J. Cardio.*, vol. 14, pp. 111–119, 1998.

[80] K. Day, *Length-dependent modulation of mammalian cardiomyocyte electrophysiology: experimental findings and biocomputational analysis*. A dissertation submitted in partial fulfilment of requirements for Doctor of Philosophy, (Deparment of Physiology) at Oxford University, 1996.

[81] L. Tung, "Detrimental effects of electrical fields on cardiac muscle," *Proc. IEEE*, vol. 84, pp. 366–378, 1996.

[82] R. W. F. II and L. Tung, "Factors governing mechanical stimulation in frog hearts," *Am. J. Physiol.*, vol. 277, pp. H2311–2320, 1999.

[83] G. Isenberg, V. Kazanski, D. Kondratev, M. F. Gallitelli, I. Kiseleva, and A. Kamkin, "Differential effects of stretch and compression on membrane currents and $[na^+]_c$ in ventricular myocytes," *Prog. Biophys. Mol. Biol.*, vol. 82, pp. 43–56, 2003.

[84] G. C. L. Bett and F. Sachs, "Whole-cell mechanosensitive currents in rat ventricular myocytes activated by direct stimulation," *J. Membrane Biol.*, vol. 173, pp. 255–263, 2000.

[85] A. Nesbitt, P. J. Cooper, and P. Kohl, "Re-discovering commotio cordis," *The Lancet*, vol. 357, pp. 1195–1197, 2001.

[86] E. N. Harvey, "The effect of high frequency sound waves on heart muscle and other irritable tissues," *Am. J. Physiol.*, vol. 91, pp. 284–290, 1929.

[87] S. I. Zakharov, K. Y. Bogdanov, L. R. Gavrilov, V. P. Yushin, and

L. V. Rozenshtraukh, "Action of ultrasound on strength of contraction and action potential of the papillary muscle of the rat heart," *Byulleten' Eksperimental'noi Biologii I Meditsiny*, vol. 107, no. 4, pp. 423–426, 1989.

[88] D. Dalecki, B. Keller, E. Cartensen, D. Neel, J. Palladino, and A. Noodergraaf, "The effect of high frequency sound waves on heart muscle and other irritable tissues," *Ultrasound Med. Biol.*, vol. 17, no. 4, pp. 341–346, 1991.

[89] D. Dalecki, B. Keller, C. Raeman, and E. Carstensen, "Effects of pulsed ultrasound on the frog heart: thresholds for changes in cardiac rhythm and aortic pressure," *Ultrasound Med. Biol.*, vol. 19, no. 5, pp. 385–390, 1993.

[90] D. Dalecki, C. Raeman, and E. Carstensen, "Effects of pulsed ultrasound on the frog heart: an investigation of heating as a potential mechanism," *Ultrasound Med. Biol.*, vol. 19, no. 5, pp. 391–398, 1993.

[91] D. Dalecki, "Mechanical bioeffects of ultrasound," *Annu. Rev. Biomed. Eng.*, vol. 6, pp. 229–248, 2004.

[92] K. Tachibana, "Emerging technologies in therapeutic ultrasound: Thermal ablation to gene delivery," *Hum. Cell*, vol. 17, pp. 7–15, 2004.

[93] R. K. Schlicher, H. Radhakrishna, T. P. Tolentino, R. P. Apkarian, V. Zarnitsyn, and M. R. Prausnitz, "Mechanism for intracellular delivery by acoustic cavitation," *Ultrasound in Med. and Biol.*, vol. 32, no. 6, pp. 915–924, 2006.

[94] B. C. Towe and R. Rho, "Ultrasonic cardiac pacing in the porcine model," *IEEE Trans. Biomed. Eng.*, vol. 53, no. 7, pp. 1446–1448, 2006.

[95] N. T. Wells, *Biomedical ultrasonics*. New York, NY: Academic Press, 1976.

[96] D. Wise, *Bioinstrumentation and Biosensors*. New York, NY: Marcel Dekker, 1991.

[97] A. S. O. Rudenko and S. Emelianov, "Effects of pulsed ultrasound on the frog heart: an investigation of heating as a potential mechanism," *J. Acoust. Soc. Am.*, vol. 99, no. 5, pp. 2791–2798, 1996.

[98] L. A. Cyster, D. M. Grant, K. G. Parker, and T. L. Parker, "The effect of

surface chemistry and structure of titanium nitride (tin) films on primary hippocampal cells," *Biomol. Eng.*, vol. 19, pp. 171–175, 2002.

[99] U. Egert, B. Schlosshauer, S. Fennrich, W. Nisch, M. Fejtl, T. Knott, T. Muller, and H. Hammerle, "The effect of surface chemistry and structure of titanium nitride (tin) films on primary hippocampal cells," *Brain Res. Prot.*, vol. 2, pp. 229–242, 1998.

[100] T. Gabay, M. B.-. David, I. Kalifa, R. Sorkin, Z. R. Abrams, E. B.-. Jacob, and Y. Hanein, "Electro-chemical and biological properties of carbon nanotube based multi-electrode arrays," *Nanotechnology*, vol. 18, pp. 1–6, 2007.

[101] I. S. Son and A. Lal, "A multifunctional silicon-based microscale surgical system," in *Technical Digest of the Solid-State Sensor, Actuator and Microsystems Workshop (Hilton Head 2000)*, 2000.

[102] C. Lee and A. Lal, "Silicon ultrasonic horns for thin film accelerated stress testing," in *Proceedings of the IEEE Ultrasonics Symposium*, vol. 2, 2001, pp. 867–870.

[103] S. Tsai, Y. Song, T. Tseng, Y. Chou, W. Chen, and C. Tsai, "High-frequency, silicon-based ultrasonic nozzles using multiple fourier horns," *IEEE Trans. Ultrason., Ferroelect., Freq. Contr.*, vol. 51, no. 3, pp. 277–285, 2004.

[104] S. P. Dimaio and S. E. Sacudean, "Needle insertion modelling and simulation," *Proceedings of the IEEE International Conference on Robotics and Automation*, pp. 2098–2105, 2002.

[105] A. M. Okamura, C. Simone, and M. D. O'Leary, "Force modeling for needle insertion into soft tissue," *IEEE Transactions on Biomedical Engineering*, vol. 51, no. 10, pp. 1707–1716, October 2004.

[106] A. Menciassi, A. Eisinberg, G. Scalari, C. Anticoli, M. C. Carrozza, and P. Dario, "Force feedback-based microinstrument for measuring tissue properties and pulse in microsurgery," in *Proceedings of the 2001 IEEE International Conference on Robotics and Automation*, Seoul, Korea, May 2001, pp. 626–631.

[107] E. Obermier, P. Kopystynski, and R. Niebl, "Characteristics of polysilicon layers and their application in sensors," in *Proceedings of the IEEE Solid-State Sensors Workshop*, 1986, pp. 19–35.

[108] S. J. Silber, "Microsurgical tese and the distribution of spermatogenesis in non-obstructive azoospermia," *Hum. Reprod.*, vol. 15, no. 11, pp. 2278–2284, 2000.

[109] Male infertility: Sperm retrieval techniques, james buchanan brady foundation, department of urology, cornell weill medical college. [Online]. Available: http://www.cornellurology.com/infertility/srt/azoospermia.shtml

[110] P. Devroey, S. J. Silber, and Z. Nagy, "Ongoing pregnancies and birth after intracytoplasmic sperm injection (icsi) with frozen-thawed epididymal spermatozoa," *Hum. Reprod.*, vol. 10, pp. 903–906, 1995.

[111] S. J. Silber, P. Nagy, and J. Liu, "The use of epididymal and testicular spermatozoa for intracytoplasmic sperm injection: The genetic implications for male infertility," *Hum. Reprod.*, vol. 10, pp. 2031–2043, 1995.

[112] S. J. Silber, A. C. V. Steirteghem, and P. Devroey, "Sertoli cell only revisited," *Hum. Reprod.*, vol. 10, pp. 1031–1032, 1995.

[113] Z. Zuckerman, L. J. Rodriguez-Rigau, and D. B. Weiss, "Quantitative analysis of the seminiferous epithelium in human testicle biopsies and the relation of spermatogenesis to sperm density," *Fertil. Steril.*, vol. 30, pp. 448–455, 1978.

[114] S. J. Silber and L. J. Rodriguez-Rigau, "Quantitative analysis of testicle biopsy: determination of partial obstruction and prediction of sperm count after surgery for obstruction," *Fertil. Steril.*, vol. 36, pp. 480–485, 1981.

[115] S. J. Silber, J. Liu, and A. C. V. Steirteghem, "Normal pregnancies resulting from testicular sperm extraction and intracytoplasmic sperm injection for azoospermia due to maturation arrest," *Fertil. Steril.*, vol. 66, pp. 110–117, 1996.

[116] S. J. Silber, Z. Nagy, and P. Devroey, "Distribution of spermatogenesis in the testicles of azoospermic men: The presence or absence of spermatids in the testes of men with germinal failure," *Hum. Reprod.*, vol. 12, pp. 2422–2428, 1997.

[117] P. N. Schlegel, G. D. Palermo, and M. Goldstein, "Testicular sperm extraction with intracytoplasmic sperm injection for non-obstructive azoospermia," *Urology*, vol. 49, pp. 435–440, 1997.

[118] I. Craft, M. Tsirigotis, E. Courtauld, and G. Farrer-Brown, "Testicular needle aspiration as an alternative to biopsy for the assessment of spermatogenesis," *Hum. Reprod.*, vol. 12, pp. 1483–1487, 1997.

[119] S. Friedler, A. Raziel, and D. Strassburger, "Testicular sperm retrieval by percutaneous five needle sperm aspiration compared with testicular sperm extraction by open biopsy in men with non-obstructive azoospermia," *Hum. Reprod.*, vol. 12, pp. 1488–1491, 1997.

[120] P. N. Schlegel, "Testicular sperm extraction: microdissection improves sperm yield with minimal tissue excision," *Hum. Reprod.*, vol. 14, no. 1, pp. 131–135, 1999.

[121] F. Piefke, "Chord length distribution of the ellipse," *Lithuanian Mathematical Journal*, vol. 19, no. 3, pp. 325–333, 1979.

[122] A. Hennig and H. Elias, "Contributions to the geometry of sectioning. *vii*. elliptical cylinders," *Z. Wiss. Mikrosk.*, vol. 66, no. 4, pp. 226–234, 1964.

[123] J. J. Boyle, J. Jenkins, I. C. Mckay, A. R. Mcphaden, and G. B. M. Lindop, "An assessment of the distortion of arteries due to sectioning in endomyocardial biopsies," *J. Pathol.*, vol. 181, pp. 243–246, 1997.

[124] M. Amer, W. Zohdy, T. A. E. Naser, H. Hosny, M. Arafa, and E. Fakhry, "Single tubule biopsy: a new objective microsurgical advancement for testicular sperm retrieval in patients with nonobstructive azoospermia," *Fertil. Steril.*, vol. 89, no. 3, pp. 592–596, 2008.

[125] T. Y. Wing and A. K. Christensen, "Morphometric studies on rat seminiferous tubules," *Am. J. Anat.*, vol. 165, pp. 13–25, 1982.

[126] J. R. Latendresse, A. R. Warbrittion, H. Jonassen, and D. M. Creasy, "Fixation of testes and eyes using davidsons fluid: Comparison with bouins fluid and conventional davidsons fluid," *Toxicol. Pathol.*, vol. 30, no. 4, p. 524533, 2002.

[127] F. Gaytan, M. C. Lucena, E. Munoz, and R. Paniagua, "Morphometric aspects of rat testis development," *J. Anat.*, vol. 145, pp. 155–159, 1986.

[128] T. M. M. N. C. Mills and A. R. Means, "Morphometric and biochemical changes which occur during postnatal development and maturation of the rat testis," *Biol. Reprod.*, vol. 17, pp. 124–130, 1977.

[129] S. Ariyaratne, I. Kim, N. Mills, I. Mason, and C. M.-. Handagama, "Effects of ethane dimethane sulfonate on the functional structure of the adult rat testis," *Arch. Androl.*, vol. 49, pp. 313–326, 2003.

[130] Z.-. W. Yang, L.-. S. Kong, Y. Guo, J.-. Q. Yin, and N. Mills, "Histological changes of the testis and epididymis in adult rats as a result of leydig cell destruction after ethane dimethane sulfonate treatment: a morphometric study," *Asian J. Androl.*, vol. 8, no. 3, pp. 289–299, 2006.

[131] R. L. Whitmore, *Rheology of the Circulation*. Garland Publishing, 1994.

[132] R. S. Rosenson, A. McCormick, and E. F. Uretz, "Distribution of blood viscosity values and biochemical correlates in healthy adults," *Clinical Chemistry*, vol. 42, pp. 1189–1195, 1996.

[133] S. Chien, "Blood rheology in myocardial infarction and hypertension," *Biorheology*, vol. 23, no. 6, pp. 633–653, 1986.

[134] T. Somer and H. J. Meiselman, "Disorders of blood viscosity," *Annals of Medicine*, vol. 25, pp. 31–39, 1993.

[135] S. G. Wanamethee, P. H. Whincup, A. G. Shaper, A. Rumley, L. Lennon, and G. D. O. Lowe, "Circulating inflammatory and hemostatic biomarkers are associated with risk of myocardial infarction and coronary death, but not angina pectoris, in older men," *J. .Thromb. Haemost.*, vol. 7, pp. 1605–1611, 2009.

[136] L. J. Tamariz, J. H. Young, J. S. Pankow, H. C. Yeh, M. I. Schmidt, B. Astor, and F. L. Brancati, "Blood viscosity and hematocrit as risk factors for type 2 diabetes mellitus: the atherosclerosis risk in communities (aric) study," *Am. J. .Epidemiol.*, vol. 168, no. 10, pp. 1153–1160, 2008.

[137] D. R. Gross and N. H. Hwang, *The Rheology of Blood, Blood Vessels and Associated Tissues*. Sitjthoff and Noordhoff, 1981.

[138] R. B. Devereux, D. B. Case, M. H. Alderman, T. G. Pickering, S. Chien, and J. H. Laragh, "Possible role of increased blood viscosity in the hemodynamics of systemic hypertension," *Am. J. Cardiol.*, vol. 85, pp. 1265–1268, 2000.

[139] M. V. Kameneva, J. F. Antaki, M. J. Watach, H. S. Borovetz, and R. L. Kormos, "Heparin effect on red blood cell aggregation," *Biorheology*, vol. 31, no. 3, pp. 297–304, 1994.

[140] W. H. Reinhart, A. Haeberli, J. Stark, and P. W. Straub, "Influence of blood withdrawal and anticoagulant on clotting activity, hematologic data, and certain rheologic measurements," *Journal of Laboratory and Clinical Medicine*, vol. 115, no. 1, pp. 98–103, 1990.

[141] J. Crouch, B. A. Keagy, J. A. Schwartz, J. R. Wilcox, and G. J. Johnson, "The effect of heparin on whole-blood viscosity," *Current Surgery*, vol. 43, no. 5, pp. 395–398, 1986.

[142] W. I. Rosenblum, "In vitro measurements of the effects of anticoagulants on the flow properties of blood: The relationship of these effects to red cell shrinkage," *Blood*, vol. 31, no. 2, pp. 234–241, 1968.

[143] H. Muramatsu, M. Suda, T. Ataka, A. Seki, E. Tamiya, and I. Karube, "Piezoelectric resonator as a chemical and biochemical sensing device," *Sensors Actuators*, vol. 21A, no. 1-3, pp. 362–368, 1990.

[144] S. J. Martin, A. J. Ricco, and R. C. Hughes, "Acoustic wave devices for sensing in liquids," in *4th International Conference on Solid-State Sensors and Actuators (Transducers'87)*, Tokyo, Japan, June 1987, pp. 478–481.

[145] B. A. Martin, S. W. Wenzel, and R. M. White, "Viscosity and density sensing with ultrasonic plate waves," *Sensors Actuators*, vol. 22A, no. 1-3, pp. 704–708, 1990.

[146] H. L. Bandey, R. W. Cernosek, W. E. L. III, and L. E. Ondrovic, "Blood rheological characterization using the thickness-shear mode resonator," *Biosens. and Bioelec.*, vol. 7, pp. 1605–1611, 2009.

[147] T. J. Cheng, H. C. Chang, and T. M. Lin, "A piezoelectric quartz crystal sensor for the determination of coagulation time in plasma and whole blood," *Biosens. and Bioelec.*, vol. 13, no. 2, pp. 147–156, 1998.

[148] A. Ramkumar, X. Chen, and A. Lal, "Silicon ultrasonic horn driven microprobe viscometer," 2006, pp. 1449–1452.

[149] N. G. Tsierkezos and I. E. Molinou, "Thermodynamic properties of water + ethylene glycol at 283.15, 293.15, 303.15, and 313.15 k," *Journal of Chemical and Engineering Data*, vol. 43, pp. 989–993, 1998.

[150] W. C. Wang, M. Afromowitz, and B. Hannaford, "Technique for mechanical

measurement using optical scattering from a micro-pipette," *IEEE Trans. Biomed. Eng.*, vol. 41, no. 3, pp. 298–304, 1994.

[151] G. G. Stokes, "On some cases of fluid motion," *Proceedings of the Cambridge Philosophical Society*, vol. 8, pp. 105–137, 1843.

[152] C. Riesch, E. K. Reichel, F. Keplinger, and B. Jakoby, "Characterizing vibrating cantilevers for liquid viscosity and density sensing," *J. Sensors*, no. 697062, pp. 1–9, 2008.